



The University of
Nottingham

On The Investigation of Bridge Buffet- ing Simulation Techniques

To my family

Zhe Liu, B. Eng and M. Eng (Res)

**Thesis submitted to the University of Nottingham for the Degree of
Doctor of Philosophy**

2011.08

**School of Civil Engineering
University of Nottingham**

**BEST COPY
AVAILABLE**

**TEXT BOUND INTO
THE SPINE**

To my family

Acknowledgment

Firstly I would like to express my thanks to my supervisors, Dr. John Owen and David Hargraves, whose supports throughout my research helped me to finish this dissertation.

I would also like to express my deepest thanks to both the Chinese and UK governments, for supplying me the scholarship and giving me an opportunity to study at the University of Nottingham to do an advanced research project.

My deepest appreciation is reserved for my family and Tom Bentley, who is my best friend and gave me so much help in my thesis writing. Firstly I want to thank to my father and mother, if without their help and inspiration, I couldn't have persisted in my PhD study. At the same time I want to express my deepest thanks to my wife who spent four years waiting for my graduation. It is very important that she brought new life to my family. I hope this paper can be dedicated to my two year old daughter and my wife, and I hope their future life will be full of happiness.

Abstract

The buffeting response is a type of vibration caused by wind turbulence. As the bridge span and structural complexity increase, this kind of response is notable. Therefore more accurate analysis simulation methods are needed to investigate this aerodynamic phenomenon. The aim of this thesis is to review, discuss and compare the different bridge buffeting simulation approaches in the frequency domain and find the possibility of Computational Fluid Dynamic (CFD) method application in bridge buffeting prediction.

In this thesis, the conventional bridge buffeting statistical analysis methods considering the influence of different parameters such as mode coupling, self-excited forces and aerodynamic admittance on the simulation results are firstly reviewed and compared. Since wind turbulence may not excite all structural vibration modes in some frequency ranges, an alternative approach based on the Proper Orthogonal Decomposition (POD) is proposed to study the effective turbulence contribution to the structural vibration. However due to the complexity of turbulence, quasi-steady theory is widely adopted and some semi-empirical functions such as aerodynamic admittance, joint acceptance are introduced to simplify the simulation.

With the development of CFD method, CFD simulation of bridge aerodynamic phenomena has become possible. Since the bridge buffeting response is induced by wind turbulence, it is very important to capture the time varying characteristics of wind turbulence. In CFD technique, to close the Navier-Stokes equations and reflect unsteady characteristics, turbulence modelling is always adopted. At present Direct Numerical Simulation (DNS) is an accurate model to capture the time variation unsteady characteristic of the wind turbulence. However, the problems of civil engineering are always high Reynolds numbers, which make the simulation of aerodynamic phenomena of civil engineering impractical based on DNS method. Therefore an alternative model, known as Large Eddy Simulation (LES), becomes popular. In this thesis an unsteady inlet boundary generation technique based on an Autoregressive Moving Average (ARMA) model is proposed to simulate the unsteady inflow turbulence. 3D LES will be selected to validate the applicability of this model in the prediction of the unsteady characteristic of buffeting simulation by investigating the flow characteristic around a square cylinder under different mesh density and different LES model such as standard LES model, dynamic LES model and WALE model at Reynolds number 13,000. Before comparing the influence of inflow boundary condition with turbulence intensity (5%) on the flow around a square cylinder, an empty domain is selected to validate current inflow turbulence generation technique. Major steps of Fluid Structure Interaction (FSI), suitable for future simulation of bridge structural buffeting response, are proposed to predict the structural buffeting response induced by the inflow turbulence. To test the propose procedure of FSI, a square cylinder will be used, the across-flow oscillation of square cylinder with constant damping ratio will be considered to investigate the influence of steady inlet boundary condition and unsteady one on the response of structure. In addition different LES models are considered to compare their influence on the response of square cylinder.

Chapter

1 Introduction.....	1
1.1 <i>Background</i>	<i>1</i>
1.2 <i>Problem</i>	<i>1</i>
1.3 <i>Assumption</i>	<i>3</i>
1.4 <i>Objective</i>	<i>4</i>
1.5 <i>Methodology</i>	<i>4</i>
1.6 <i>Contents</i>	<i>5</i>
2 Overview of Bridge Aerodynamic Phenomena.....	7
2.1 <i>Introduction</i>	<i>7</i>
2.2 <i>Bridge Flutter Theory's Introduction</i>	<i>8</i>
2.2.1 <i>Bridge Flutter Response Formulation</i>	<i>8</i>
2.2.2 <i>Bridge Flutter Analysis Theory's Development</i>	<i>8</i>
2.3 <i>Bridge Buffeting Analysis Theory's Development</i>	<i>9</i>
2.3.1 <i>Bridge Buffeting Definition</i>	<i>9</i>
2.3.2 <i>Bridge Buffeting Theory's Development in Frequency Domain</i>	<i>9</i>
2.3.3 <i>Uncertainties of Bridge Buffeting Theory</i>	<i>18</i>
2.3.4 <i>Bridge Buffeting Time Domain Analysis Method</i>	<i>24</i>
2.3.4.1 <i>Wind Load Composition</i>	<i>26</i>
2.3.4.2 <i>Gust Wind Velocity Simulation Technique</i>	<i>26</i>
2.3.5 <i>Buffeting Prediction Based on Deterministic Technique</i>	<i>27</i>
2.4 <i>Vortex Shedding Introduction</i>	<i>29</i>
2.5 <i>Galloping Response Introduction</i>	<i>31</i>
2.6 <i>Conclusions</i>	<i>31</i>
3 Turbulence Models and FSI Techniques in Bridge Buffeting Prediction.....	33
3.1 <i>Introduction</i>	<i>33</i>

3.2	<i>Turbulence Models' Development</i>	33
3.2.1	Steady RANS Model.....	35
3.2.2	URANS Model.....	35
3.2.3	LES and DES Models	36
3.2.3.1	DES Model.....	36
3.2.3.2	LES Model.....	39
3.2.4	DNS Model.....	43
3.3	<i>Difficulties of Applying LES in CWE</i>	43
3.4	<i>Coupled System</i>	45
3.5	<i>Solution Scheme of Coupled System</i>	46
3.5.1	Monolithic Schemes.....	47
3.5.2	Partition or Staggered Schemes.....	47
3.6	<i>Grid Deformation Approach</i>	50
3.7	<i>Interfacing Procedures of Fluid and Structure Solves</i>	51
3.8	<i>Conclusions</i>	53
4	Bridge Buffeting Response Simulation in Frequency Domain	54
4.1	<i>Introduction</i>	54
4.2	<i>Assumptions and Methodology</i>	54
4.2.1	Assumptions.....	54
4.2.2	Methodology.....	54
4.3	<i>Computational Theory Description</i>	55
4.3.1	Wind Load Discretization.....	55
4.3.2	Bridge Buffeting Numerical Calculation Method.....	58
4.4	<i>Test Case and Parameters</i>	62
4.4.1	General Information of Test Case.....	62
4.4.2	Design Parameters of Test Case.....	64
4.4.3	Wind Velocity Power Spectrum Models.....	65

4.5 Results Analysis.....	68
4.5.1 Structure Self-vibration Modes Analysis.....	68
4.5.2 Results Analysis Based on the Multimode Aeroelastic Coupling Method	72
4.5.3 Results Analysis Based on POD Buffeting Theory.....	78
4.5.3.1 Effective Turbulence Investigation Based on POD Method...79	
4.5.3.2 Buffeting Response Prediction.....	84
4.6 Conclusions.....	88
5 Inlet Turbulence Generation Technique Based On ARMA Model.....	90
5.1 Introduction.....	90
5.2 Inlet Turbulence Generation Techniques.....	90
5.2.1 Discussion on the Generation Techniques	90
5.2.2 Wind Velocity Simulation Process Based On ARMA Model.....	94
5.2.3 Inlet Turbulence Generation Procedure.....	97
5.3 Validation of Inlet Turbulence Generation Technique Based on ARMA Model.....	99
5.3.1 Parameters of Simulation.....	99
5.3.2 Simulation Results Discussion.....	104
5.4 Conclusions.....	115
6 Buffeting Prediction Based On LES Model.....	116
6.1 Introduction.....	116
6.2 Numerical Simulation of Square Cylinder.....	116
6.3 Numerical Description of Test Cases.....	117
6.4 Results and Discussions.....	120
6.4.1 Simulation Results of Steady Inlet boundary Condition.....	120
6.4.2 Simulation Results of Unsteady Inlet boundary Condition.....	139
6.5 Conclusions.....	159

7 Buffeting Response Prediction Based On FSI.....	161
7.1 <i>Introduction.....</i>	<i>161</i>
7.2 <i>Description of Simulation Cases.....</i>	<i>161</i>
7.3 <i>Square Cylinder Response's Prediction Based on Different LES Models.....</i>	<i>163</i>
7.3.1 <i>Result Discussion of Steady Inlet Boundary Condition.....</i>	<i>164</i>
7.3.2 <i>Result Discussion of Unsteady Inlet Boundary Condition.....</i>	<i>171</i>
7.3.3 <i>Result Comparison of Two Inlet Boundary Conditions.....</i>	<i>177</i>
7.4 <i>Conclusions.....</i>	<i>189</i>
8 Conclusions and Future Work.....	190
8.1 <i>Conclusions.....</i>	<i>190</i>
8.2 <i>Future Work.....</i>	<i>191</i>
Reference.....	R1
Appendix.....	A1
Published Papers.....	P1

List of Figures

Chap 1

Fig 1.1.1 Tacoma Narrows Bridge collapse (Smith. Doug, 1974)1

Fig 1.2.1 Different aerodynamic phenomena of bridge.....2

Fig 1.2.2 Different stages of aerodynamic phenomena.....2

Chap 2

Fig 2.1.1 Bridge aerodynamic phenomena vs reduced velocity.....7

Fig 2.3.1 Horizontal velocity component spectrum (S_u).....20

Fig 2.3.2 Sears's aerodynamic admittance.....21

Fig 2.3.4 Spatial coherence function of horizontal velocity component.....23

Fig 2.3.5 Proposed aerodynamic nonlinear analysis framework (Chen *et al.*, 2001a).....25

Fig 2.3.6 Wake buffeting configuration and parameters (Hangan and Vickery, 1999).....27

Fig 2.4.1 Flow pattern of different aspect ratio rectangular (Naudascher and Wang, 1993).....29

Fig 2.5.1 Bluff body wake galloping.....31

Chap 3

Fig 3.2.1 Schematic diagram of turbulence modelling in CWE.....34

Fig 3.2.2 Idealized spectrum of turbulent kinetic energy of isotropic turbulence with respect to the wavenumber k and schematic of the extent of modeling employed by the traditional simulation DNS, LES, and RANS. The vertical dotted line marks the aim of Hybrid LES/RANS methods (Jochen and Dominic, 2008).....34

Fig 3.2.3 Simulation of flow past a circular cylinder based on RANS and URANS model (Spalart, 2000)35

Fig 3.5.1 Four staggered explicit procedures.....49

Fig 3.7.1 Coupled fluid-structure flow diagram.....51

Fig 3.7.2 Schematic figure of extrapolation procedure.....52

Chap 4

Fig 4.3.1 Bridge deck displacement component.....55

Fig 4.3.2 Self-excited force on bridge deck system.....	56
Fig 4.3.3 Spatial beam element of 12 degrees.....	57
Fig 4.4.1 Bridge location.....	62
Fig 4.4.2 Bridge plan.....	63
Fig 4.4.3 Bridge deck section.....	63
Fig 4.4.4 Finite element model of a cable stayed bridge.....	64
Fig 4.4.5 Flutter derivatives based on Theodorsen function.....	65
Fig 4.4.6 Velocity (v) power spectrum	66
Fig 4.4.7 Velocity (w) power spectrum	66
Fig 4.4.8 PSD matrix $S_{vv}(M, M, n)$ of different frequencies (x and y axis express the space point number, z axis is the matrix value)	67
Fig 4.4.9 PSD matrix $S_{ww}(M, M, n)$ of different frequencies (x and y axis express the space point number, z axis is the matrix value).....	68
Fig 4.5.1 Major mode shapes of bridge system.....	72
Fig 4.5.2 Displacement RMS value at the mid-span of bridge deck.....	74
Fig 4.5.3 Displacement RMS value with self-excited force at the mid-span of bridge deck.....	76
Fig 4.5.4 Displacement RMS value with aerodynamic admittance at the mid-span of bridge deck	78
Fig 4.5.5 Spectral eigenvalues and eigenvectors of the turbulence components.....	80
Fig 4.5.6 Modal truncation on the PSDF of the turbulence components at the mid-span of the bridge deck.....	80
Fig 4.5.7 Cross-modal participation coefficients of turbulence components.....	81
Fig 4.5.8 Spectral content of effective turbulence.....	82
Fig 4.5.9 3D representation of the coherence function of longitudinal and vertical turbulence components 1 st mode frequency.....	83
Fig 4.5.10 Coherence function of the effective turbulence components at 1 st mode frequency...	83

Fig 4.5.11 Coherence function of the effective turbulence components at the mid-span of bridge deck.....	84
Fig 4.5.12 RMS value of the displacements along the bridge deck axis without self-excited force and aerodynamic admittance.....	85
Fig 4.5.13 RMS value of the displacements along the bridge deck axis with aerodynamic admittance.....	86
Fig 4.5.14 RMS value of the displacements along the bridge deck axis with self-excited force....	86
Fig 4.5.15 RMS value of the displacements along the bridge deck axis with self-excited force and aerodynamic admittance.....	87

Chap 5

Fig 5.2.1 Schematic figurer of deterministic inlet turbulence generation technique.....	91
Fig 5.2.2 Schematic presentation of computation based on Nozawa and Tamura method (Nozawa and Tamura, 2002).....	92
Fig 5.2.3 The direction of inlet velocity input and velocity components.....	97
Fig 5.2.4 Velocity component generation interpolate point at the inlet boundary.....	98
Fig 5.3.1 Boundary conditions.....	100
Fig 5.3.2 Domain mesh (a: coarse mesh, b: fine mesh).....	100
Fig.5.3.3 Coherence function of velocity components for the inlet boundary at the frequency 0.1 Hz (a: u , b: v and w).....	101
Fig 5.3.4 Schematic figure of monitor points position ($B=0.2m$, $D=0.2m$).....	102
Fig 5.3.5 Velocity components' time history curves at different monitor points.....	103
Fig 5.3.6 Velocity components' time history curves at P8 along different positions (coarse mesh).....	105
Fig 5.3.7 Velocity components PSD at monitor point (P8) along different positions.....	107
Fig 5.3.8 Velocity components' autocorrelation coefficient for monitor point (P8) along different locations (coarse mesh).....	109

Fig 5.3.9 Velocity components spatial cross-correlation coefficient at monitor point P6 and P8 (coarse mesh).....	110
Fig 5.3.10 Dimensionless velocity component mean value along different positions.....	111
Fig 5.3.11 Dimensionless velocity component RMS value along different positions.....	112
Fig 5.3.12 Velocity component (u) mean and RMS value of LES standard and dynamic model.....	112
Fig 5.3.13 Velocity component (v) mean and RMS value of LES standard and dynamic model.....	113
Fig 5.3.14 Velocity component (w) mean and RMS value of LES standard and dynamic model.....	113
Fig 5.3.15 Velocity components time history of different meshes at monitor point P8.....	114
Fig 5.3.16 Velocity components' PSD value of different mesh for the monitor point P4 at the position $X/B=3$	115

Chap 6

Fig 6.3.1 LES1, LES2 and LES3 mesh grid.....	118
Fig 6.3.2 Domain dimension and boundary conditions.....	118
Fig 6.3.3 Monitor points position.....	120
Fig 6.4.1 Lift coefficient's time history curves of LES1, LES2 and LES3.....	121
Fig 6.4.2 Lift coefficient's time history curves of LES1 (Standard), LES1 (Dynamic) and LES1 (WALE).....	121
Fig 6.4.3 Power spectrum of lift force for LES1, LES2 and LES3.....	122
Fig 6.4.4 Power spectrum of lift force for LES1 (standard), LES1 (Dynamic) and LES1 (WALE).....	123
Fig 6.4.5 Square cylinder's Strouhal number vs Reynolds number.....	125
Fig 6.4.6 Square cylinder's drag coefficient vs Reynolds number.....	126
Fig 6.4.7 Streamwise velocity component (u) time averaged value along the centre line.....	127
Fig 6.4.8 Time averaged value of nondimensional velocity components along the vertical middle of the top side surface of square cylinder.....	129

Fig 6.4.9 Nondimensional Reynolds stress along the center line.....131

Fig 6.4.10 Nondimensional Reynolds stress along the vertical middle line of the top side surface of square cylinder.....132

Fig 6.4.11 RMS value of nondimensional velocity components along the centre line.....134

Fig 6.4.12 RMS value of nondimensional velocity components along the vertical middle line of the top side surface of square cylinder.....135

Fig 6.4.13 Instantaneous isosurface value of velocity component (u) of current simulations...137

Fig 6.4.14 Velocity components' time history of LES1, LES2 and LES3 at point P1.....138

Fig 6.4.15 Velocity components' time history of LES1 (Standard), LES1 (Dynamic) and LES1 (WALE) at point P1.....138

Fig 6.4.16 Lift and drag coefficient time history of different LES models with inflow turbulence at the nondimensional time step.....139

Fig 6.4.17 Lift coefficient curves of the case IC1 and LES1 at the nondimensional time step range (200-250).....140

Fig 6.4.18 Power spectra of lift coefficient for the case IC1 of different LES models and the case LES1141

Fig 6.4.19 Time averaged value of dimensionless streamwise velocity components along the centre line of simulation domain.....143

Fig 6.4.20 Time averaged value of dimensionless velocity components along the middle line vertical to the square cylinder.....144

Fig 6.4.21 Dimensionless Reynolds stress along the center line of the domain.....146

Fig 6.4.22 Time averaged value of dimensionless Reynolds Stress along the middle line vertical to the square cylinder.....147

Fig 6.4.23 RMS value of dimensionless velocity components along the centre line of the domain150

Fig 6.4.24 RMS value of dimensionless velocity components along the middle line vertical to the square cylinder.....151

Fig 6.4.25 Instantaneous vorticity Z value for the case IC1 of different LES models and the case LES1.....152

Fig 6.4.26 Instantaneous pressure value for the case IC1 of different LES models and the case LES1.....153

Fig 6.4.27 Velocity components' time history of different LES models at the monitor point P1154

Fig 6.4.28 Velocity components' spectra of the case LES1 and IC1 at point 1.....156

Fig 6.4.29 Velocity components' spectra of the case LES1 and IC1 at point 2.....157

Fig 6.4.30 Velocity components' spectra of the case LES1 and IC1 at point 3.....157

Fig 6.4.31 Velocity components' spectra of the case LES1 and IC1 at point 4.....158

Chap 7

Fig 7.3.1 Lift coefficient of different LES models at the steady inlet boundary condition.....164

Fig 7.3.2 Lift coefficient of different LES models of the steady inlet boundary condition at nondimensional time steps (100-200).....165

Fig 7.3.3 Response stage vs lift coefficient of standard LES model at the steady inlet boundary condition.....165

Fig 7.3.4 Velocity response of different LES models at the steady inlet boundary condition166

Fig 7.3.5 Displacement response of different LES models at the steady inlet boundary condition167

Fig 7.3.6 PSD values of lift force of different LES models at the steady inlet boundary condition168

Fig 7.3.7 PSD values of displacement response for different LES models at the steady inlet boundary condition.....169

Fig 7.3.8 Pressure contour of square cylinder from different LES models of the steady inlet boundary condition at different time steps.....	170
Fig 7.3.9 Lift coefficient of different LES models at the unsteady inlet boundary condition	171
Fig 7.3.10 Drag coefficient of different LES models at the unsteady inlet boundary condition	172
Fig 7.3.11 Velocity response of different LES models at the unsteady inlet boundary condition	172
Fig 7.3.12 Displacement response of different LES models at the unsteady inlet boundary condition.....	173
Fig 7.3.13 Lift force PSD of different LES models at the unsteady inlet boundary condition	174
Fig 7.3.14 Displacement PSD of different LES models at the unsteady inlet boundary condition	175
Fig 7.3.15 Pressure contour of square cylinder from different LES models of the unsteady inlet boundary condition at different time steps.....	176
Fig 7.3.16 Drag coefficient of different LES models for two inlet boundary conditions.....	177
Fig 7.3.17 Lift coefficient of different LES models for two inlet boundary conditions.....	179
Fig 7.3.18 Velocity response of different LES models for two inlet boundary conditions.....	181
Fig 7.3.19 Displacement response of different LES models for two inlet boundary conditions	182
Fig 7.3.20 Lift force PSD of different LES models for two inlet boundary conditions.....	183
Fig 7.3.21 Displacement PSD of different LES models for two inlet boundary conditions.....	183
Fig 7.3.22 Mechanical admittance of different inlet boundary conditions.....	184
Fig 7.3.23 Response displacemnt for the reduced velocity (V_r).....	186

Fig 7.3.24 Lateral forces coefficients of square cylidner vs attack angle α by Laneville (1975).....187

Fig.7.3.25 Response of square cylinder by different LES models and the quasi-steady theory (Sc=20)188

Lists of Tables

Chap 2

Table 2.3.1 Velocity component spectra $S_{u,v,w}$ ($x = nL / \bar{u}_{10}$, here $L = 1200\text{m}$, \bar{u}_{10} is the mean wind velocity at 10m height; $x_z^{u,v,w} = nL_z^{u,v,w} / \bar{u}(z)$; $L_z^{u,v,w}$ is the mean scale of eddy, $f = nz / \bar{u}(z)$ is the Monin coordinate; $\bar{u}(z)$ is the mean wind velocity at z height; β_u is the nondimensional turbulence intensity factor) (Solari *et al.*, 2001).....19

Chap 4

Table 4.4.1 Static aerodynamic coefficients of bridge deck.....65

Table 4.5.1 Bridge first 50 modes frequency.....68

Table 4.5.2 Bridge mid-span horizontal displacement RMS value of different mode combination methods (m).....73

Table 4.5.3 Bridge mid-span vertical displacement RMS value of different mode combination methods (m).....73

Table 4.5.4 Bridge mid-span twist angle RMS value of different mode combination methods (degree).....73

Table 4.5.5 Self-excited force’s effects on the horizontal displacement at the mid-span (m)75

Table 4.5.6 Self-excited force’s effects on the vertical displacement at the mid-span (m).....75

Table 4.5.7 Self-excited force’s effects on the twisting angle at the mid-span (degree).....75

Table 4.5.8 Aerodynamic admittance’s effects on the horizontal displacement RMS value (m)...77

Table 4.5.9 Aerodynamic admittance’s effects on the vertical displacement RMS value (m).....77

Table 4.5.10 Aerodynamic admittance’s effects on the twisting angle RMS value (degree).....77

Table 4.5.11 Influence of aerodynamic parameters on the RMS value of mid-span of the bridge deck axis considering 10 spectral modes.....88

Chap 5

Table 5.3.1 Inlet turbulence parameters.....99

Chap 6

Table 6.3.1 Simulation domain dimension.....119

Table 6.3.2 Summary of Computational cases: time step (Δt), uniform cell size at the upstream of cylinder (Δ_{up}), the downstream of cylinder (Δ_{down}), near the cylinder (Δ_{near}) and the spanwise direction of cylinder $\Delta_{spanwise}$ 119

Table 6.3.3 Computational cases parameters.....119

Table 6.3.4 Positions of monitor points in the computational domain.....120

Table 6.4.1 General aerodynamic parameters of square cylinder.....124

Table 6.4.2 General aerodynamic parameters of square cylinder under the inflow turbulence boundary.....142

Chap 7

Table 7.3.1 General aerodynamic parameters of square cylinder of different inlet boundary conditions concerning FSI.....185

Table 7.3.2 Square cylinder response value (y/D) based on different LES models at $Vr=7.5$188

Nomenclature

Chap 2

A :	Area of bluff body projected to the wind velocity
$A_{u_{ij}}, A_{w_{ij}}$:	Participation factors matrix
A_s, A_d :	Stiffness and damping item in the self-excited force matrix
A_{bu}, A_{bw} :	Horizontal and vertical item in the buffeting force matrix
B :	Bridge deck width.
C_{AD}, K_{AE} :	Aerodynamic damping and stiffness matrices
C_L, C_D, C_M :	Bridge section static lift, drag and twist force coefficients
C'_L, C'_D, C'_M :	Bridge section static lift, drag and twist force coefficients with the relationship of the angle of incidence
D :	Cylinder diameter
F_{se}, F_b :	Self-excited force and buffeting force matrix
$F(t)$	External load
F_G :	Self weight
F_{st} :	Static wind force
$F_b(t)$:	Buffeting force
$F_{se}(t)$:	Self excited force
f :	Natural Frequency
f_h :	Heaving vibration frequency
f_α, ω_α :	Twisting frequency and circular frequency
H_i^*, A_i^* :	Flutter derivatives in vertical, lateral and torsional direction
$H_i(n), \overline{H_i(n)}$:	i th principal component complex frequency response function
$K = fB/U$:	Reduced frequency
$L_{u,v,w}$:	Integral length scale of the turbulence component
$L_z^{u,v,w}$:	Mean scale of eddy
$\bar{L}, \bar{D}, \bar{W}$:	Lift force , drag force and twist moment induced by the mean wind velocity
m :	Mass
M, C, K :	System generalized mass, damping and stiffness matrix

$Q_{se}, Q_b :$	Self excited force and buffeting force matrix
$Q(t) :$	External forces matrix
$q(t) :$	Generalized mode displacement
$\tilde{q}_i(n), \tilde{u}(n), \tilde{w}(n) :$	Fourier transforms of $q_i(t), u(t)$ and $w(t)$ respectively
$R :$	Covariance matrix
Re:	Real operator
$\tilde{q}_n(n), \tilde{q}_w(n) :$	Vectors of the generalized Fourier transforms of the principal components of $u(t)$ and $w(t)$
$St :$	Strouhal number
$S(\omega) :$	Modal response PSD matrix
$S_u(n), S_w(n) :$	Horizontal and vertical velocity component power spectrum
$U :$	Mean velocity
$\bar{u}_{10} :$	Mean wind velocity at 10m height
$\bar{u}(z_1) :$	Mean wind velocity at z_1 height
$u(t), w(t) :$	Horizontal and vertical wind velocity component matrix of time varying
$\kappa :$	Coefficient of bluff section
$r :$	Bridge section inertial radius
$\omega_h :$	Heaving vibration circular frequency
$\rho :$	Air density
$k :$	Decay factor
$\delta :$	Reduced frequency based on the bridge deck width
$\alpha_e^l(t), \alpha_e^h(t) :$	Low frequency (large length scale) and high-frequency (small length scale)
$h, p, \alpha :$	Vertical, horizontal and twisting displacement
$\chi_{Lu}, \chi_{Lw}, \chi_{Du}, \chi_{Mu}, \chi_{Mw} :$	Aerodynamic admittance function
$\xi_i, n_i :$	i th generalized damping ratio and frequency ($i = 1, 2, \dots, N ; N = \text{total number of structural modes}$)
$\Phi_i^T :$	i th modal shape transpose matrix
$\Phi :$	Structural modal shape matrix
$*, T :$	Complex conjugate and matrix transpose operation
$U_0 :$	Free stream velocity,

U_w :	Free stream-line velocity at separation
$\eta, \dot{\eta}$:	Nondimensional structure displacement and velocity item
μ :	Mass ratio
C_a, ε, ν :	Nondimensional aerodynamic parameters

Chap 3

C_{des} :	DES constant
C_{b1}, C_{b2}, C_{w1} :	One-equation DES model constant
C_w :	WALE model constant
C_k, C_ε :	Dynamic subgrid kinetic energy transport model constants
C_s :	Smagorinsky constant
d :	Turbulent length scale in One-equation DES model
f_2, f_w :	One-equation DES model constant
F_s, F_1, F_2 :	DES model constant
k :	Turbulent kinetic energy
L_s :	Mixing length for subgrid scales
ℓ_1, ℓ_ε :	Turbulent length scales in SST DES model
n :	Time step counter
\bar{P} :	Pressure mean part
\bar{p} :	Filtering pressure
p' :	Pressure fluctuation part
P :	Production term
\bar{S}_{ij} :	Rate-of-strain tensor in LES model
S_{ij}^d :	Traceless part of the square of the velocity gradient tensor
$\bar{U}, \bar{V}, \bar{W}$:	Velocity component mean part
u', v', w' :	Velocity component fluctuating part
U_c :	Convective velocity
U_i :	Velocity component item
\bar{u}_1 :	Averaged value velocity
$\overline{u'_i u'_j}$:	Reynolds stress term

$u(x,t)$:	Velocity
$\bar{u}(x,t)$:	Resolved scaled velocity
$u'(x,t)$:	Subgrid scale velocity
V :	Volume of the computational cell
x_i, x_j :	Grid space
y :	The distance to the nearest wall
Y :	Destruction term
Ω_{ij} :	Rotation rate tensor
$\alpha, \beta, \sigma_{\omega 2}$:	SST DES model constants
ν_t :	Eddy viscosity
$\tilde{\nu}_t$:	Turbulent kinematic eddy viscosity
ν_{SGS} :	Subgrid-scale turbulent viscosity in LES model
Δ :	Cell length or the filter width
$\Delta x_{\xi}, \Delta x_{\eta}, \Delta x_{\zeta}$:	Cell length in the three grid directions ξ, η and ζ
δ :	Boundary layer thickness
ε :	Dissipation rate
ω :	Vorticity
ℓ_t :	Turbulent length scales
η :	Strain parameter
β^* :	Constant of $k - \omega$ SST model
μ :	Kinematic viscosity
μ_t :	Turbulence viscosity
Δ_f :	Filter-size
ν_{sgs} :	Effective SGS viscosity
τ_{ij} :	Sub-grid-scale stresses
κ :	Von Karman constant
ρ :	Air density
$\sigma_{\tilde{\nu}_t}$:	One-equation DES model constant
ν	Posstion coefficient

Chap 4

$[A_s], [A_d]$:	12×12 aerodynamic stiffness matrix and damping matrix
C_{re} :	Exponential decay coefficient of $\mathcal{E}(t)$ along r
L :	Length of element
M, M' :	Points along the deck axis
r, r' :	Coordinates of the points along the deck axis
S_{vv}, S_{ww} :	Gust wind velocity component PSD matrix
S_{vw} :	Gust wind velocity component v and w cross spectrum density (CSD) matrix
$S_{Q_b}^1(\omega)$:	Generalized buffeting force PSD
$S_{Q_b}^2(\omega)$:	Generalized buffeting force CSD
\ddot{X}, \dot{X}, X :	Multiple degree system node acceleration, velocity and displacement
v, w :	Gust wind vertical and horizontal velocity component
u_* :	Friction velocity
$\{\delta_i\}, \{\dot{\delta}_i\}$:	Node displacement and velocity vector
z_0 :	Roughness length
$\sigma_\epsilon, L_\epsilon(M)$:	Standard deviation and the integral length scale
Λ :	Eigenvalue matrix
A :	Matrix from an exterior boundary integral modelling
D_x, D_y :	Finite difference operation on the variable x and y
\ddot{d}, \dot{d}, d :	Vectors of the nodal accelerations, velocities, and displacements
E :	A type of mass matrix plus a free surface integral
$\{F^{ext}(t)\}$:	Generalized vector of external forces acting on the structure
F_I :	Vector of interface interaction
F_θ :	Vector of external forces
H :	Stiffness matrix
h_1 :	Coupling term
h_0 :	Matrix includes boundary conditions and external forces
$i = 1, 2, \dots, n$	Index number
k :	Iteration counter

$M, C, K :$	Generalized structure mass, damping and stiffness matrix
$m, s :$	Master and slave
$N :$	Total number of modes of structure
$p :$	Fluid pressure
$w(t), \dot{w}(t) \ddot{w}(t) :$	Generalized displacement, velocity and acceleration vectors
$w_{p_T} :$	Translation component
$w_{p_R} :$	Rotational component
$\Phi :$	Modal matrix
$\omega_i :$	Natural frequency for the i th mode
$\xi_i :$	Corresponding damping parameter for that mode
$\alpha_1, \beta_1 :$	Parameters in Newmark scheme
$\rho :$	Fluid density
$\mu :$	Viscosity coefficient.
$\alpha :$	Decay function
$\varepsilon :$	Arbitrary small number
$\beta :$	Coefficient about the stiffness
$\sim :$	New position
$\nu :$	Possion coefficient

Chap 5

$i = 1, 2, \dots, m$	Index number
$k = 1, 2, \dots, N :$	
$a_{ip}(k), b_{ip}(k) :$	Gaussian variables
$c_x, c_y, c_z :$	Decay coefficients of x , y and z direction
$H_{ip} :$	Lower triangular matrix
$I_u, I_v, I_w :$	Turbulence intensity x , y and z direction
$L_{x,y,z} :$	The integral length scale of three directions
$N :$	Number of subdivisions of the frequency domain
$N_p :$	Number of the points
$p :$	Order of AR model
$q :$	Order of MA model

$S_{ji}(\omega)$:	Multidimensional cross-spectrum matrix
U_i :	Mean velocity at point i
$\bar{u}(z_k)$:	Mean wind velocity between two points i and j
u, v, w	Streamwise, vertical and lateral velocity components
θ_{ij} :	Time lag
σ	Standard deviation
ω_u :	Cut-off frequency
ω_l :	Beginning frequency

Chap 6

B	The width of square cylinder
D	The height of square cylinder
Δt	Time step
Δ_{up}	Uniform cell size At the upstream of cylinder
Δ_{down}	Uniform cell size at the downstream of cylinder
Δ_{near}	Uniform cell size near the cylinder
$\Delta_{spanwise}$	Uniform cell size of the spanwise diction of cylinder
\bar{C}_D	Drag coefficient mean value
C_L^{rms}	RMS value of lift coefficient
C_D^{rms}	RMS value of drag coefficient
St	Strouhal number

Chap 7

ξ	Viscous damping ratio of structure
δ	The displacement relative to the previous mesh locations
∇	Control volume size
Γ_{disp}	Mesh stiffness
C_{stiff}	Stiffness model exponent

Chap 1 Introduction

1.1 Background

Long span bridges are prone to the influence of dynamic loads such as earthquakes, moving traffic and the wind etc. When the wind load influence is large enough, it will induce structural instability and can even lead to catastrophe. Therefore it is important for engineers to consider the influence from the wind load in bridge wind resistance design and analysis. In particular the failure of Tacoma Narrows Bridge (Fig.1.1.1) attracted much more attentions from civil engineers and researchers on bridge wind engineering using different methods such as wind tunnel experiment, theory analysis and numerical analysis. Thanks to the numerical analysis method, the bridge aerodynamic theory and the development of numerical modelling, the bridge aerodynamic phenomena numerical simulation becomes possible. This thesis will focus on the study about the numerical simulation approach of bridge buffeting response among all bridge aeroelastic analysis approaches.

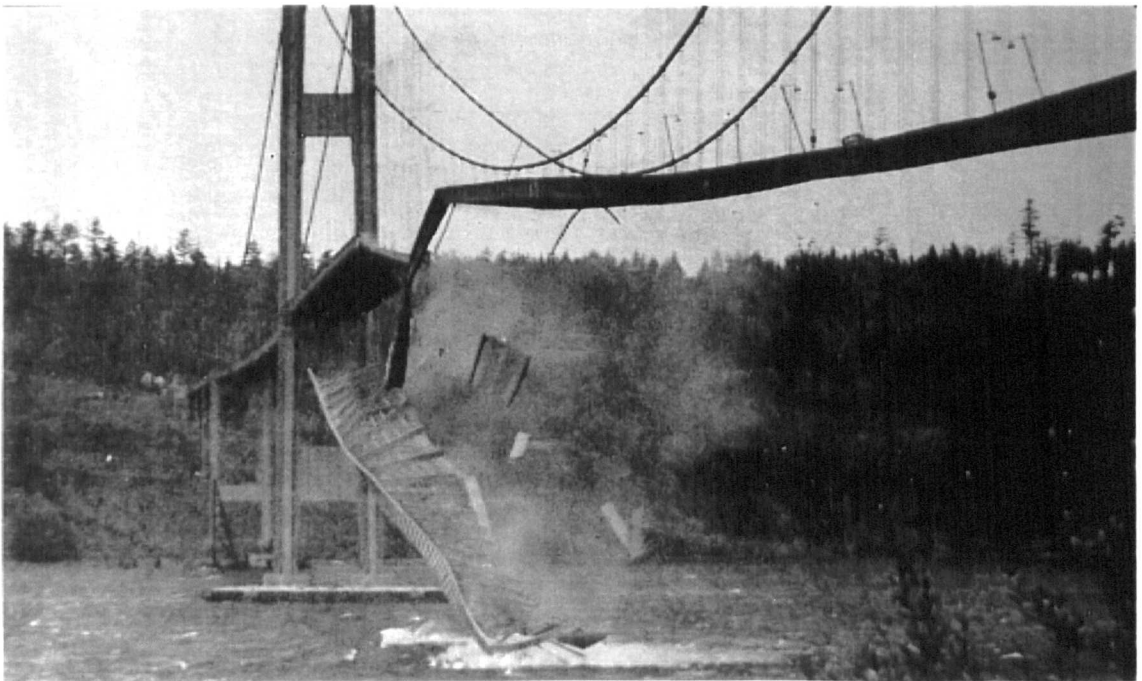


Fig 1.1.1 Tacoma Narrows Bridge collapse (Smith. Doug, 1974)

1.2 Problem

In general the bridge aerodynamic phenomena can be divided into two types according to the vibration amplitude. One is the limited amplitude vibration, causing the serviceable discomfort and dynamic fatigue and containing vortex-induced vibration, buffeting vibration, wake-induced vibration and Rain/wind induced vibration. The other is the divergent amplitude vibration, which includes galloping, flutter and wake instability, causing structural catastrophe (Fig.1.2.1). However among the above discussed vibration, buffeting vibration should be paid more attention due to the complexity of the vibration mode shape of bridge structure generated with the increase in the span

of modern bridges inducing structural vibration modes coupling. The conventional buffeting analytical method considering single structure vibration mode are not suitable for modern super large span bridge designs and new methods considering the multimode contribution are needed. In addition the past bridge aerodynamic analysis methods only studied single aerodynamic phenomena, which can not satisfy future large-span bridge aerodynamics analysis. Especially for the bridge buffeting response, which is caused by the turbulence of wind, it exists in the whole process of bridge vibration. The Interactions of different aerodynamic phenomena occur (Fig.1.2.2) and the aerodynamic coupled effects should be considered in the bridge buffeting prediction. So in current study the multimode aerodynamic coupling buffeting analysis will be performed (see chapter 3).

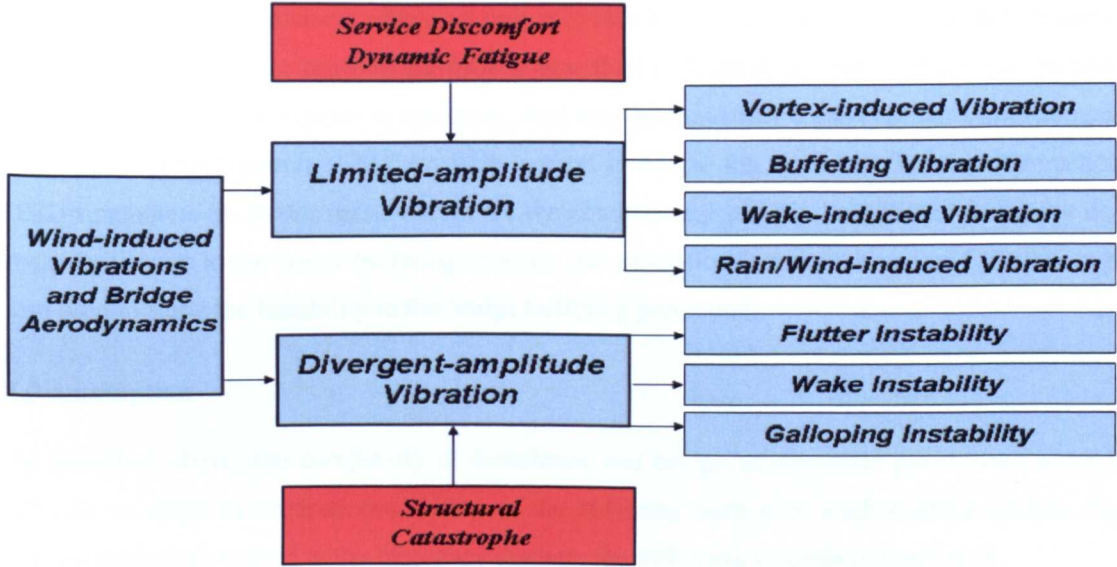


Fig 1.2.1 Different aerodynamic phenomena of bridge

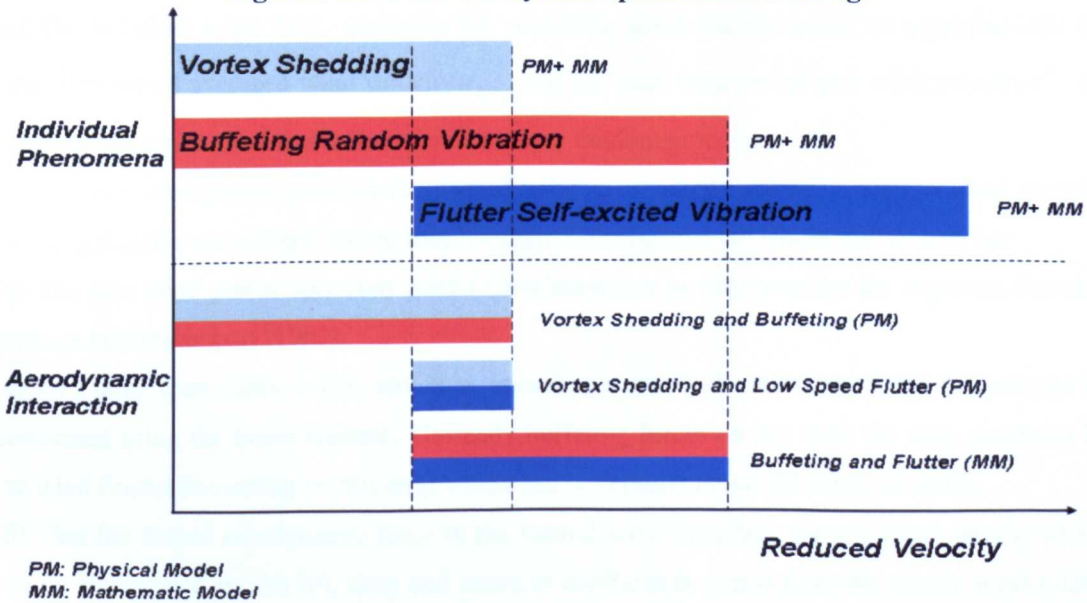


Fig 1.2.2 Different stages of aerodynamic phenomena

Due to the complexities of bridge aerodynamic analysis, the general analytical methods suitable for bridge aerodynamic phenomena such as flutter, buffeting, vortex shedding and galloping are

based on either experimental model or theoretical model. The experimental model includes the section modelling, taut-strip modelling and scaled full-bridge modelling. Theory model includes the physical, mathematical and semi-empirical models. Some limitations exist in these models. For the experimental study, cost and realization time in these experimental approaches may be a problem, and parametric analyses during the bridge design phase often generate unacceptable results. Hence, reduction of the turn-over time for the aerodynamic bridge characterization is highly desirable. While for the theoretical model, quasi-steady assumptions, some simplified numerical models or semi-empirical models are always applied to consider the uncertainties of wind turbulence in the analysis procedure. So the Computational Fluid Dynamics (CFD) method has been applied to overcome above limitations, which not only provides an effective tool to study the aerodynamic phenomena in the bridge engineering from a pure fluid flow point of view, but also can be conducted on the general computer at low costs. And this analysis method can combine other Computational Structure Dynamic (CSD) analysis method to realize the Fluid and Structure Interaction (FSI) simulation. So in this thesis except for the conventional statistical method of frequency domain application in the bridge buffeting analysis, the simulation technique based on CFD theory is also used to study the feasibility in the bridge buffeting prediction.

1.3 Assumption

As described above, the complexity of turbulence and bridge aerodynamic phenomena make it difficult to adopt an accurate description of the buffeting from pure mathematical models. For general analytical method in the frequency domain, the following assumptions are used:

- (1) The turbulent wind field, assuming the oncoming wind velocity u can be separated into the long time period averaged wind velocity u_{mean} and the short time period gust wind velocity u' , the wind fluctuation is treated as a Gaussian stationary random process.
- (2) The gust wind power spectrum is assumed to be an ergodicity average smooth random process, meaning that the unit sample record time average can substitute the whole sample average.
- (3) The gust wind power spectrum spatial correlation can be expressed by the exponent function proposed by Davenport (1962).
- (4) To a large span elastic bridge structure, assuming it satisfy the strip theory, the analysis can be performed using the beam element. Unsteady buffeting forces on any strip are only produced by the wind fluctuation acting on this strip which can be representative for whole structure.
- (5) That the forced aerodynamic force in the natural wind boundary layer is quasi-steady, which can be represented by the lift, drag and moment coefficients gotten from the steady wind tunnel experiments. Unsteady buffeting loads can be modelled as quasi-steady forces by some simple approximations

Compared to the quasi-steady assumptions in the conventional buffeting analyses in the frequency domain, the CFD buffeting response prediction method simulates the wind turbulence based on the following assumptions.

(6) The variation in the flow direction should be slow so that production and dissipation of the turbulence are more or less in balance and the turbulence structure should be isotropic, the small eddies satisfy the Boussinesq hypothesis assumption.

(7) That the turbulence is fully developed, which makes it possible to use the Large Eddy Simulation (LES) method.

1.4 Objective

The objective of this research is to review and summarize the development of buffeting theory and simulation approaches and discuss the possibility in the application of the CFD method in the buffeting simulation. In order to achieve the objective, it is necessary to accomplish the following sub objectives.

(1) To summarize the development of the conventional buffeting analysis method and discuss the application in bridge wind engineering.

(2) To study the influence of parameters such as aerodynamic admittance, self excited force and modes combination methods on the structural buffeting response based on the frequency domain analytical method

(3) To propose an alternative buffeting analytical method for studying the effects of effective turbulence on bridge structures based on the Proper Orthogonal Decomposition (POD) method.

(4) To discuss the possibility and reliability of LES approach in predicting the unsteady characteristics of square cylinder based on different LES models.

(5) To investigate the influence of inflow turbulence boundary conditions on the flow characteristics and discuss the possibility of using this method for simulating bridge buffeting.

(6) To predict the buffeting response of a square cylinder at the steady and unsteady boundary conditions.

1.5 Methodology

To obtain the above objectives, an investigation will be divided into several stages. The first stage is to review the development history of bridge buffeting theory and the general analysis method. Then the buffeting response analysis in the frequency domain is performed on a cable stayed bridge. In this stage, aerodynamic admittance, self-excited force and mode combination techniques will be selected to investigate the influence on the simulation results. After that a new gust wind response analysis method based on the POD technique to study the effective turbulence effects will be presented. In conventional buffeting analyses, random vibration theory and structure

dynamic theory will be used. The commercial code ANSYS is used to study the structure vibration mode and get the mode shape, while MATLAB is adopted to perform data processing. All the above analysis methods are based on the Finite Element (FE) model. Different from the FEM, the CFD method based on the Finite Volume Method (FVM) in the Euler coordinate to discretize the Navier-Stokes equations will be applied in the third stage. However the problems of civil engineering are large scale ones with high Reynolds number, which can not be solved by the Direct Numerical Simulation (DNS) method directly. Currently Large Eddy Simulation (LES) model will be a suitable one to approximate the time varying characteristics of wind flow, here the standard LES model, LES dynamic model and Wall Adaptive Local Eddy-Viscosity (WALE) model will be considered. 3D square cylinder is selected as the simulation target. To consider the effect of upwind turbulence on the flow around the bluff body, the time varying inflow turbulence boundary, based on the digital filtering technique-Autoregressive Moving Averaged (ARMA) method, will be proposed in this research and then realized in the commercial code MATLAB and User FORTRAN of ANSYS_CFX. In the CFD analysis, the commercial code ANSYS-CFX will be adopted to perform the LES analysis. For the buffeting response prediction, the FSI technique will be adopted to study the response of a square cylinder. To simulate the buffeting response of square cylinder under the inflow turbulence, firstly the response of square cylinder with the steady inlet boundary is studied in the vertical direction, and then the unsteady inflow turbulence boundary condition is applied. To compare the influence of LES models on the response of square cylinder, different LES models are considered with the steady and unsteady boundary condition.

1.6 Contents

In chapter 1, the introduction to the background of bridge buffeting, the assumptions, and the adopted methodologies have been presented.

Chapter 2 simply overviews bridge aerodynamic phenomena, such as flutter, buffeting, vortex shedding and galloping. Major discussions are put on the buffeting theory and simulation method. The widely used buffeting analysis method based on the single modal, multimodal aeroelastic coupling, multimodal aerodynamic coupling state-space and POD approaches in the frequency domain are introduced in more detail.

Chapter 3 summarizes the development of turbulence modelling in Computational Wind Engineering (CWE). Some problems existing in this field are also presented. Turbulence modelling, such as the Reynolds Averaged Navier-Stokes (RANS), Unsteady Reynolds Averaged Navier-Stokes (URANS), Detached Eddy Simulation (DES) and LES used in the CFD, is overviewed. Before proposing FSI model suitable for bridge buffeting analysis, the numerical description of the structure system model, the solution of coupled system and moving grid technique to map the deformation of the structure system are introduced. And then the major steps for FSI simulation of bridge buffeting prediction are introduced.

Based on the theory already introduced in chapter 2, in chapter 4 the buffeting frequency domain analytical method based on FEM is proposed and the major algorithm is described. A cable stayed bridge is used to validate the above proposed method and different parameters, such as self excited force, aerodynamic admittance and mode coupling, effects on the buffeting response are discussed. At the same time the effective turbulence contribution on the bridge buffeting response is discussed. In the POD analysis, the influences of self excited force and aerodynamic admittance on the buffeting response are also discussed and the final analysis results are compared with the results generated by previously conventional buffeting simulation technique.

In chapter 5 the generation technique of unsteady inlet velocity based on ARMA model is proposed. To validate the correctness of this method, an empty domain with coarse and fine mesh densities is adopted and turbulence intensity of 5% is considered. Then the time history data and power spectra of different monitor points' velocity components at different mesh densities are compared. And the standard and dynamic LES models are considered to compare the influence of different models on the simulation results.

In Chapter 6 firstly a square cylinder with zero turbulence intensity is used to validate the feasibility of current LES to capture the unsteady characteristics of buffeting based on the previous description of 3D LES theory in chapter 4. The influence of spanwise depth, mesh density and different LES models such as standard LES, LES dynamic and WALE on the simulation results is discussed and compared with other experimental and numerical results. And then the unsteady inlet boundary with 5% turbulence intensity generated by the proposed technique is applied to investigate the flow characteristics around the square cylinder considering different LES models, the simulation results are compared with the case without inflow turbulence, and the velocity spectra in the upwind direction are captured to compare with the target spectra.

In chapter 7, based on the FSI procedure proposed in chapter 3, a square cylinder with a constant damping ratio (5%) is adopted to compare the influence of steady and unsteady inlet boundary condition on the response of square cylinder, the across-flow vibration is considered in these simulations. Different LES models are used to compare the influence of turbulence model on the response of square cylinder.

Chapter 8 draws conclusions on current work done in this research and provides suggestions and recommendations for further work.

Chap 2 Overview of Bridge Aerodynamic Phenomena

2.1 Introduction

The Tacoma Narrows Bridge disaster of 1940 brought researchers' attention to wind induced bridge vibration phenomena, such as flutter, buffeting, galloping and vortex shedding. With the development of the modern bridge span and the complex topography conditions, bridges are more susceptible to the actions of strong wind. Generally, within the reduced velocity range the bridge structure response induced by the wind can be divided into the limit amplitude response in the low and medium velocity range (vortex-induced response) and the divergent amplitude response (flutter and galloping) in the high velocity range, however buffeting response occurs in the whole reduced velocity range (Fig.2.1.1). In this chapter, the flutter response is firstly described, and then the buffeting theory development and uncertainties factors of buffeting analysis will be presented, buffeting analysis method based on statistical method in frequency and time domain will also be described in detail, and those buffeting analysis based on deterministic method (experiment method) is also discussed. After the description of buffeting theory, the vortex shedding and galloping response will also be discussed briefly.

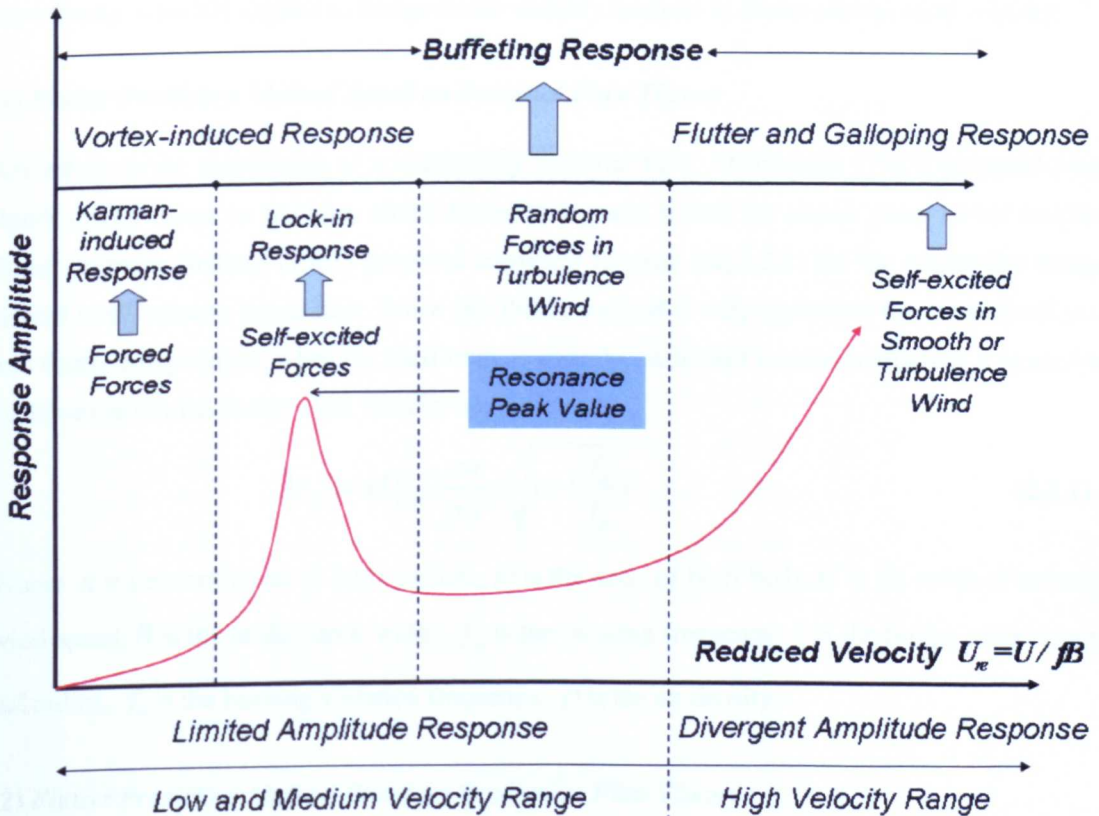


Fig 2.1.1 Bridge aerodynamic phenomena vs reduced velocity

U is the mean velocity, f is the frequency, B is the bridge deck width.

2.2 Bridge Flutter Theory's Introduction

2.2.1 Bridge Flutter Response Formulation

Among the bridge aerodynamic phenomena, bridge flutter response is a type of divergent self-excited response. It occurs when the energy absorbed by the vibrating bridge structure from the surrounding air flow is larger than the energy dissipated by the structural damping during the structural vibration. Different section shape flutter vibration will have different flutter response mechanisms. The relationship of amplitude and phase angle between twist and bending freedom movement for the streamlined section is mainly influenced and changed by the wind velocity. While for the bluff cross section, the wind velocity mainly influences and changes the twisting freedom movement amplitude and phase angle of bluff body section, causing twist vibration and aerodynamic negative damping.

2.2.2 Bridge Flutter Analysis Theory's Development

Bridge flutter research is to predict the flutter stability and to determine flutter critical condition wind velocity. Bridge flutter theory developed from the Potential flow theory to modern separated flow theory, which is applied to bridge flutter stability analysis to obtain critical wind velocity.

(1) Flutter Prediction Method Based on Potential Flow Theory

According to the assumption of nonstationary potential flow, Theodorsen (1935) proposed plate flutter theory based on the plate airfoil flutter theory and solved the classic panel airfoil coupled flutter problem. Selberg (1961) proposed empirical formula (Eq.2.2.1) for the suspension bridge critical wind velocity calculation. Since this theory method is only applied in the streamlined section flutter computation, when the bluff body is considered, a bluff section coefficient κ is used to evaluate the critical flutter wind velocity approximately.

$$U_{cr} = \kappa U f_{\alpha} \left[\frac{mr}{\rho B^3} \right] \sqrt{1 - \left(\frac{f_h}{f_{\alpha}} \right)^2} \quad (2.2.1)$$

Where κ is the coefficient of bluff section, m is the mass of bluff body, U is the mean of velocity wind speed, B is the bridge deck width, f_{α} is the twisting frequency, r is the bridge section inertial radius, f_h is the heaving vibration frequency, ρ is the air density.

(2) Flutter Prediction Method Based on Separation Flow Theory

Theodorsen's theory is proposed only based on the nonstationary potential flow moving along the plate panel and ignores the flow separation. Once the flow is separated, the potential flow flutter theory may be limited. Especially with the complexity of bridge deck shape, the flow separation always happens. For this reason, the alternative flutter theory based on the separated flow should be proposed.

Scanlan (1971, 1978a) suggested the modification on the Theodorsen plate panel theory, and proposed the aerodynamic parameters-flutter derivatives based on the section model from the wind tunnel experiment, then created a linear unsteady aerodynamic model (Eq.2.2.2a and Eq.2.2.2b). In Scanlan's theory, the self-excited force on the bridge structure can be described through the 6 to 18 aerodynamic flutter derivatives, and then applied the aerodynamic force on the 2D section and the whole 3D bridge computation model to calculate the flutter response and get the critical flutter wind velocity.

$$L = \frac{1}{2} \rho U^2 B \left[KH_1^*(K) \frac{\dot{h}}{U} + KH_2^*(K) \frac{B\dot{\alpha}}{U} + K^2 H_3^*(K) \alpha \right] \quad (2.2.2a)$$

$$M = \frac{1}{2} \rho U^2 B^2 \left[KA_1^*(K) \frac{\dot{h}}{U} + KA_2^*(K) \frac{B\dot{\alpha}}{U} + K^2 A_3^*(K) \alpha \right] \quad (2.2.2b)$$

Where h and α is the vertical and twisting displacement, H_i^* and A_i^* ($i = 1, 2, 3$) are the flutter derivatives in heaving and torsional direction, $K = fB/U$ is the reduced frequency.

2.3 Bridge Buffeting Analysis Theory's Development

2.3.1 Bridge Buffeting Definition

The vibration response of bridge structure induced by the gust wind (buffeting response) also attracted many attentions at the same time, when much research focused on the flutter response. In particularly the need for the light bridge deck system in modern bridge design tends to bring some of the natural frequency of vibration modes closer together and enhance the possibility of the coupling of mode response. Different from the bridge flutter response, bridge buffeting response is a type of response induced by unsteady loading developing irregularly in space and time (Simiu and Scanlan, 1996). There are two types of buffeting: one type is caused by turbulence in the airflow, which produces significant vertical and torsional motions of a bridge even at low wind speed, the other type is caused by the wake disturbance from the upwind neighbouring structures or obstacles, which is known as wake buffeting. In this kind buffeting, the velocity fluctuations are clearly associated with the turbulence shed in the wake of an upstream body. Wake buffeting is common in urban areas with many tall structures. The development of buffeting theory will be discussed in great detail in the following subsections.

2.3.2 Bridge Buffeting Theory's Development in Frequency Domain

(1) *Single Mode Buffeting Theory*

The pioneering study on the buffeting response is Liepmann (1952), who provided an analytical solution to the buffeting problem of aircraft wings based on the strip assumption. Davenport (1962) firstly applied statistical method to the flexible, line-like structures buffeting response analysis. To consider the spatial correlation of turbulence enveloping the bluff body and variation along the

bridge deck width, aerodynamic admittance coefficient is considered in the buffeting force expression (Eq.2.3.1). To consider the wind velocity correlation relationship along the length of the structure, the joint acceptance is applied in this analysis. Davenport used the quasi-steady aerodynamic model (Eq.2.3.2) to calculate the buffeting force, and the aerodynamic force on the bluff body can be expressed as:

$$L_b(t) = 2\bar{L}\chi_{Lu} \frac{u(t)}{U} + \frac{d\bar{L}}{d\alpha}\chi_{Lw} \frac{w(t)}{U} \quad (2.3.1a)$$

$$D_b(t) = 2\bar{D}\chi_{Du} \frac{u(t)}{U} \quad (2.3.1b)$$

$$M_b(t) = 2\bar{M}\chi_{Mu} \frac{u(t)}{U} + \frac{d\bar{M}}{d\alpha}\chi_{Mw} \frac{w(t)}{U} \quad (2.3.1c)$$

Where u and w are the horizontal and vertical time varying wind velocity component, U is the mean wind velocity, χ_{Lu} , χ_{Lw} , χ_{Du} , χ_{Mu} , χ_{Mw} are the aerodynamic admittance functions depending on the bridge section geometric shape and vary with the reduced wind velocity, \bar{L} , \bar{D} and \bar{M} are the lift force, drag force and twist moment induced by the mean wind velocity, which can be expressed as:

$$\bar{L} = \frac{1}{2}\rho U^2 AC_L \quad (2.3.2a)$$

$$\bar{D} = \frac{1}{2}\rho U^2 AC_D \quad (2.3.2b)$$

$$\bar{M} = \frac{1}{2}\rho U^2 AC_M \quad (2.3.2c)$$

Where C_L , C_D , C_M is the bridge section static lift, drag and twist force coefficients, A is the area of bluff body projected to the wind velocity. After the Fourier transformation, the buffeting force power spectrum can be expressed as:

$$S_L(n) = 4\bar{L}^2 |\chi_{Lu}|^2 \frac{S_{uu}(n)}{U^2} + \left(\frac{d\bar{L}}{d\alpha}\right)^2 |\chi_{Lw}|^2 \frac{S_{ww}(n)}{U^2} \quad (2.3.3a)$$

$$S_D(n) = 4\bar{D}^2 |\chi_{Du}|^2 \frac{S_{uu}(n)}{U^2} \quad (2.3.3b)$$

$$S_M(n) = 4\bar{M}^2 |\chi_{Mu}|^2 \frac{S_{uu}(n)}{U^2} + \left(\frac{d\bar{M}}{d\alpha}\right)^2 |\chi_{Mw}|^2 \frac{S_{ww}(n)}{U^2} \quad (2.3.3c)$$

Structural response values such as power spectrum, maximum value and Root Mean Square (RMS) value under the gust wind can be computed based on random theory and the whole buffeting response of the structure can be evaluated in the general mode coordinate system.

(2) Multimode Aeroelastic Coupling Buffeting Theory

In the above proposed single mode buffeting theory, Davenport considered the turbulence spatial correlation effect by introducing the aerodynamic admittance, the joint acceptance function is adopted to reflect the buffeting force correlation along the span direction. For the structures with the similar dimension in both directions, this simplified method can be accepted. To single mode buffeting theory, the aerodynamic stiffness, damping and the aerodynamic coupling effect are neglected. However, with the increasing of bridge span the structural vibration mode frequencies are closer to each other and mode coupling effect will be clear which can not be predicted by the method proposed by Davenport, and with the increasing of wind speed the aeroelastic coupling will be also clear. Scanlan (1978a, 1978b) firstly proposed the flutter and buffeting coupling analysis theory to consider the effects of aeroelastic coupling and mode coupling. Based on the quasi-steady aerodynamic theory, Scanlan suggested the bridge buffeting force can be described as Eq.2.3.4.

$$L_b(t) = \frac{1}{2} \rho U^2 B \left[C_L \left(2 \frac{u(t)}{U} \right) + (C'_L + C_D) \frac{w(t)}{U} \right] \quad (2.3.4a)$$

$$D_b(t) = \frac{1}{2} \rho U^2 B \left[C_D \left(2 \frac{u(t)}{U} \right) + C'_D \frac{w(t)}{U} \right] \quad (2.3.4b)$$

$$M_b(t) = \frac{1}{2} \rho U^2 B^2 \left[C_M \left(2 \frac{u(t)}{U} \right) + C'_M \frac{w(t)}{U} \right] \quad (2.3.4c)$$

Where C'_L , C'_D and C'_M is the derivative of static lift, drag and twist force coefficients with the relationship of the angle of incidence. As shown above Eq.2.3.4 expression is a little different from the Davenport theory buffeting force expression. Scanlan buffeting force expression adopts the aerodynamic coefficient without aerodynamic admittance in the expression. In general the motion governing equation in mode coordinates can be expressed as:

$$\mathbf{M}\ddot{\mathbf{q}} + \mathbf{C}\dot{\mathbf{q}} + \mathbf{K}\mathbf{q} = \mathbf{Q}_{se} + \mathbf{Q}_b \quad (2.3.5)$$

Here \mathbf{M} , \mathbf{C} and \mathbf{K} are the system generalized mass, damping and stiffness matrix, \mathbf{Q}_{se} and \mathbf{Q}_b are self excited force and buffeting force matrix respectively, to consider the aeroelastic influence, the self-excited forces (\mathbf{Q}_{se}) are included in the external force. When performing analysis, this item will be moved into the structure damping (\mathbf{C}) and stiffness item (\mathbf{K}). Based on the random vibration theory and applying Fourier Transform into Eq.2.3.5, the power spectral density (PSD) of response \mathbf{q} in the generalized mode coordinate can be expressed as:

$$\mathbf{S}(\omega) = \mathbf{H}^*(\omega) \mathbf{S}_{Q_b}(\omega) \mathbf{H}(-\omega)^T \quad (2.3.6)$$

In the conventional aeroelastic coupling buffeting analysis, the transfer function matrix can be expressed as:

$$\mathbf{H}(\omega) = \left(-\omega^2 \mathbf{M} + i\omega \left(\mathbf{C} - \frac{1}{2} \rho U b \mathbf{A}_d(ik) \right) + \mathbf{K} - \frac{1}{2} \rho U^2 \mathbf{A}_s(ik) \right)^{-1} \quad (2.3.7)$$

The PSD matrices ($\mathbf{S}_{Q_b}(\omega)$) of \mathbf{Q}_b can be written as

$$\mathbf{S}_{Q_b}(\omega) = \left(\frac{1}{2} \rho U^2 \right)^2 \left[\mathbf{A}_{bu}^*(k) \mathbf{S}_u(\omega) \mathbf{A}_{bu}^T(k) / U^2 + \mathbf{A}_{bw}^*(k) \mathbf{S}_w(\omega) \mathbf{A}_{bw}^T(k) / U^2 \right] \quad (2.3.8)$$

$\mathbf{S}_u(\omega)$ and $\mathbf{S}_w(\omega)$ are the horizontal and vertical velocity component PSD respectively. The superscript * and T denotes the complex conjugate and matrix transpose operation. The mean square value of the response can be calculated by integrating power spectrum over the frequency range of consideration.

In the large span bridge buffeting analysis, to consider the higher mode contribution on the buffeting response, mode combination method such as the Square Root of Sum of Squares (SRSS) is widely adopted. Scanlan (1978b) firstly proposed the multimode buffeting analysis and applied mode by mode SRSS technique to buffeting analysis. Jain *et al.* (1996) developed the multi-mode analytical procedure for buffeting further based on the Complete Quadratic Combination (CQC) technique, in which the aerodynamic coupling is considered and flutter derivatives are used to express the damping and stiffness matrices of system. Finally the PSD of the physical displacement can be obtained from the PSD of the respective generalized displacement component.

If the transfer matrix is assumed to be narrow-banded and the force spectra are constant around the mode frequencies, the covariance matrix \mathbf{R} can be expressed in a closed form (Chen *et al.*, 2003)

$$\mathbf{R} = \int_0^\infty \text{Re} \left[\mathbf{S}_{Q_b}(\omega) \right] d\omega = \sum_{j=1}^m \sum_{l=1}^m I_{jj} I_{ll} \rho_{jl} \text{Re} \left[\mathbf{S}_{Q_{bc}^j}(\omega_{jl}) \right] / (K_j K_l) \quad (2.3.9)$$

Where

$$I_{jj} = \sqrt{\frac{\pi \omega_j}{4 \xi_j}}; I_{ll} = \sqrt{\frac{\pi \omega_l}{4 \xi_l}}; K_j = m_j \omega_j^2; K_l = m_l \omega_l^2 \quad (2.3.10)$$

$$\rho_{jl} = \frac{8 \sqrt{\xi_j \xi_l} (\beta_{jl} \xi_j + \xi_l) \beta_{jl}^{3/2}}{(1 - \beta_{jl}^2)^2 + 4 \xi_j \xi_l \beta_{jl} (1 + \beta_{jl}^2) + 4 (\xi_j^2 + \xi_l^2) \beta_{jl}^2} \quad (2.3.11)$$

$$\mathbf{S}_{Q_{bc}^j}(\omega_{jl}) = 0.5 \left[\mathbf{S}_{Q_{bc}^j}(\omega_j) + \mathbf{S}_{Q_{bc}^j}(\omega_l) \right] \quad (2.3.12)$$

Where $\beta_{jl} = \omega_j / \omega_l$ with $0 \leq \rho_{jl} \leq 1$; $\rho_{jj} = \rho_{ll} = 1$ and $\rho_{jl} = \rho_{lj} \leq 1$, ω_j and ω_l are well separated and Re is real operator. The above mode response combination expression is CQC approach. From CQC expression, it can be found that the correlation coefficient of the two mode response components depends on the frequency ratio, damping ratio and intermode coupling as well. When the mode frequencies are well separated, which means $\rho_{jl} = \rho_{lj} \approx 0$ ($j \neq l$), then \mathbf{R} can be written as:

$$R = \sum_{j=1}^m I_{jj}^2 \operatorname{Re} \left[S_{Q_{w_j}''}(\omega_j) \right] / K_j^2 \quad (2.3.13)$$

This mode response combination formation is SRSS combination approach.

(3) Multimode Aeroelastic Coupling State Space Buffeting Theory

Miyata and Yamada (1988) adopted structural equations of physical coordinates for the complex eigenvalue computation without iterative calculations. However these buffeting analysis techniques require large computational effort till now, Matsumoto and Chen (1994) and Chen *et al.* (20001a) adopted the state-space transformation on the dynamic governing equation Eq.2.3.5 to perform the buffeting analysis considering aeroelastic and mode coupling effects, the detailed procedure can be seen in Appendix 1, here only some key steps are described, so the buffeting force can be expressed as:

$$L_b(t) = \frac{1}{2} \rho U^2 B \left[C_L \chi_{Lu} \left(2 \frac{u(t)}{U} \right) + (C_L' + C_D) \chi_{Lw} \frac{w(t)}{U} \right] \quad (2.3.14a)$$

$$D_b(t) = \frac{1}{2} \rho U^2 B \left[C_D \chi_{Du} \left(2 \frac{u(t)}{U} \right) + (C_D' - C_L) \chi_{Dw} \frac{w(t)}{U} \right] \quad (2.3.14b)$$

$$M_b(t) = \frac{1}{2} \rho U^2 B^2 \left[C_M \chi_{Mu} \left(2 \frac{u(t)}{U} \right) + C_M' \chi_{Mw} \frac{w(t)}{U} \right] \quad (2.3.14c)$$

In the above buffeting force expressions, Chen *et al.* (2000b, 2001b) combined the Davenport and Scanlan theory together and considered the aerodynamic admittance and aerodynamic coefficient influence on the buffeting force. Chen *et al.* (2000b) expressed the self excited force item (Q_{se}) and buffeting force item (Q_b) in Eq.2.3.14 with the following expressions:

$$Q_{se} = \frac{1}{2} \rho U^2 \left(A_s(ik) \mathbf{q} + \frac{B}{U} A_d(ik) \dot{\mathbf{q}} \right) \quad (2.3.15a)$$

$$Q_b = \frac{1}{2} \rho U^2 \left(A_{bu}(ik) \frac{u}{U} + A_{bw}(ik) \frac{w}{U} \right) \quad (2.3.15b)$$

Here A_s and A_d can be determined by experimental data, which can be approximated in terms of a rational function, the detailed formula expressions can be seen in paper by Chen *et al.* (2000a, 2001b).

To calculate the structural response, the transfer function needs matrix inversion at each discrete frequency and hence needs high computational cost in the above described multi-mode buffeting theory. To overcome such time consuming procedure, Chen *et al.* (2001a, 2002b) presented a frequency independent state-space equation to describe the bridge and aerodynamic system, which can be transformed into linear time-invariant state-space expression as:

$$\dot{Y}(t) = AY(t) + BQ_b(t) \quad (2.3.16)$$

Applying Fourier transform to Eq.2.3.16, based on the theory proposed by Chen *et al.* (2002b) by decomposing the response into complex mode response components, the transfer function matrix of Eq.2.3.16 can be rewritten as:

$$\mathbf{H}(\omega) = \sum_{j=1}^M H_{j0}(\omega)((i\omega)\mathbf{E}^j + \mathbf{F}^j) \quad (2.3.17)$$

Where,

$$\mathbf{E}^j = \Phi_j \Theta_j^T + \Phi_j^* \Theta_j^{*T}, \quad \mathbf{F}^j = -(\Phi_j \Theta_j^T \lambda_j^* + \Phi_j^* \Theta_j^{*T} \lambda_j) \quad (2.3.18)$$

$$H_{j0}(\omega) = \frac{1}{m_j(\omega_j^2 - \omega^2 + i2\xi_j \omega_j \omega)} \quad (2.3.19)$$

Using the transfer matrix in terms of the complex mode properties, the PSD matrix of the mode response can be expressed as:

$$\mathbf{S}(\omega) = \sum_{j=1}^M \sum_{l=1}^M H_{j0}^*(\omega) H_{l0}(\omega) \mathbf{S}_{Q_{bc}^j}(\omega) \quad (2.3.20)$$

Where,

$$\mathbf{S}_{Q_{bc}^j}(\omega) = [(i\omega)\mathbf{E}^j + \mathbf{F}^j] \mathbf{S}_{Q_b}(\omega) \left[(-i\omega)(\mathbf{E}^l)^T + (\mathbf{F}^l)^T \right] \quad (2.3.21)$$

The explanation of symbols in above equations can be seen in Appendix 1. Response PSD can also be calculated based on Eq.2.3.20, mode combination methods such as SRSS and CQC can be used when considering the mode contribution. To consider the influence of multimode and mode coupling on the bridge buffeting response, the CQC method is considered by Chen *et al.* (2000a, 2000b, 2001b), who presented that the use of multimode aerodynamic coupling in the large span bridge buffeting analysis is very important in the high wind velocity range. If the transfer matrix is assumed to be narrow-banded and the force spectra are constants around the mode frequencies, the item $\mathbf{S}_{Q_{bc}^j}(\omega)$ in the covariance \mathbf{R} (Eq.2.3.9) can be substituted with the current item $\mathbf{S}_{Q_{bc}^j}(\omega)$ (Eq.2.3.21) to form a closed form (Chen *et al.*, 2002b). The mode combination approach SRSS and CQC based on the state-space can then be used.

(4) Proper Orthogonal Decomposition (POD) Buffeting Theory

In the above buffeting analysis methods, it is assumed that all gust wind within the whole calculated frequency range has influences on the buffeting response of bridge system. However, with the deep knowledge into the gust wind loads, it is found that gust wind loads may not excite the structural response in all frequency ranges. Solari and Tubino (2007) proposed the Double Mode Transformation (DMT) method to consider the contribution of gust wind on the buffeting of long bridges. DMT technique includes both the joint transformation into principal coordinates of the structural displacements (modal analysis) and of the loading exciting the bridge. Turbulence field is expressed as the effective turbulence proposed by Solari and Tubino (2007), whereby the effec-

tive turbulence is determined using the Proper Orthogonal Decomposition (POD). The POD method deals with the variation in wind turbulence in space and time, which can consider the effective turbulence component contribution on exciting structure vibration through the orthogonal decomposition of the wind velocity spectrum. So the effective turbulence can be realized by considering the part of the actual turbulence which really excites the structure response. Based on this concept the turbulence field can be only reconstructed with the necessary POD modes.

In the POD buffeting analysis approach, the structure system is assumed to have the classical damping, which can be decoupled into the k th modal response $q_k(t)$ and simplified as:

$$\ddot{q}_k(t) + 2\xi_k(2\pi n_k)\dot{q}_k(t) + (2\pi n_k)^2 q_k(t) = \Phi_k^T Q(t) \quad (2.3.22)$$

Where ξ_k and n_k are the k th generalized damping ratio and frequency ($k = 1, 2, \dots, m$, $m =$ total number of structural modes), Φ_k^T is modal shape transpose matrix and $Q(t)$ represents external forces, which can be expressed as the sum of self excited force (F_{se}) and buffeting force (F_b), where the self excited force is ignored. Substituting the buffeting force expression Eq.2.3.4 into Eq.2.3.22, it can be rewritten as:

$$\ddot{q}_k(t) + 2\xi_k(2\pi n_k)\dot{q}_k(t) + (2\pi n_k)^2 q_k(t) = \frac{\rho B}{2} \Phi_k^T [C_u u(t) + C_w w(t)] \quad (2.3.23)$$

In the frequency domain, after including Fourier transform to the above equation, it can be rewritten as

$$\tilde{q}_k(n) = \frac{\rho B}{2} \Phi_k^T H_k(n) [C_u(n)\tilde{u}(n) + C_w(n)\tilde{w}(n)] \quad (2.3.24)$$

Here the transfer matrix can be expressed as:

$$H_k(n) = \frac{1}{(-(2\pi n)^2 + 2i\xi_k(2\pi n)(2\pi n_k) + (2\pi n_k)^2)} \quad (2.3.25)$$

Where $\tilde{q}_k(n)$, $\tilde{u}(n)$, $\tilde{w}(n)$ are the generalised Fourier transforms of $q_k(t)$, $u(t)$ and $w(t)$ respectively, $H_k(n)$ is the complex frequency response function related to k th principal component. The generalized Fourier transformations of $u(t)$ and $w(t)$ can be expressed as a series of orthogonal POD eigenvectors:

$$\tilde{u}(n) = \Delta_u(n)\tilde{q}_u(n) \cong \sum_{j=1}^M \delta_{uj}(n)\tilde{q}_{uj}(n) \quad (2.3.26a)$$

$$\tilde{w}(n) = \Delta_w(n)\tilde{q}_w(n) \cong \sum_{j=1}^M \delta_{wj}(n)\tilde{q}_{wj}(n) \quad (2.3.26b)$$

Where $\tilde{q}_u(n)$ and $\tilde{q}_w(n)$ are the vectors of the generalized Fourier transforms of the principal components of $u(t)$ and $w(t)$, i.e. $S_{yu}(n) = \Lambda_u(n)$, $S_{yw}(n) = \Lambda_w(n)$, $M \leq m$ indicates the number of modes to be retained when applying a modal truncation technique. It is worth noticing that

the POD representation provided by Eq.2.3.26 corresponds to the expression of the power spectral density matrix of the turbulence components by the spectral decompositions:

$$\mathbf{S}_u(n) = \Delta_u(n)\Lambda_u(n)\Delta_u^*(n) \cong \sum_{j=1}^M \delta_{uj}(n)\delta_{uj}^*(n)\eta_{uj}(n) \quad (2.3.27a)$$

$$\mathbf{S}_w(n) = \Delta_w(n)\Lambda_w(n)\Delta_w^*(n) \cong \sum_{j=1}^M \delta_{wj}(n)\delta_{wj}^*(n)\eta_{wj}(n) \quad (2.3.27b)$$

Substituting Eq.2.3.26 into Eq.2.3.24 yields:

$$\tilde{q}_k(n) = \frac{\rho B}{2} H_k(n) \left[\sum_{j=1}^M A_{u_{kj}}(n)\tilde{q}_{u_j}(n) + A_{w_{kj}}(n)\tilde{q}_{w_j}(n) \right] \quad (2.3.28a)$$

$$A_{u_{kj}}(n) = \phi_k^T C_u \delta_{uj}(n) \quad (2.3.29a)$$

$$A_{w_{kj}}(n) = \phi_k^T C_w \delta_{wj}(n) \quad (2.3.29b)$$

With $A_{u_{kj}}$ and $A_{w_{kj}}$ being participation factors, which quantify the influence of the j th spectral mode of the longitudinal and vertical turbulence components respectively on the k th structural mode. They are the k th and j th terms of the matrices $\mathbf{A}_u(n)$ and $\mathbf{A}_w(n)$, referred to as the cross-modal participation spectral matrices related to $u(t)$ and $w(t)$ respectively.

The above procedure ignores the self excited force influence. In general the self excited force can be expressed as the sum of the aerodynamic damping item and stiffness item:

$$\mathbf{F}_{se} = \mathbf{F}_{aerodamping} + \mathbf{F}_{aeroelastic} = \mathbf{C}_{AD}\dot{\mathbf{q}}(t) + \mathbf{K}_{AE}\mathbf{q}(t) \quad (2.3.30)$$

Where, $\mathbf{F}_{se} = \left\{ \mathbf{F}_{se}^L \quad \mathbf{F}_{se}^D \quad \mathbf{F}_{se}^M \right\}^T$ is the self-excited force item in three directions. Based on the Scanlan (1978a, 1978b) proposed self-excited force, substituting the self excited force expression into the system governing equation, the equation can be written as in the coordinate:

$$\mathbf{M}\ddot{\mathbf{q}}(t) + \mathbf{C}\dot{\mathbf{q}}(t) + \mathbf{K}\mathbf{q}(t) = \mathbf{C}_{AD}\dot{\mathbf{q}}(t) + \mathbf{K}_{AE}\mathbf{q}(t) + \mathbf{F}_b(t) \quad (2.3.31)$$

where \mathbf{C}_{AD} and \mathbf{K}_{AE} are the aerodynamic damping and stiffness matrices, written as:

$$\mathbf{C}_{AD} = \begin{bmatrix} \dot{h} & \dot{p} & \dot{\alpha} \\ \frac{1}{2}\rho U^2 B \times \left(K \frac{H_1^*}{U} & K \frac{H_5^*}{U} & K \frac{H_2^*}{U} \right) \\ \frac{1}{2}\rho U^2 B \times \left(K \frac{P_1^*}{U} & K \frac{P_5^*}{U} & K \frac{P_2^*}{U} \right) \\ \frac{1}{2}\rho U^2 B^2 \times \left(K \frac{A_1^*}{U} & K \frac{A_5^*}{U} & K \frac{A_2^*}{U} \right) \end{bmatrix} \begin{matrix} F_h \\ F_p \\ F_\alpha \end{matrix} \quad (2.3.32a)$$

$$\mathbf{K}_{AE} \begin{bmatrix} h & p & \alpha \\ \frac{1}{2} \rho U^2 B \times \left(K^2 \frac{H_4^*}{B} & K^2 \frac{H_6^*}{B} & K^2 H_3^* \right) \\ \frac{1}{2} \rho U^2 B \times \left(K^2 \frac{P_4^*}{B} & K^2 \frac{P_6^*}{B} & K^2 P_3^* \right) \\ \frac{1}{2} \rho U^2 B \times \left(K^2 \frac{A_4^*}{B} & K^2 \frac{A_6^*}{B} & K^2 A_3^* \right) \end{bmatrix} \begin{bmatrix} F_h \\ F_p \\ F_\alpha \end{bmatrix} \quad (2.3.32b)$$

Where H_i^* , P_i^* , A_i^* are the flutter derivatives in three directions (h, p, α) ($i=1, \dots, 6$), h, p, α are three direction displacement, while $\dot{h}, \dot{p}, \dot{\alpha}$ are three directions relative to velocity respectively.

Moving the aerodynamic damping and stiffness item to the left side, Eq.2.3.31 can be simplified as:

$$\mathbf{M}\ddot{\mathbf{q}}(t) + \mathbf{C}^* \dot{\mathbf{q}}(t) + \mathbf{K}^* \mathbf{q}(t) = \mathbf{F}_b(t) \quad (2.3.33)$$

Where $\mathbf{C}^* = \mathbf{C} - \mathbf{C}'_{AD}$ and $\mathbf{K}^* = \mathbf{K} - \mathbf{K}'_{AE}$ ($I = h, p, \alpha$), according to the processing method in the equation above, the decoupled system dynamic governing equation can be simplified as:

$$\tilde{q}_k(n) = \frac{\rho B}{2} \Phi_k^T \overline{H_k(n)} [C_u(n) \tilde{u}(n) + C_w(n) \tilde{w}(n)] \quad (2.3.34)$$

Here the transfer function can be expressed as:

$$\overline{H_k(n)} = \frac{1}{\left(-(2\pi n)^2 + i^* \left(2\xi_k (2\pi n_k) - \phi_k^T C'_{AE} \phi_k \right) (2\pi n) + \left((2\pi n_k)^2 - \phi_k^T K'_{AE} \phi_k \right) \right)} \quad (2.3.35)$$

After getting the transfer function expression for the conditions without self excited force and with self excited force, the PSD of the structure system response can be calculated based on random vibration theory. The PSD matrix of the principal components and of the bridge response can be evaluated as:

Without self excited force

$$\mathbf{S}_p(n) = \frac{1}{4} \rho^2 B^2 \left[|\chi_u|^2 \mathbf{H}(n) \mathbf{A}_u(n) \Lambda_u(n) \mathbf{A}_u^*(n) \mathbf{H}(n)^* + |\chi_w|^2 \mathbf{H}(n) \mathbf{A}_w(n) \Lambda_w(n) \mathbf{A}_w^*(n) \mathbf{H}(n)^* \right] \quad (2.3.36a)$$

$$\mathbf{S}_q(n) = \Phi \mathbf{S}_p(n) \Phi^T \quad (2.3.36b)$$

With self excited force

$$\overline{\mathbf{S}}_p(n) = \frac{1}{4} \rho^2 B^2 \left[|\chi_u|^2 \overline{\mathbf{H}(n)} \mathbf{A}_u(n) \Lambda_u(n) \mathbf{A}_u^*(n) \overline{\mathbf{H}(n)}^* + |\chi_w|^2 \overline{\mathbf{H}(n)} \mathbf{A}_w(n) \Lambda_w(n) \mathbf{A}_w^*(n) \overline{\mathbf{H}(n)}^* \right] \quad (2.3.37a)$$

$$\overline{\mathbf{S}}_q(n) = \Phi \overline{\mathbf{S}}_p(n) \Phi^T \quad (2.3.37b)$$

Where $\mathbf{H}(n) = \text{diag} \{H_1(n), \dots, H_m(n)\}$ and $\overline{\mathbf{H}(n)} = \text{diag} \{\overline{H_1(n)}, \dots, \overline{H_m(n)}\}$ are the complex frequency response matrices of the principal coordinates, Φ is the structural modal shape matrix.

2.3.3 Uncertainties of Bridge Buffeting Theory

From the previously proposed buffeting analyses, it can be seen that the buffeting analysis method is a kind of semi-theoretical and semi-empirical approach. Some parameters and assumptions must be provided to complete the final analysis. Among the various parameters for the buffeting calculations, finite element model analysis can be used to determine the natural frequencies and mode shapes accurately and wind tunnel section model tests can be used to get the static force coefficients. The other uncertainties are therefore the total damping of each mode, the wind velocity spectra, and the frequency-dependent functions describing the correlation of wind loading, namely the joint acceptance or coherence function for correlation along the span and the two-dimensional aerodynamic admittance for the correlation over the bridge deck cross section.

(1) Wind Spectrum Characteristics

Wind velocity spectrum is one important parameter influencing the buffeting response analysis and determined based on large volumes of field test data by the statistical method. Until now many wind velocity spectrum have been proposed. Among these, the Von Karman velocity component spectra are most widely used since 1948, Von Karman (1948) proposed the spectrum equation (Eq.2.3.38a and Eq.2.3.38b) based on wind tunnel experiments by creating a turbulent homogeneous and isotropic flow field.

$$\frac{nS_u(n)}{\sigma_u^2} = \frac{4f_{new}L_u/z}{[1 + 70.8(f_{new}L_u/z)^2]^{5/6}} \quad (2.3.38a)$$

$$\frac{nS_{v,w}(n)}{\sigma_{v,w}^2} = \frac{4f_{new}L_{v,w}/z [1 + 755.2(f_{new}L_{v,w}/z)^2]}{[1 + 283.2(f_{new}L_{v,w}/z)^2]^{11/6}} \quad (2.3.38b)$$

Where $f_{new} = fz / \bar{u}(z)$, $L_{u,v,w}$ is the integral length scale of the turbulence component.

Solari *et al.* (2001) summarized the wind velocity spectra found in the literatures as shown in Table.2.3.1. According to these spectra, turbulence intensities and turbulence length scale are the main two factors considered in wind spectrum analyses.

Table 2.3.1 Velocity component spectra $S_{u,v,w}$ ($x = fL / \bar{u}_{10}$, here $L = 1200\text{m}$, \bar{u}_{10} is the mean wind velocity at 10m height, $x_z^{u,v,w} = fL_z^{u,v,w} / \bar{u}(z)$, $L_z^{u,v,w}$ is the mean scale of

eddy, $f_{new} = fz / \bar{u}(z)$ is the Monin coordinate, $\bar{u}(z)$ is the mean wind velocity at z height, β_u is the nondimensional turbulence intensity factor) (Solari *et al.*, 2001)

Spectrum Name	$fS_u(z; f) / u_*^2$	$fS_v(z; f) / u_*^2$	$fS_w(z; f) / u_*^2$
Davenport	$\frac{4x^2}{(1+x^2)^{4/3}}$		
Simiu	$\frac{200f_{new}}{(1+20f_{new})^{5/3}}$		
Von Karman	$\frac{4\beta_u x_z^u}{(1+70.8(x_z^u)^2)^{5/6}}$	$\frac{4\beta_v x_z^v (1+755.2(x_z^v)^2)}{(1+283.2(x_z^v)^2)^{11/6}}$	$\frac{4\beta_w f (1+755.2(x_z^w)^2)}{(1+283.2(x_z^w)^2)^{11/6}}$
Kaimal	$\frac{105f_{new}}{(1+33f_{new})^{5/3}}$	$\frac{17f_{new}}{(1+9.8f_{new})^{5/3}}$	$\frac{2f_{new}}{(1+5.3f_{new}^{5/3})}$
Tieleman	$\frac{20.53\beta_u f_{new}}{(1+475.1f_{new}^{5/3})}$		
Panofsky			$\frac{6f_{new}}{(1+4f_{new})^2}$

From Table.2.3.1, besides Davenport spectrum, a relationship can be observed between the magnitude and frequency as shown in Fig.2.3.1, only horizontal velocity spectra are plotted in Fig.2.3.1. From Fig.2.3.1, it can be found that the values will be different at the same frequency due to the difference of spectrum's expressions, Kaimal spectrum indicates a straight varying process, for other spectrum the varying process is a curve shape.

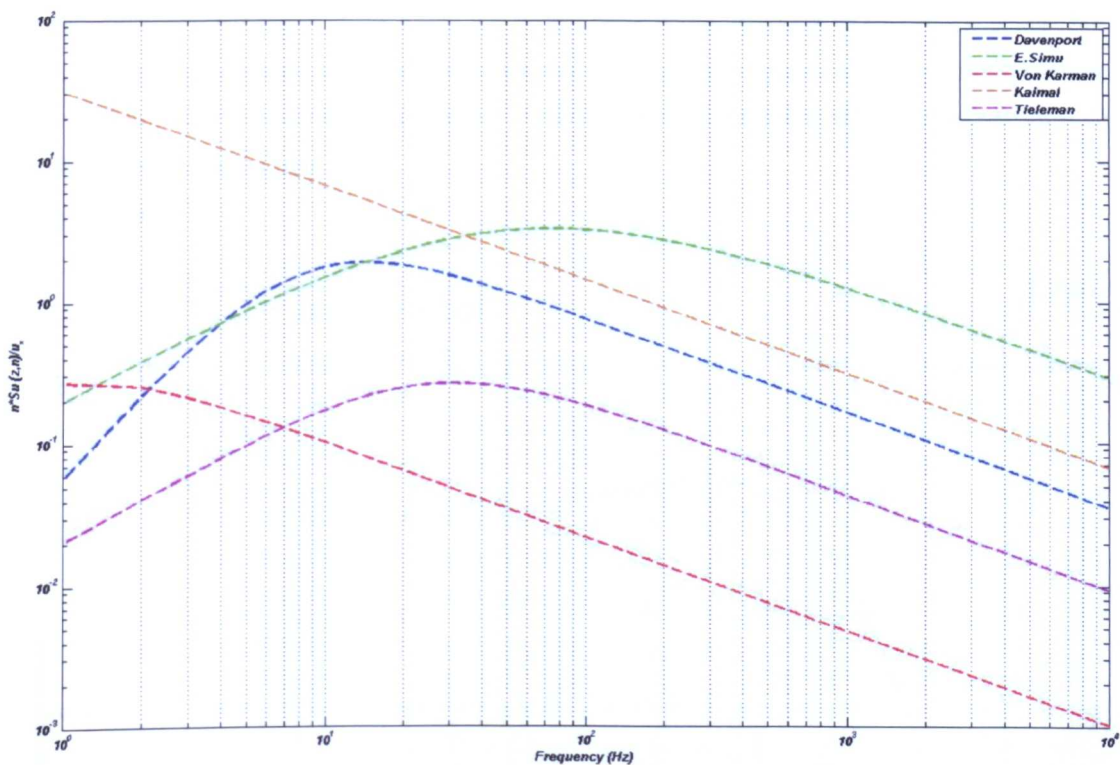


Fig 2.3.1 Horizontal velocity component spectrum (S_u)

(2) Damping

Damping is another key factor to determine the amplitude of vibrations with any mechanism. Generally, the total damping of bridge structure consists of two parts: the structural damping and aerodynamic damping. Structure damping is determined by the structural material characteristics. Aerodynamic damping of bridge system can be estimated based on the quasi-steady theory or based on the flutter derivatives through the wind tunnel model tests. Davenport (1962) first estimated the aerodynamic damping (Eq.2.3.39) for slender structures. The aerodynamic damping is proportional to wind speed and inversely proportional to natural frequency of the mode of vibration based on quasi-steady theory for a uniform slender horizontal structure in a wind normal to its axis. Scanlan and Tomko (1971) adopted the flutter derivatives to express the aerodynamic damping.

$$\zeta_{aero} = \frac{\rho B U}{8\pi f m} \left[\frac{dC_L}{d\alpha} \right]_{\alpha=0} \tag{2.3.39}$$

Since aerodynamic damping can be dominant over structural damping or potentially be negative, it can have a major effect on the response to buffeting.

(3) Aerodynamic Admittance

Aerodynamic admittance is a function representing both body shape and dimensions related with the characteristics of the turbulence. Davenport (1962) proposed the aerodynamic admittance to

consider pressure varying in space along the bridge deck width direction to realize the bridge buffeting response prediction. The Sears aerodynamic admittance is approximated by Eq.2.3.40 and often used as the aerodynamic admittance of vertical buffeting and torsional buffeting respectively. This function can be written as:

Sears function:

$$|\chi_L^w(\delta)|^2 = \frac{a + \delta}{a + (\pi a + 1)\delta + 2\pi\delta^2} \quad (2.3.40)$$

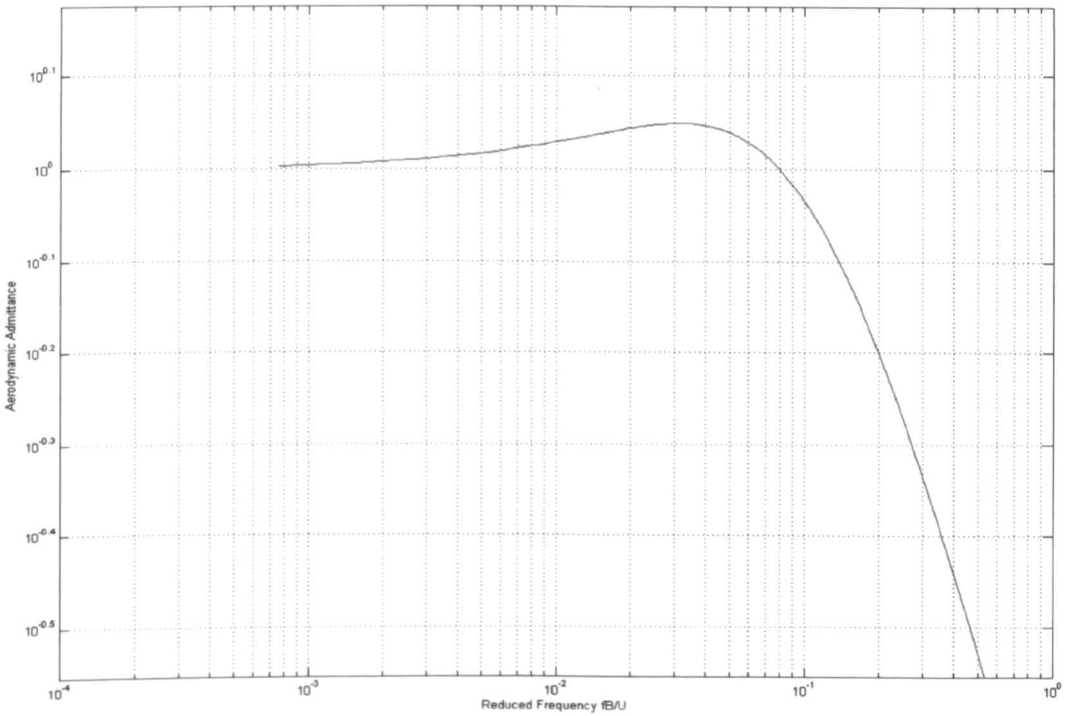


Fig 2.3.2 Sears' aerodynamic admittance

Where $a = 0.1811$, $\delta (= \pi fB / U)$ is the reduced frequency, B is the deck width.

For a given body aerodynamic admittance is a frequency-dependent function. Fig.2.3.2 plots Sears's suggested aerodynamic admittance, a decrease in the aerodynamic admittance with increasing frequency corresponds to the fact that the smaller turbulent eddies have shorter wavelengths, thus those eddies with higher frequencies will suffer a loss of coherence more rapidly than do the larger eddies (Scanlan *et al.*, 1996). To investigate the characteristics of aerodynamic admittance, Sankaran and Jancauskas (1992) utilized wind tunnel experiment technique to evaluate the aerodynamic admittance for 2D rectangular cylinder with aspect ratio (10:1, 6:1 and 4:1), in which the smooth and turbulence inflow condition were considered. From the experimental results, it was found that at low turbulence flow, Sear's function can substantially underestimate the aerodynamic admittance of 2D rectangular cylinder. The extent of this under estimation increases with decreasing aspect ratio. However, as the small-scale turbulence increases, the aerodynamic admittance converges to Sear's function. Kobayashi *et al.* (1992) also adopted wind tunnel experiment

approach to study the aerodynamic admittance for the rectangular cylinder with ratio 2:1 and 5:1 at the smooth and turbulence inflow condition. It was found that the obtained admittances of horizontal and vertical components are almost the same with the change of turbulence characteristics in the range tested.

The assumption in aerodynamic admittance appears to be useful for the slender line-like structures with a body characteristic of the length smaller than the scales of the turbulence longitudinal components. In fact the wind pressure induced by the turbulence is unsteady and varying with the time and space. Especially for the buffeting lift forces on the advanced bridge decks with the closed-box girders, the width of which has a similar dimension to the length scales of the vertical components of the gusts in the span-wise direction. To get more accurate description about the aerodynamic admittance, Larose and Mann (1998) proposed the empirical models of aerodynamic admittance and span-wise coherence of the aerodynamic forces based on the experiments on closed-box girder bridge decks. And then Larose (2003) adopted the experiment in model and full scale to study the spatial distribution of the dynamic gust loading for line-like structures, the final results were compared with the theoretical analysis based on the lifting-surface theory. It was found that the cross-correlation coefficient of the lift forces was larger than the correlation coefficient of the oncoming turbulence when the scales of the wind vertical component in the span-wise direction are similar to the deck width. This was combined with a deficit in cross-sectional aerodynamic admittance. It is caused by the wind gusts, limited in size, distorted and broken up as impinging on a long-span bridge deck. In this process the vortices tends to spread laterally, increasing the span-wise cross-correlation of their effect. The 3-D model based on an analysis of two arbitrary horizontal wave vectors showed qualitative agreement with the experimental description of the aerodynamic admittance and the spatial distribution of the gust loading on bridge decks, which helped understand the generation of lift on a chord-wise strip and explained the observed larger span-wise co-coherence of the forces when compared to the co-coherence of the incident wind for the situation where the strip assumption is not applicable (Larose, 2003). From the analysis, an empirical model for the gust loading for closed-box girder bridge deck was proposed to overcome the limits of strip assumption was found.

(4) Joint Acceptance (Space Coherence) Function

The concept of joint acceptance function, or space coherence function, was introduced by Davenport (1962) to express the coherence of longitudinal turbulence components between points. Solari *et al.* (2001) presented this concept further, reflecting the cross correlation of the same turbulence components at different position points' p_1 and p_2 . Three types of functions are adopted in the buffeting analysis, which can be expressed as the following equations:

$$R_{u,v,w}(p_1, p_2; n) = \exp \left\{ - \frac{2n \sqrt{\sum_r C_{r-u,v,w}^2 |r_1 - r_2|^2}}{\bar{u}(z_1) + \bar{u}(z_2)} \right\} \tag{2.3.41a}$$

$$R_{u,v,w}(p_1, p_2; n) = \exp \left\{ - \frac{2n \sum_r C_{r-u,v,w} |r_1 - r_2|}{\bar{u}(z_1) + \bar{u}(z_2)} \right\} \quad (2.3.41b)$$

$$R_{u,v,w}(p_1, p_2; n) = \exp \left\{ - \frac{2nC_{r-u,v,w} \sqrt{\sum_r |r_1 - r_2|^2}}{\bar{u}(z_1) + \bar{u}(z_2)} \right\} \quad (2.3.41c)$$

As described in the paper written by Solari *et al.* (2001), the exponential decay coefficient used in the space coherence function will be different. Two points with the same height and the decay coefficients can be used to compare the variation in space coherence function with respect to different frequency, here. Only the *u* component space coherence function is plotted in the following figure. Fig.2.3.4 plots the comparison from Eq.2.3.41a to c, in this figure the frequency is from 0 Hz to 10 Hz, the coefficient $C_u = 8.0$, $C_v = 8.0$ and $C_w = 8.0$, the two points distance is assumed to be 1m, the averaged velocity value is assumed to be 10m/s.

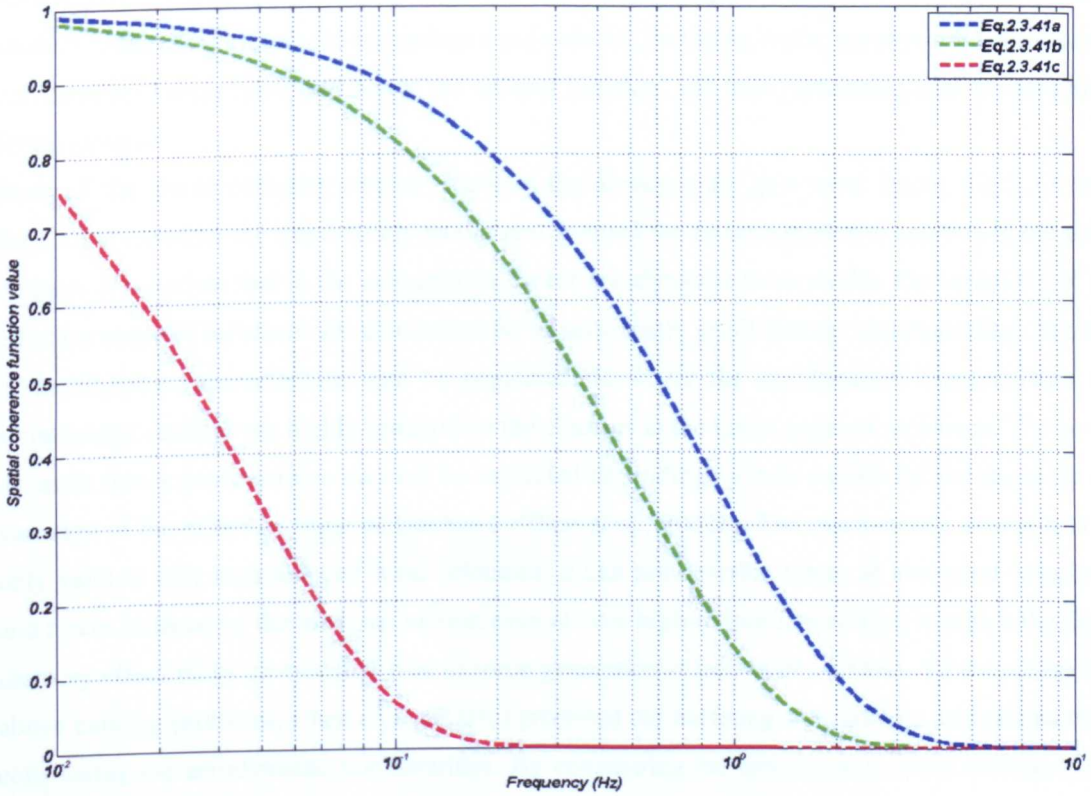


Fig 2.3.4 Spatial coherence function of horizontal velocity component

From Fig.2.3.4, it can be found that the coherence value decreases as the frequency increases, at the same time it can be also found that the value based on the Eq.2.3.41a is larger than the other two functions. The value from Eq.2.3.41c drops quickly before 0.2Hz, and the other two values drop quickly in the range of 0-4 Hz.

2.3.4 Bridge Buffeting Time Domain Analysis Method

In the above discussions about the bridge buffeting analysis method, the proposed methods are based on the frequency domain analysis and limited to linear structures excited by the stationary wind loads. Due to simple realisation and effective calculation, the bridge structure's buffeting analysis method of frequency domain is most widely adopted, but it has some limitations. For example, it can not reflect the structural nonlinear characteristic or consider the aerodynamic nonlinear factors. To overcome such problems, the analytical methods in the time domain are provided. Kovacs *et al.* (1992) performed the wind induced vibration time history analysis to the Helgeland Bridge in Norway, which has a span of 425m. Boonyapinyo *et al.* (1999) and Chen *et al.* (2000a, 2000b) study the flutter and buffeting in the time domain. Boonyapinyo *et al.* (1999) adopted Roger's unsteady aerodynamic self excited model, performing time domain buffeting analysis on the 1990m span Akashi Kaikyo Bridge. The multi-dimensional Autoregressive Moving Average (ARMA) model was utilized to simulate random wind velocity and bridge structure buffeting response with the state space method. Chen (2002a, 2002b) adopted a type of Autoregressive (AR) model to build the bridge section random wind velocity, buffeting force, aerodynamic admittance and combined acceptance function in the rational function, and then performing time domain buffeting analysis.

Most of the above buffeting studies modelled the aerodynamic gust wind forces (Eq.2.3.4 and Eq.2.3.14) based on the quasi-steady theory and adopted the linear aeroelastic analysis in the time domain. It is known that in the conventional linear aerodynamic force model, the variations of an effective angle of incidence are assumed to be so sufficiently small that the corresponding changes of aerodynamic characteristics can be neglected. However the aerodynamic characteristics of some bridge sections are highly sensitive to the changes in the mean angle of incidence. The aerodynamic forces nonlinearities may not be neglected depending on their sensitivity and the range of variation of the effective angle of incidence (Chen *et al.*, 2002b). The quasi-steady assumption is only valid at very high reduced wind velocities. It can not describe forces at low-wind velocities and forces induced by the torsional motion even at very high-reduced velocities, in which the fluid memory effect plays an essential role in force generation (Chen *et al.*, 2000a). To overcome the above existing problems, Chen *et al.* (2001c) proposed the buffeting time domain analysis method considering the aerodynamic nonlinearities. By considering the aerodynamic force nonlinearities through the static force coefficients, the quasi-steady force model can be expressed as a nonlinear function of the effective angle of incidence α_e , with corresponding force coefficients. While the effective angle of incidence is a function of structural motion and incoming wind fluctuations and formulated for quasi-steady aerodynamic forces, it is not in a straightforward manner for the unsteady cases (Chen *et al.*, 2002a, 2002b). Diana *et al.* (1998, 1999) suggested different effective angles of incidence for lift and pitching moment components of the unsteady aerodynamic forces for a nonlinear force model. Chen *et al.* (2003) divided the effective angle of incidence into low

frequency (large length scale) and high-frequency (small length scale) components to model the nonlinear aerodynamic forces.

$$\alpha_e(t) = \alpha_e^l(t) + \alpha_e^h(t) \tag{2.3.42}$$

Where l and h express the low-frequency (including static component) and high-frequency components respectively. The low and high frequency ranges are separated at a critical frequency. Chen *et al.* (2003) assumed the first natural frequency as the critical frequency. The low-frequency turbulence is modelled to introduce changes in the mean angle of incidence influencing bridge aerodynamics, and the high frequency turbulence is modelled to alter the flow structure around the bridge section. Hence the aerodynamics and the resulting forces can be modelled by directly using the aerodynamic characteristics measured in turbulence flow conditions.

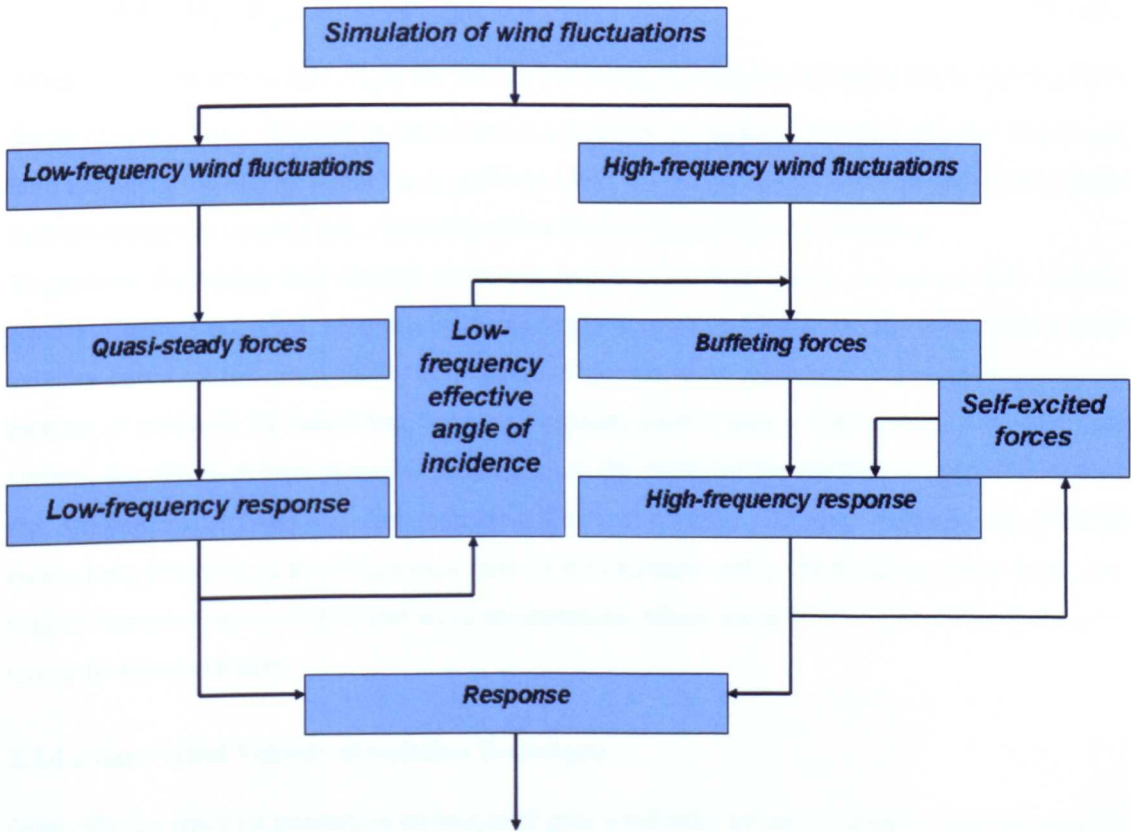


Fig 2.3.5 Proposed aerodynamic nonlinear analysis framework (Chen *et al.*, 2001a)

The proposed aerodynamic nonlinear aeroelastic buffeting analysis approach by Chen *et al.* (2003) can be seen in Fig.2.3.5. In this analysis frame, the low and high frequency components of the nonlinear aerodynamic forces are approximated by using the rational function approximation (RFA) to express the buffeting parameters as functions of reduced velocity at varying angles of incidence. The nonlinear unsteady forces can be calculated in the time domain, following which the dynamic response is calculated by using the Newmark Beta step-by-step integration scheme. Chen *et al.* (2001a, 2001b and 2001c) presented an integrated state-space system model with a vector-valued white noise input to describe the dynamic responses of bridges under the action of

multi-correlated winds. This method considered the unsteady aerodynamic forces, the attendant motions of the structure and the structural and aerodynamic coupling effects among structure modes. Because the assessment of unsteady aerodynamic forces in the time domain requires identification of aerodynamic impulse response functions, it is difficult for a direct determination of these functions for the bluff bridge section, and techniques based on the wind tunnel tests have not been well established. So Chen *et al.* (2000a, 2000b, 2001a, 2001b, 2001c) approximated the unsteady aerodynamics in the time domain with RFA function.

2.3.4.1 Wind Load Composition

In general, the external load $\mathbf{F}(t)$ applied to the bridge structure system can be simplified as:

$$\mathbf{F}(t) = \mathbf{F}_G + \mathbf{F}_{st} + \mathbf{F}_b(t) + \mathbf{F}_{se}(t) \quad (2.3.43)$$

Where, \mathbf{F}_G is the self weight, \mathbf{F}_{st} is the static wind force, $\mathbf{F}_b(t)$ is the buffeting force, and $\mathbf{F}_{se}(t)$ is the self excited force. The self excited force is a function of displacement and velocity. The linear item including the displacement has a stiffness effect known as aerodynamic stiffness. The linear item including the velocity has a damping effect known as aerodynamic damping.

To perform the bridge time domain buffeting analysis, the first step is to express time varying wind buffeting load. Until now the buffeting force is expressed by using the time history wind velocity based on the quasi-steady assumption. Since the gust wind load is a random process, a number of methods for simulating stationary random wind velocity time history, with specified spectral density, have been proposed so far, such as the Artificial Neural Networks (ANN) method, the Autoregressive (AR) and Autoregressive Moving Average (ARMA) methods, the Wavelet method etc. However, a lot of data exist both in the literature and in the building codes on the statistical characterization of different wind environments which allow for the generation of parameters to be selected easily.

2.3.4.2 Gust Wind Velocity Simulation Technique

Generally the artificial generation technique of gust wind velocity can be divided into two classes: (1) one is to adopt the series of sine and/or cosine functions based on the superposition of waves with the same amplitude (Constant Amplitude Wave Superposition (CAWS) method or spectrum method). The earliest research work on the subject was done by Shinozuka (1970), who proposed a method of simulation to simulate multivariate and multidimensional random processes based on the wave superposition. Later developments of the methods allowed better quality and greater numerical efficiency to be achieved. Shinozuka and Jan (1972) proposed a method of simulation based on superposition of evenly spaced frequency components having appropriate amplitudes. Deodatis (1996) used the fast Fourier transform (FFT) technique to simulate the ergodic multivariate stochastic processes to save the simulation cost.

(2) The other one adopts the application of linear filters to sequences of random numbers (linear filtering). Wyatt and May (1973) used a regressive-type technique to generate partially correlated wind forces. In 1976, Saul (1976) suggested a procedure to generate partially correlated wind fluctuations having the same spectral density. Iwatani (1982) suggested the AR filtering technique to generate multiple wind histories. Samaras *et al.* (1985), Mignolet and Spanos (1990), Li and Kareem (1990) used the ARMA model to simulate the random process of wind field. The detailed procedure ARMA digital method discussed in the above can be seen in chapter 6.

Besides the above discussed method, some research combined above two techniques together named as the hybrid method to simulate the random process. Li and Kareem (1993) simulated the multivariate random process based the hybrid Discrete Fourier Transform (DFT) and digital filtering approach. Facchini (1996) used a hybrid model to simulate the Gaussian cross-correlated wind velocity fluctuations. The model is based on the theory of expansions in convergent series of proper functions of the realizations of the target process. The coefficients of the expansion are generated by means of an extended AR filter.

2.3.5 Buffeting Prediction Based on Deterministic Technique

In the above discussions, the conventional bridge buffeting analysis methods mainly based on the random vibration theory and statistical method are overviewed and discussed. At the same time as stated in the above section, the wake buffeting (Fig.2.3.6) is the second kind of buffeting. Some investigations about such buffeting have been done based on two simple geometry shaped bluff bodies such as circular cylinders (Zdravkovich, 1977) and square cylinders with experimental technique (Hangan and Vickery, 1997, 1998 and 1999).

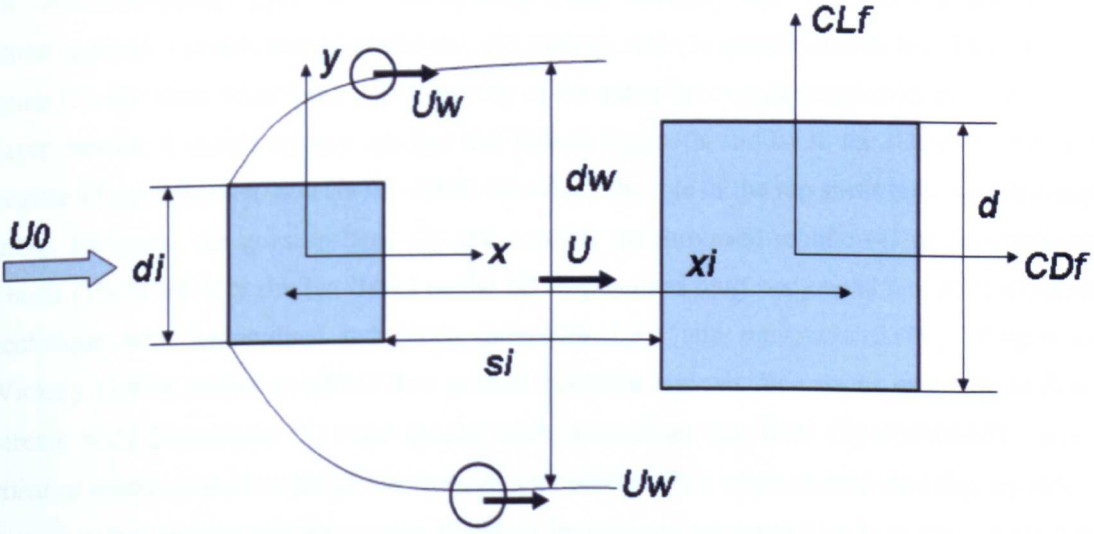


Fig 2.3.6 Wake buffeting configuration and parameters (Hangan and Vickery, 1999)

Index: U_0 : Free stream velocity, U_w : Free stream-line velocity at separation

Zdravkovich (1977) reviewed the flow characteristics of two identical circular cylinders in various arrangements. Five flow regimes were identified according to a function of the inter obstacle spac-

ing: (1) to very small distance, the shear layer separating from the first cylinder overshoot the second one at the downstream direction. The wake characteristics are similar to a single body's one and vortex shedding is formed by the vorticity generated on the upstream cylinder. (2) The shear layer from the upstream cylinder alternately reattaches on the sides of the second one. This process is synchronized with the vortex shedding period. (3) With the gap increasing quasi-steady reattachment occurs on the second cylinder and irregular shedding and loading occur. (4) When second cylinder's location is close to the end of the upstream recirculation region, the boundary layer formation on it is disturbed and the vortex street becomes intermittent. (5) For much larger gap the vortex shedding downstream of the two cylinders is no longer synchronized generating two distance vortex streets. Zhang and Melbourne (1992) also studied the flow interference between two circular cylinders in tandem at Reynolds number 110,000 with turbulence intensities 0.4%, 4.5% and 10.5% by the experimental approach, through which the flow switching for regimes (2) and (3) was also investigated.

Besides the research about the circular cylinder, Sakamoto and Haniu (1988) studied the buffeting for tall (free-ended) square cross-section, surface-mounted obstacles in a thick, turbulent boundary layer. From the drag and vortex shedding behaviour, several regimes as a function of gap length are identified: (1) stable reattachment, (2) unstable reattachment, (3) stable synchronized and (4) unstable synchronized. In regime (1) no vortex shedding is detected. Regime (2) is bistable. When the flow reattaches on the second cylinder, vortices are shed from its wake. Otherwise, vortices are shed from the first one. Regime (3) is described by synchronized vortex shedding triggered by the upstream body and in regime (4) an additional Strouhal frequency appears on the downstream cylinder, suggesting binary vortex shedding. Martinuzzi and Havel (2000) investigated the buffeting of surface-mounted tandem cubic obstacles in a thin boundary layer and could identify at least three regimes: (1) alternate reattachment, (2) lock-in, and (3) quasi-isolated. For the lock-in regime (2), the shear layer motion over the top of the cubes is strongly coupled to the lateral shear layer motion. It is still unclear whether this lock-in regime is similar to the stable synchronized regime (3) of Sakamoto and Haniu (1988), for which the role of the top shear layer appears negligible. However, the quasi-isolated (3) and unstable synchronized regime (4) of Sakamoto and Haniu (1988) are very similar. Based on the 2D sharp-edged bluff body wind tunnel experimental technique with longitudinal turbulence intensities 1.3% and transverse 0.46%, Hangan and Vickery (1999) further identified five general buffeting regimes for various upstream to downstream body dimensions: (1) close spacing with insignificant gap flow, (2) intermittent reattachment of upstream shear layer on the downstream cylinder, (3) a synchronized shedding regime, (4) quasi-isolated regime with two vortex shedding frequencies corresponding to the two wake flows with little interference, (5) isolated with no interference. These regimes are qualitatively similar to those found by Zhang and Melbourne (1992) for circular cylinders. Havel *et al.* (2001) studied the buffeting of 2D and 3D sharp-edged bluff bodies in tandem at moderate Reynolds number with

experimental technique, the influence of bluff body separation distance on the aerodynamic loading varying and macroscale flow characteristics was presented.

The above experimental studies suggest that wake buffeting flow of different shape bluff bodies shares many qualitative similarities, however the gap distance between two bluff bodies determine the influence of wake buffeting and flow regimes.

2.4 Vortex Shedding Introduction

Two aerodynamic phenomena: flutter and buffeting have been discussed in the above contents. However there is still one more important aerodynamic phenomenon: vortex shedding. Vortex shedding is a wake-induced effect occurring on bluff bodies such as bridge decks and pylons. Wind flowing against a bluff body forms a stream of alternating vortices called a Von Karman vortex street. These vortex streets generate structural vibration known as Vortex Induced Vibration (VIV). When studying vortex shedding, the most important parameter is the Strouhal number, which creates the connection between the vortex shedding frequencies, bluff body diameter and flow velocity.

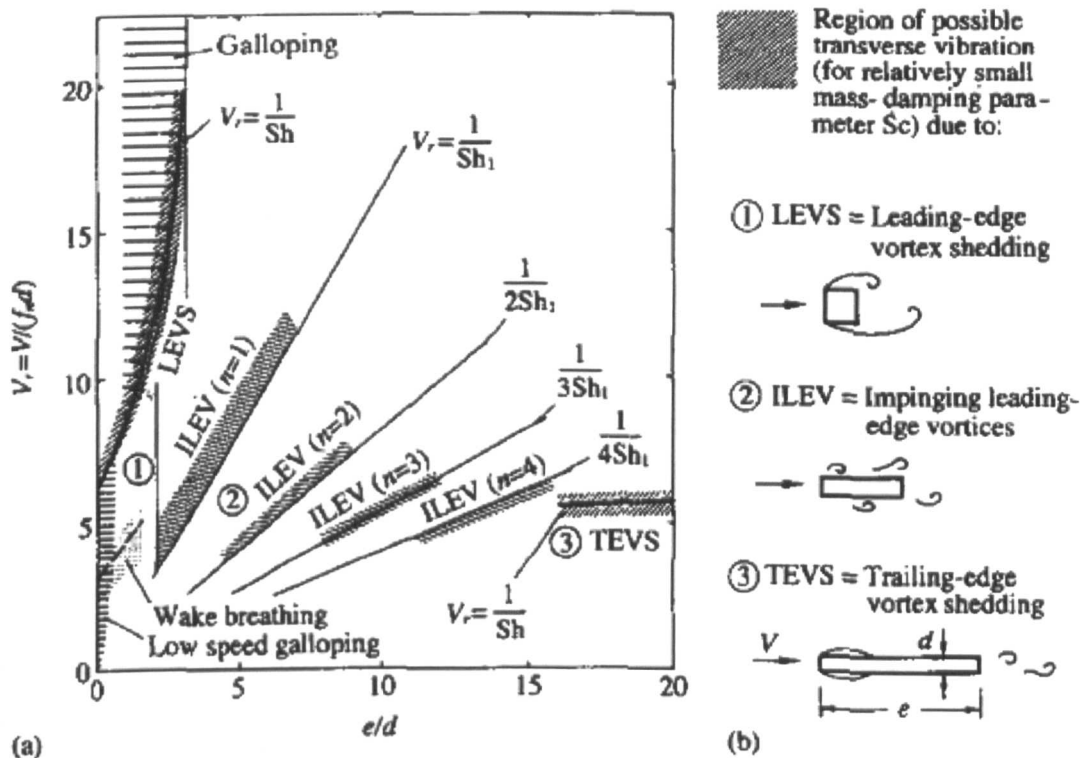


Fig 2.4.1 Flow pattern of different aspect ratio rectangular (Naudascher and Wang, 1993)

Due to the geometrical similarity to the bridge deck, the rectangular section is widely used as the study target. When the steady flow travels around the square cylinder, it will separate at the front of the bluff body firstly, and then the shear layer will be generated at the top and bottom layer near the bluff body. Parker and Welsh (1981) also discussed flow regimes according to the aspect ratio at zero incidence angles. LEVS happens in the range of roughly $0 < B/D < 1$ (B : the length of

the body, D : the height of the body) without reattaching separation streamlines for smooth flow, within these ranges of LEVS, the vortex formation is strongly controlled by the dynamics in the low-base pressure region. Naudascher and Wang (1993) presented rectangular prisms with three kinds of vortex-induced excitation including Leading-Edge Vortex Shedding (LEVS) (Fig.2.4.1 (b)-1), Impinging Leading-Edge Vortices (ILEV) (Fig.2.4.1-(b)-2), and Trailing-Edge Vortex shedding (TEVS) (Fig.2.4.1-(b)-3) at zero incidence. Lyn *et al.* (1995) did work at higher Reynolds number of 21,400. It was pointed out that high Reynolds stress components at region of peak vorticity and fully turbulent flow in the near wake region. The flow separation is fixed at the corner. This kind of vortex shedding is called as the Leading Edge Vortex Shedding (LEVS) as discussed previously. Deniz and Staubli (1997) presented that, if the ratio slightly exceeds 2, the trailing edge would have a higher frequency than the vortex shedding. While to the short body with a ratio <2 , the aspect ratio had no influence on the leading edge vortices and the leading edge vortices made up the vortex street with a dominant frequency equal to vortex shedding frequency, to the large ratio problem, the trailing edge vortices will separate and reattach onto the side of the body. Bunge *et al.* (2003) proposed that the shape of the body played a predominant role in the resonance behaviour. The bluff bodies with a long aspect ratio will generate eddies emerging at the leading edge, but impinging on the surface again downstream, resulting in a reattachment of the flow followed by a subsequent separation at the trailing edge. Apart from the aspect ratio discussed in the above, the Reynolds number is another parameter affecting the vortex shedding frequency and Strouhal number. Okajima (1982) investigated the relationship between the Strouhal number and Reynolds number for rectangular sections with ratio of 1 to 4.

Although the vortex induced vibration is a kind of limiting amplitude vibration with the self excited characteristics, in the engineering practice, this kind of vibration is still needed to be predicted. The classical vortex shedding mathematical model is Van der Pol model to describe a simple harmonic motion. However, due to the nonlinearity in the bridge structural system and aerodynamic force, Simiu and Scanlan (1996) proposed a combination mode to consider the nonlinear influence, which can be written as:

$$F_v = \mu f C_a \left(1 - \varepsilon |\eta|^{2\nu} \right) \dot{\eta} \quad (2.4.1)$$

In vortex shedding simulation with FEM, Eq.2.4.1 can be rewritten as:

$$F_v = \mu f C_a \left(1 - \frac{\varepsilon |\eta|^{2\nu}}{(2\nu + 1)(2\pi f)^{2\nu}} \right) \dot{\eta} \quad (2.4.2)$$

Where $\eta, \dot{\eta}$ are the nondimensional structure displacement and velocity item, $\mu = \rho D^2 / m$ is the mass ratio, ρ is the density, D is the bluff body diameter, f is the oscillation frequency, C_a, ε, ν are the non-dimensional aerodynamic parameters, which are determined by measuring the structural response under the representative wind condition.

2.5 Galloping Response Introduction

The last aerodynamic phenomenon is known as galloping. Novak (1969) discussed the aeroelastic galloping of prismatic bodies and presented that galloping responses belong to self-excited vibrations with a single uncoupled mode. Galloping oscillation is caused by the instability of the bluff body cross section typical of slender structures with special cross-sectional shapes such as, rectangular or “D” sections or the effective sections of some ice-coated power line cables (Simiu and Scanlan, 1996), Novak (1972) also investigated other shape structure galloping oscillations such as the prismatic structures. Galloping always occurs when structural vibration is caused by the negative aerodynamic damping. According to the different mechanisms by which galloping takes place, both across-wind galloping and wake galloping can occur (Fig.2.5.1). Across-wind galloping is where a structure will vibrate in large amplitude in the vertical direction to the wind flow when the structural vibration frequency is much lower than the frequency of vortex shedding at the same section. The Glauert-Den Hartog (Simiu and Scanlan, 1996) criterion (Eq.2.5.1) is always adopted as the structure galloping instability criterion.

$$\left(\frac{dC_L}{d\alpha} + C_D \right)_0 < 0 \tag{2.5.1}$$

Where C_L is the lift coefficient, and C_D is the drag coefficient

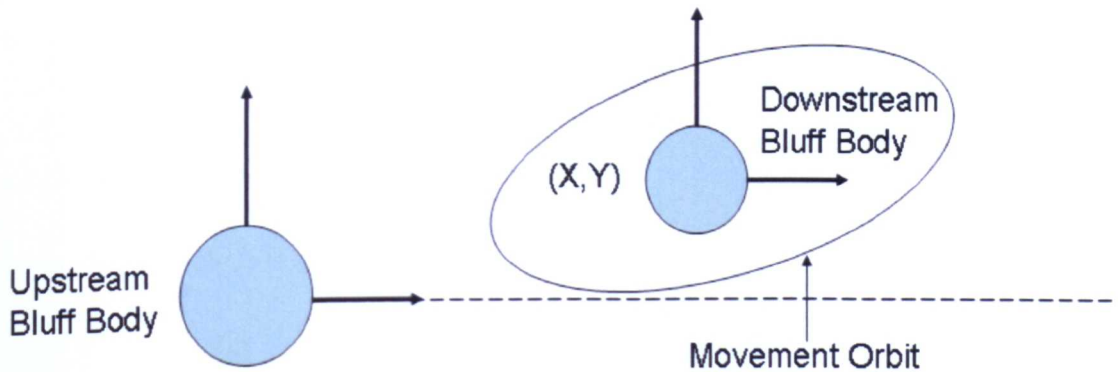


Fig 2.5.1 Bluff body wake galloping

Wake galloping occurs when two or more structures situated in the same flow, and the frequency of response downstream structure is low compared to its vortex-shedding frequency and to that of the structure located upstream.

2.6 Conclusions

In this chapter, aerodynamic phenomena such as flutter, buffeting, vortex shedding and galloping occur in bridge wind engineering were introduced. From this chapter, it can be found that the buffeting response induced by the gust wind load occurs throughout the whole reduced velocity range, and can be coupled with aerodynamic phenomena such as flutter or galloping leading to increasing response amplitude in the bridge response. The conventional bridge buffeting response prediction has been conducted in the frequency domain using spectral analysis approaches. The time domain

approach is most appropriate if the analysis involves structural and aerodynamic nonlinearities. Most of the studies about the time domain analysis of buffeting response are based on quasi-steady aerodynamic forces due to the inability to model frequency dependent unsteady aerodynamics characteristics in time domain. Besides the above contents, wake buffeting studied in the past with experiments is also discussed.

To investigate the bridge buffeting response, a case (a cable-stayed bridge) study on the bridge buffeting response and the influence of different parameters such as aerodynamic admittance, self excited force and modal coupling etc will be discussed in chapter 4.

Chap 3 Turbulence Models and FSI Techniques in Bridge Buffeting Prediction

3.1 Introduction

In chapter 2, the conventional analysis methods of buffeting response based on the FEM have been reviewed, which are also known as the semi-experimental and statistical approach. Although these methods have been widely used, the engineers are striving for more accurate numerical simulation techniques to avoid using some semi-experimental functions such as joint acceptance or aerodynamic admittance and quasi-steady assumption. The numerical simulation technique based on CFD theory provides one way to consider the variation process of turbulence around the structure and the influence of structural vibration and deformation on the flow field around the structure, in which the interactions between the wind flow and the bluff body structure, known as the fluid structure interaction (FSI), are done by combining the structural dynamic analysis method with the CFD theory together to solve coupled systems. Tamura (1999) discussed the reliability of the CFD method for studying wind structure interaction problems, comparing the numerical results with the experimental results for rectangular cylinder, or bluff plate single degree or multi-degree oscillation. It could be found that the reliability of CFD estimation is sufficient for wind structure interaction problems in comparison with the experimental data. Also CFD can provide more useful knowledge and information which are very difficult to obtain by the experimental technique. In this chapter turbulence models suitable for capturing the time varying and random characteristics in buffeting simulation will be discussed. Then the FSI technique and partition algorithm suitable for the prediction of buffeting response are also described, and the major steps for bridge buffeting response based on FSI is proposed.

3.2 Turbulence Models' Development

It is known that directly solving Navier-Stokes equation (NSE) is difficult, especially for High Reynolds numbers. Turbulence models can be classified into either direct numerical simulation (DNS) or indirect numerical simulation (IDNS) (Fig.3.2.1) based on the filtering technique (space or time average on the items in NSE) to NSE. DNS method can capture the turbulence by solving NSE directly without introducing any models, but it needs fine mesh density and is only restricted to low Reynolds numbers problems with simple geometrical dimension. So IDNS models are introduced to overcome such problems, which can be divided into Reynolds Averaged Navier Stokes (RANS) model by calculating the statistical average of the solution directly to express the turbulence statistical characteristic, the Large Eddy simulation (LES) model calculating only the low frequency part in space directly and adopting the filtering technique to resolve the large scale eddies and simulating small scale eddies based on model, the hybrid RANS and LES model or the Detached Eddy Simulation (DES) model using the RANS model to solve the near zone problem and LES model to simulate the large eddies of outside zone.

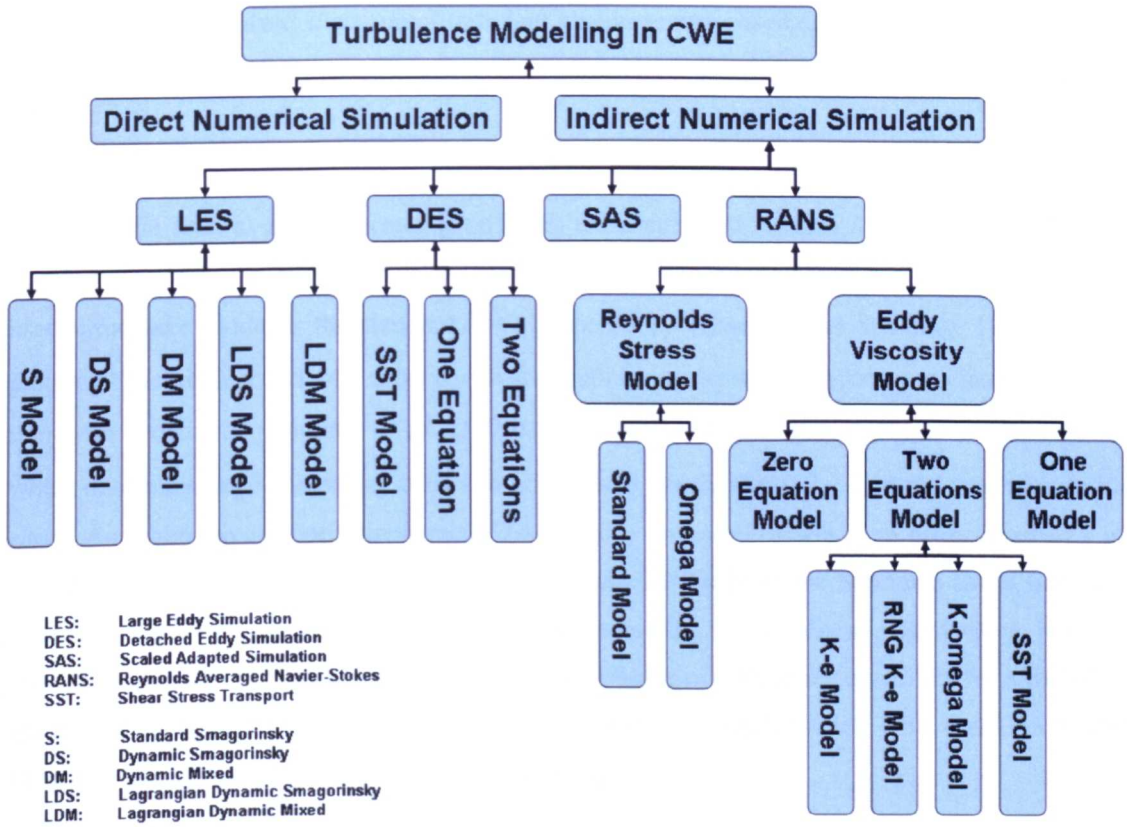


Fig 3.2.1 Schematic diagram of turbulence modelling in CWE

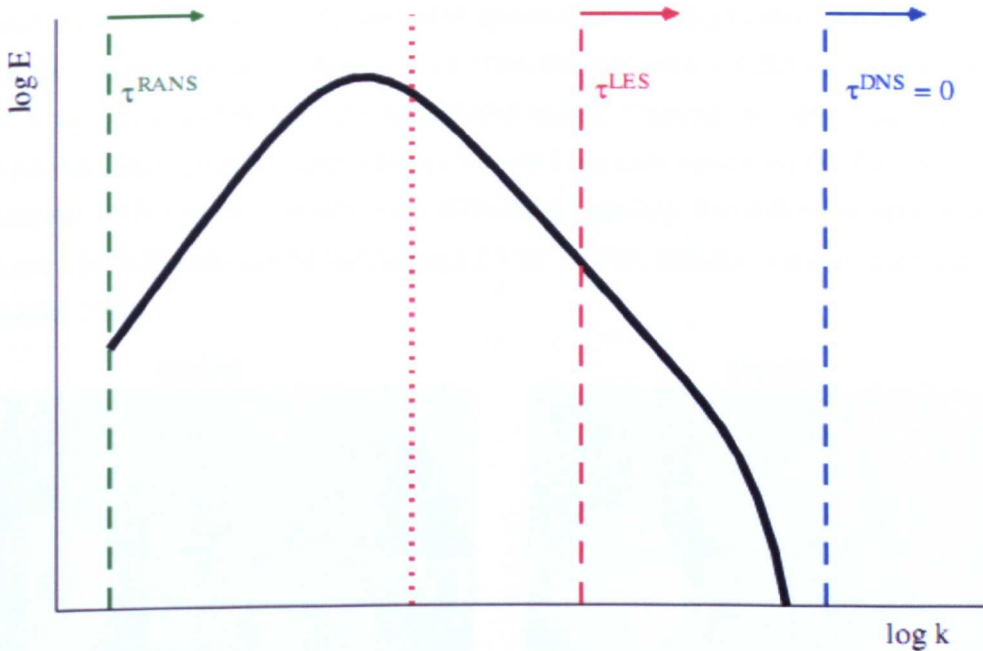


Fig 3.2.2 Idealized spectrum of turbulent kinetic energy of isotropic turbulence with respect to the wavenumber k and schematic of the extent of modelling employed by the traditional simulation DNS, LES, and RANS. The vertical dotted lines mark the aim of the Hybrid LES/RANS methods. (Jochen and Dominic, 2008)

Fig.3.2.2 plots the solved spectrum of turbulent kinetic energy based on different turbulence modelling. The spectrum of turbulent kinetic energy solved by turbulence models will be different.

3.2.1 Steady RANS Model

Applying the time average processing on NSE, extra turbulent stresses known as the Reynolds stress is generated. To NSE, turbulence modelling is introduced. The well established and widely used turbulence model is the standard $k - \epsilon$ proposed by (Launder and Spalding, 1974) by expressing the turbulence kinetic energy with k equation and the rate of turbulence viscous dissipation with ϵ equation. Launder *et al.* (1975) proposed Reynolds stress equation model (RSM), which consumes large computing costs and performs as poorly as the $k - \epsilon$ model in some special cases. And then the algebraic stress model (ASM) was proposed, which is an economical way of considering the anisotropy of Reynolds stress without fully solving the Reynolds stress transport equations. Although the steady RANS model can obtain the statistically averaged value, it is not enough to capture the unsteady and random characteristics of turbulence especially for simulating the buffeting phenomena in CWE, the unsteady RANS (URANS) model, DES and LES model should be used to simulate the unsteady characteristics.

3.2.2 URANS Model

Flow passing around bluff bodies such as the high-rise building or bridge deck system will generate complex phenomena such as the separation and reattachment, high turbulence, large-scale turbulence and curved shear layers (Rodi *et al.*, 1997b). It is difficult to predict the time varying fluctuation of such flow with the time averaged RANS model. Therefore the more complex URANS model provides an alternative method known as very large eddy simulation (VLES), which relies on traditional RANS models but which are deliberately unsteady. The difference between RANS model and URANS model can be seen in Fig.3.2.3 for the flow simulation around a circular cylinder (Spalart, 2000).

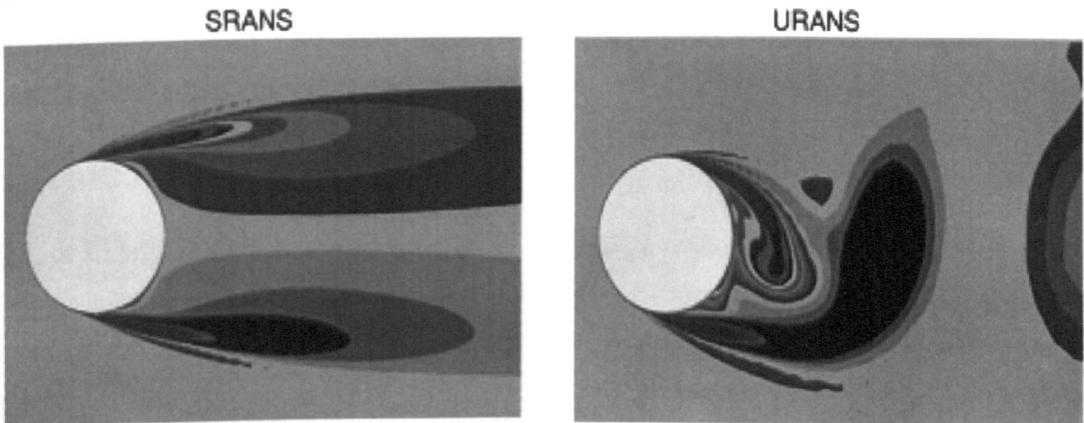


Fig 3.2.3 Simulation of flow past a circular cylinder based on RANS and URANS model (Spalart, 2000)

In URANS model, the variables such as velocity term or pressure term are not only a function of the space coordinates but also a function of time. The unsteady NSE for incompressible flow can be written as:

$$\frac{\partial U_i}{\partial x_i} = 0 \quad (3.2.3a)$$

$$\frac{\partial U_i}{\partial t} + \frac{\partial}{\partial x_j} (U_i U_j) = -\frac{1}{\rho} \frac{\partial p}{\partial x_i} + \nu \frac{\partial^2 U_i}{\partial x_j \partial x_j} - \frac{\partial \overline{u'_i u'_j}}{\partial x_j} \quad (3.2.3b)$$

To close the above equations, the Reynolds stresses term ($\overline{u'_i u'_j}$) can be expressed with the mean velocity gradient via the eddy viscosity. Because eddy-viscosity models can not properly account for history and transport effects on turbulence, with such effects being very important to complex separated flows region, the Reynolds stress model has been proposed. This is because it can include the transport effects by solving model transport equations to get the individual stresses without employing the eddy viscosity concept (Rodi, 1997a). The disadvantage of such model is that this model catches the turbulence fluctuations based on the time averaged statistical model in total and the turbulence model used in URANS should depend on the type of flow.

3.2.3 LES and DES Models

Although the URANS model can be used to study the time varying characteristic of gust wind turbulence, it relies on the formal existence of a spectral gap between the time scales of the mean transient flow and the residual turbulence, while this gap is almost nonexistent in bluff-body flows. Particularly in the wake regime, the duration of the flow distortion due to unsteady effects is much smaller than the intrinsic time scale of the turbulence and the assumption of a spectral gap is excessively violated (Lubcke *et al.*, 2001). Alternative turbulence models such as LES and DES, reflecting the turbulence random characteristics more accurately have been supplied. Rodi (1997a) compared the difference of simulation results between the LES and RANS models when flow passed around a square cylinder and cube. It was found that the flow around a square cylinder simulated by a standard $k - \epsilon$ model generated poor results because of periodic motion's under-prediction, while LES predicted very well.

3.2.3.1 DES Model

DES, or Hybrid RANS/LES, is a hybrid technique used to reduce the cost of LES whilst still retaining accuracy and reliability. It was first proposed by Spalart and Allmaras (1992) for the prediction of turbulent flows at high Reynolds numbers based on the RANS and LES model. The basic model applied in the majority of DES applications is the Spalart-Allmaras one-equation model (Spalart and Allmaras, 1992). Menter (1994) further developed DES model based on the standard $k - \omega$ SST model named as two-equation model. Then Travin *et al.* (2000) developed a two equations DES model and applied it in study of flow around a circular cylinder. Due to the simplicity

of DES and non-zonal formulation, and only a single equation without explicitly expressing the zone between RANS and LES, the transition between them is seamless. According to the application of RANS model in DES, the DES model can be divided into the following types.

(1) One-equation DES Model

A DES model based on one-equation proposed by Spalart and Allmaras (1992) can be written as:

$$\frac{\partial \rho \tilde{v}_t}{\partial t} + \frac{\partial \rho \bar{u}_j \tilde{v}_t}{\partial x_j} = \frac{\partial}{\partial x_j} \left(\frac{\mu + \mu_t}{\sigma_{\tilde{v}_t}} \frac{\partial \tilde{v}_t}{\partial x_j} \right) + \frac{C_{b2} \rho}{\sigma_{\tilde{v}_t}} \frac{\partial \tilde{v}_t}{\partial x_j} \frac{\partial \tilde{v}_t}{\partial x_j} + P - Y \quad (3.2.4)$$

Where ρ is the air density, \tilde{v}_t is the turbulent kinematic eddy viscosity, $\sigma_{\tilde{v}_t}$ is the constant, μ and μ_t are the kinematic viscosity and turbulence viscosity respectively, and C_{b2} is the constant. The production term P and the destruction term Y have the form

$$P = C_{b1} \rho \left(\bar{S} + \frac{\tilde{v}_t}{\kappa^2 d^2} f_2 \right) \tilde{v}_t \quad (3.2.5)$$

$$\bar{S} = (2 \bar{S}_{ij} \bar{S}_{ij})^{1/2}, \bar{S}_{ij} = \frac{1}{2} \left(\frac{\partial \bar{U}_i}{\partial x_j} + \frac{\partial \bar{U}_j}{\partial x_i} \right) \quad (3.2.6)$$

$$Y = C_{w1} \rho f_w \left(\frac{\tilde{v}_t}{d} \right) \quad (3.2.7)$$

Where C_{b1} , f_2 , κ , C_{w1} , f_w are constant. Spalart *et al.* (1997) in the DES model proposed d as the minimum of the RANS turbulent length scale d and the cell length $\Delta = \max(\Delta x_\xi, \Delta x_\eta, \Delta x_\zeta)$

$$\tilde{d} = \min(d, C_{des} \Delta) \quad (3.2.8)$$

$\Delta x_\xi, \Delta x_\eta$ and Δx_ζ denote the cell length in the three grid directions ξ, η and ζ respectively. The constant C_{des} is usually set to 0.65. In the boundary layer $d < C_{des} \Delta$ and thus the model operates in RANS mode. Outside the turbulent boundary layer $d > C_{des} \Delta$ so that the model operates in LES mode.

(2) Two-equation DES Model

In one-equation model, the turbulence length scale is obtained from the wall distance, which is not a relevant turbulent length scale in many situations. Recently, a DES model based on two-equation models was created by Travin *et al.* (2000), in which the turbulent length scale is either obtained from the two turbulent quantities ($k^{3/2} / \epsilon$ or $k^{1/2} / \omega$) or the filter width Δ . A model based on the $k - \epsilon$ model can be expressed as:

$$\frac{\partial k}{\partial t} + \frac{\partial}{\partial x_j} (\bar{U}_j k) = \frac{\partial}{\partial x_j} \left[(\mu + \mu_t) \frac{\partial k}{\partial x_j} \right] + P_k - \frac{k^{3/2}}{\ell_\epsilon} \quad (3.2.9)$$

$$\frac{\partial \mathcal{E}}{\partial t} + \frac{\partial}{\partial x_j} (\bar{U}_j \mathcal{E}) = \frac{\partial}{\partial x_j} \left[\left(\mu + \frac{\mu_t}{\sigma_\epsilon} \right) \frac{\partial \mathcal{E}}{\partial x_j} \right] + \frac{\mathcal{E}}{k} (C_1 P_k - C_2 \mathcal{E}) \quad (3.2.10)$$

$$P_k = 2\mu_t \bar{S}_{ij} \bar{S}_{ij}, \quad \mu_t = C_\mu k^{1/2} \ell_t \quad (3.2.11)$$

Where k is the turbulent kinetic energy. The turbulent length scales ℓ_t and ℓ_ϵ are computed as:

$$\ell_t = \min \left(\frac{k^{3/2}}{\mathcal{E}}, C_k \Delta / C_\mu \right) \quad (3.2.12a)$$

$$\ell_\epsilon = \min \left(\frac{k^{3/2}}{\mathcal{E}}, \Delta / C_\mu \right) \quad (3.2.12b)$$

The above expressions apply in the region where the turbulent length scales are obtained from Δ (LES model) and the \mathcal{E} equation is still solved, but \mathcal{E} is not used. In the RANS model the major part of the turbulence is modelled. When the model switches to LES model, the turbulence is supposed to be represented by the resolved turbulence.

(3) $k - \omega$ SST DES Model

To Wilcox's $k - \omega$ model, it behaves well near solid walls and needs no corrections for low Reynolds numbers, whereas to the SST model, it limits the eddy-viscosity by forcing the turbulent shear stress to be bounded by the constant times the turbulent kinetic energy inside boundary layers, which improves the model's performance on the flows with strong adverse pressure gradients and separation (Fu *et al.*, 2007). So Menter (1994) proposed the standard $k - \omega$ SST model, which can be written as:

$$\frac{\partial k}{\partial t} + \frac{\partial}{\partial x_j} (\bar{U}_j k) = \frac{\partial}{\partial x_j} \left[\left(\nu + \frac{\nu_t}{\sigma_k} \right) \frac{\partial k}{\partial x_j} \right] + P_k - \beta^* k \omega \quad (3.2.13)$$

$$\frac{\partial \omega}{\partial t} + \frac{\partial}{\partial x_j} (\bar{U}_j \omega) = \frac{\partial}{\partial x_j} \left[\left(\nu + \frac{\nu_t}{\sigma_\omega} \right) \frac{\partial \omega}{\partial x_j} \right] + \alpha \frac{P_k}{\nu_t} - \beta \omega^2 + 2(1 - F_1) \sigma_{\omega 2} \frac{1}{\omega} \frac{\partial k}{\partial x_i} \frac{\partial \omega}{\partial x_i} \quad (3.2.14)$$

$$F_1 = \tanh(\xi^4), \quad \xi = \min \left[\max \left\{ \frac{\sqrt{k}}{\beta^* \omega y}, \frac{4\sigma_{\omega 2} k}{CD_\omega y^2} \right\} \right] \quad (3.2.15)$$

$$\nu_t = \frac{a_1 k}{\max(a_1 \omega, SF_2)}, \quad (3.2.16)$$

$$F_2 = \tanh(\eta^2), \quad \eta = \max \left\{ \frac{2k^{1/2}}{\beta^* \omega y}, \frac{500\nu}{y^2 \omega} \right\} \quad (3.2.17)$$

Where y is the distance to the nearest wall and ω is the vorticity, α , β and $\sigma_{\omega 2}$ are the constants.

The SST model behaves as a $k - \omega$ model near the wall ($F_1 = 1$) and a $k - \epsilon$ model far from the

wall ($F_1 = 0$). All coefficients are blended between the $k - \omega$ and $k - \epsilon$ model using function F_1 . Menter (2003) modified the dissipation term in the k equation as:

$$\beta^* k \omega \rightarrow \beta^* k \omega F_{DES}, F_{DES} = \max \left\{ \frac{L_t}{C_{DES} \Delta}, 1 \right\} \quad (3.2.18)$$

$$\Delta = \max \{ \Delta x, \Delta y, \Delta z \}, L_t = \frac{k^{1/2}}{\beta^* \omega} \quad (3.2.19)$$

Where DES modification is meant to switch the turbulent length scale from a RANS length scale ($k^{1/2} / \omega$) to a LES length scale (Δ) when the grid is sufficiently fine. When F_{DES} is larger than one, the dissipation term in the k equation increases which in turn decreases k and thereby also the turbulent viscosity. With a smaller turbulent viscosity in the momentum equations, the modelled dissipation is reduced and the flow is induced to go unsteady. The result is that a large part of the turbulence is resolved rather than being modelled.

In some cases, it may happen that the F_{DES} term switches to DES in the boundary layer as Δz is smaller than the boundary layer thickness δ . Menter (2004) and Strelets (2001) suggested Eq.3.2.20 preventing such situations in the DES model.

$$F_{DES} = \max \left\{ \frac{L_t}{C_{DES} \Delta} (1 - F_s), 1 \right\}, F_s = 0, F_1 \text{ or } F_2 \quad (3.2.20)$$

3.2.3.2 LES Model

Although DES model can capture the unsteady characteristic of turbulence and be suitable for buffeting simulation, different URANS model is still applied in DES for handling the near wall zone area, which may influence the gust effects in the buffeting simulation and reduce the energy spectrum prediction (Fig.3.2.2). Recently, with the computing power increasing and the development of high-order numerical methods, LES becomes an alternative approach to simulate the buffeting. Here the large eddies are computed in a time-dependent simulation that uses a set of 'filtered' equations, which can supply more information of turbulence (Fig.3.2.2). For Reynolds averaging, the filtering process generates additional unknown items that must be modelled in order to achieve closure. Rodi *et al.* (1995) stated that LES resolved only larger-scale motion, and that the effect of the small-scale motion which can not be resolved on a given grid needed to be modelled. Two ways have been adopted till now, one is to determine turbulent stresses introduced by the subgrid-scale fluctuations by the subgrid-scale model, and the other is to leave the energy withdrawal to numerical damping by a numerical scheme introducing a certain amount of numerical dissipation. LES has its own potential and power, the advantage is that the error induced by the turbulence model will be reduced by modelling less of the turbulence (and solving more). The most successful LES has been done using high-order spatial discretization, with great care being taken to resolve all scales larger than the inertial subrange.

Applying the filtering operation on the momentum equation of NSE, it can be rewritten as:

$$\frac{\partial \bar{u}_i}{\partial t} + \frac{\partial \bar{u}_i \bar{u}_j}{\partial x_j} = -\frac{1}{\rho} \frac{\partial \bar{p}}{\partial x_i} + \frac{\partial}{\partial x_j} \left(\nu \frac{\partial \bar{u}_i}{\partial x_j} \right) - \left(\frac{\partial \tau_{ij}}{\partial x_j} \right) \rightarrow \tau_{ij} = \overline{u_i u_j} - \bar{u}_i \bar{u}_j \quad (3.2.21)$$

↑

(Sub-grid scale (SGS) turbulent stress)

Due to the filtering procedure, the velocity can be divided into the resolved part ($\bar{u}(x, t)$) and SGS part ($u'(x, t)$) and the filtering process means that some energy can not be solved and needs to be modelled (Fig.3.2.2). In general, the filtering process is determined by the grid resolution. As described in Eq.3.2.21, the unknown SGS stresses ($\tau_{ij} = \overline{u_i u_j} - \bar{u}_i \bar{u}_j$) resulting from the filtering operation is generated. According to the SGS stress (τ_{ij}), the modern SGS turbulence models can be divided into the following types:

1. *Standard Smagorinsky Model*
2. *Dynamic Smagorinsky Model*
3. *WALE Model*
4. *Dynamic Subgrid Kinetic Energy Transport Model*

(1) Standard Smagorinsky Model

To achieve the above equation (Eq.3.2.21) closure, extra modelling is needed. So the SGS turbulent stress mode proposed by Smagorinsky (1963), which is an eddy viscosity model, can be written as:

$$\tau_{ij} - \frac{1}{3} \tau_{kk} \delta_{ij} = -2\nu_{SGS} \bar{S}_{ij} \quad (3.2.22)$$

Where ν_{SGS} is the SGS turbulent viscosity, and \bar{S}_{ij} is the rate-of-strain tensor for the resolved scale defined by

$$\bar{S}_{ij} = \frac{1}{2} \left(\frac{\partial \bar{u}_i}{\partial x_j} + \frac{\partial \bar{u}_j}{\partial x_i} \right) \quad (3.2.23)$$

The simple and earliest model was the Smagorinsky-Lilly model proposed by Smagorinsky (1963), in which model the eddy-viscosity modelled by

$$\nu_{SGS} = (C_s \bar{\Delta})^2 |\bar{S}|, \quad |\bar{S}| = \sqrt{2\bar{S}_{ij}\bar{S}_{ij}} \quad (3.2.24)$$

Where $\bar{\Delta}$ is computed using $\bar{\Delta} = V^{1/3} = (\Delta x \Delta y \Delta z)^{1/3}$. C_s is the Smagorinsky constant, and V is the volume of the computational cell. In general C_s is between 0.1 and 0.25, Lilly adopted a value of 0.17 for C_s for homogeneous isotropic turbulence in the inertial subrange. However, this value will generate excessive damping of large-scale fluctuations in the presence of mean shear and in

transitional flows near solid wall boundary and be reduced in such regions. In short, C_S is not a universal constant. Despite some shortcomings, such as no universal constant applicable to different types of flow, the Smagorinsky-Lilly model is widely used to study the flow around different shaped bluff bodies at the different Reynolds number conditions. A C_S value of around 0.1 is still an accepted value to yield the best results for a wide range of flows.

(2) Dynamic Smagorinsky Model

To overcome the Smagorinsky-Lilly model shortcoming discussed above, Lilly (1992) and Germano *et al.* (1996) proposed a procedure separately in which the Smagorinsky model constant C_S is dynamically computed based on the information provided by the resolved scales of motion (Eq.3.2.25). The model constant C_S is automatically calculated based on the two filters with different characteristic scales, grid filter (a overbar: $\bar{\quad}$) and test filter (a caret over the overbar: $\hat{\quad}$) to avoid specifying it in advance in the dynamic procedure (Germano *et al.*, 1996).

$$C_S = -\frac{1}{2} \frac{B_{ij} M_{ij}}{M_{kl}^2} \tag{3.2.25}$$

$$B_{ij} = \overline{\overline{u_i u_j}} - \hat{\overline{u_i u_j}} = T_{ij} - \overline{\tau_{ij}} \tag{3.2.26}$$

where B_{ij} is the Leonard stress, which relates the “resolved turbulent stresses”, $T_{ij} = \overline{\overline{u_i u_j}} - \hat{\overline{u_i u_j}}$ is the subtest stresses. In the dynamic SGS model, Zang *et al.* (1993) proposed a model named the dynamic mix model (Eq.3.2.27) to control the excessive back-scattering caused by the dynamic SGS model through combining the dynamic SGS model and the scale-similarity model.

$$\tau_{ij} - \frac{1}{3} \tau_{kk} \delta_{ij} = -2(C_S \overline{\Delta})^2 |\overline{S}| \overline{S}_{ij} + B_{ij} - \frac{1}{3} B_{kk} \delta_{ij} \tag{3.2.27}$$

Where C_S is calculated as the following equations.

$$C_S = -\frac{1}{2} \frac{M_{ij} (B_{ij} - H_{ij})}{M_{kl}^2} \tag{3.3.28}$$

$$M_{ij} = \hat{\Delta}^2 \left| \hat{S} \right| \hat{S}_{ij} - \overline{\overline{\Delta}^2} \left| \overline{S} \right| \overline{S}_{ij} \tag{3.2.29}$$

$$H_{ij} = \overline{\overline{\hat{u}_i \hat{u}_j}} - \hat{\overline{\hat{u}_i \hat{u}_j}} - (\overline{\overline{u_i u_j}} - \overline{\overline{\hat{u}_i \hat{u}_j}}) \tag{3.2.30}$$

So this model automatically adopts smaller model parameters, adapts the parameters near wall region, and compensates the error in the length scale by adjusting the parameters in the model.

(3) Wall Adapted Local Eddy-Viscosity (WALE) Model

Nicoud and Ducros (1999) proposed new subgrid scale model named WALE for Large eddy simulation in complex geometries. The WALE SGS model does not need to adopt an explicit damping function to consider the local near-wall flow structure and wall damping effects, so the eddy viscosity is modelled by

$$v_{SGS} = \rho L_S^2 \frac{(S_{ij}^d S_{ij}^d)^{3/2}}{\underbrace{(\bar{S}_{ij} \bar{S}_{ij})^{5/2} + (S_{ij}^d S_{ij}^d)^{5/4}}_{\text{near-wall modification}}} \quad (3.2.31)$$

Where L_S and S_{ij}^d in the WALE model are defined as:

$$L_S = \min(\kappa d, C_w V^{1/3}) \quad (3.2.32)$$

$$S_{ij}^d = \frac{1}{2}(\bar{g}_{ij}^2 + \bar{g}_{ji}^2) - \frac{1}{3}\delta_{ij}\bar{g}_{kk}^2, \bar{g}_{ij} = \frac{\partial \bar{u}_i}{\partial x_j} \quad (3.2.33)$$

The default value of the WALE constant C_w is 0.325, found to yield satisfactory results for a wide range of flow. The other notations are the same as in the Smagorinsky-Lilly model. The WALE model is proposed to return the correct wall asymptotic behaviour for wall bounded flows.

(4) Dynamic Subgrid Kinetic Energy Transport Model

The standard or dynamic Smagorinsky-Lilly model discussed previously is essentially an algebraic model, in which the SGS stress is parameterized by the resolved velocity scales. Local equilibrium is assumed between the transferred energy through the grid-filter scale and the dissipation of kinetic energy at small SGS. To overcome the assumption Kim and Menon (1997) proposed the dynamic SGS kinetic energy model, in which the SGS turbulence can be better modelled by accounting for the transport of the subgrid-scale turbulence kinetic energy. In this model, the SGS kinetic energy is defined as

$$k_{SGS} = \frac{1}{2}(\overline{u_k^2} - \bar{u}_k^2) \quad (3.2.34)$$

The subgrid-scale eddy viscosity is computed using k_{SGS} as

$$v_{SGS} = C_k k_{SGS}^{1/2} \bar{\Delta} \quad (3.2.35)$$

Where $\bar{\Delta}$ is the filter-size computed from grid volume. The SGS stress can then be written as:

$$\tau_{ij} - \frac{2}{3}k_{SGS}\delta_{ij} = -2C_k k_{SGS}^{1/2} \bar{\Delta} \bar{S}_{ij} \quad (3.2.36)$$

k_{SGS} is obtained by solving its transport equation

$$\frac{\partial \bar{k}_{SGS}}{\partial t} + \frac{\partial \bar{u}_j \bar{k}_{SGS}}{\partial x_j} = -\tau_{ij} \frac{\partial \bar{u}_i}{\partial x_j} - C_\epsilon \frac{k_{SGS}^{3/2}}{\bar{\Delta}} + \frac{\partial}{\partial x_j} \left(\frac{\mu_t}{\sigma_k} \frac{\partial k_{SGS}}{\partial x_j} \right) \quad (3.2.37)$$

The model constants (C_k, C_ϵ) are automatically calculated from the resolved velocity field as in the dynamic Smagorinsky model. σ_k is set 1.0.

Although LES can solve the large scale eddies directly and model the small scale eddies, supplying much more unsteady information than DES and URANS, it still needs very high resolution for the high Reynolds numbers at the wall boundary and is not widely applied in complex flow which needs non-uniform smoothing.

3.2.4 DNS Model

The most accurate approach to resolve turbulence is to solve the Navier-Stokes equations without any averaging or approximation of the other specific model. Only numerical discretizations are applied whose errors can be estimated and controlled. All scales of fluid motions are resolved, which is called a direct numerical simulation (DNS), and it is suitable for the buffeting prediction in the spatial scale (the Kolmogorov turbulence length scale η) and temporal scale (time scale τ) of turbulence, which can be expressed as:

$$\eta = \left(\frac{\mu^3}{\epsilon} \right)^{1/4}, \quad \tau = \left(\frac{\mu}{\epsilon} \right)^{1/2} \quad (3.2.38)$$

Where, μ is the kinematic viscosity and ϵ is the turbulence dissipation rate per unit mass. As Eq.3.2.38 defines the spatial and temporal scales of turbulence, to make sure that all of the turbulence structure can be captured, the computation domain should be large enough to catch the largest turbulence eddy and the more fine grids are needed to catch the smallest eddies, as least as the physical domain is to be considered. These requirement ensures a large volume of grids in the computational domain ($Re^{9/4}$) and a large number of time steps which are proportional to Re^3 . This is limited by computational memory and speed, especially for the high Reynolds number conditions and complex geometry which are widely existing problems in wind engineering. Now its application is mainly restricted in the low Reynolds number conditions and simple geometrical condition, however DNS model is difficult to be applied in the CWE field due to the high computational cost.

3.3 Difficulties of Applying LES in CWE

Although the CFD method and LES model have been applied in CWE, there are still some difficulties existing in its application, Murakami (1998) proposed some problems existing in the CWE such as difficulties in which there is a high Reynolds number flow, difficulties related to the inlet and outlet flow condition and difficulties related with the sharp edge of bluff body, near wall treatment.

(1) High Reynolds Number

In general, civil engineering structures such as bridges and buildings are large scale. When applying CFD to solve such problems, the unsteady NSE solution needs to take into account all the space and time scales of the solution. The Reynolds number of the flow field treated in CWE can be more than 10^8 , which requires fine grid resolution to calculate and represent all scales solutions and for a higher Reynolds number, more grid is needed. This kind of situation requires much more computer resources.

(2) Inflow and Outflow Boundary Condition

Because almost all civil engineering structures are located in fully developed turbulent fields and the bluff body aerodynamics are influenced by the upwind direction turbulence, which is very important for the buffeting prediction, it is impossible to use conventional boundary conditions with mean values in LES computations or DNS. This is one difficulty preventing the wide application of LES in CWE in practice. So effectively simulating the time varying inlet boundary condition is very important. To consider the inflow turbulence, several techniques have been investigated by researchers, such as Kondo *et al.* (1997), Lund *et al.* (1998), Thomas and Williams (1999), Longest *et al.* (2000), Smirnov (2001), Nozawa and Tamura (2002), Schluer *et al.* (2004), Kempf *et al.* (2005) and Elaine *et al.* (2005). The simplest method is to store the time history of velocity fluctuations given from a preliminary LES computation. Second is the artificial generation method in which velocity fluctuations are given by the inverse Fourier transform of prescribed energy spectrum and turbulence intensity. Since the treatment of the turbulent inflow boundary condition is very important subject for wind engineering applications, attention and effort should be devoted to this technique. The artificial inflow turbulence generation technique and inlet boundary condition resolution method based on filtering technique will be described and discussed in chapter 5.

The treatment of an outflow boundary is another important subject to be investigated in the application of LES in CWE. At the outflow boundary as the reflection of pressure happens, an outflow boundary condition with a gradient of zero is always adopted.

(3) Grid Stretching Difficulty

In the analysis of the flow field around a bluff body, the grid stretching technique is always adopted to reduce the computation cost. Based on this technique, the grid resolution is usually to be coarser at the position farther from the bluff body. To the zone very near the bluff body, the grid mesh density is very high. If a large ratio of grid stretching is designed, it will cause numerical oscillation. The cut-off wave number of energy spectrum between resolved scale and subgrid scale modelled is related to the grid size. When the stretching ratio between two neighbouring grids is too large, the cut-off wave numbers will be different. Thus the SGS turbulent energy for

two grids are significantly different. This difference leads to numerical oscillation. This suggests that composite grid technique in LES should be used with caution.

(4) Near Wall Treatment

As discussed above, CWE problems include high Reynolds numbers and fluid field around the complex bluff bodies. Vortices' characteristics of small length and spacing dominate the flow at the near wall zone. Whether the ensemble averaged turbulence model or filter turbulence model is applied in them, the near wall region or the sublayer is still one problem to be handled. In LES calculations no-slip condition is used at wall boundary condition, which strictly requires high resolution at the near wall region especially for the high Reynolds numbers cases. Otherwise the scales of motions contributing most to the transfer of turbulent momentum in the viscous sublayer can not be resolved. Since sufficient resolution is not usually possible, the employment of a near-wall model similar to the wall functions used in RANS calculations is preferred, more suitable for a high Reynolds number. Piomelli and Balaras (2002) reviewed the wall layer models for LES. Since the wall models were basically developed for attached flows, it will be questionable if they are applicable in separated flow regions.

3.4 Coupled System

In above discussions, the turbulence models suitable for the buffeting simulation are also reviewed. And the simulation technique of FSI should be used to predict the bridge buffeting response. So the governing equations of two systems are coupled together to solve such problems. According to the coupling degree the coupling relationship can be classified into: fully coupled model, loosely coupled and closely coupled model, the solution algorithms for different coupling systems are different. The following content will introduce the coupling system and the counterpart solution procedure.

(1) Fully or Strongly Coupled

In the fully coupled model, the governing equations reformulated by combining fluid and structural equations of motion are solved and integrated in time simultaneously. In such a procedure, fluid equations in an Eulerian reference system, and structural equations in a Lagrangian system are dealt with at the same time. Such processing leads to the matrices being several orders of magnitude stiffer for structural systems compared to fluid systems. Therefore it is almost impossible to solve the equations using a monolithic computational scheme for large-scale problems. In addition with the limitation of grid size, such a fully coupled model is only applied in more simple 2D problems without consuming much computation time. For the complex nonlinear problem, the portioned or staggered algorithm will be used.

(2) Loosely or Weakly Coupled

Unlike the fully coupled analysis, in the loosely coupled analysis procedure the structural and fluid equations are solved with two separate solvers, which can only keep external interaction between the fluid and structural system. So two different computational grids (structured or unstructured) are generated in two systems, which are not able to coincide at the boundary. To overcome such a problem, the interfacing technique should be developed for exchanging information back and forth between the structure and fluid. Kamakoti and Shyy (2004) compared different solvers for fluid and structure models as well as the interfacing methodologies, although the selection of different solvers is flexible, the coupling procedure leads to a loss in accuracy as the modules are updated only after partial or complete convergence. The loosely coupled approach is only limited to some problems with small perturbation or moderate nonlinearity.

(3) Closely Coupled

Due to the limitation in the fully coupled and the loosely coupled procedure, a closely coupled one is proposed, which is one of the most widely used methods in studying FSI problems. The closely coupled model not only supplies different solvers for fluid and structural systems but also couples the solvers easily and considers the large deformation. It is an especially efficient method to handle complex nonlinear problems. In this approach, fluid and structure system equations are solved separately with different solvers but can be coupled together with exchange of information at the interface or the boundary through an interface module. The surface loads are firstly mapped from the CFD surface grid onto the structure grid. The displacements from the structure grid is then mapped onto the CFD surface grid, the surface displacement are transferred back to the CFD mesh, causing deformation of the CFD surface mesh. A moving boundary technique is then applied to enable re-meshing of the entire CFD domain.

3.5 Solution Scheme of Coupled System

Although the coupling procedure for structure and fluid has been proposed to solve FSI problem, the solution of such coupled fluid system and structure system is a major problem in FSI. To solve the governing equations of fluid and structure system, the methods for the numerical solution can be divided into two kinds:

- 1) Monolithic schemes where the differential equations for the different variables are all solved together which is suitable for strongly coupled problems.
- 2) Staggered or partition schemes where the different variables are solved separately and there may or may not be iteration between them, which is suitable for strongly, loosely and closely coupled problems.

3.5.1 Monolithic Schemes

For the simple and small scale structural problems, only one or two vibration degrees of freedom are considered. The fluid and the structural equations of motion can be combined into a single formulation. A “monolithic” fully explicit or fully implicit treatment of the coupled fluid/structure equations of motion is possible. Zienkiewicz and Bettess (1978) described the motion equation of the structure in Lagrange coordinates with the finite element space discretisation and the fluid field as the nodal pressures in the fluid of the form by neglecting the convective acceleration and viscosity effect in Navier-Stokes and continuity equation in Eulerian coordinates after the space discretisation by finite elements. However the non-symmetric matrix multiplying the second derivative term can cause difficulty in the monolithic approach. To overcome such difficulty Zienkiewicz and Taylor (1985) also presented the Newmark two-step and two-stage time-stepping algorithm. The Newton-Raphson algorithm, the modified Newton-Raphson algorithm, and the Quasi- and Secant-Newton methods can also be adopted. Although the monolithic method for solving coupled problems seems very direct and simple to be implemented, it has disadvantages. Due to the combination of the governing equations of fluid system and structure system, direct solution of such large size matrix is difficult for the large size practical or nonlinear problems, in which the fluid and structural parts may have different time scales and hence require different time-stepping schemes.

3.5.2 Partition or Staggered Schemes

For a monolithic scheme, the simultaneous solution is computationally challenging and unmanageable. To overcome the disadvantages, the staggered or partition methods has been proposed to discretize the spatial and time variation in FSI. For FSI problems, the structural system and the fluid system can also be expressed as a second order equation. While for the fluid field the NSE is nonlinear in Euler coordinates, the structural equations and the semi-discrete equations governing the pseudo-structural fluid grid system may be linear or nonlinear in Lagrange systems. Currently the algorithm for the partition solution schemes can be divided into explicit solution scheme (Farhat and Lesoinne, 2000), implicit solution scheme (Matthies and Steindorf, 2002 and 2003, Dettmer and Peric, 2007) and other schemes such as semi-implicit scheme (Fernandez *et al.*, 2007, Fernandez and Moubachir, 2005). The choice for the solution schemes may be influenced by software availability or problem requirement.

(1) Implicit Analysis Schemes

The implicit solution scheme is one way to solve the coupling procedure of FSI, which can maintain the energy conservation at each time step or iteration of the coupling algorithm by exchanging the information such as the vector of pressure and deformation between the fluid domain and structure domain. Cervera *et al.* (1996) discussed the computational efficiency and implementation of block-iterative schemes for FSI problems, the Block-Gauss-Seidel (BGS) or block-total-step

and the Block-Jacobi (BJ) or block-single-step was proposed. Besides BGS and BGJ techniques, Matthies and Steindorf (2002, 2003) proposed Block-Newton (BN) technique. Based on the algorithm proposed by Matthies and Steindorf (2002, 2003) the fluid and structural governing equations can be discretized and expressed as:

$$\text{Fluid:} \quad N(v^{(n+1)}, p^{(n+1)}, d^{(n+1)}, \dot{d}^{(n+1)}) = 0 \quad (3.5.1a)$$

$$\text{Structure:} \quad S(d^{(n+1)}, \dot{d}^{(n+1)}) = h(v^{(n+1)}, p^{(n+1)}) \quad (3.5.1b)$$

Where n is the iteration counter. In general the CFD solver adopts a few subcycle iterations for each time step to reach the convergence criterion, while the CSD solver may or may not iterate according to the complexity of the structural model. Here for the simplicity, the CSD solver is considered to be an efficient iterative solver with only one iteration. Only single time step is considered, the time step counter is n , the expression $x = (v, p)$ and $y = (d, \dot{d})$ will be adopted to represent the fluid and structure variables respectively.

$$\text{Fluid:} \quad x_{k+1} - F(x_k, y_k) = 0 \quad (3.5.2a)$$

$$\text{Structure:} \quad y_{k+1} - G(x_{k+1}, y_k) = 0 \quad (3.5.2b)$$

The BJ (for $k = i - 1$) or BGS (for $k = i$) iterations method can be used to solve Eq.3.5.2, i is the iteration counter:

1. $x_{k+1} = F^{k_1}(x_k, y_k)$, k_1 iterations of the CFD solver,
2. $y_{k+1} = G^{k_2}(x_{k+1}, y_k)$, k_2 iterations of the CSD solver,
3. Check for convergence.

Although the convergence rate of the BGS method is twice higher than that of the BJ method when applied to the linear problems, the convergence speed for both methods is still slow. A faster method named Block-Newton (BN) had been proposed by Matthies and Steindorf (2002, 2003) to solve the strongly coupled nonlinear FSI problem. The basic one step of BN method for the coupled system Eq.3.5.2 can be expressed as:

$$\begin{pmatrix} D_x f(x_k, y_k) & D_y f(x_k, y_k) \\ D_x g(x_k, y_k) & D_y g(x_k, y_k) \end{pmatrix} \begin{pmatrix} \Delta x_k \\ \Delta y_k \end{pmatrix} = - \begin{pmatrix} f(x_k, y_k) \\ g(x_k, y_k) \end{pmatrix} \quad (3.5.3)$$

Where D_x and D_y expresses the finite difference operation on the variable x and y

$$f(x_k, y_k) = x_k - F(x_k, y_k) \quad (3.5.4a)$$

$$g(x_k, y_k) = x_k - G(x_k, y_k) \quad (3.5.4b)$$

$$\Delta x_k = x_{k+1} - x_k \quad (3.5.5a)$$

$$\Delta y_k = y_{k+1} - y_k \quad (3.5.5b)$$

The detailed solution algorithm can be seen in Matthies and Steindorf (2002, 2003) paper.

(2) *Explicit Solution Scheme*

Farhat and Lesoinne (2000) described four explicit solution schemes to solve FSI problems, which are the Conventional Serial Staggered (CSS) algorithm, Improved Serial Staggered (ISS) solution procedure, Conventional Parallel Staggered (CPS) algorithm and improved Parallel Staggered (IPS) solution procedure. These four schemes are plotted in Fig.3.5.1.

Fig.3.5.1 (a) shows the steps involved in each loop of the CSS procedure. Although CSS algorithm is a very basic and straightforward procedure, it is only first order accurate in time and violates the Geometric Conservation Law (GCL). To overcome such problems in CSS scheme, an improved procedure named ISS is provided (see Fig.3.5.1 (b)), which has the potential of reducing the total aeroelastic simulation time. The ISS procedure is an improvement on the CSS procedure that ensures high accuracy by exchanging the feedback information between the fluid and structural fields within a time step, and this process is performed by considering an extra half-step taken by the CFD solver. Besides the serial solution algorithm the parallel one is another choice. Fig.3.5.1 (c) indicates the steps involved in every loop of the CPS procedure. CPS procedure allows the CFD and CSD solver to run in parallel mode, however, the main disadvantage is that the time step size needs to be kept as small as possible to maintain the stable solution. To ensure the continuity of velocity as well as the position of the fluid and structural meshes on the common boundary and improve the accuracy of CPS method, a procedure named as IPS is provided. Fig.3.5.1 (d) plots the main step. The main feature is that the computations performed during this first half of a cycle of the IPS procedure are identical to those performed during a cycle of the CPS method (Farhat and Lesoinne, 2000).

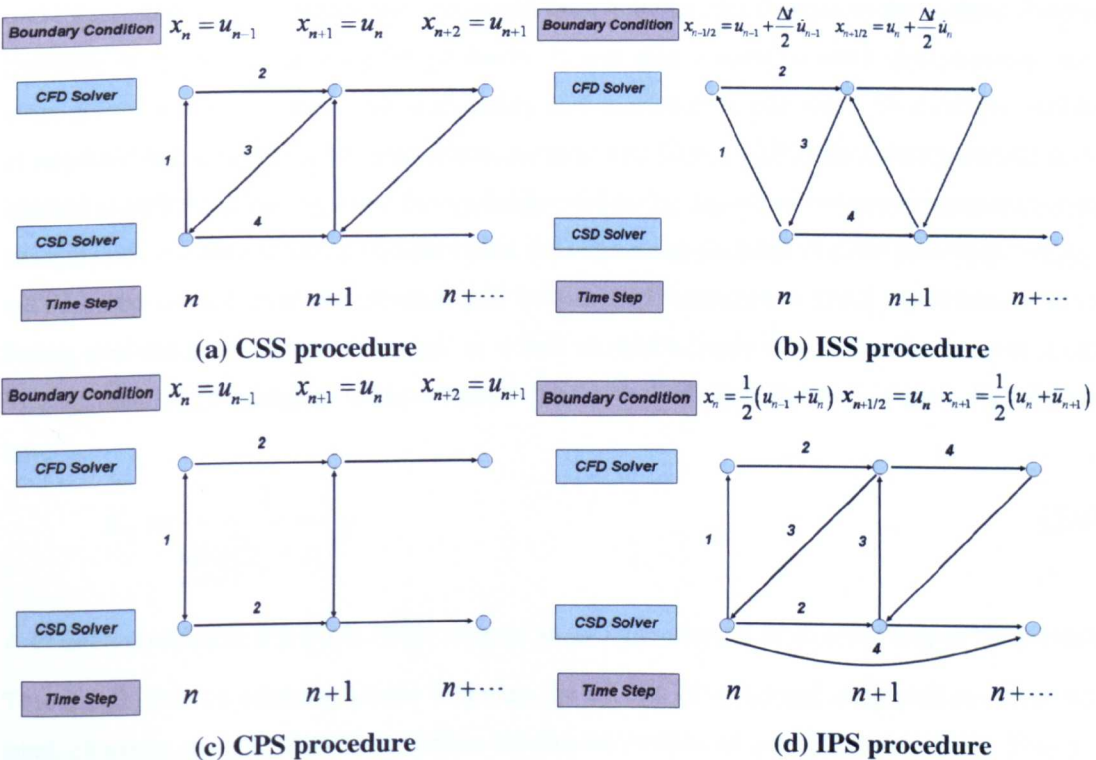


Fig 3.5.1 Four explicit staggered procedures

The detailed description about the above four explicit staggered algorithms can be seen in Farhat and Lesoinne paper (Farhat and Lesoinne, 2000)

3.6 Grid Deformation Approach

Another problem for FSI Since the structural deformation or movement needs to be mapped on the fluid domain mesh, it is also important to ensure that the fluid domain grid is appropriate to represent structural deformation. And an efficient technique to reflect grid deformation not only follows the structural movements, but also needs to keep a good quality in numerical simulation.

The simplest method but not the most efficient one known as the spring analogy method was proposed by Batina (1990, 1991), which regenerated new grid zone around the body after each step of its motion and eliminated the number of node deletion/insertion process. A rigid body small amplitude motion is assumed using the spring factor to control the mesh movement. The value of spring factor K is an important factor in this method. As mesh motion occurs, cells eventually exceed the prescribed limits. These cells are detected and marked for remeshing. This method can deal with large deformations but it is computationally expensive for a larger grid mesh due to the iterative method. Eriksson (1982) proposed a three-stage transfinite interpolation (TFI) technique to remesh single block domain, however it was not applicable for multi-block domains. To find an approach suitable for multi-block domains, Hartwich and Agrawal (1997) combined the spring analogy method with the TFI method, in which spring analogy was used to move the boundary edges of the blocks whereas TFI was used to remesh the surface and interior volume of each block. Bhardwaj *et al.* (1998) utilized a simple algebraic shearing technique to generate the grid deformation by redistributing the grid points along grid lines in a direction normal to the surface. Potential problems occurred for the complex geometry. It was also limited to small deformations, while large deformations generated poor grid quality and crossover of grid lines. To avoid the problem of negative volumes during FSI simulation, Degand and Farhat (2002) described torsional spring method at each mesh points, while this technique makes the algorithm consume expensive computational cost. Cavagna *et al.* (2002) discussed the efficient application of CFD aeroelastic methods with commercial software. An efficient grid deformation technique to avoid any nonlinear model during grid deformation was proposed, in which method a linear elastic continuum with a local Young modulus proportional to the minimal dimensional of each element adopted the following law.

$$E_{el} = \frac{1}{\min_{j,k \in el} \|x_j - x_k\|^\beta} \quad (3.6.1)$$

A Possion coefficient $\nu \in [0; 0.35]$ is selected to avoid numerical ill conditioning of the problem. This distribution of stiffness allows relieving the effects of structural deformations from inner small elements near the bluff body surface leaving the burden on outer larger elements. This technique can make the mesh deform without large distortions and is suitable for any element shape

and also for Navier-Stokes hybrid meshes with tetrahedrons and hexahedrons. Tang (2007) proposed moving mesh method to generate a mapping from a regular domain in a parameter space to an irregularly shaped domain in physical space. By connecting points in the physical space corresponding to discrete points in the parameters space, the physical domain can be covered with a computational mesh suitable for the solution of finite difference/element equations.

3.7 Interfacing Procedures of Fluid and Structure Solvers

The CSD utilizes a Lagrangian or material fixed-coordinate system, and CFD mesh systems adopt the Eulerian or spatially fixed-coordinate system. To solve them in a coupling interaction problem, a suitable interface technique between two systems should be developed. A typically coupled fluid and structure analysis diagram is presented in Fig.3.7.1.

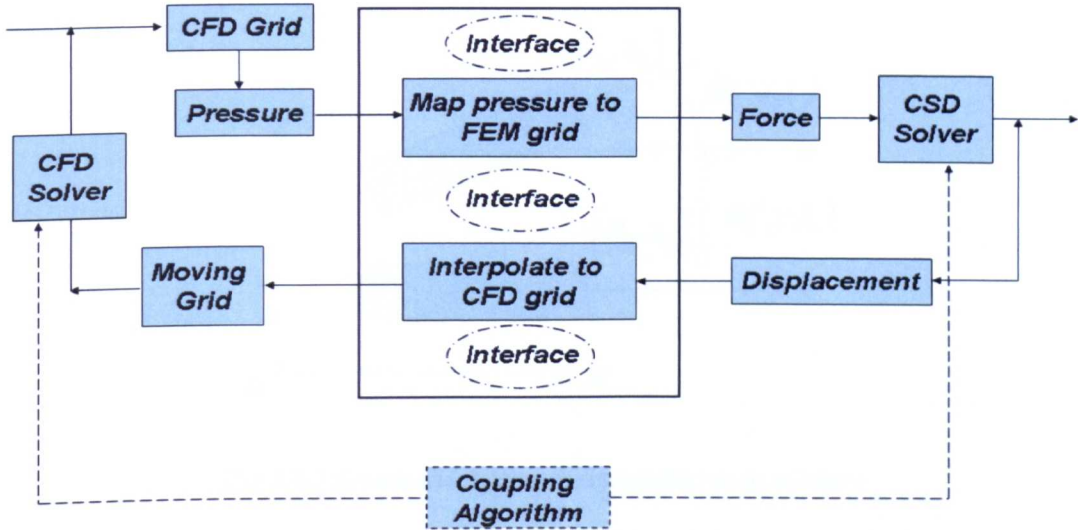


Fig 3.7.1 Coupled fluid-structure flow diagram

In Fig.3.7.1, the surface pressure of CFD interface grid needs to be mapped from the CFD grid system onto the structural grid to obtain the forces at every time step, and then through the CSD solver the displacements of structure are obtained from the CSD grid system and interpolated onto the CFD grid by the interface technique to obtain the CFD surface grid. After getting the CFD grid, the grid should be reflected to the mesh of CFD domain according to the moving grid technique and the domain is calculated by CFD solver again. During the process of CSD calculation and CFD calculation a coupling algorithm is needed.

For the interfacing technique, it is very important to preserve the accuracy in the data exchange process in order to obtain the correct FSI results. Generally, the structural grid is unstructured or coarser than the CFD grid, so it is important for accurate interpolating to transfer surface loads from the CFD grid to the structural grid. The bridge deck system can be simplified as beam elements, so the displacement of the beam at any instant along the spanwise direction can be represented by:

$$w_s = \{w_1 \quad w_2 \quad w_3 \mid \theta_1 \quad \theta_2 \quad \theta_3\}^T \quad (3.7.1)$$

Where w represents the vertical deflection, θ is the twist at each spanwise section and the subscripts 1, 2, 3 denote displacements in x , y and z directions, respectively. Since there was only deflection in the vertical plane and rotation about the elastic axis, the deflection of a CFD grid point P can be written as

$$w_p = w_{P_T} + w_{P_R} \quad (3.7.2)$$

Where, w_{P_T} is the translation component and w_{P_R} is the rotational component. The translation and rotation component at the position of CFD spanwise grid can be obtained by a linear interpolation with CSD spanwise grid points. The new locations of the CFD surface grid can be obtained by an extrapolation technique (Fig.3.7.2).

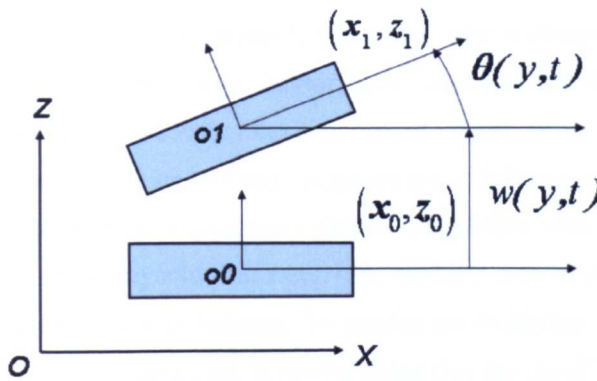


Fig 3.7.2 Schematic figure of extrapolation procedure

In Fig.3.7.2, subscript 0 denotes the original location of the CFD surface grid points and subscript 1 denotes the new location. After obtaining w and θ at each CFD grid spanwise location, the new location is obtained using Eq.3.7.3.

$$x_1 = x_0 \cos \theta + z_0 \sin \theta \quad (3.7.3a)$$

$$z_1 = z_0 \cos \theta - x_0 \sin \theta + w \quad (3.7.3b)$$

Based on the above content, the following steps can be summarized for the bridge structure buffeting response FSI simulation:

- (1) Construct the structure system finite element model based on the simulation need.
- (2) Perform the steady-state CFD computation as the initial guess for the beginning of the coupled computation.
- (3) Perform the unsteady CFD calculation based on the initial guess and obtain the aerodynamic forces on the surface of bridge deck system
- (4) Map the aerodynamic forces onto the structural system mesh
- (5) Perform the CSD computation to obtain the finite element model deformation
- (6) Map the displacements onto the CFD surface mesh grid

(7) Remesh the fluid system grid based on the displacements transferred from the CSD calculation with the moving grid technique

(8) Repeat (3)—(7) using the current solution as the initial guess for the next time step.

The proposed procedure can be realized by the home code or commercial code. For commercial code, the fluid system can be solved with software such ANSYS_CFX or FLUENT, while for the structural system calculation, NASTRAN, ANSYS or ABAQYS can be used. To realize the information exchanging between two systems, the build-in language for example USER_FORTRAN in ANSYS_CFX, or general C language in FLUENT, can be adopted.

3.8 Conclusions

Although different turbulence models have been applied into the CWE to simulate the bluff body aerodynamics, difficulties such as high Reynolds numbers, near wall resolution, inlet and outlet boundary conditions still exist, which need further study, especially for the bridge buffeting prediction, the inflow turbulence or unsteady inlet boundary is important. At the same time, it can be found that DNS is a better simulation method to capture the turbulence random and time varying characteristics, but it needs finer grids and has a larger computation cost. This model is still suitable for the problems of lower Reynolds numbers. LES model is a more suitable model for studying time varying characteristics of turbulence. To predict the buffeting response, the numerical procedure based on FSI theory is provided. It can be found that the closely coupled procedure has been accepted in the engineering field, which can be applied in future bridge buffeting response prediction. To realize the influence of structural movement on the grid system, the moving grid technique can be used.

Chap 4 Bridge Buffeting Response Simulation in Frequency Domain

4.1 Introduction

In previous chapters, the development of bridge buffeting analysis theory and simulation techniques have been overviewed and discussed. In this chapter, the assumptions, methodology and computational theory based on FEM are presented. A cable stayed bridge is adopted as the analysis model, and frequency domain analysis based on the conventional multi-modes aeroelastic coupling method and newly proposed POD technique are applied in the current simulation case. The influence of mode combination method such as Square Root of the Sum of the Squares (SRSS), aerodynamic admittance, self-excited force and Complete Quadratic Combination (CQC) on the simulation results in the frequency domain will be presented in this chapter.

4.2 Assumptions and Methodology

4.2.1 Assumptions

Several assumptions are always adopted to deal with bridge buffeting response simulation more effectively. For the turbulent wind field, it is assumed that the oncoming wind velocity can be the superposition between the mean velocity within the long period and gust wind velocity within the short period. Gust wind velocities are assumed to be a stationary, ergodic and steady random process. For a large span bridge structure, the beam deck system can be approximated by beam elements. The aerodynamic force lift, drag and torsional coefficients can be derived from the steady wind tunnel experiment. Assuming the self excited force to be linear, it can be expressed from the flutter derivatives, also using the steady wind tunnel experiment. The aerodynamic flutter forces are expressed as linear functions of velocity and displacement. When carrying out the frequency analysis method, the structure is assumed to be linear system with classical damping and to satisfy the modal superposition and small deformation condition.

4.2.2 Methodology

FEM is an effective method of studying the structural steady and dynamic characteristics and widely used in the bridge design and analysis. So in this chapter the analysis procedure of bridge buffeting response based on FEM in the frequency domain is introduced, in which the random vibration theory based on FEM is used to obtain the PSD value of buffeting response. For the structural mode analysis in the bridge buffeting simulation, commercial finite element analysis code ANSYS is used. Then, the mode shape matrix can be obtained and the bridge buffeting simulation based on the conventional buffeting analysis and POD approach can be done.

4.3 Computational Theory Description

In chapter 2 the bridge buffeting theory in the frequency domain had been simply introduced. In this section the analysis method based on FEM will be introduced in the following contents.

4.3.1 Wind Load Discretization

In general the aerodynamic load is mainly composed of three types: gust wind load, the load induced by the bridge structure movement and the load from the vortex shedding. The gust wind load is also known as the buffeting force which had been discussed in chapter 2. Here only the self excited force the flutter force is shown. In linear aerodynamics, lift load, drag load and torsional load can be expressed as the following form according to the aerodynamic flutter derivatives.

$$L_f = \frac{1}{2} \rho U^2 B \left[KH_1^* \frac{\dot{h}}{U} + KH_2^* \frac{B\dot{\alpha}}{U} + K^2 H_3^* \alpha + K^2 H_4^* \frac{h}{B} + KH_5^* \frac{\dot{p}}{U} + K^2 H_6^* \frac{p}{B} \right] \quad (4.3.1a)$$

$$D_f = \frac{1}{2} \rho U^2 B \left[KP_1^* \frac{\dot{p}}{U} + KP_2^* \frac{B\dot{\alpha}}{U} + K^2 P_3^* \alpha + K^2 P_4^* \frac{p}{B} + KP_5^* \frac{\dot{h}}{U} + K^2 P_6^* \frac{h}{B} \right] \quad (4.3.1b)$$

$$M_f = \frac{1}{2} \rho U^2 B^2 \left[KA_1^* \frac{\dot{h}}{U} + KA_2^* \frac{B\dot{\alpha}}{U} + K^2 A_3^* \alpha + K^2 A_4^* \frac{h}{B} + KA_5^* \frac{\dot{p}}{U} + K^2 A_6^* \frac{p}{B} \right] \quad (4.3.1c)$$

Where ρ is the air density, U is the oncoming mean wind velocity, B is the bridge deck width, $K = Bf / U$ is the reduced frequency. h , p and α are the structure vertical, lateral and torsional displacement respectively. In Fig.4.3.1 H_i^* , P_i^* and A_i^* ($i=1,2,\dots,6$) are the aerodynamic flutter derivatives, which are the function of reduced frequency K .

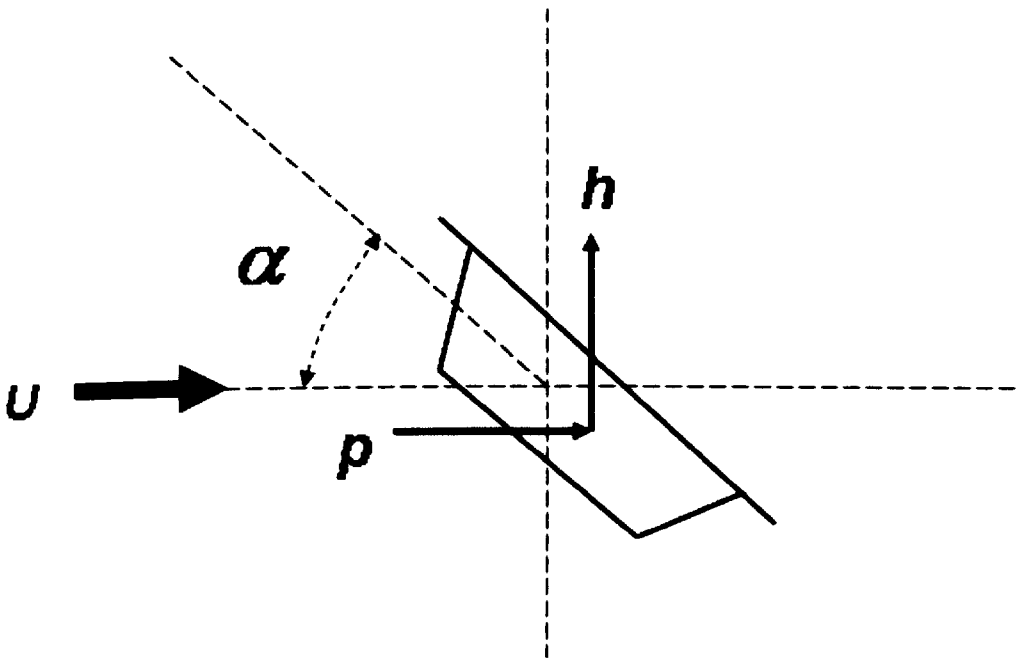


Fig 4.3.1 Bridge deck displacement component

Eq.4.3.1 expresses the bridge deck system self excited force per meter. To transform the average distributed load into the node form, which can be applied to each end of the element, see Fig.4.3.2.

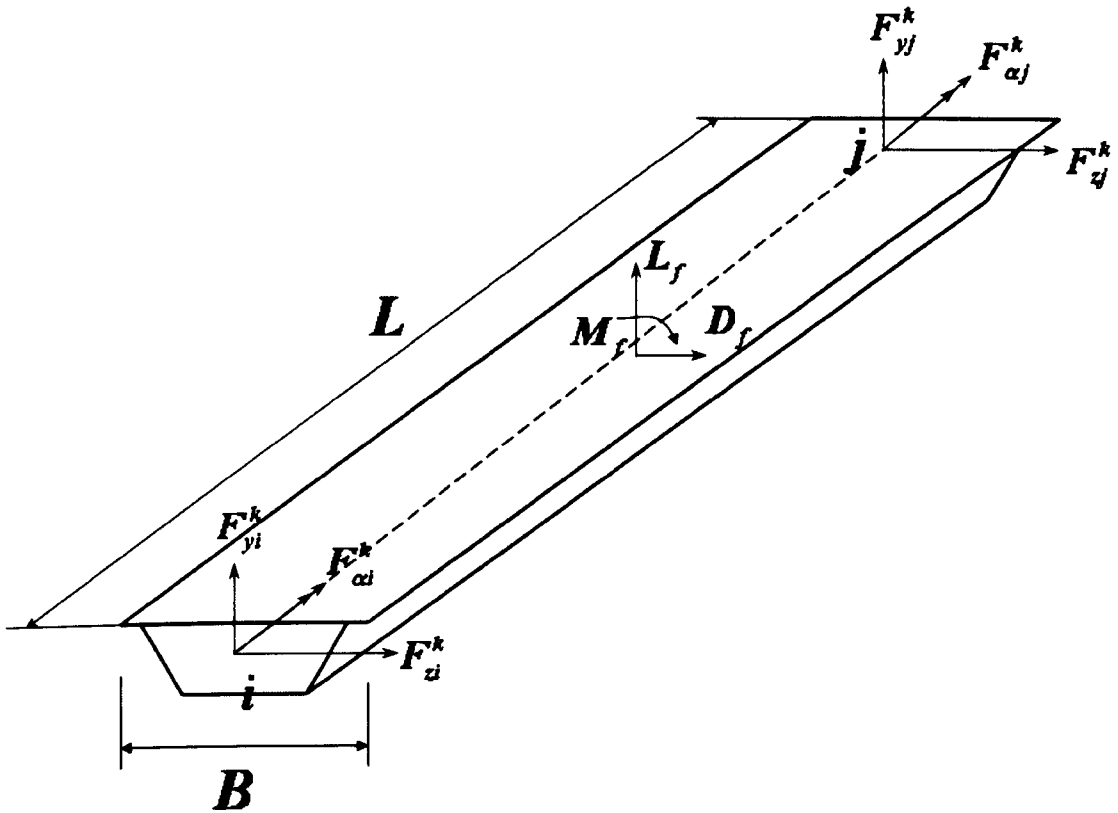


Fig 4.3.2 Self-excited force on bridge deck system

When the bridge deck system is discretized by the space beam element with 12 degrees based on the FEM, as shown in Fig.4.3.3, the equivalent node force induced by the average distributed self-excited forces on the k th element with length L can be expressed as:

While the node displacement and velocity vector are:

$$\{\delta_l\} = \{u_l, v_l, w_l, \alpha_l, \beta_l, \gamma_l\}^T \quad (4.3.5a)$$

$$\{\dot{\delta}_l\} = \{\dot{u}_l, \dot{v}_l, \dot{w}_l, \dot{\alpha}_l, \dot{\beta}_l, \dot{\gamma}_l\}^T \quad (4.3.5b)$$

The 12×12 aerodynamic stiffness matrix $[A_s]$ and damping matrix $[A_d]$ have the following form:

$$[A_s^k] = \frac{1}{4} \rho U^2 L K^2 \begin{bmatrix} 0 & 0 & 0 & 0 & 0 & 0 & 0 & 0 & 0 & 0 & 0 & 0 \\ 0 & H_4^* & H_6^* & -BH_3^* & 0 & 0 & 0 & 0 & 0 & 0 & 0 & 0 \\ 0 & P_6^* & P_4^* & -BP_3^* & 0 & 0 & 0 & 0 & 0 & 0 & 0 & 0 \\ 0 & -BA_4^* & BA_6^* & B^2 A_3^* & 0 & 0 & 0 & 0 & 0 & 0 & 0 & 0 \\ 0 & 0 & 0 & 0 & 0 & 0 & 0 & 0 & 0 & 0 & 0 & 0 \\ 0 & 0 & 0 & 0 & 0 & 0 & 0 & 0 & 0 & 0 & 0 & 0 \\ 0 & 0 & 0 & 0 & 0 & 0 & 0 & 0 & 0 & 0 & 0 & 0 \\ 0 & 0 & 0 & 0 & 0 & 0 & 0 & H_4^* & H_6^* & -BH_3^* & 0 & 0 \\ 0 & 0 & 0 & 0 & 0 & 0 & 0 & P_6^* & P_4^* & -BP_3^* & 0 & 0 \\ 0 & 0 & 0 & 0 & 0 & 0 & 0 & -BA_4^* & BA_6^* & B^2 A_3^* & 0 & 0 \\ 0 & 0 & 0 & 0 & 0 & 0 & 0 & 0 & 0 & 0 & 0 & 0 \\ 0 & 0 & 0 & 0 & 0 & 0 & 0 & 0 & 0 & 0 & 0 & 0 \end{bmatrix} \quad (4.3.6a)$$

$$[A_d^k] = \frac{1}{4} \rho U B L K \begin{bmatrix} 0 & 0 & 0 & 0 & 0 & 0 & 0 & 0 & 0 & 0 & 0 & 0 \\ 0 & H_1^* & H_5^* & -BH_2^* & 0 & 0 & 0 & 0 & 0 & 0 & 0 & 0 \\ 0 & P_5^* & P_1^* & -BP_2^* & 0 & 0 & 0 & 0 & 0 & 0 & 0 & 0 \\ 0 & -BA_1^* & BA_5^* & B^2 A_2^* & 0 & 0 & 0 & 0 & 0 & 0 & 0 & 0 \\ 0 & 0 & 0 & 0 & 0 & 0 & 0 & 0 & 0 & 0 & 0 & 0 \\ 0 & 0 & 0 & 0 & 0 & 0 & 0 & 0 & 0 & 0 & 0 & 0 \\ 0 & 0 & 0 & 0 & 0 & 0 & 0 & 0 & 0 & 0 & 0 & 0 \\ 0 & 0 & 0 & 0 & 0 & 0 & 0 & H_1^* & H_5^* & -BH_2^* & 0 & 0 \\ 0 & 0 & 0 & 0 & 0 & 0 & 0 & P_5^* & P_1^* & -BP_2^* & 0 & 0 \\ 0 & 0 & 0 & 0 & 0 & 0 & 0 & -BA_1^* & BA_5^* & B^2 A_2^* & 0 & 0 \\ 0 & 0 & 0 & 0 & 0 & 0 & 0 & 0 & 0 & 0 & 0 & 0 \\ 0 & 0 & 0 & 0 & 0 & 0 & 0 & 0 & 0 & 0 & 0 & 0 \end{bmatrix} \quad (4.3.6b)$$

4.3.2 Bridge Buffeting Numerical Method Based on FEM

So far the self-excited force and buffeting force expressions have been described in the above content. Following is how to compute them based on the FEM from frequency domain to time domain. When the FEM is adopted, the bridge structure dynamic governing equation can be expressed as:

$$M\ddot{X} + C\dot{X} + KX = F_{se} + F_b \quad (4.3.7)$$

Where M , C and K is the system mass, damping and stiffness matrix separately, \ddot{X} , \dot{X} and X are the multi degree system node acceleration, velocity and displacement, F_{se} and F_b are the node equivalent flutter and buffeting force vectors. As the self-excited force per element has been presented in the above and the bridge deck system buffeting force per unit length expression has been described in chapter 2, the buffeting force can be expressed as:

$$L_b = \frac{1}{2} \rho U^2 B \left[C_L \left(2 \frac{v}{U} \right) + (C'_L + C_D) \frac{w}{U} \right] \quad (4.3.8a)$$

$$D_b = \frac{1}{2} \rho U^2 B \left[C_D \left(2 \frac{v}{U} \right) + (C'_D - C_L) \frac{w}{U} \right] \quad (4.3.8b)$$

$$M_b = \frac{1}{2} \rho U^2 B^2 \left[C_M \left(2 \frac{v}{U} \right) + C'_M \frac{w}{U} \right] \quad (4.3.8c)$$

Here only the buffeting force per element node needs to be described based on FEM. v and w are the gust wind velocity components at the element coordinates. Assuming the element located in the plane is vertical to the horizontal wind direction, $v' = v$, $w' = w \cos \theta$, where v and w are the gust wind velocity component at the vertical and horizontal direction respectively. θ is the angle between the element coordinate x^e and global coordinate X . Therefore Eq.4.3.8 can be rewritten as:

$$P_b = 0.5 \rho U (C_{bv} v + C_{bw} w) \quad (4.3.9)$$

Where

$$P_b = \begin{Bmatrix} L_b \\ D_b \\ M_b \end{Bmatrix}, C_{bv} = B \begin{Bmatrix} 2C_L \\ 2C_D \\ 2BC_M \end{Bmatrix}, C_{bw} = B \cos \theta \begin{Bmatrix} C'_L + C_D \\ C'_D \\ BC'_M \end{Bmatrix}$$

If the bridge deck divided by the FE is small enough, it can be assumed that the vertical and horizontal gust wind components are linear in the element and can be expressed as:

$$v = \begin{bmatrix} 1 - \frac{x}{L} & \frac{x}{L} \end{bmatrix} \begin{Bmatrix} v_1 \\ v_2 \end{Bmatrix} = A v^e \quad (4.3.10a)$$

$$w = \begin{bmatrix} 1 - \frac{x}{L} & \frac{x}{L} \end{bmatrix} \begin{Bmatrix} w_1 \\ w_2 \end{Bmatrix} = A w^e \quad (4.3.10b)$$

Where, 1 and 2 express the element ends, x is the element axis position, and L is the length of the element.

In the element coordinate, the equivalent node load on the element induced by the buffeting is:

$$F_b^e = \int_L B^T P_b dx = 0.5 \rho U \left(\int_L B^T C_{bv} A dx v^e + \int_L B^T C_{bw} A dx w^e \right) = 0.5 \rho U (A_{bv}^e v^e + A_{bw}^e w^e)$$

(4.3.11)

Where, $A_{bv}^e \mathbf{v}^e$ and $A_{bw}^e \mathbf{w}^e$ expresses the vertical and horizontal gust wind buffeting force matrix per element; and \mathbf{B} is the interpolating function:

$$\mathbf{B} = \begin{bmatrix} 0 & -N_1 & 0 & 0 & 0 & -N_3 & 0 & -N_2 & 0 & 0 & 0 & N_4 \\ 0 & 0 & -N_1 & 0 & N_3 & 0 & 0 & 0 & -N_2 & 0 & -N_4 & 0 \\ 0 & 0 & 0 & -N_5 & 0 & 0 & 0 & 0 & 0 & -N_6 & 0 & 0 \end{bmatrix}$$

(4.3.12)

Where

$$N_1 = 1 - 3\left(\frac{x}{L}\right)^2 + 2\left(\frac{x}{L}\right)^3, N_2 = 3\left(\frac{x}{L}\right)^2 - 2\left(\frac{x}{L}\right)^3, N_3 = x\left(1 - \frac{x}{L}\right)^2, N_4 = x\left(1 - \frac{x}{L}\right)^2,$$

$$N_4 = \frac{x^2}{L}\left(1 - \frac{x}{L}\right), N_5 = 1 - \frac{x}{L}, N_6 = \frac{x}{L}$$

$$A_{bv}^e \mathbf{v}^e = \frac{-BL}{30} \begin{bmatrix} 0 & 21C_L & 21C_D & 20BC_M & -3LC_D & 3LC_L \\ 0 & 9C_L & 9C_D & 10BC_M & -2LC_D & 2LC_L \\ 0 & 9C_L & 9C_D & 10BC_M & -2LC_D & 2LC_L \\ 0 & 21C_L & 21C_D & 20BC_M & -3LC_D & 3LC_L \end{bmatrix}^T \quad (4.3.13a)$$

$$A_{bw}^e \mathbf{w}^e = \frac{-BL \cos \theta}{60} \begin{bmatrix} 0 & 21(C'_L + C'_D) & 21C'_D & 20BC'_M & -3LC'_D & 3L(C'_L + C'_D) \\ 0 & 9(C'_L + C'_D) & 9C'_D & 10BC'_M & -2LC'_D & 2L(C'_L + C'_D) \\ 0 & 9(C'_L + C'_D) & 9C'_D & 10BC'_M & -2LC'_D & 2L(C'_L + C'_D) \\ 0 & 21(C'_L + C'_D) & 21C'_D & 20BC'_M & -3LC'_D & 3L(C'_L + C'_D) \end{bmatrix}^T \quad (4.3.13b)$$

Transforming the element buffeting force into global coordinate, the complete structure equivalent node buffeting force can be expressed as:

$$\mathbf{F}_b^e = 0.5\rho U (\mathbf{A}_{bv} \mathbf{v} + \mathbf{A}_{bw} \mathbf{w}) \quad (4.3.14)$$

According to the above buffeting introduction, Eq.3.3.7 can be written as:

$$M\ddot{\mathbf{X}} + C\dot{\mathbf{X}} + K\mathbf{X} - \omega^2 \mathbf{A}_{se} \mathbf{X} = 0.5\rho U (\mathbf{A}_{bv} \mathbf{v} + \mathbf{A}_{bw} \mathbf{w}) \quad (4.3.15)$$

Assuming that bridge structure buffeting response can be approximated by superposition of the first m order mode,

$$\mathbf{X} = \Phi \mathbf{q} \quad (4.3.16)$$

Multiplying Eq.4.3.7 Φ^T on the left side, gives

$$\ddot{\mathbf{q}} + \bar{C}\dot{\mathbf{q}} + \Lambda \mathbf{q} - \omega^2 \bar{A}_{se} \mathbf{q} = \mathbf{Q}_b \quad (4.3.17)$$

Where Λ is the eigenvalue matrix, $\bar{A}_{se} = \Phi^T \mathbf{A}_{se} \Phi$ and $\bar{C} = \Phi^T C \Phi$ is the generalized buffeting force vector and damping matrix, $\mathbf{Q}_b = 0.5\rho U (\bar{A}_{bv} \mathbf{v} + \bar{A}_{bw} \mathbf{w})$, $\bar{A}_{bv} = \Phi^T \mathbf{A}_{bv}$ and $\bar{A}_{bw} = \Phi^T \mathbf{A}_{bw}$.

Based on the random vibration theory, according to the CQC method to calculate the generalized mode response vector \mathbf{q} and node displacement vector \mathbf{X} PSD:

$$\mathbf{S}_q(\omega) = \mathbf{F}\mathbf{T}^*(\omega)\mathbf{S}_{Q_b}(\omega)\mathbf{F}\mathbf{T}^T(\omega) \quad (4.3.18)$$

$$\mathbf{S}_X(\omega) = \mathbf{\Phi}\mathbf{F}\mathbf{T}^*(\omega)\mathbf{S}_{Q_b}(\omega)\mathbf{F}\mathbf{T}^T(\omega)\mathbf{\Phi}^T \quad (4.3.19)$$

Where $\mathbf{F}\mathbf{T}(\omega)$ is the frequency response transfer function:

$$\mathbf{F}\mathbf{T}(\omega) = \left[-\omega^2(\mathbf{I} + \bar{\mathbf{A}}_{se}) + i\omega\bar{\mathbf{C}} + \mathbf{A} \right]^{-1} \quad (4.3.20)$$

* and T express the matrix conjugate and transfer respectively.

To generalized buffeting force PSD:

$$\mathbf{S}_{Q_b}(\omega) = \mathbf{S}_{Q_b}^1(\omega) + \mathbf{S}_{Q_b}^2(\omega) \quad (4.3.21)$$

where

$$\mathbf{S}_{Q_b}^1(\omega) = 0.25\rho^2U^2 \left(\bar{\mathbf{A}}_{bv}\mathbf{S}_{vv}\bar{\mathbf{A}}_{bv}^T + \bar{\mathbf{A}}_{bw}\mathbf{S}_{ww}\bar{\mathbf{A}}_{bw}^T \right) \quad (4.3.22a)$$

$$\mathbf{S}_{Q_b}^2(\omega) = 0.25\rho^2U^2 \left(\bar{\mathbf{A}}_{bv}\mathbf{S}_{vw}\bar{\mathbf{A}}_{bv}^T + \bar{\mathbf{A}}_{bw}\mathbf{S}_{vw}\bar{\mathbf{A}}_{bw}^T \right) \quad (4.3.22b)$$

\mathbf{S}_{vv} and \mathbf{S}_{ww} is the gust wind velocity component PSD matrix, $\mathbf{S}_{vw} = \mathbf{S}_{vw}^*$ is the gust wind velocity component v and w cross spectrum density (CSD) matrix, $\mathbf{S}_{Q_b}^1(\omega)$ is the generalized buffeting force PSD induced by the gust wind velocity component v and w , $\mathbf{S}_{Q_b}^2(\omega)$ is the generalized buffeting force CSD generated by the gust wind velocity component v and w .

Because $\mathbf{S}_q = \mathbf{S}_q^{(1)} + \mathbf{S}_q^{(2)}$, $\mathbf{S}_X = \mathbf{S}_X^{(1)} + \mathbf{S}_X^{(2)}$, which can be written as:

$$\mathbf{S}_{q_{ij}}^{(r)}(\omega) = \sum_{k=1}^m \sum_{l=1}^m \mathbf{F}\mathbf{T}_{ik}^*(\omega)\mathbf{S}_{Q_{kl}}^{(r)}(\omega)\mathbf{F}\mathbf{T}_{jl}(\omega) \quad (4.3.23a)$$

$$\mathbf{S}_{X_i}^{(r)}(\omega) = \sum_{k=1}^m \sum_{l=1}^m \phi_{ik}\mathbf{S}_{Q_{kl}}^{(r)}(\omega)\phi_{jl}(\omega) \quad (4.3.23b)$$

Where $r = 1, 2$. Therefore the generalized mode response and node displacement variance with CQC method,

$$\sigma_{q_{ii}}^2 = \int_0^\infty \left(\mathbf{S}_{q_{ii}}^{(1)}(\omega) + \left| \mathbf{S}_{q_{ii}}^{(2)}(\omega) \right| \right) d\omega \quad (4.3.24a)$$

$$\sigma_{X_i}^2 = \int_0^\infty \left(\mathbf{S}_{X_i}^{(1)}(\omega) + \left| \mathbf{S}_{X_i}^{(2)}(\omega) \right| \right) d\omega = \sum_{k=1}^m \sum_{l=1}^m \phi_{ik} \left(\mathbf{S}_{q_{kl}}^{(1)}(\omega) + \left| \mathbf{S}_{q_{kl}}^{(2)}(\omega) \right| \right) \phi_{il} \quad (4.3.24b)$$

When the generalized buffeting force CSD can be ignored, that is $\mathbf{S}_{Q_{ij}}^{(r)}(\omega) = 0$ ($i \neq j$), so

Eq.4.3.23a can be written as:

$$\mathbf{S}_{q_{ij}}^{(r)}(\omega) = \sum_{k=1}^m \mathbf{F}\mathbf{T}_{ik}^*(\omega)\mathbf{S}_{Q_{kk}}^{(r)}(\omega)\mathbf{F}\mathbf{T}_{jk}(\omega) \quad (4.3.25)$$

If the aerodynamic coupling between the vibration mode is ignored, that is $H_{ij}(\omega) = 0 (i \neq j)$,

$S_{q_{ij}}^{(r)}(\omega) (r = 1, 2)$ is:

$$S_{q_{ij}}^{(r)}(\omega) = FT_{ii}^*(\omega) S_{Q_{ij}}^{(r)}(\omega) FT_{jj}(\omega) \quad (4.3.26)$$

If ignoring the generalized buffeting force CSD and vibration mode coupling, it can be:

$$S_{q_{ii}}^{(r)}(\omega) = |FT_{jj}(\omega)|^2 S_{Q_{ii}}^{(r)}(\omega), S_{q_{ij}}^{(r)}(\omega) = 0 (i \neq j, r = 1, 2) \quad (4.3.27)$$

Therefore the vibration mode buffeting response without mode coupling can be expressed based on the SRSS combination method,

$$SRSS(X_i) = \sqrt{\sigma_{X_{i,1}}^2 + \sigma_{X_{i,2}}^2 + \dots + \sigma_{X_{i,m}}^2} \quad (4.3.28)$$

Where m is the mode number. From the above, it is found that CQC is an accurate method, while SRSS method includes some assumptions ignoring the mode combination.

4.4 Test Case and Parameters

4.4.1 General Information of Test Case

The test case is simplified based on the prototype of Wu Han JunShan Yangtze fourth bridge, the detailed location of the bridge is the red line in Fig.4.4.1. This bridge is divided into three parts, including the north part, Junshang part and south part. This main span of this bridge is 649m, and the bridge deck is the box girder shape (see Fig.4.4.3). This bridge is one with double towers, whose shape is reverse Y (see Fig.4.4.2), and the detail demission of this bridge can be seen in Fig.4.4.2 and Fig.4.4.3.



Fig 4.4.1 Bridge location

4.4.2 Design Parameters of Test Case

The test case - a cable stayed bridge (Fig.4.4.2) detailed design parameters can be seen in this section. In general in the large span bridge structure analysis, the bridge system can be approximated with the plane or space spar system. The pile and tower part can be simplified as the two node spatial beam element, while the cable can be simplified as the two node spar or link element. For this case, the whole bridge can be approximated with the beam and cable element. In ANSYS, element type beam 4 (with 6 degrees at every node end) is adopted to simulate the bridge deck system and tower and pile, and element type link 10 (with 3 degrees at every node end) is used to simulate the cable. After performing the above simplification, the whole bridge system finite element model can be seen in Fig.4.4.4.

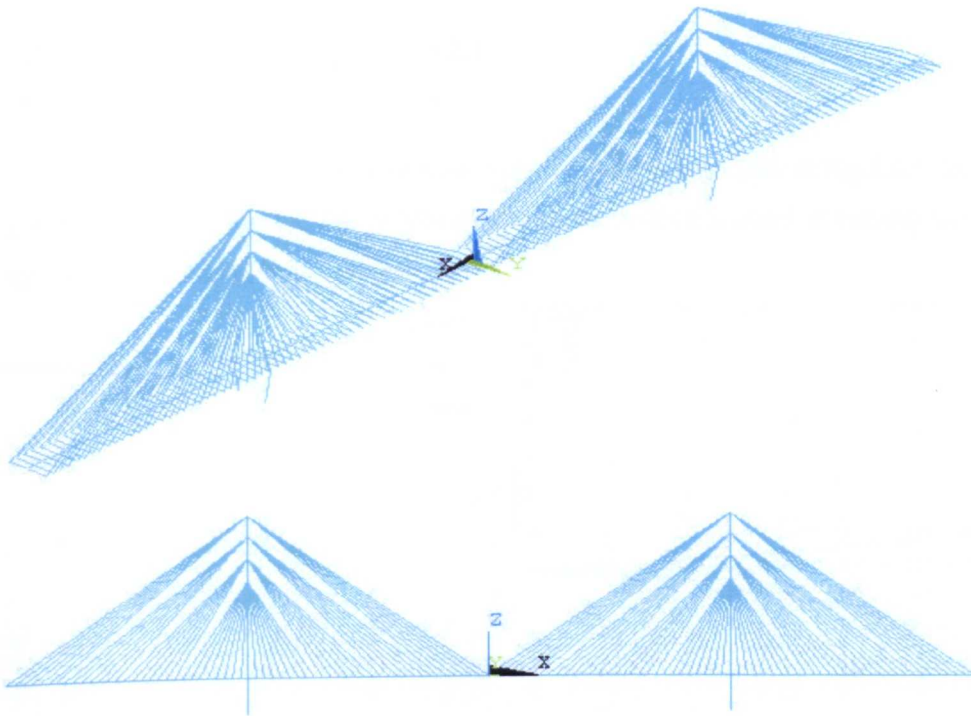


Fig 4.4.4 Finite element model of a cable stayed bridge

The general aerodynamic parameters used in this analysis are listed in the Table.4.4.1. Table.4.4.1 lists the aerodynamic static lift, drag and torsional coefficients considering a zero value of the angle of incidence of the mean wind velocity. The values obtained are from low speed boundary wind tunnel at Southwest Jiaotong University (XNJD-1), the tunnel dimension being 2.4m (Width) \times 2.0m (Height) \times 16m (Length).

Table 4.4.1 Static aerodynamic coefficients of bridge deck

C_D	C_L	C_M	C'_D	C'_L	C'_M
0.099	-0.045	0.016	-0.173	0.335	0.159

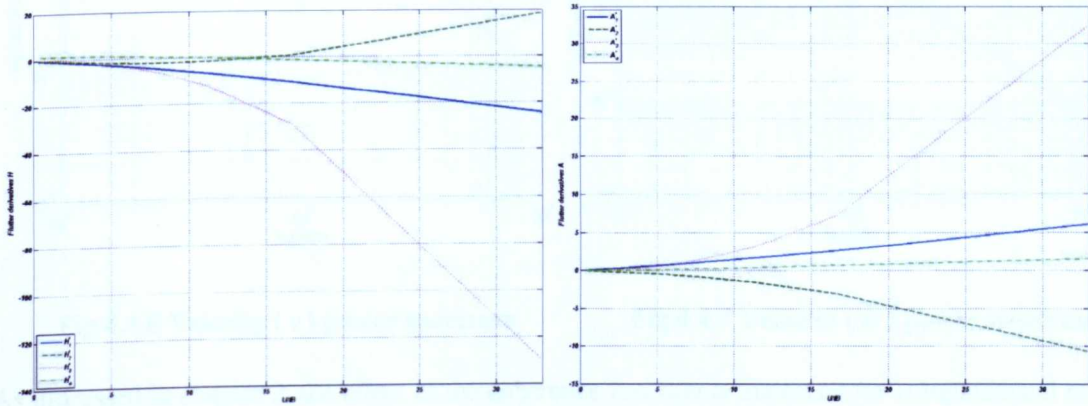
In the frequency domain analysis, the flutter derivatives used in this analysis can reference the thin plate flutter derivatives based on the Theodorsen function $C(K) = F(K) - iG(K)$.

$$H_1^* = -\frac{2\pi F(K)}{K}, H_2^* = -\frac{2\pi}{K} \left(1 + F(K) - \frac{2G(K)}{K} \right), H_3^* = -\frac{2\pi}{K^2} \left(F(K) + \frac{2G(K)}{K} \right)$$

$$H_4^* = -\frac{2\pi G(K)}{K}, A_1^* = \frac{\pi F(K)}{K}, A_2^* = \frac{K}{2\pi} \left(-1 + F(K) - \frac{2G(K)}{K} \right)$$

$$A_3^* = \frac{\pi}{K^2} \left(F(K) + \frac{kG(K)}{2} \right), A_4^* = \frac{\pi G(K)}{K}$$

Where $k = 0.5B\omega/U$, the flutter derivatives varying trend can be seen in Fig.4.4.5. In the following part of the analysis, the bridge structure response will be studied at varying mean wind velocity conditions ranging from 10m/s to 60m/s.



(a) Flutter derivatives H

(b) Flutter derivatives A

Fig 4.4.5 Flutter derivatives based on Theodorsen function

4.4.3 Wind Velocity Power Spectrum Models

The turbulent wind field along the bridge deck is modelled as 117 independent random processes with the longitudinal and the vertical turbulence components at the nodes of the model. Their Power Spectrum Density Function (PSDF) (Fig.4.4.6 and Fig.4.4.7) and coherence functions are given by (Solari and Piccardo, 2001):

$$\frac{fS_v(M;n)}{\sigma_v^2} = \frac{6.868 fL_v(M)/U(M)}{[1 + 10.302 fL_v(M)/U(M)]^{5/3}} \tag{4.4.1}$$

$$\frac{fS_w(M;n)}{\sigma_w^2} = \frac{6.103 fL_w(M)/U(M)}{1+63.181(fL_w(M)/U(M))^{5/3}} \quad (4.4.2)$$

$$Coh(M, M'; n) = \exp\left\{-\frac{2f \sqrt{\sum_r C_{r\epsilon}^2 |r-r'|^2}}{U(M)+U(M')}\right\} \quad (\epsilon = v, w) \quad (4.4.3)$$

Where σ_ϵ and $L_\epsilon(M)$ are the standard deviation and the integral length scale, respectively, of the turbulence component $\epsilon(t) = v(t), w(t)$, $r = y, z$ and $r = y', z'$ are the coordinates of the points M and M' along the deck axis, $C_{r\epsilon}$ is the exponential decay coefficient of $\epsilon(t)$ along r . A roughness length $z_0 = 0.015$ m has been assumed, the mean wind velocity is modelled by a logarithmic profile with a friction velocity $u_* = 1.9$ m/s, using the model proposed by Solari and Piccardo (2001), $\sigma_v = 5.13$ m/s, $\sigma_w = 2.57$ m/s, $C_{yv} = C_{zv} = 10$ and $C_{zw} = 3$.

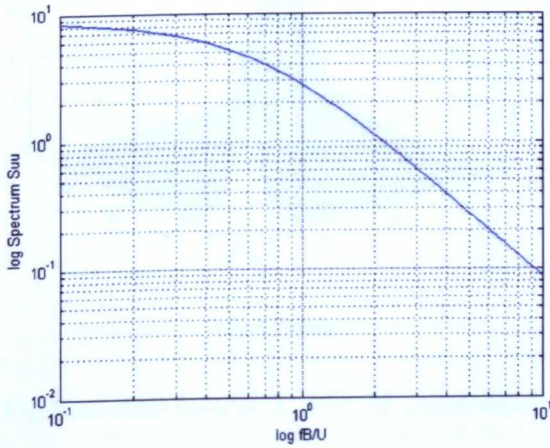


Fig 4.4.6 Velocity (v) power spectrum

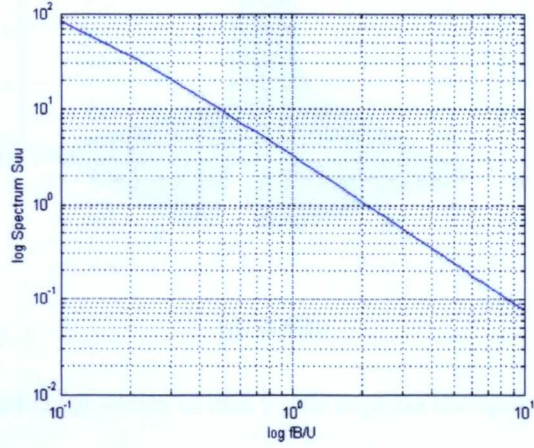
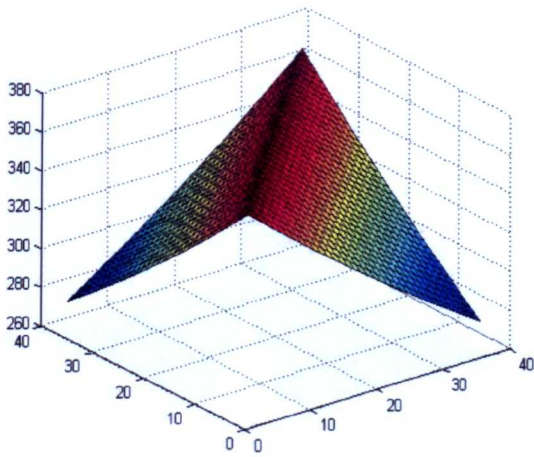
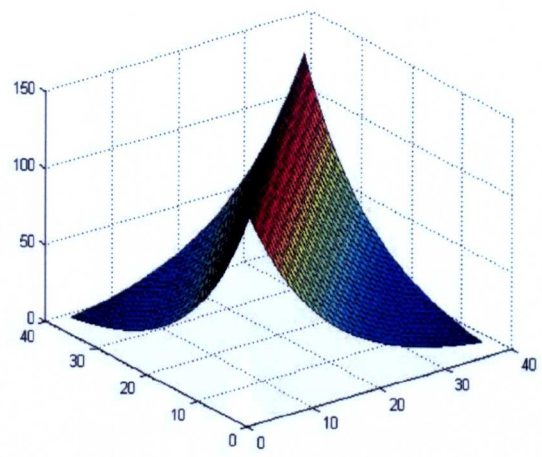


Fig 4.4.7 Velocity (w) power spectrum

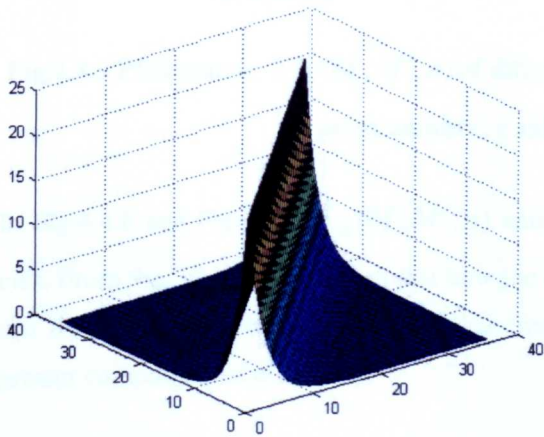
As discussed in chapter 2, the effect of the coherence function is important for computational reasons in wind velocity component simulation. For example, in the case of a long span bridge: many points on the bridge are located at considerable distances between each other. Therefore matrix $S_{\epsilon\epsilon}(M, M', n)$ becomes 'sparse' for any frequency values, which makes the computation efficient. On the other hand, in the presence of a 'compact' distribution of points over space, the signal in one point is strongly correlated to the signal in all the other points causing the sparseness to be lost.



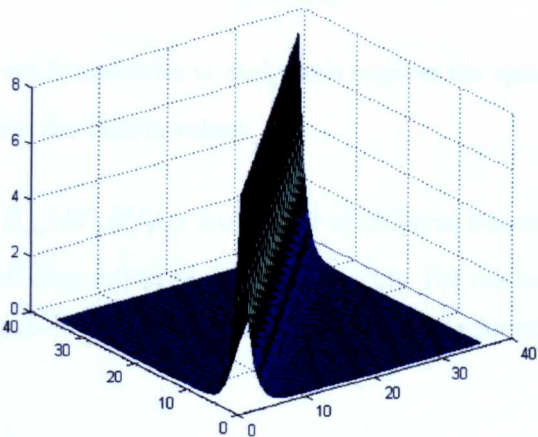
(a) 0.001Hz



(b) 0.01Hz

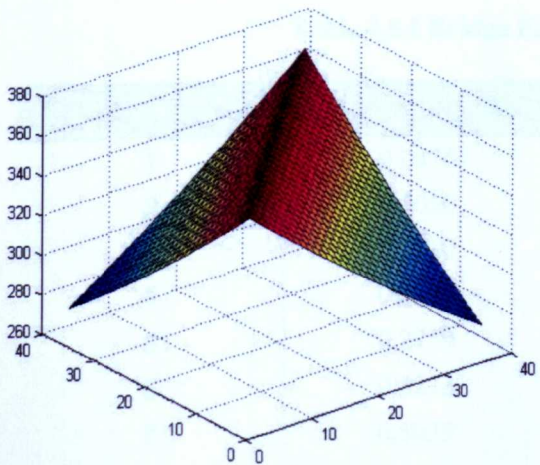


(c) 0.05Hz

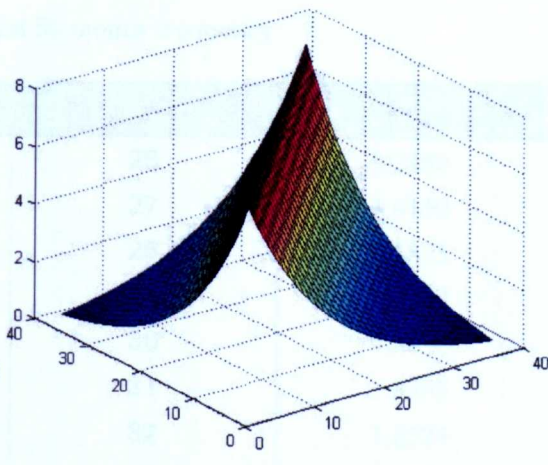


(d) 0.1Hz

Fig 4.4.8 PSD matrix $S_{vv}(M, M', n)$ of different frequencies (x and y axis express the space point number, z axis is the matrix value)



(a) 0.001Hz



(b) 0.01Hz

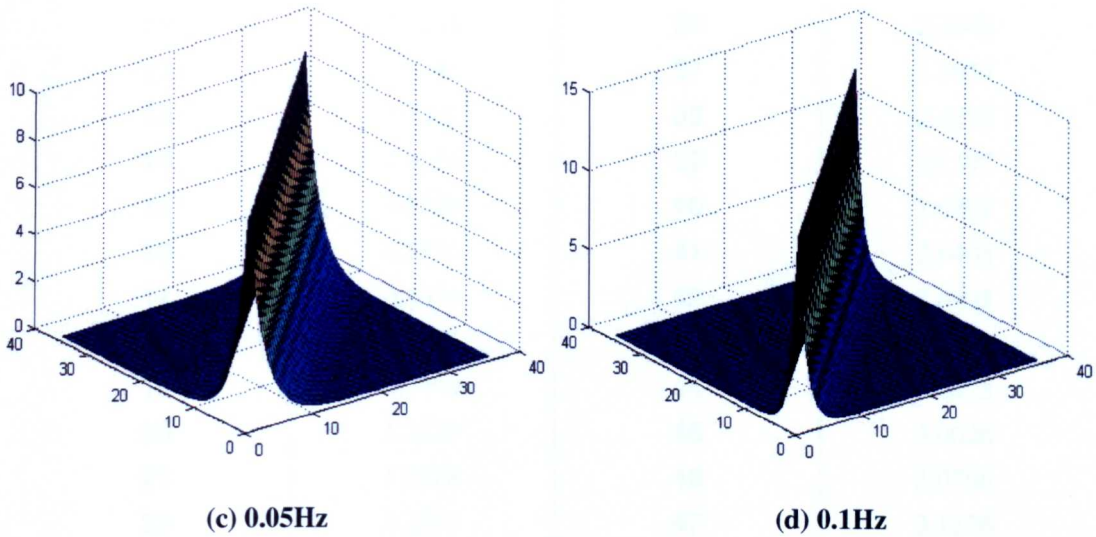


Fig 4.4.9 PSD matrix $S_{wv}(M, M', n)$ of different frequencies (x and y axis express the space point number, z axis is the matrix value)

In Fig.4.4.8 and Fig.4.4.9, $S_{vv}(M, M', n)$ and $S_{wv}(M, M', n)$ are plotted at different frequencies. From the figures it is evident that how the off-diagonal terms disappear quickly. For this reason these terms can be ignored for higher frequencies (in the domain of interest) to achieve a greater computational efficiency.

4.5 Results Analysis

4.5.1 Structure Self -vibration Modes Analysis

In this section, the first 50 mode frequencies will be considered, which are listed in Table.4.5.1. In Fig.4.5.1 the major mode shapes are plotted.

Table 4.5.1 Bridge first 50 modes frequency

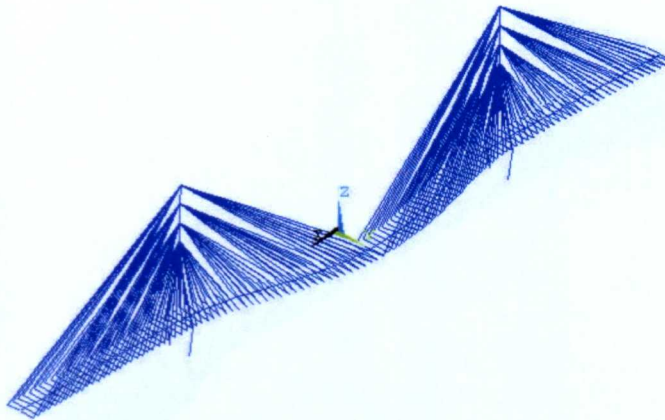
Mode Number	Frequency (Hz)	Mode Number	Frequency (Hz)
1	0.0976	26	1.3486
2	0.1050	27	1.4150
3	0.2710	28	1.5875
4	0.2712	29	1.7957
5	0.2759	30	1.8234
6	0.3273	31	1.8385
7	0.5039	32	1.8574
8	0.5128	33	1.9326
9	0.5137	34	1.9401
10	0.6091	35	1.9409

11	0.6164	36	2.2840
12	0.6345	37	2.4057
13	0.7082	38	2.4073
14	0.8074	39	2.6397
15	0.8528	40	2.6397
16	0.8535	41	2.6403
17	0.8634	42	2.6993
18	0.8646	43	3.0018
19	0.9449	44	3.0473
20	1.2220	45	3.0626
21	1.2528	46	3.0766
22	1.2557	47	3.1376
23	1.2675	48	3.1871
24	1.3418	49	3.1947
25	1.3431	50	3.3418

Fig.4.5.1 shows the bridge major vibration mode shape in the first 10 mode shapes. It can be found that as self vibration frequency increases, the structure shows a more complicated vibration mode. In Fig.4.5.1 S is the symmetry, AS is the asymmetry, V is the vertical deformation, H is the horizontal deformation and T is the torsional mode. 1 is the first order and 2 is the second order.

DISPLACEMENT
STEP=1
SUB =1
FREQ=.097601
DMX =.335E-03

ANSYS



(1) S-V-1



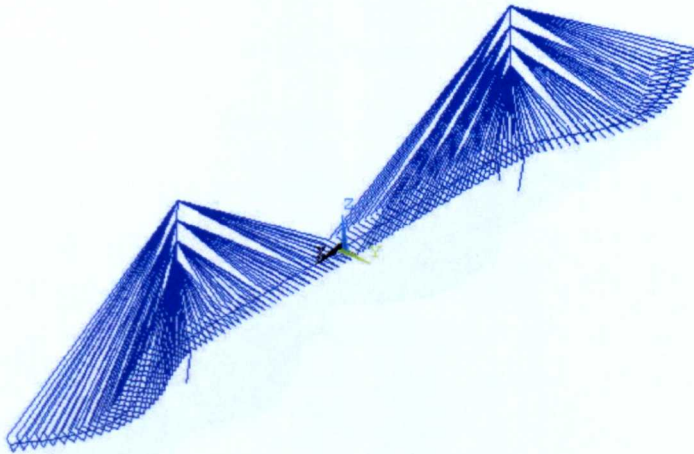
DISPLACEMENT
STEP=1
SUB =3
FREQ=.271045
DMX =.314E-03



(2) AS-T-1



DISPLACEMENT
STEP=1
SUB =4
FREQ=.27117
DMX =.318E-03



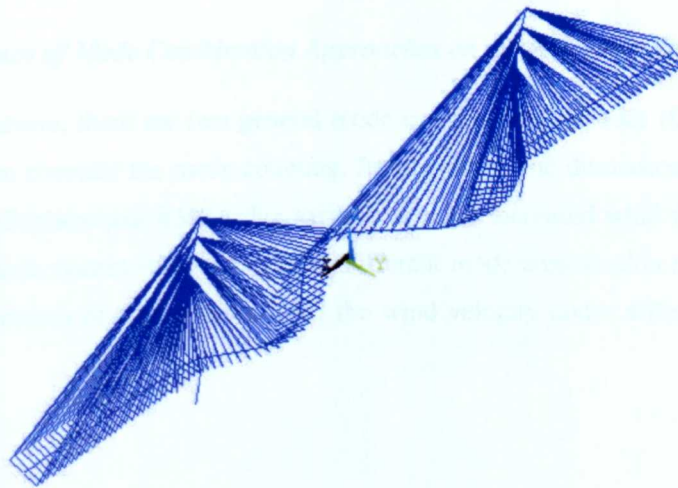
(3) S-H-1

DISPLACEMENT
STEP=1
SUB =5
FREQ=.275984
DMX =.313E-03



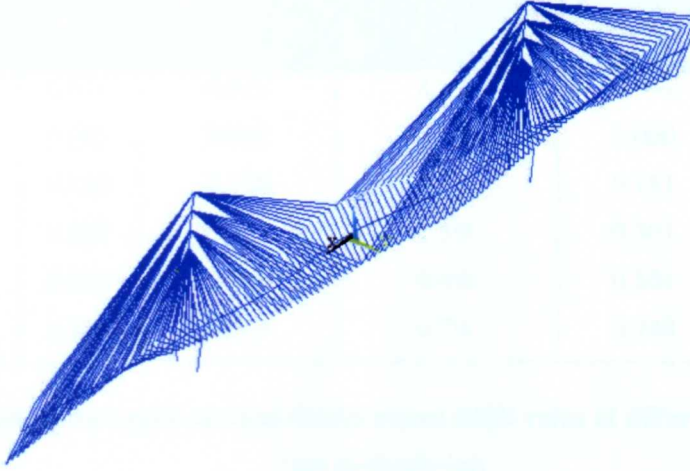
(4) AS-H-2

DISPLACEMENT
STEP=1
SUB =8
FREQ=.512768
DMX =.315E-03



(5) S-T-1

DISPLACEMENT
 STEP=1
 SUB =10
 FREQ=.609128
 DMX =.427E-03



(6) S-T-2

Fig 4.5.1 Major mode shapes of bridge system

The following contents will discuss the influence of different parameters on the frequency domain analysis results, which mainly consider the different mode combination method (CQC and SRSS), self-excited force and aerodynamic admittance influence.

4.5.2 Results Analysis Based on the Multimode Aeroelastic Coupling Method

(1) The Influence of Mode Combination Approaches on the Buffeting Response

As suggested above, there are two general mode combination methods (CQC method and SRSS method) used to consider the mode coupling. In this part of the discussion, Table.4.5.2-4.5.4 lists the calculated displacement RMS value varying with the increased wind velocity at the mid-span of the bridge deck system value considering different mode combination methods. Fig.4.5.2 plots the variation process of displacement with the wind velocity under different mode combination techniques.

Table 4.5.2 Bridge mid-span horizontal displacement RMS value of different mode combination methods (m)

Result Velocity	A:CQC	Multi-mode SRSS method		Single mode method	
		B:20 modes	$\frac{ B-A }{A} \times 100\%$	C: single mode	$\frac{ C-A }{A} \times 100\%$
10	0.012	0.011	8.3%	0.011	8.3%
20	0.066	0.062	6.1%	0.060	9.1%
30	0.169	0.156	7.7%	0.151	10.7%
40	0.327	0.322	1.5%	0.301	8.0%
50	0.512	0.508	0.8%	0.501	2.1%
60	0.768	0.763	0.7%	0.748	2.6%

Table 4.5.3 Bridge mid-span vertical displacement RMS value of different mode combination methods (m)

Result Velocity	A:CQC	Multi-mode SRSS method		Single mode method	
		B:20 modes	$\frac{ B-A }{A} \times 100\%$	C: single mode	$\frac{ C-A }{A} \times 100\%$
10	0.039	0.038	2.6%	0.038	2.6%
20	0.143	0.140	2.1%	0.135	5.6%
30	0.293	0.282	3.8%	0.270	7.8%
40	0.442	0.405	8.4%	0.382	13.6%
50	0.642	0.556	13.4%	0.518	19.3%
60	0.827	0.674	18.5%	0.622	24.8%

Table 4.5.4 Bridge mid-span twisting angle RMS value of different mode combination methods (degree)

Result Velocity	A:CQC	Multi-mode SRSS method		Single mode method	
		B:20 modes	$\frac{ B-A }{A} \times 100\%$	C: single mode	$\frac{ C-A }{A} \times 100\%$
10	0.025	0.025	0.0%	0.023	8.0%
20	0.107	0.107	0.0%	0.102	4.7%
30	0.291	0.282	3.1%	0.273	6.2%
40	0.574	0.521	9.2%	0.501	12.7%
50	1.042	0.854	18.0%	0.820	21.3%
60	1.893	1.221	35.5%	1.171	38.1%

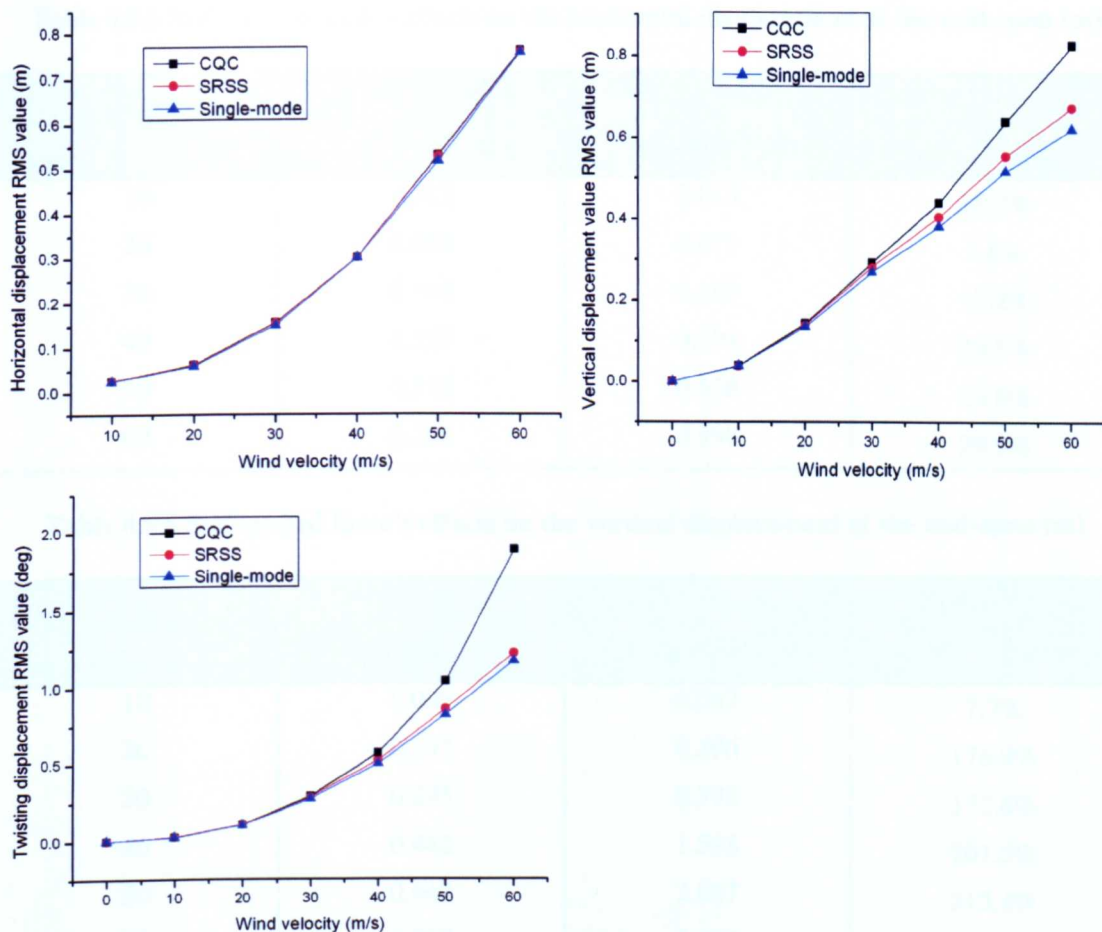


Fig 4.5.2 Displacement RMS value at mid-span of bridge deck

From the above figures and tables, it can be found that the single mode buffeting response will underestimate the main beam vertical and twisting response due to the mode coupling effects, and the response magnitude will be larger with the wind speed increasing. However, for the beam horizontal RMS response value of the displacement, the difference between the CQC method and SRSS method is not clear. At the high wind velocity zone, the value based on the CQC method are larger than from the SRSS method, which further indicates that CQC method can consider the higher mode contribution to the response and the wind velocity can trigger a higher order vibration mode.

(2) The Influence of Self-excited force on the Buffeting Response

As discussed in chapter 2, aerodynamic elastic coupling is a very important factor to influence the buffeting response, especially for the long span bridge. Here the buffeting response considering the aeroelastic coupling effects at the mid-span of the bridge deck system are listed in Table.4.5.5-4.5.7 based on the CQC method. The variation of response with wind velocity is plotted in Fig.4.5.3.

Table 4.5.5 Self-excited force's effects on the horizontal displacement at the mid-span (m)

Wind velocity	A: self excited force	B: without the self excited force	$\frac{ B-A }{A} \times 100\%$
10	0.012	0.015	25.0%
20	0.066	0.071	7.6%
30	0.169	0.198	17.2%
40	0.327	0.394	20.5%
50	0.512	0.638	24.6%
60	0.768	0.998	29.9%

Table 4.5.6 Self-excited force's effects on the vertical displacement at the mid-span (m)

Wind velocity	A: self excited force	B: without the self excited force	$\frac{ B-A }{A} \times 100\%$
10	0.039	0.042	7.7%
20	0.143	0.396	176.9%
30	0.293	0.798	172.4%
40	0.442	1.598	261.5%
50	0.642	2.667	315.4%
60	0.827	3.892	370.6%

Table 4.5.7 Self-excited force's effects on the twisting angle at the mid-span (degree)

Wind velocity	A: self excited force	B: without the self excited force	$\frac{ B-A }{A} \times 100\%$
10	0.025	0.029	16.0%
20	0.107	0.192	79.4%
30	0.291	0.498	71.1%
40	0.574	0.990	72.5%
50	1.042	1.712	64.3%
60	1.893	2.693	42.3%

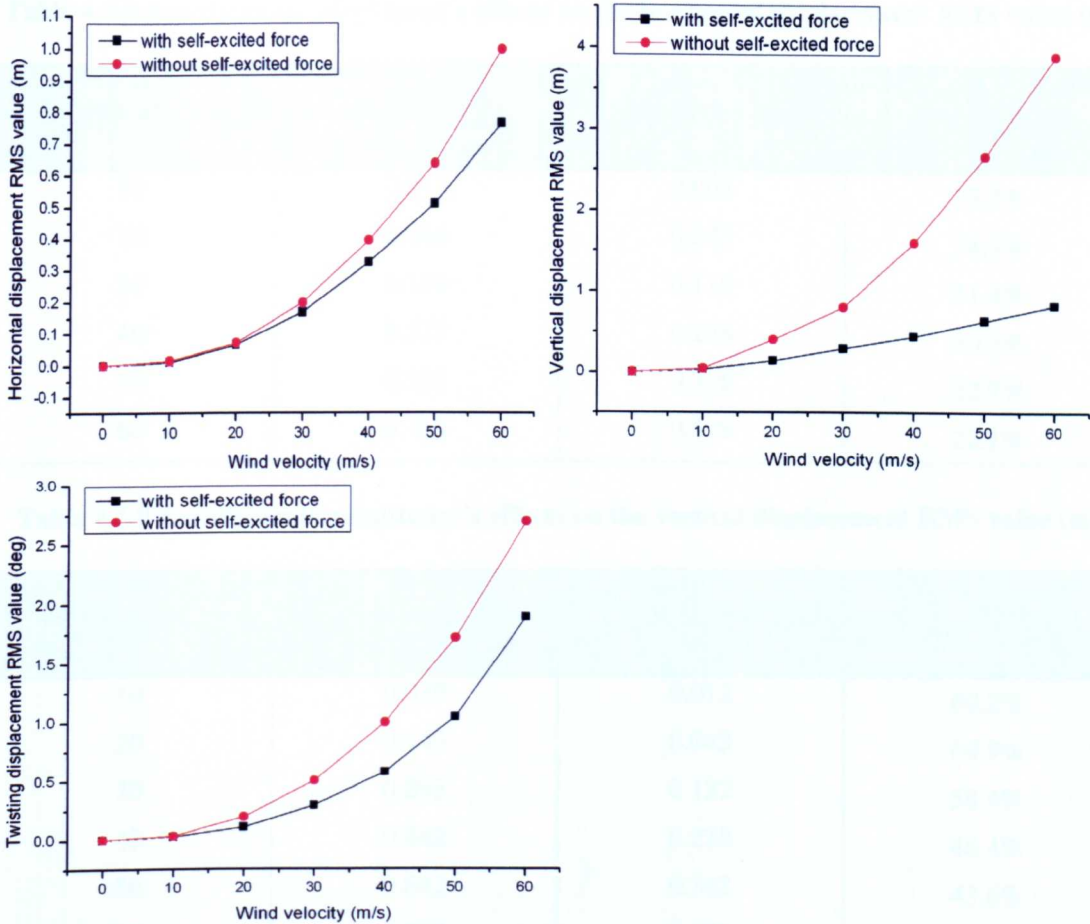


Fig 4.5.3 Displacement RMS value with self-excited force at the mid-span of bridge deck

From above tables and figures, it can be found that with the wind velocity increasing, the vertical, horizontal displacement and twist angle are also increasing for both conditions A and B. Comparing between A and B, it is also found that the analysis results considering the self-excited forces are smaller than those without considering it, as plotted in Fig. 4.5.3. It is because that the self excited force generates the aerodynamic damping and stiffness and changes the bridge structure system damping and stiffness, which adds additional stiffness and damping in the structure and restrains the structure response magnitude.

(3) The Influence of Aerodynamic Admittance on Buffeting Response

Aerodynamic admittance is another factor influencing the buffeting analysis results discussed in chapter 2. Here, two cases are considered, one assumes the aerodynamic admittance equal to 1, and the other adopts the Sears function. To consider the aeroelastic coupling effect, the self excited force is considered in this part of analysis. For the aim of simplification, the cable system influence is not considered in this part of the simulation. Table.4.5.8-4.5.11 lists the RMS value of displacements varying with the velocity separately at the mid-span of the bridge deck system. The variation process is also plotted in Fig.4.5.4.

Table 4.5.8 Aerodynamic admittance's effects on the horizontal displacement RMS value (m)

Wind velocity	A: Admittance = 1	B: Sears function	$\frac{ B-A }{A} \times 100\%$
10	0.012	0.008	33.3%
20	0.066	0.043	34.8%
30	0.169	0.116	31.4%
40	0.327	0.228	30.3%
50	0.512	0.396	22.7%
60	0.768	0.598	22.1%

Table 4.5.9 Aerodynamic admittance's effects on the vertical displacement RMS value (m)

Wind velocity	A: Admittance = 1	B: Sears function	$\frac{ B-A }{A} \times 100\%$
10	0.039	0.012	69.2%
20	0.143	0.043	69.9%
30	0.293	0.122	58.4%
40	0.442	0.228	48.4%
50	0.642	0.362	43.6%
60	0.827	0.476	42.4%

Table 4.5.10 Aerodynamic admittance's effects on the twisting angle RMS value (degree)

Wind velocity	A: Admittance = 1	B: Sears function	$\frac{ B-A }{A} \times 100\%$
10	0.025	0.012	52.0%
20	0.107	0.051	52.3%
30	0.291	0.103	64.6%
40	0.574	0.273	52.4%
50	1.042	0.486	53.4%
60	1.893	0.846	55.3%

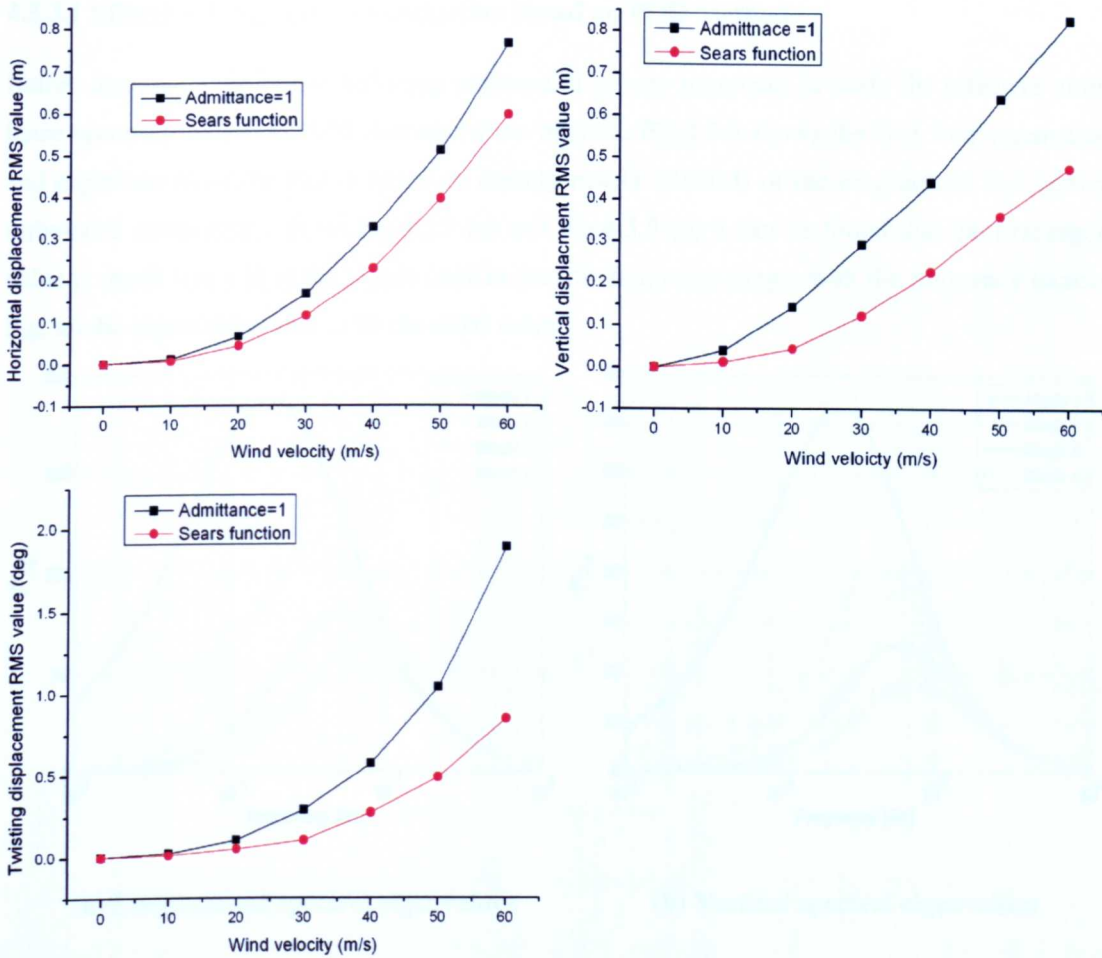


Fig 4.5.4 Displacement RMS value with aerodynamic admittance at the mid-span of bridge deck

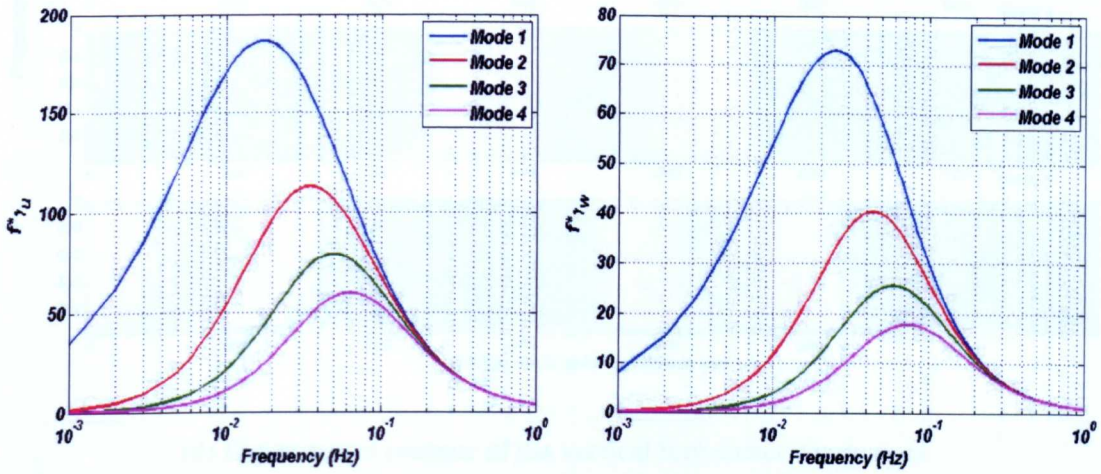
From the above tables, it can be found the response magnitude is increasing with the velocity increasing. At the same time comparing the simulation results between the condition A and B, it can be found that the value with aerodynamic admittance is smaller than the one without aerodynamic admittance, this variation is plotted clearly in Fig.4.5.4.

4.5.3 Results Analysis Based on POD Buffeting Theory

The above case study mainly focuses on the conventional multimodal aeroelastic coupling buffeting response analysis. As described in chapter 2, not all wind turbulence in frequency range can excite the structural response, so the effective turbulence analysis technique based the POD method is one to study the effective turbulence influence on the bridge buffeting response. In this part of the study, the cable stayed bridge buffeting response analysis based on the POD method will be performed. The influence of the effective turbulence mode, aerodynamic admittance and self-excited force on the bridge response will be investigated.

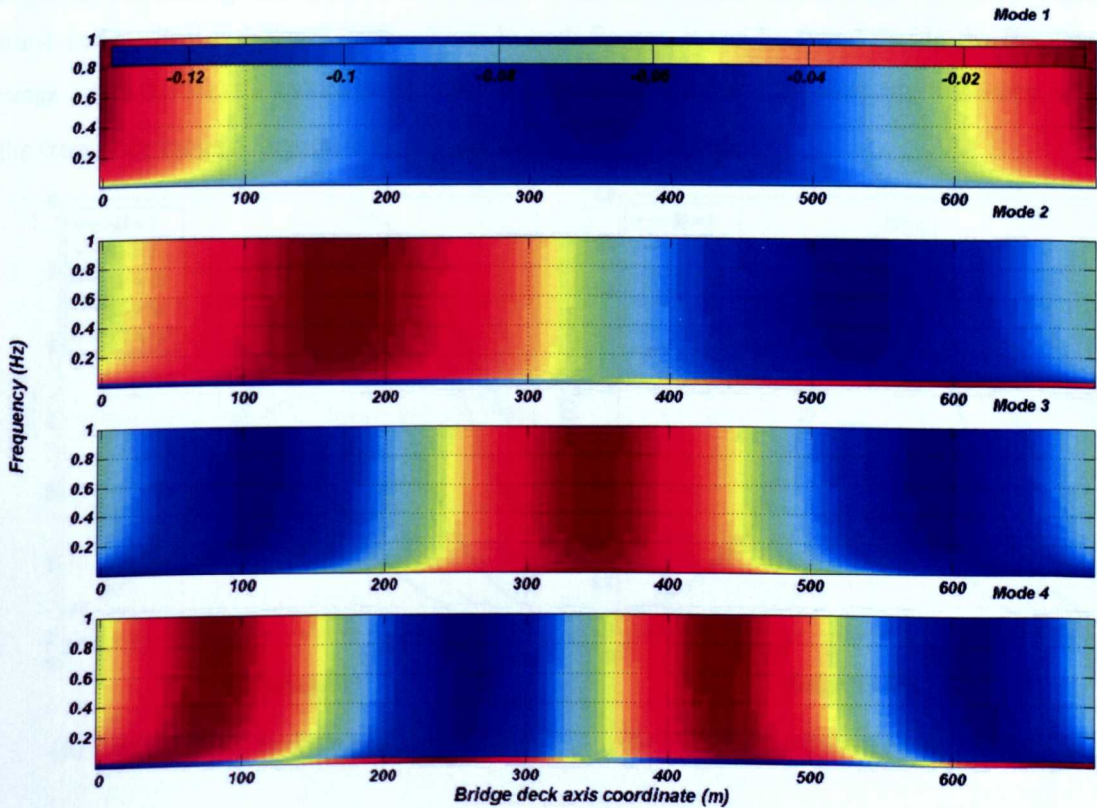
4.5.3.1 Effective Turbulence Investigation Based on POD Method

Before discussing the bridge buffeting response, it is very important to study the effective turbulence spectrum based on POD decomposition method. Fig.4.5.5 shows the first four eigenvalues and eigenvectors of the power spectrum density matrix (PSDM) of the longitudinal and vertical turbulence components. From Fig.4.5.5 (a) and Fig.4.5.5 (b) it can be found that the first eigenvalue is much larger than the higher ones in the low frequency range, with the frequency increasing, all the eigenvalues tend to be the same value.

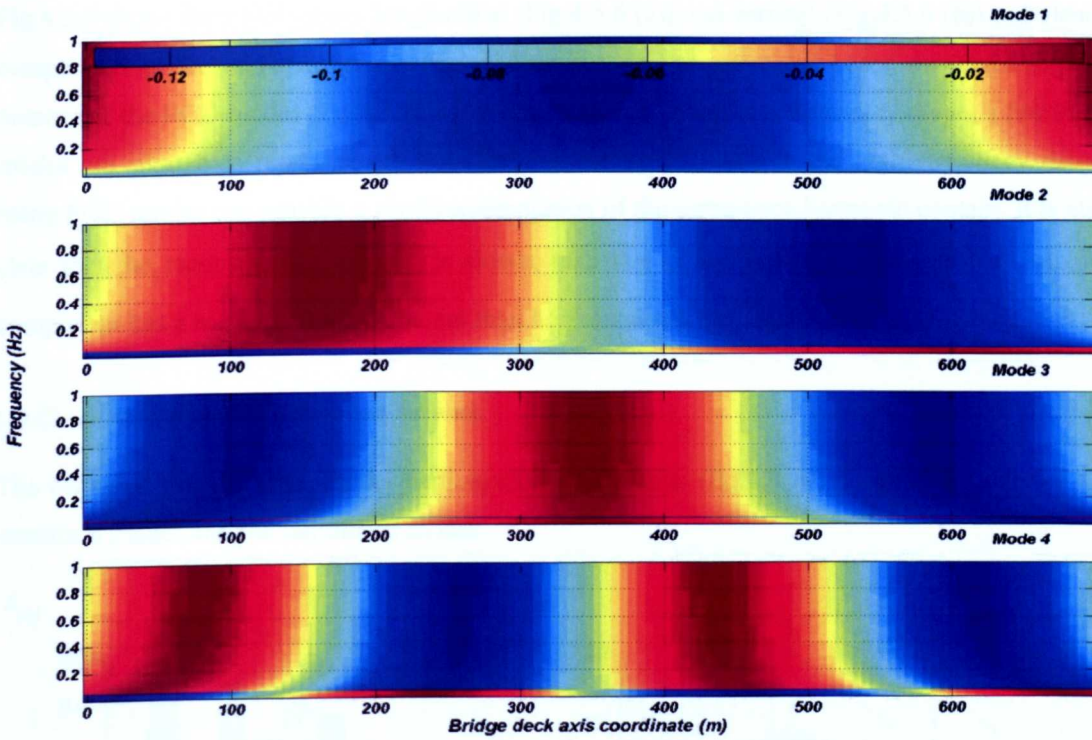


(a) Longitudinal spectral eigenvalues

(b) Vertical spectral eigenvalues



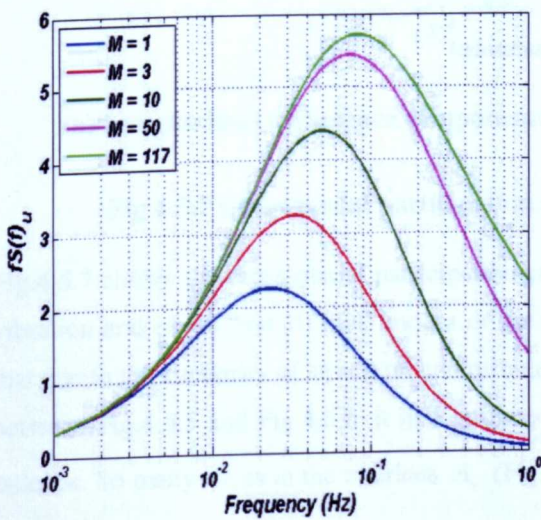
(c) Eigenvectors contour of the longitudinal turbulence component



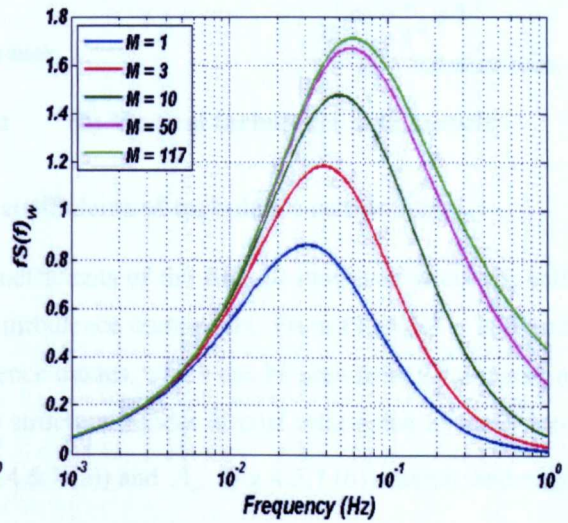
(d) Eigenvectors contour of the vertical turbulence component

Fig 4.5.5 Spectral eigenvalues and eigenvectors of the turbulence components

Fig.4.5.5 (c) and Fig.4.5.5 (d) plot the contour of first four corresponding eigenvectors of longitudinal and vertical turbulence components. In both figures, it can be found that in the frequency range ($f > 0.3$ Hz) the modes do not exhibit relevant variations on the changing frequency, when the frequency range is beyond 0.3 Hz, their shapes tend to change.



(a) Longitudinal turbulence component



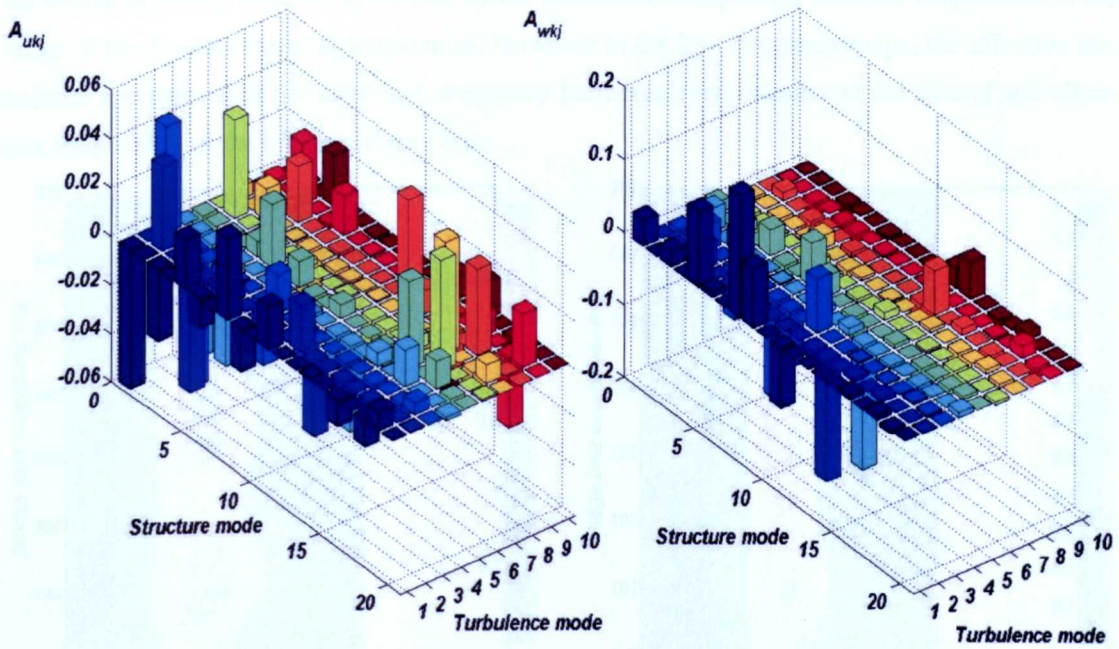
(b) Vertical turbulence component

Fig 4.5.6 Modal truncation on the PSDF of the turbulence components at the mid-span of the bridge deck

Fig.4.5.6 shows the PSDF of the longitudinal (Fig.4.5.6 (a)) and vertical (Fig.4.5.6 (b)) turbulence components at the mid-span of the bridge deck system, reconstructed based on increasing the number of the POD modes (Eq.2.3.26). It is apparent that, in the low frequency range, a few POD modes are enough to represent the turbulence components, while in the high frequency range, many POD modes can provide a good representation of the turbulence harmonic content. It is also clear that the reconstruction of $w(t)$ is slower than that of $u(t)$, because the vertical velocity component has a higher harmonic content than horizontal velocity component $u(t)$.

(I) Cross-modal participation coefficients

The evaluation of the cross-modal participation coefficients (Eq.2.3.29) needs to be clear of the structural modes and the turbulence modes.



(a) Longitudinal turbulence components (b) Vertical turbulence components

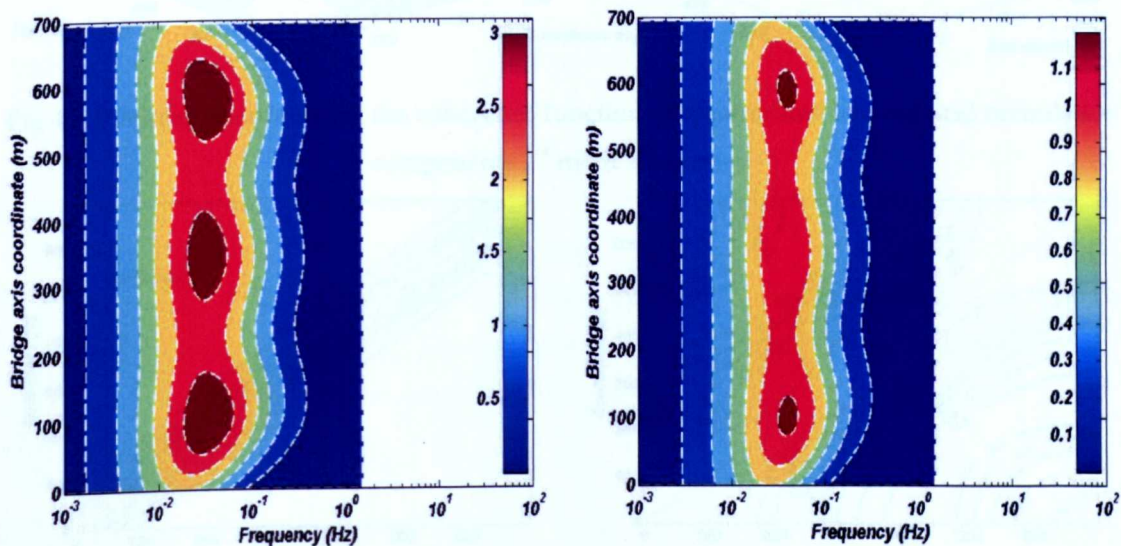
Fig 4.5.7 Cross-modal participation coefficients of turbulence components

Fig.4.5.7 shows the cross-modal participation coefficients of the first 20 modes of structural self vibration and of the first 10 POD modes of the turbulence component. From Fig.4.5.7 it is found that due to the similarity of structural and turbulence modes, which can be seen from a comparison between Fig.4.5.5 and Fig.4.5.6, it makes many structural modes almost orthogonal to many turbulence. So many terms in the matrices A_u (Fig.4.5.7 (a)) and A_w (Fig.4.5.7 (b)) vanish, and only a few turbulence modes excite a few structural modes. Especially for the matrix A_w there are many items vanishing. Only the first 5 modes of the vertical turbulence excited the bridge, except for the 8th and 10th mode which excites the structural 13th mode. However for the matrix A_u , the

longitudinal turbulence modes excite different structural modes, the contribution on the structural mode is clear.

(2) *Effective turbulence*

As described above, the effective turbulence can be described as that part of the actual turbulence exciting the structural response. Here the turbulence field can be reconstructed with only the necessary POD modes, $M = 10$ modes in this case. The spectral properties of the effective turbulence can be estimated by Eq.2.3.27. Fig.4.5.8 (a) and (b) respectively shows the PSDF of the longitudinal and vertical effective turbulence along the whole length of the bridge. It is clear that the harmonic content of the effective turbulence is concentrated in the low frequency range ($n < 0.3$ Hz for the longitudinal turbulence, $n < 0.5$ Hz for the vertical turbulence). It can be understood that the bridge buffeting response is excited by the turbulence components with the frequencies in the range of the lowest structural frequencies. However in the low frequency range, the effective turbulence spectrum does not have high frequency harmonic components and the natural self vibration frequencies of the bridge are very low.



(a) Longitudinal turbulence component

(b) Vertical turbulence component

Fig 4.5.8 Spectral content of effective turbulence

Fig.4.5.9 shows a 3-D coherence function comparison between the actual (a) and effective (b) longitudinal turbulence components. Fig.4.5.10 shows the same comparison based on the contour-plots. It is clear that, the coherence function of the actual turbulence decreases quickly with increasing distance $|y - y'|$ reaching zero close to the main diagonal (where $y = y'$), the coherence function of the effective turbulence keeps a unit value in a broad band around $y = y'$, and tends to be zero only far from the main diagonal. To the vertical turbulence component, the same situation occurs.

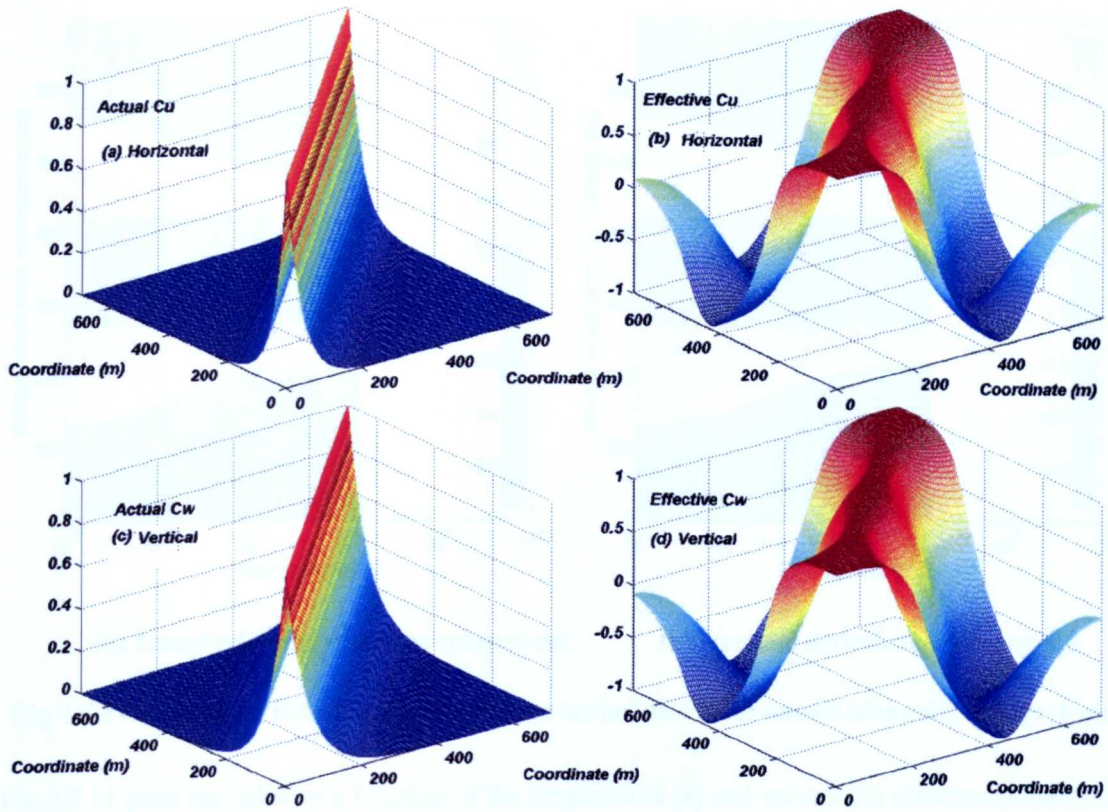


Fig 4.5.9 3D representation of the coherence function of longitudinal and vertical turbulence components 1st mode frequency

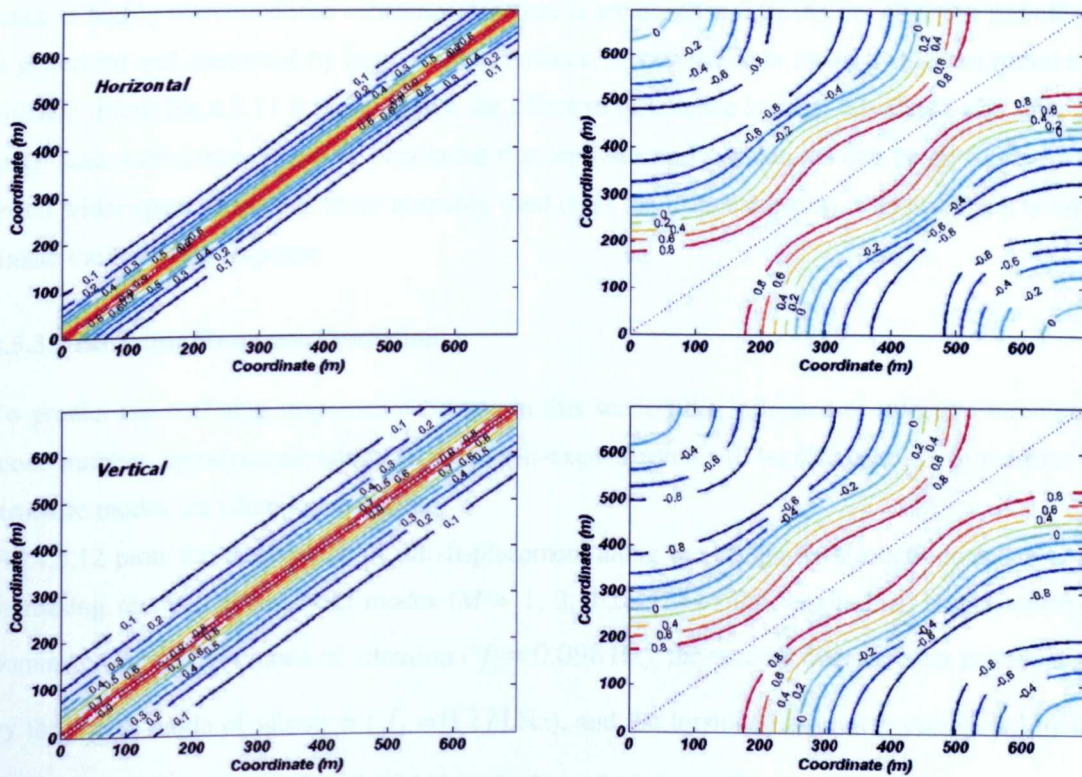
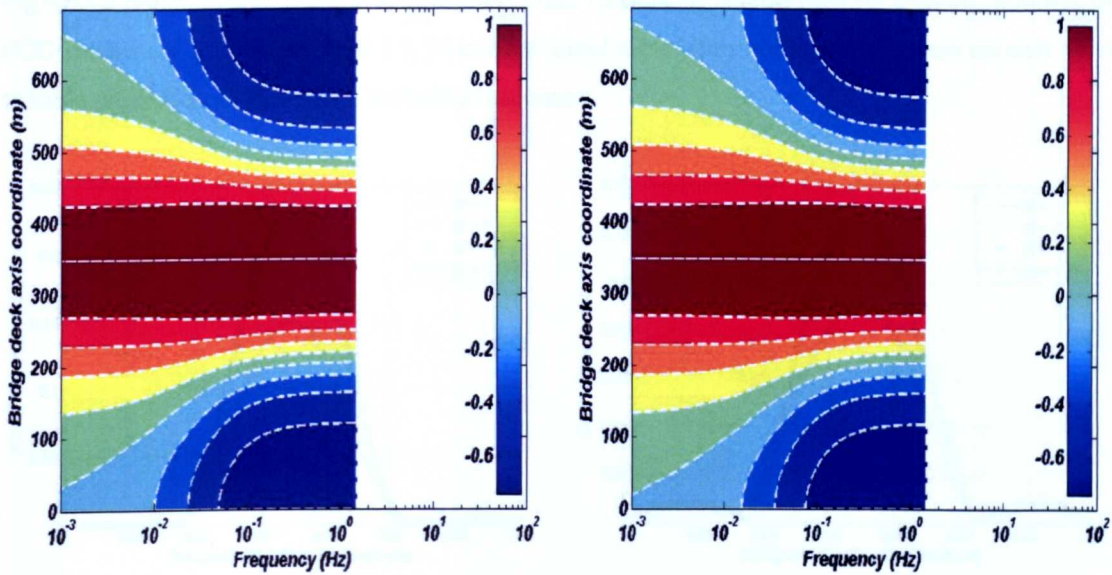


Fig 4.5.10 Coherence function of the actual and effective longitudinal and vertical turbulence components at 1st mode frequency



(a) Longitudinal turbulence component

(b) Vertical turbulence component

Fig 4.5.11 Coherence function of the effective turbulence components along the bridge deck

Fig.4.5.11 plots the coherence function of the longitudinal (a) and vertical (b) effective turbulence components with the variation of frequency along the bridge deck coordinate. At the location of the mid-span of the bridge deck, it is apparent that in a wide frequency range the effective turbulence is highly correlated (the coherence function is greater than 0.8). As the effective turbulence is generated and controlled by large scale turbulence, its coherence is stronger than the actual turbulence. From Fig.4.5.11 it is found that the effective turbulence is more correlated also than the large scale turbulence. It can be concluded that analyses and simulations can be performed with much wider space steps than those normally used (here the distance is 6m), which will not overestimate the buffeting response.

4.5.3.2 Buffeting Response Prediction

To predict the buffeting response of bridge, in this section the influence of effective turbulence mode number, aerodynamic admittance and self-excited force will be discussed. Here the first 10 structure modes are taken into account.

Fig.4.5.12 plots the RMS value of the displacement along the bridge deck length considering an increasing number of the POD modes ($M = 1, 3, 10, 117$) of the longitudinal displacement is dominated by the first mode of vibration ($f_1 = 0.098$ Hz), the vertical displacement is dominated by the fourth mode of vibration ($f_4 = 0.271$ Hz), and the torsional rotation is dominated by the ninth mode of vibration ($f_9 = 0.514$ Hz). In Fig.4.5.12 the self-excited force and aerodynamic admittance are not considered.

Fig.4.5.12 indicates that even if the turbulent field can not be represented by a small numbers of POD modes ($M = 1, 3$) in Fig.4.5.5, in current simulation 10 turbulence modes are enough for a suitable prediction of the bridge buffeting response.

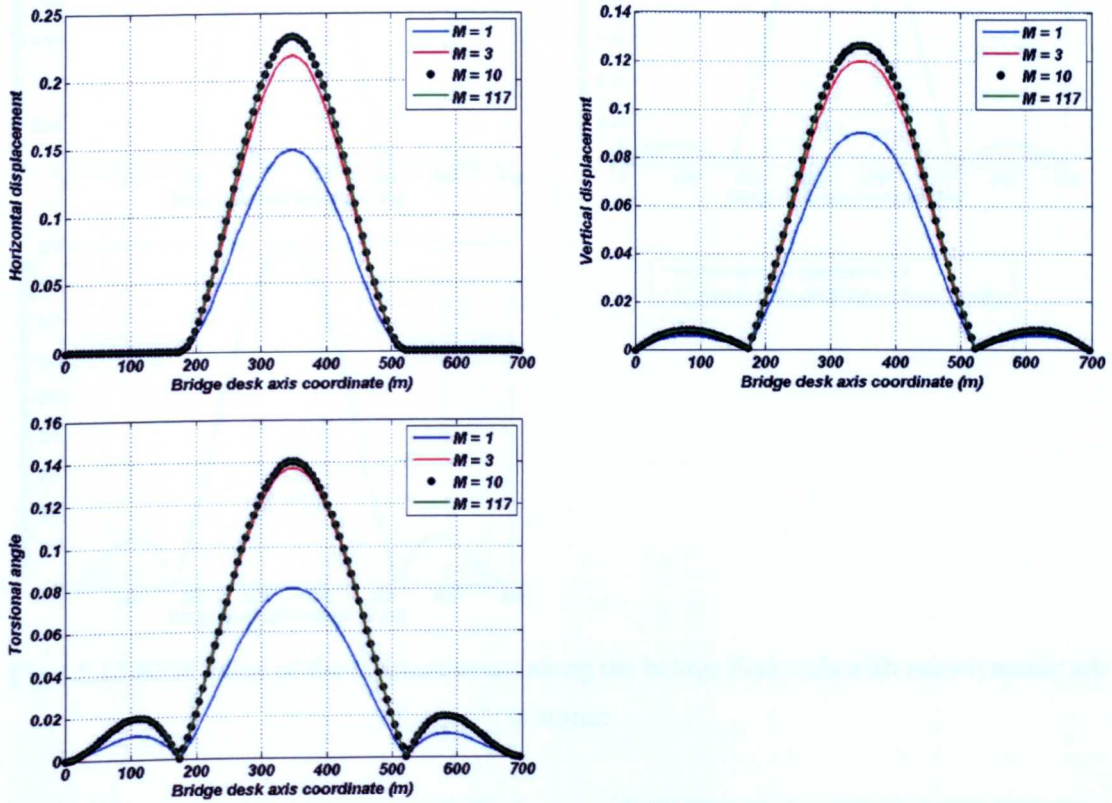


Fig 4.5.12 RMS value of the displacements along the bridge deck axis without self-excited force and aerodynamic admittance

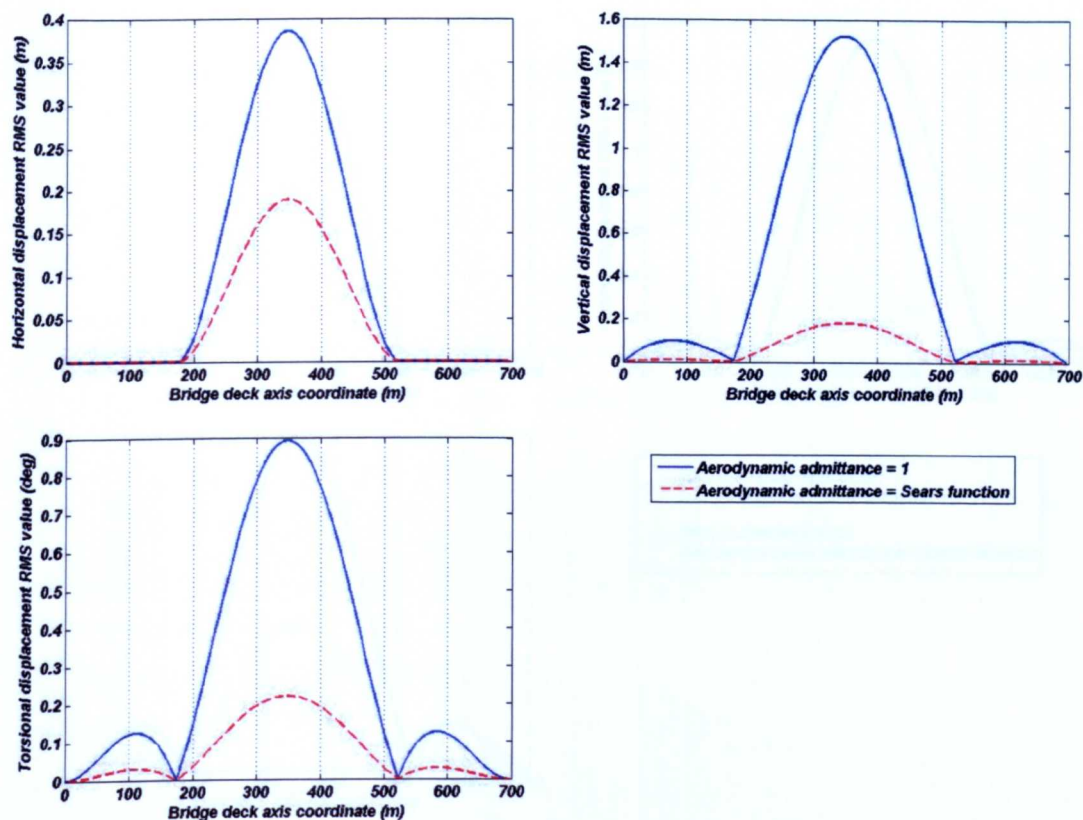


Fig 4.5.13 RMS value of the displacements along the bridge deck axis with aerodynamic admittance

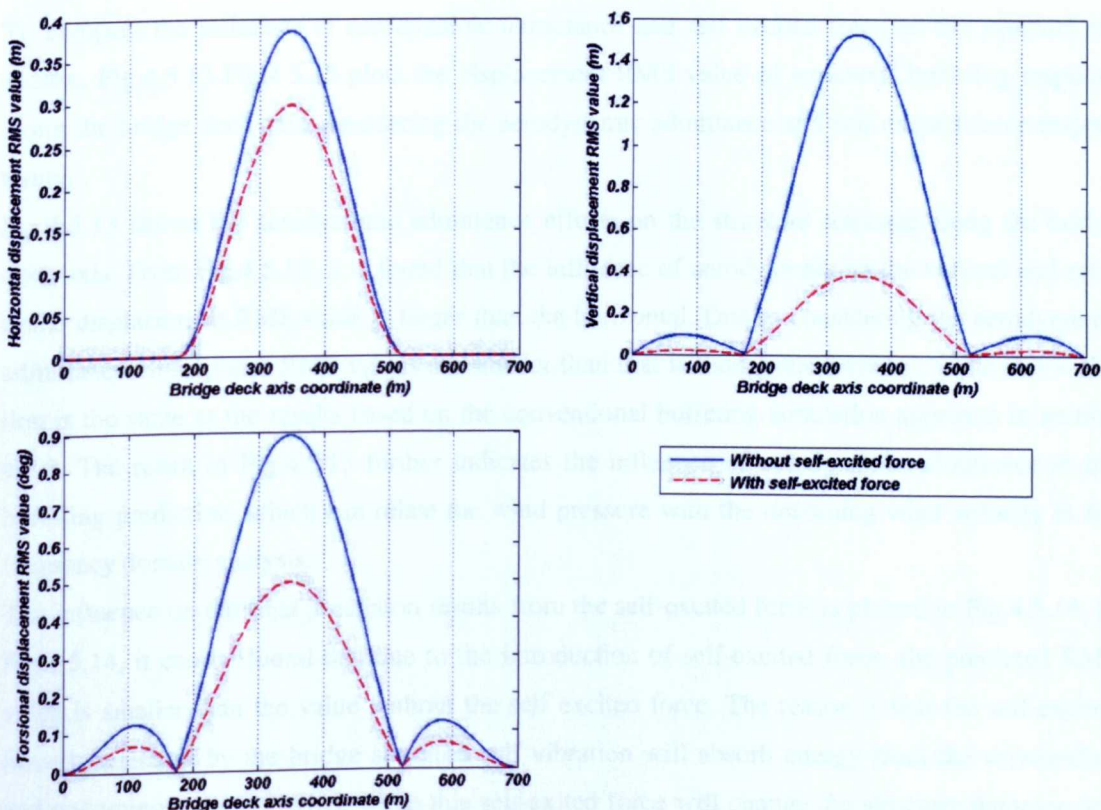


Fig 4.5.14 RMS value of the displacements along the bridge deck axis with self-excited force

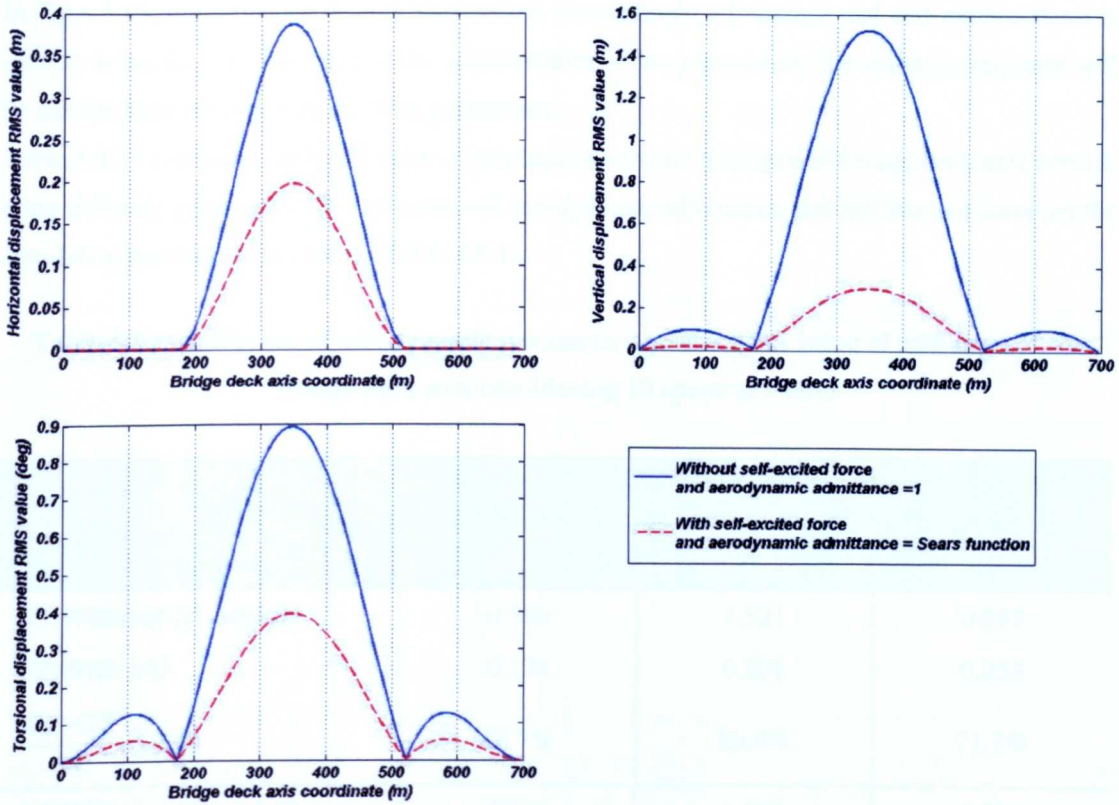


Fig 4.5.15 RMS value of the displacements along the bridge deck axis with aerodynamic admittance and self excited force

To compare the influence of aerodynamic admittance and self excited force on the structure response. Fig.4.5.13-Fig.4.5.15 plots the displacement RMS value of structural buffeting response along the bridge deck axis considering the aerodynamic admittance and self excited force respectively.

Fig.4.5.13 shows the aerodynamic admittance effects on the structure response along the bridge deck axis. From Fig.4.5.13, it is found that the influence of aerodynamic on the vertical and rotational displacement RMS value is larger than the horizontal. Due to considering the aerodynamic admittance all response RMS values are smaller than that without considering it, while this variation is the same as the results based on the conventional buffeting simulation approach in section 4.5.2. The result in Fig.4.5.13 further indicates the influence of aerodynamic admittance in the buffeting prediction, which can relate the wind pressure with the oncoming wind velocity in the frequency domain analysis.

The influence on the final prediction results from the self-excited force is plotted in Fig.4.5.14. In Fig.4.5.14, it can be found that due to the introduction of self-excited force, the predicted RMS value is smaller than the value without the self excited force. The reason is that the self-excited forced generated by the bridge structure self vibration will absorb energy from the surrounding and oncoming turbulent wind, while this self-excited force will change the structure damping and stiffness, it is the same as the founding in section 4.5.2.

In Fig.4.5.15, the influence of both parameters: aerodynamic admittance and self-excited force is plotted. It can be found that due to the consideration of two parameters, the structure response will be smaller than the case without both parameters.

Table.4.5.11 compares the RMS value of displacement at the mid-span of bridge deck axis considering different parameters. The influence of aerodynamic admittance and self-excited force on the simulation results is very clear in Table.4.5.11.

Table 4.5.11 Influence of aerodynamic parameters on the RMS value of mid-span of the bridge deck axis considering 10 spectral modes

Conditions \ Displacement	Horizontal (m)	Vertical (m)	Torsional (deg)
C1: Without (A and S)	0.386	1.521	0.893
C2: With (A)	0.198	0.201	0.253
$\frac{ C2 - C1 }{C1} \times 100\%$	48.7%	86.8%	71.7%
C1: Without (A and S)	0.386	1.521	0.893
C2: With (S)	0.298	0.379	0.498
$\frac{ C2 - C1 }{C1} \times 100\%$	22.8%	75.1%	44.2%
C1: Without (A and S)	0.386	1.521	0.893
C2: With (A and S)	0.197	0.296	0.395
$\frac{ C2 - C1 }{C1} \times 100\%$	48.9%	80.5%	55.8%

Index: A: aerodynamic admittance, S: Self-excited force

From the above discussion of results in figures and table, it is found that the structural response variation from current buffeting prediction based on POD method agree with the conventional buffeting simulation method.

4.6 Conclusions

In this chapter, a case study based on the multimode aeroelastic coupling method and POD method is presented. In the above analysis, parameters such as aerodynamic admittance, aeroelastic coupling and effective turbulence and their influence on the buffeting response has been discussed. The following conclusions can be drawn from the above discussions.

(1) Based on the discussions about the aerodynamic admittance and self excited force, when performing the bridge buffeting response analysis, the self-excited force and aerodynamic admittance

will influence the final analysis results clearly. The self excited force will change the structural damping and stiffness. In the conventional method flutter analysis and buffeting analysis are resolved individually, neglecting the flutter response influence on the buffeting response, especially at the critical wind velocity condition. This method may be suitable for the short-span bridge, however for the long-span bridge, the dynamic characteristics are very complex, so aerodynamic coupling should be considered.

(2) The conventional mode combination method (SRSS) neglects coupling effects to simplify the computation, while the multiple modes coupling technique - CQC can consider the coupling between different modes. The CQC method should be proposed in the future buffeting response analysis of large span bridge, in which due to the low structural damping, more flexible and nonlinear, the mode coupling effect will be clearer.

(3) POD method can be used to study the bridge structure's gust wind response analysis and investigate the relationship between the effective turbulence contributing to the bridge structure response. Based on the POD method, it can be found that only a few turbulence modes which can excite the bridge lower modes induced by the gust wind, in the buffeting response prediction based on POD approach, small numbers of POD modes are enough to represent the bridge buffeting response, the higher turbulence modes are almost orthogonal to the structural modes.

Chap 5 Inlet Turbulence Generation Technique Based On ARMA Model

5.1 Introduction

In chapter 3, one of the difficulties or unresolved problems in current CFD simulation is the simulation of unsteady inlet boundary condition. Generally to simplify the simulations the inlet velocity is assumed to be steady in general CFD simulations of civil engineering structures, which ignores the influence of turbulence from the upwind direction and influences the unsteady characteristics of flow. However the unsteady inlet boundary condition is very important for the bridge buffeting simulation based on CFD technique. To overcome this problem, the time varying inflow turbulence generation algorithm based on ARMA model is presented in this chapter. The time history data of velocity components generated by ARMA model with the turbulence intensity (5%) is validated firstly in an empty domain.

5.2 Inlet Turbulence Generation Techniques

5.2.1 Discussions on the Generation Techniques

As described in chapter 2, the power spectra or time history data of velocity components are important for the bridge buffeting response simulation in the frequency and time domain. In CFD simulations, the generation approach of velocity fluctuations for an inflow boundary condition (inflow turbulence) of LES with prescribed spatial correlation and turbulence intensity is one of the most important unresolved issues in CFD research as discussed in chapter 3. The instantaneous streamwise velocity component $u_m(x, y, z, t)$ at any space point m can be described as the sum of a mean part $\bar{u}_m(x, y, z, t)$ and a random part $u'_m(x, y, z, t)$. (x, y, z : the coordinate of spatial points). However the generation of the random part is a problem when realizing the inflow turbulence. In CFD field, based on the generation procedure, the inflow turbulence simulation technique can be divided into the statistical reconstruction and deterministic reconstruction, while the statistical reconstruction method has been discussed roughly in chapter 2. In this section the procedure of realizing these two methods suitable for CFD is presented.

(1) Deterministic Inflow Turbulence Generation Technique

It is simple for this method to define the inflow boundary condition, which can generate the inflow boundary from the separate part called the precursor or auxiliary computational part (Fig.5.2.1). This method is adopted by Friedrich and Arnal (1990) to investigate the backward-facing step flow. In this auxiliary simulation domain the flow is also spatially developed and has its own inflow conditions. After extracting the sample inflow data, the velocity profile at the inflow boundary is rescaled and re-introduced at the inlet based on the law of the wall or defect law, assuming the spatial development of a boundary layer on a smooth surface (Tamura, 2008). When the fluctuating part is calculated based on the RANS model, it neglects the turbulent fluctuations entirely

and uses the ensemble-averaged mean profiles from the RANS computations. This means that the incoming flow is steady in a sense that the velocity does not fluctuate with the time, which is known as the quasi-laminar method. An example case is the pipe flow velocity profile. Since the inflow condition is provided by a coupled, upstream, unsteady RANS simulation, an advantage of this method is that the inlet conditions can be easily realised. When the initial computation of the auxiliary part turbulence field is calculated with a LES, based on the sample plane grid at the auxiliary computational domain (Fig.5.2.1), the turbulent flow data is stored in a time series of velocity fluctuations as the inflow boundary conditions. This method requires a large computational load. However this technique is hardly practical for the general cases, especially for those with high Reynolds numbers, because it requires generating the entire flow history data and very high computational cost. At the same time, due to the auxiliary computational domain (Fig.5.2.1) being calculated separately, there is no feedback between the main simulation domain and the auxiliary part. This can become problematic and is known as one way coupling. This inflow turbulence generation technique is only suitable for the small domain calculation.

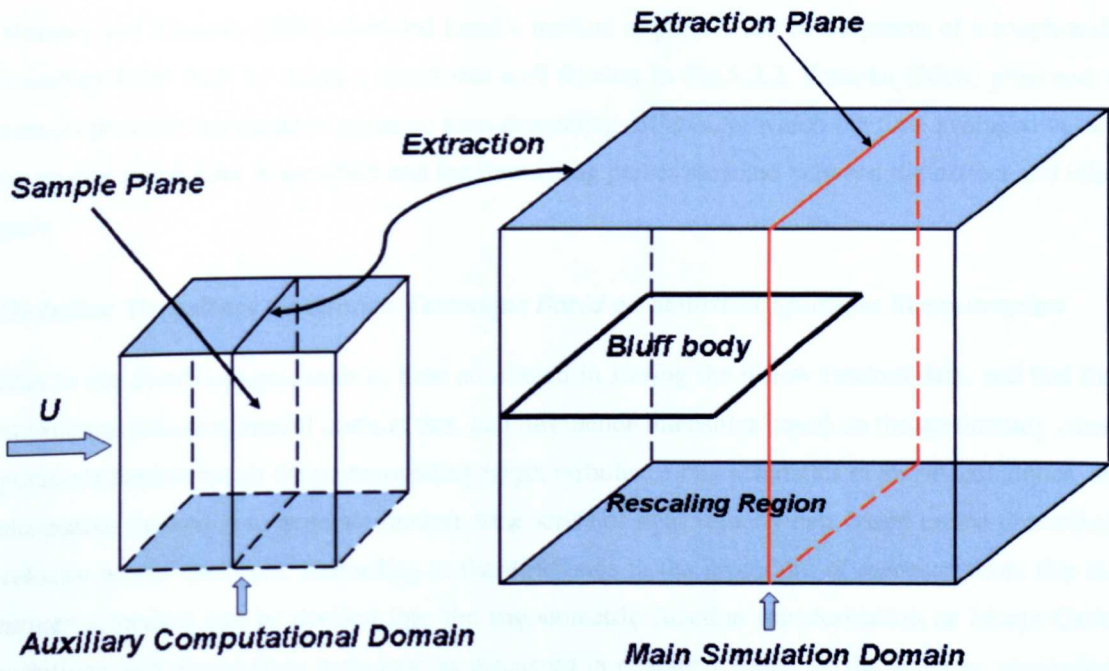


Fig 5.2.1 Schematic figure of deterministic inlet turbulence generation technique

To overcome the above problems, Lund *et al.* (1998) described another rescaling technique to generate 3D time dependent inflow data for simulating complex spatially developed boundary layers, in which the instantaneous velocity data is extracted from the extraction plane (Fig.5.2.1) in the main simulation domain without any precursor plane, which can consider the intercorrelation and feedback in the computational domain.

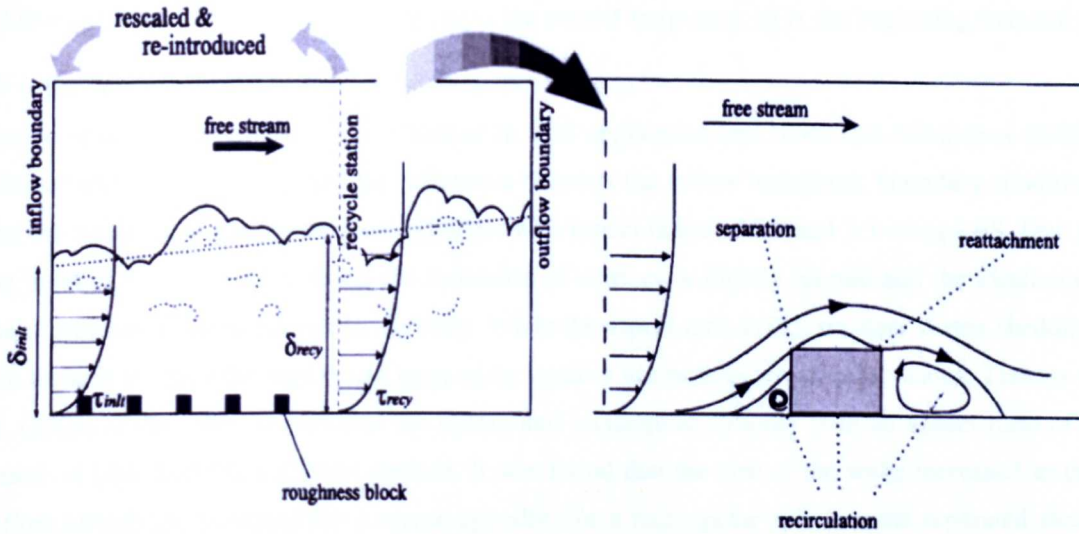


Fig 5.2.2 Schematic presentation of computation based on Nozawa and Tamura method

(Nozawa and Tamura, 2002)

Nozawa and Tamura (2002) extended Lund's method to predict the development of a rough-wall boundary-layer flow by using a roughness-wall friction in Fig.5.2.2. Kataoka (2008) proposed a pseudo-periodic technique to generate time-depending inflows, in which the time averaged velocity profile at the inlet is specified and the fluctuating part is recycled between the extract and inlet parts

(2) Inflow Turbulence Generation Technique Based on Statistical Spectrum Reconstruction

Due to the disadvantages, such as time consumed in storing the inflow random data, and that the turbulence statistics, spatial correlations, and turbulence intensities based on the preliminary computations cannot match the corresponding target turbulence characteristics in above techniques, an alternative method is to generate random time series of inlet velocity data based on the prescribed velocity power spectrum. According to the difference in the procedure of reconstruction, this alternative method can be divided into the trigonometric function transformation or Monte Carlo technique and digital filter technique as discussed in chapter 2 based on the different realization process. For the trigonometric technique, firstly the target energy power and cross power spectrum of oncoming flow turbulence is specified. This is followed by decomposing the cross power spectrum, and adopting a linear combination of trigonometric functions with random amplitudes and phase angles based on the Monte-Carlo method to obtain time varying series at m spatial points and random processes $u_i(t)$ $i = 1, 2, \dots, m$, (t is the time step) which can be expressed as:

$$u_i(t) = \sum_{p=1}^i \sum_{k=1}^N \left[a_{ip}(k) \cos \{ \omega_k t - \alpha_{ip}(k) \} + b_{ip}(k) \sin \{ \omega_k t - \alpha_{ip}(k) \} \right] \quad (5.2.1)$$

Where $i = 1, 2, \dots, m$, $a_{ip}(k)$ and $b_{ip}(k)$ are the Gaussian variables, $\omega_k = \omega_l + (k - 0.5) \Delta \omega$,

, $\Delta\omega = (\omega_u - \omega_l) / N$, $k = 1, 2, \dots, N$, ω_u is the cut-off frequency, ω_l is the beginning frequency, N is the number of subdivisions of the frequency domain.

Kondo *et al* (1997) proposed this technique in LES application and Noda and Nakayama (2003) adopted this method to compare the difference between the inflow turbulence boundary condition and the steady flow past rectangular cylinders with aspect ratios of 1.0 and 2.5 using LES. Due to the input of the inflow turbulence, the formation of vortices is slightly blurred and the location of their formation is shifted closer to the body. While the aspect ratio is 2.5, no clear vortex shedding can be seen in the wake region and large scale vortices are broken into smaller scales. Tamura *et al.* (2003) studied the flow around the square and rectangular cylinder with an aspect ratio of 2 based on LES with the statistical method. It was found that the size of the wake increased as the inflow turbulence increased for a square cylinder, for a rectangular cylinder, the separated shear layer is close to the leeward corner and reattaches to it at high inflow turbulence. Thus, a weak vortex is formed at the back of the cylinder. For both sections, turbulence reduces drag on the cylinders, but the physical mechanisms are different. Tamura (2008) stated that an oncoming flow of turbulence would change the separated shear layer and vortex formation around a prism.

Besides Kondo *et al.*(1997) and Noda and Nakayama (2003), Glaze and Frankel (2003), de With and Holdo (2005) presented a method similar to the method proposed by Kondo *et al.* (1997) called Weighted Amplitude Wave Superposition (WAWS) to simplify the generation procedure, in which only single type trigonometric function (cosine function) combination is considered.

$$u_i(t) = \sum_{p=1}^i \sum_{k=1}^N \left[H_{ip} \sqrt{2\Delta f} \cos \left[2\pi f_k^* t + \theta_{ip}(f_k) + \varepsilon_{pk} \right] \right] \quad (5.2.2)$$

Where $\Delta f = \Delta\omega / 2\pi$, $f_k^* = \omega_k / 2\pi = (\omega_l + (k - 0.5)\Delta\omega) / 2\pi$, H_{ip} is a lower triangular matrix which can be obtained from the Cholesky decomposition of multidimensional PSD matrix. Chen *et al.* (2008) also adopted above Eq.5.2.2 to generate random waves to investigate the numerical model of a round jet. Lee *et al.* (1992), Stanley *et al.* (2000) considered the velocity components cross-correlation proposed by Lund *et al.* (1998). Smirnov *et al.* (2001) also proposed a similar method based on the same correlation function as that, however the anisotropic inhomogeneous flow is simulated.

However, the above proposed WAWS technique based on Monte Carlo method needs much computational resource when generating the velocity components time history data of the space correlation points. To overcome this restriction, an alternative method known as the digital filtering technique, is proposed, which has been widely used in the generation of wind field velocity time history data. Klein *et al.* (2003) proposed the inflow turbulence generation technique based on the digital filter for LES, however this method is only suitable for single point velocity generation and only two important parameters, such as the cross-correlation and integral length, are considered in the simulation. For the random wind velocity's 3D simulation the spatially correlated inflow tur-

bulence with prescribed velocity PSD is required. In the following sections, the artificial inflow turbulence generation technique based on ARMA model is presented.

5.2.2 Wind Velocity Simulation Process Based on ARMA Model

(1) Multidimensional Velocity Components PSD Model Construction

Since the wind velocity is a spatial variation variable, the field can be constructed as a ‘multivariate multidimensional random variable’. The power spectral density (PSD) matrix of velocity components at the spatial point is a multidimensional one, which can be assumed as the form:

$$\langle S(\omega) \rangle_{N_p \times N_p} = \begin{pmatrix} S_{11}(\omega) & S_{12}(\omega) & \cdots & S_{1N_p}(\omega) \\ S_{21}(\omega) & S_{22}(\omega) & \cdots & S_{2N_p}(\omega) \\ \vdots & \vdots & \cdots & \vdots \\ S_{N_p1}(\omega) & S_{N_p2}(\omega) & \cdots & S_{N_pN_p}(\omega) \end{pmatrix}_{N_p \times N_p} \quad (5.2.3)$$

Where N_p is the number of the points, the item $S_{ij}(\omega)$ in multidimensional matrix (Eq.5.2.2) has a quite ‘classical’ expression proposed by Simiu and Scanlan (1996) as the following function:

Cross-spectrum:

$$S_{ij}(\omega) = \sqrt{S_{ii}(\omega)S_{jj}(\omega)} \text{coh}_{ij}(\omega) e^{-\omega\theta_{ij}} \quad (5.2.4)$$

In Eq.5.2.4 the classical coherence function discussed before is adopted:

Coherence:

$$\text{coh}_{ij}(x_i, y_i, z_i; x_j, y_j, z_j; \omega) = \exp\left(-\frac{\omega \sqrt{c_x^2(x_i - x_j)^2 + c_y^2(y_i - y_j)^2 + c_z^2(z_i - z_j)^2}}{2\pi \bar{u}(z_k)}\right) \quad (5.2.5)$$

Where $\bar{u}(z_k) = (\bar{u}(z_i) + \bar{u}(z_j)) / 2$ is the mean wind velocity between two points i and j , here the average wind speeds are $\bar{u}(z_i)$ and $\bar{u}(z_j)$, $\theta_{ij} = x_i / \bar{u}(z_i) - x_j / \bar{u}(z_j)$ is the time lag (where it is assumed that wind direction coincides with x) and c_x, c_y, c_z are the decay coefficients of x, y and z direction, here $c_x = 8, c_y = 6$ and $c_z = 6$.

(2) Random Velocity Generation Procedure Based on ARMA Model

The multivariate random process $\{u(t)\}_{N_p \times 1}$ based AR or ARMA model can be expressed as:

$$\{u(t)\}_{N_p \times 1} = \sum_1^p [\varphi(i)]_{N_p \times N_p} \{u(t-i\Delta t)\}_{N_p \times 1} + \sum_1^q [B(i)]_{N_p \times N_p} \{a(t-i\Delta t)\}_{N_p \times 1} \quad (5.2.6)$$

Where index 'p' refers to the order of AR in the model, while 'q' is the order of the moving average (MA) component, $[\varphi(i)]_{N_p \times N_p}$ and $[B(i)]_{N_p \times N_p}$ are the ARMA or AR model coefficient matrix, $\{a(t-i\Delta t)\}_{N_p \times 1}$ is Gaussian random white noise. Eq.5.2.6 can also be rewritten as:

$$\{u_r\} = \begin{bmatrix} [B_1] \cdots [B_i] [\varphi_1] \cdots [\varphi_q] \end{bmatrix} \begin{bmatrix} \{a_{r-1}\} \\ \vdots \\ \{a_{r-q}\} \\ \{u_{r-1}\} \\ \vdots \\ \{u_{r-p}\} \end{bmatrix} + [B_0] \{a_r\} \quad (5.2.7)$$

The items in Eq.5.2.7 can be expressed as $\{a_{r-i}\} = \{a(t-i\Delta t)\}_{N_p \times 1}$, $\{u_{r-i}\} = \{u(t-i\Delta t)\}_{N_p \times 1}$ and $\{B_i\} = \{B(-i\Delta t)\}_{N_p \times N_p} \cdot \{a(t-i\Delta t)\}_{N_p \times 1} = WN(0, \sigma)$ is the white noise signal with 0 and σ as average and standard deviation, $\{u(t-i\Delta t)\}_{N_p \times 1}$ is the vector velocities at the different point of the field. According to the Wiener-Khinchine transformation, the correlation and PSD has the following relationship:

$$R_{u_{ij}}(\tau) = \frac{1}{2\pi} \int_0^\infty S_{ij}(\omega) \cos(\omega(\tau - \theta_{ij})) d\omega \quad (5.2.8)$$

Clearly from Eq.5.2.8, given the symmetry of matrix S , it follows:

$$R_{u_{ij}}(\tau) = R_{u_{ji}}(-\tau) \rightarrow R_{uu}(\tau) = R_{uu}'(-\tau) \quad (5.2.9)$$

Eq.5.2.7 can be rewritten as the following form to calculate the ARMA coefficient:

$$\begin{bmatrix} [I] & [b] \\ [b^T] & [c] \end{bmatrix} \begin{bmatrix} [\bar{B}] \\ [\bar{\varphi}] \end{bmatrix} = \begin{bmatrix} [f] \\ [g] \end{bmatrix} \quad (5.2.10)$$

Where

$$[\bar{\varphi}] = [\varphi_1 \quad \cdots \quad \varphi_p], [\bar{B}] = [B_1 \quad \cdots \quad B_q],$$

$$[f] = \left[[R_{uu}(-1)]^T \quad \cdots \quad [R_{uu}(-q)]^T \right]^T$$

$$[g] = \left[[R_{uu}(-1)]^T \quad \cdots \quad [R_{uu}(-q)]^T \right]^T$$

$$[c] = \begin{bmatrix} R_{uu}(0)^T & \cdots & R_{uu}(q-1) & \cdots & R_{uu}(p-1) \\ \vdots & \ddots & \vdots & & \vdots \\ R_{uu}(1-q)^T & \cdots & R_{uu}(0)^T & \cdots & R_{uu}(p-q) \\ \vdots & & \vdots & \ddots & \vdots \\ R_{uu}(1-p)^T & \cdots & R_{uu}(p-q)^T & \cdots & R_{uu}(0)^T \end{bmatrix}, [I] = \begin{bmatrix} [I] & \cdots & [0] \\ \vdots & \ddots & \vdots \\ [0] & \cdots & [I] \end{bmatrix}$$

$$[b] = \begin{bmatrix} [R_{uu}(0)]^T & \cdots & [0] & \cdots & [0] \\ \vdots & \ddots & \vdots & \ddots & \vdots \\ [R_{uu}(1-q)]^T & \cdots & [R_{uu}(0)]^T & \cdots & [0] \end{bmatrix}$$

The coefficient's matrices are determined $[\bar{\varphi}]$ can be calculated according to Eq.5.2.11

$$\begin{bmatrix} [R_{uu}(0)]^T & [R_{uu}(1)]^T & \cdots & [R_{uu}(p-1)]^T \\ [R_{uu}(-1)]^T & [R_{uu}(0)]^T & \cdots & [R_{uu}(p-2)]^T \\ \vdots & \vdots & & \vdots \\ [R_{uu}(1-p)]^T & [R_{uu}(2-p)]^T & \cdots & [R_{uu}(0)]^T \end{bmatrix} \begin{bmatrix} [\varphi_1]^T \\ [\varphi_2]^T \\ \vdots \\ [\varphi_p]^T \end{bmatrix} = \begin{bmatrix} [R_{uu}(-1)]^T \\ [R_{uu}(-2)]^T \\ \vdots \\ [R_{uu}(-p)]^T \end{bmatrix} \quad (5.2.11)$$

After the coefficient's matrices $[\bar{\varphi}]$ is calculated, it is possible to estimate matrix $[B_0]$ based on Eq.5.2.12

$$[B_0][R_{uu}(0)] = [R_{uu}(0)] - \sum_{i=1}^p [\varphi(i)][R_{uu}(-i)]^T \quad (5.2.12)$$

Taking $[B_0] = [R_{uu}(0)]^T$ and assuming $[B_0]$ to be lower triangular it is possible to obtain it from Eq.5.2.12 through a Cholesky's decomposition. From the matrix $[B_0]$ the coefficient matrix $[c]$ can be estimated from the following equations:

$$\begin{aligned} [R_{uu}(0)] &= [B_0] \\ \vdots & \\ [R_{uu}(-k)] &= \sum_{k=1}^k \{\varphi_i\} [R_{uu}(i-k)] \end{aligned} \quad (5.2.13)$$

After getting the coefficient matrix needed in ARMA model, the final procedure is to get the matrix $[\bar{B}]$ based on Eq.5.2.14

$$[\bar{B}] = [f] - [b][\bar{\varphi}] \quad (5.2.14)$$

The key steps to generate time varying velocity components based on the above proposed procedure of ARMA model can be summarized as follows:

Step 1: Set the simulation point number, and then generate the target power spectrum. u , v and w velocity components spectra are generated based on the existing velocity power spectra.

Step 2: Calculate the cross-spectrum based on Eq.5.2.4

Step 3: Calculate the correlation coefficient matrix based on Eq.5.2.9

Step 4: Calculate the coefficient matrices $[\phi(i)]$ based on Eq.5.2.11

Step 5: Calculate matrix $[B_0]$ using Cholesky decomposition based on Eq.5.2.12

Step 6: Calculate matrix $[c]$ based on Eq.5.2.13

Step 7: Calculate matrix $[\bar{B}]$ based on Eq.5.2.14

Step 8: Calculate multivariate random time history data based on Eq.5.2.6

5.2.3 Inlet Turbulence Generation Procedure

The velocity generation method based on ARMA model has been presented in the preceding section, the remaining task is how to apply this time varying velocity data in the computation domain. In general the inlet velocity is applied on a face boundary in Fig.5.2.3, and the input area of inlet velocity boundary is discretized by many finite volume faces. The velocity component direction can be seen in Fig.5.2.3. After generating the time varying inlet velocity components data, these data will be applied on the point at the inlet face. Fig.5.2.4 describes the process to interpolate the data at the face point. The detailed procedure for generating inlet turbulence can be summarized as follows:

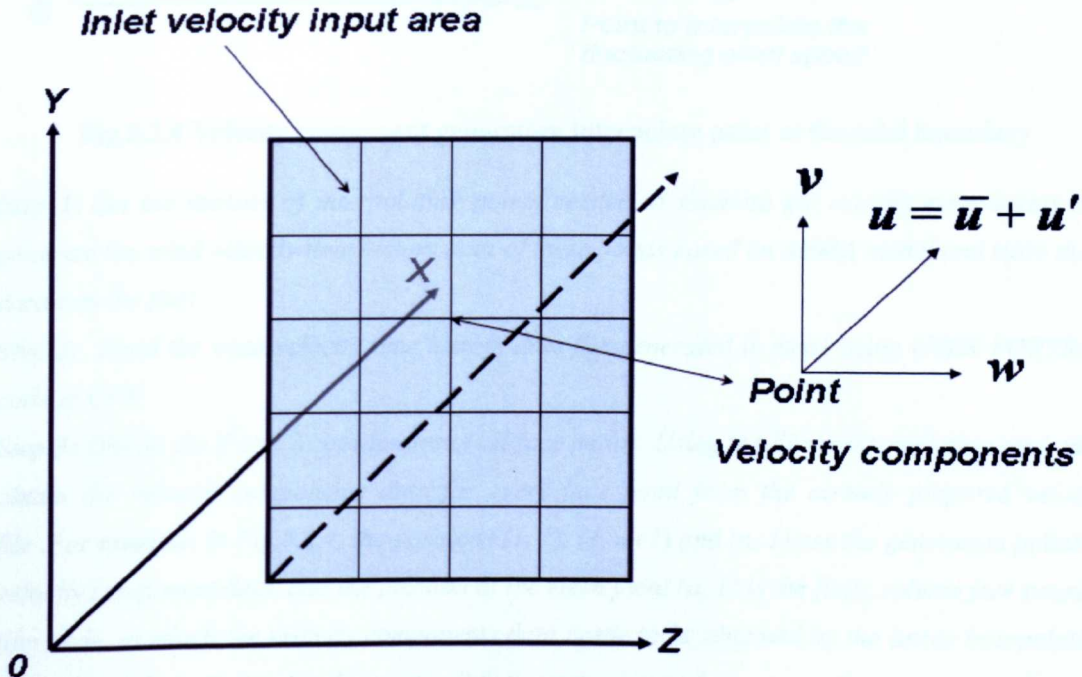


Fig 5.2.3 The direction of inlet velocity input and velocity components

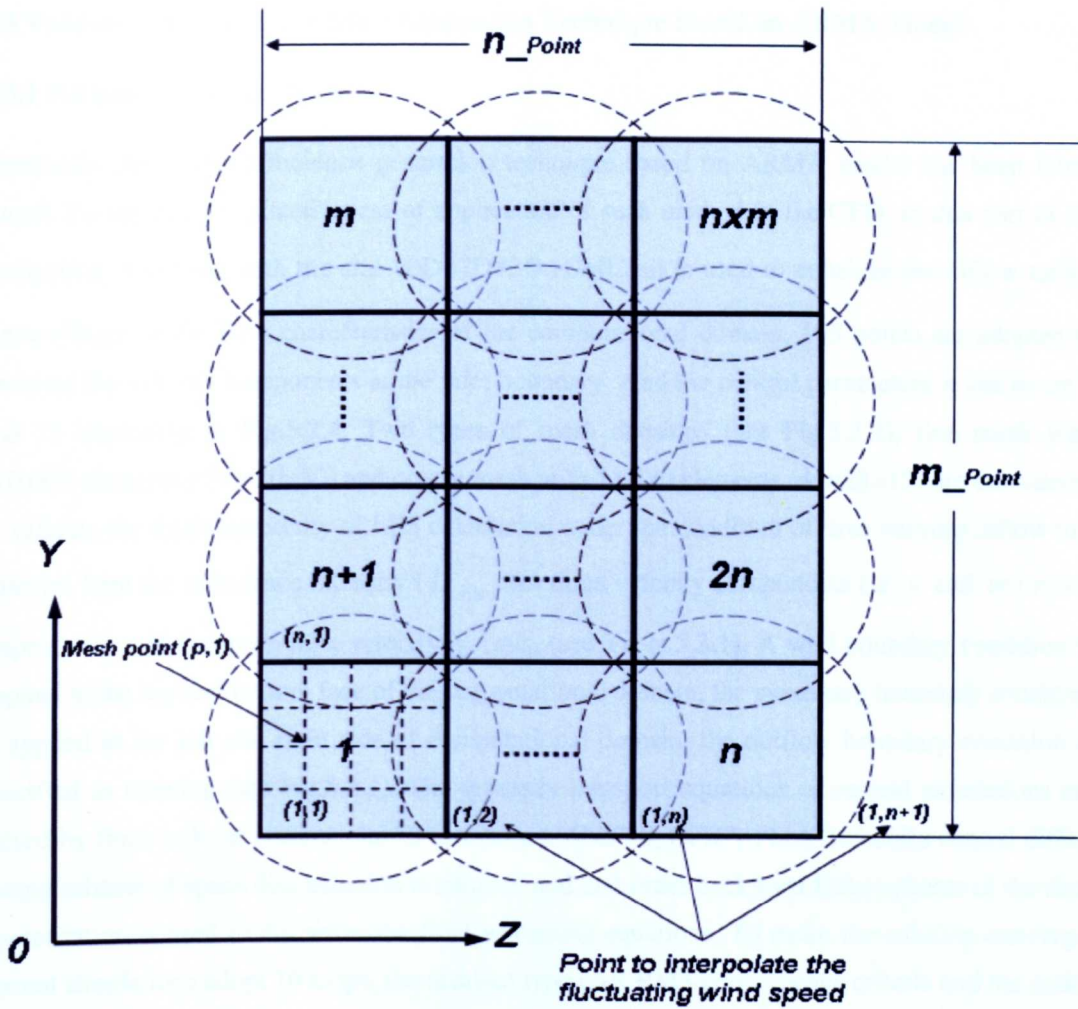


Fig 5.2.4 Velocity component generation interpolate point at the inlet boundary

Step 1: Set the number of interpolating points needed to simulate the velocity components and generate the wind velocity time history data of these points based on ARMA model and store these data into the files

Step 2: Read the wind velocity time history data file generated in step1 using USER FORTRAN code in CFX

Step 3: Obtain the Y and Z coordinates of all face points. Using the linear interpolating method to obtain the velocity components data for every face point from the already prepared velocity file. For example, in Fig.5.2.4, the positions $(1, 1)$, $(1, n+1)$ and $(n, 1)$ are the generation points of velocity component data, and the position at the mesh point $(p, 1)$ is the finite volume face connection node, at which the velocity components data needs to be obtained by the linear interpolating method and then applies this data onto all face connection nodes.

5.3 Validation of Inlet Turbulence Generation Technique Based on ARMA Model

5.3.1 Parameters of Simulation

Previously the inflow turbulence generation technique based on ARMA model has been introduced. To validate the effectiveness of application of such method in the CFD, in this part of investigation, a domain with the size $10D \times 7D \times 3D$ ($D=0.2m$) is used to consider the inflow turbulence effects on the flow characteristics of the computational domain. 105 points are adopted to generate the velocity components at the inlet boundary. And the control parameters n and m are 7 and 15 separately in Fig.5.2.4. Two types of mesh densities (see Fig.5.3.2), fine mesh with 210,000 elements ($100 \times 70 \times 30$) and coarse mesh with 13,440 elements ($40 \times 28 \times 12$) are considered to validate the mesh sensitivity of LES calculation under the condition of time varying inflow turbulence, here the turbulence intensity ($I_{u,v,w}$) for three velocity components (u , v and w) is 5% respectively and the mean inlet velocity is 1m/s. (see Table.5.3.1). A wall boundary condition is applied at the top and bottom face of the computational domain, the symmetry boundary condition is applied at the left and right side of computational domain, the outflow boundary condition is specified as opening (see Fig.5.3.1). The unsteady transport equations of current simulations are solved by finite volume commercial CFD software ANSYS_CFX V11. A 2nd order central differencing scheme of space discretisation is adopted and 2nd order backward Euler scheme of the time discretisation is used to discretize the fluid governing equations. To make the solution converge, current simulations adopt 10 loops, the residual type uses RMS convergence criteria and the residual target is 1.E-4. The block structured mesh is used in the whole computational domain. The unsteady inlet boundary of current simulation is realized by CFX USER FORTRAN code. To guarantee simulation results are reliable, the total computational time is 60s and the smallest time step is 0.01s. The domain geometry and initial mesh are generated by the mesh generator GAMBIT 2.3. The standard and dynamic LES models are considered.

Table 5.3.1 Inlet turbulence parameters

$U_{mean} (m/s)$	$I_u = \sigma_u / U_{mean}$	$I_v = \sigma_v / U_{mean}$	$I_w = \sigma_w / U_{mean}$
1.0	5%	5%	5%

In applying the proposed technique to generate the fluctuation velocity components (u , v and w) at the spatial points, here the Karman type velocity power spectrum is adopted:

$$S_{u_i}(f) = \frac{4\sigma^2 L_x / U_i}{(1 + 106.7(fL_x / U_i)^2)^{5/6}} \quad (5.3.1a)$$

$$S_{v_i}(f) = S_{w_i}(f) = \frac{4\sigma^2 L_{y,z} / U_i}{(1 + 70.8(fL_{y,z} / U_i)^2)^{5/6}} \quad (5.3.1b)$$

Where $L_{x,y,z}$ is the integral length scale of three directions respectively and here it is 0.1, the frequency range is 0~100 Hz, σ^2 is the variance of velocity component, U_i is the mean velocity at point i . The cross spectra S_{ij} between u at point i and v at point j , v at point i and w at point j and w at point i and v at point j are set to zero as: $S_{ui,vj}(f) = S_{vi,wj}(f) = S_{wi,uj}(f) = 0$
 The cross correlation coefficient is specified by the Davenport type root coherence function as Eq.5.2.5, which is plotted in Fig.5.3.3.

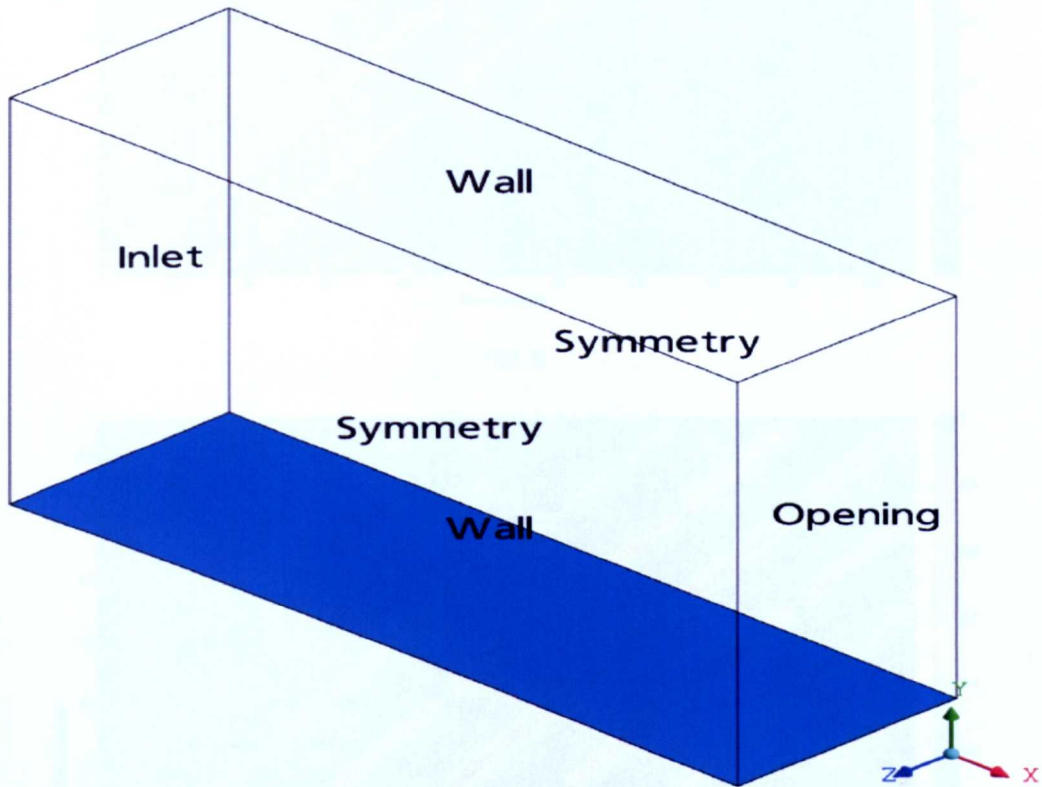
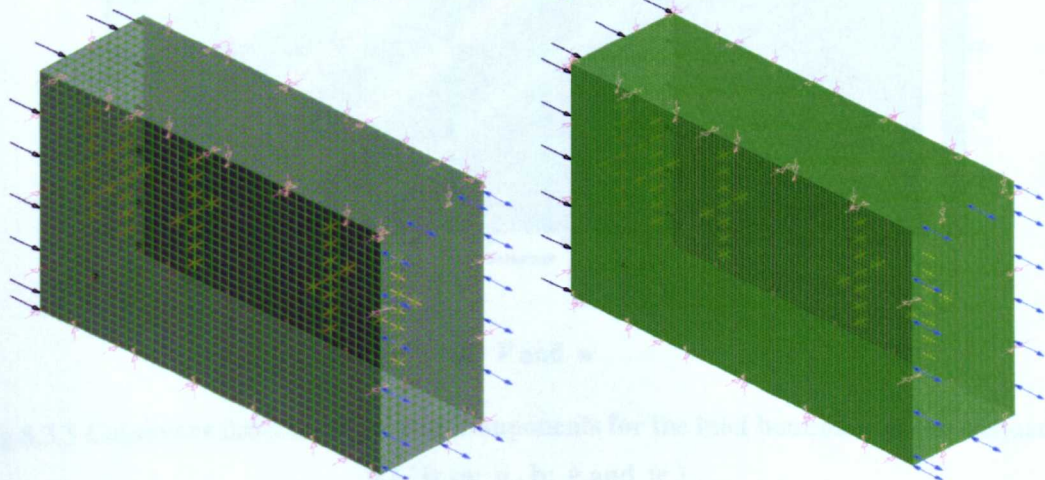


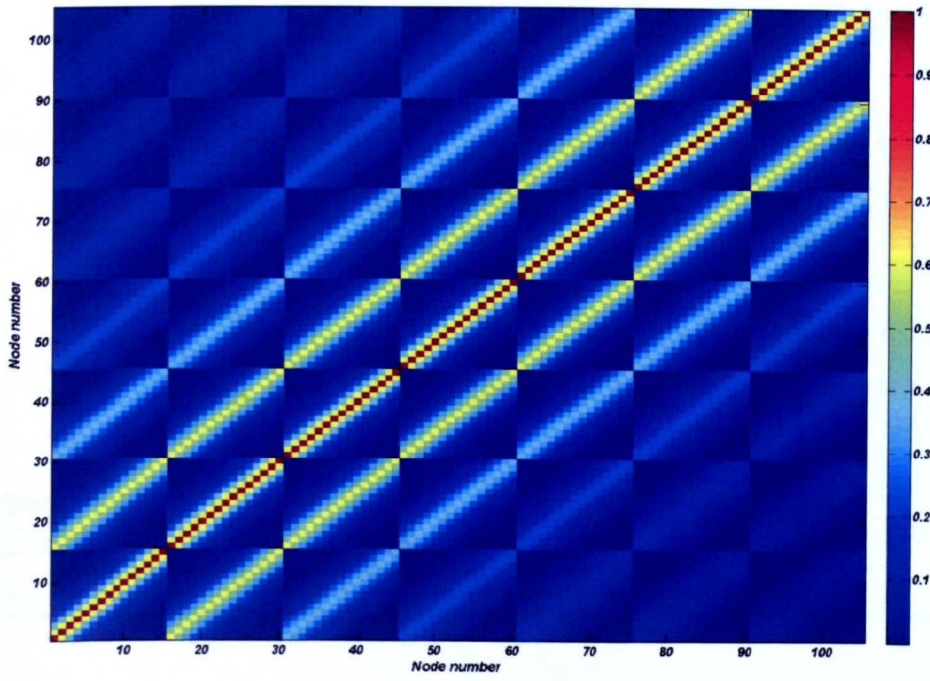
Fig 5.3.1 Boundary conditions



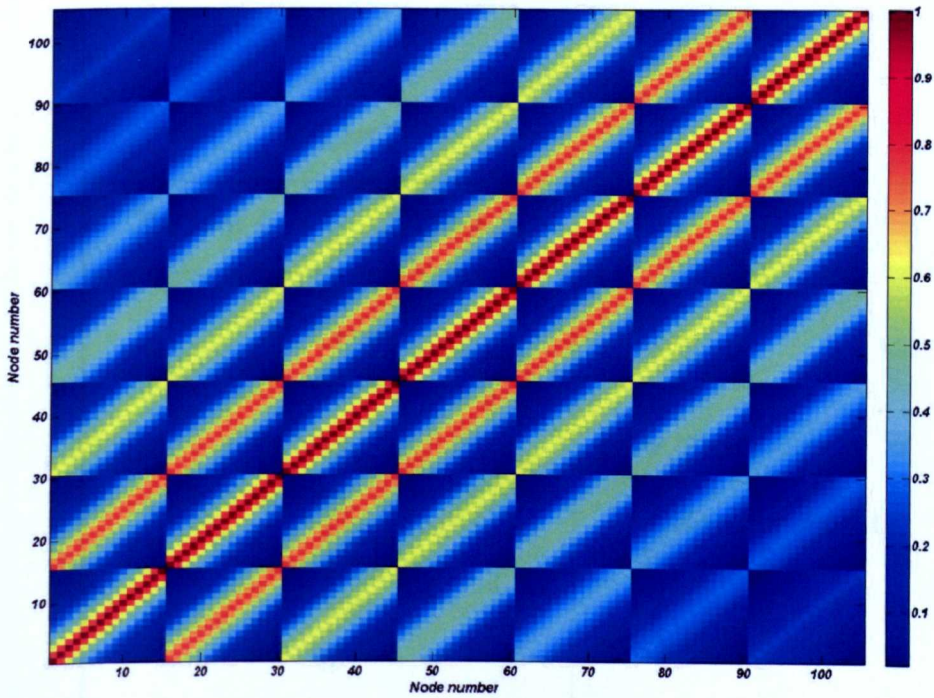
(a) Coarse mesh

(b) Fine mesh

Fig 5.3.2 Domain mesh (a: coarse mesh, b: fine mesh)



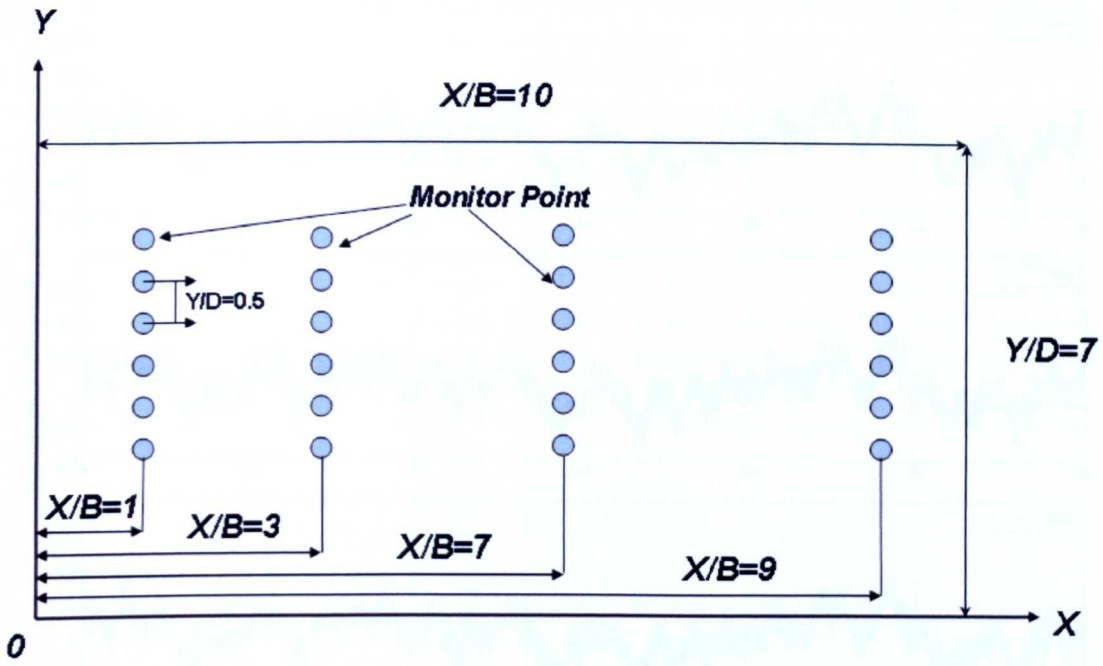
(a) u



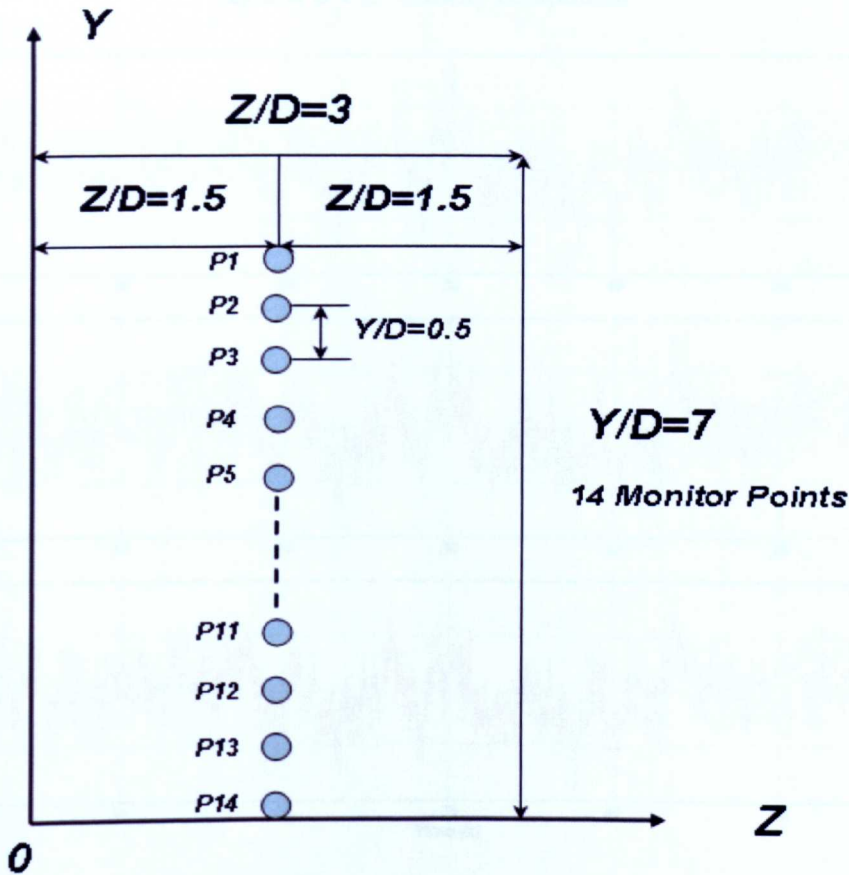
(b) v and w

Fig 5.3.3 Coherence function of velocity components for the inlet boundary at the frequency 0.1 Hz (a: u , b: v and w)

From Fig.5.3.3, it is found that the coherence value decreases with the point distance increasing.

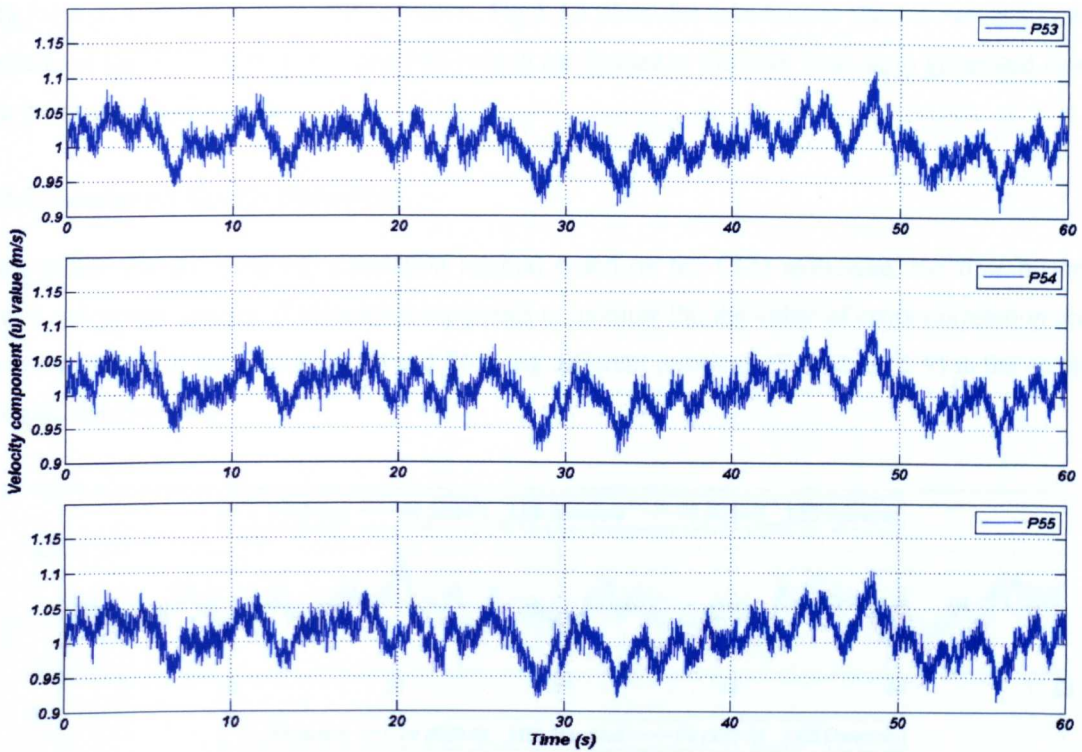


(a) Monitor point group position at XY plane

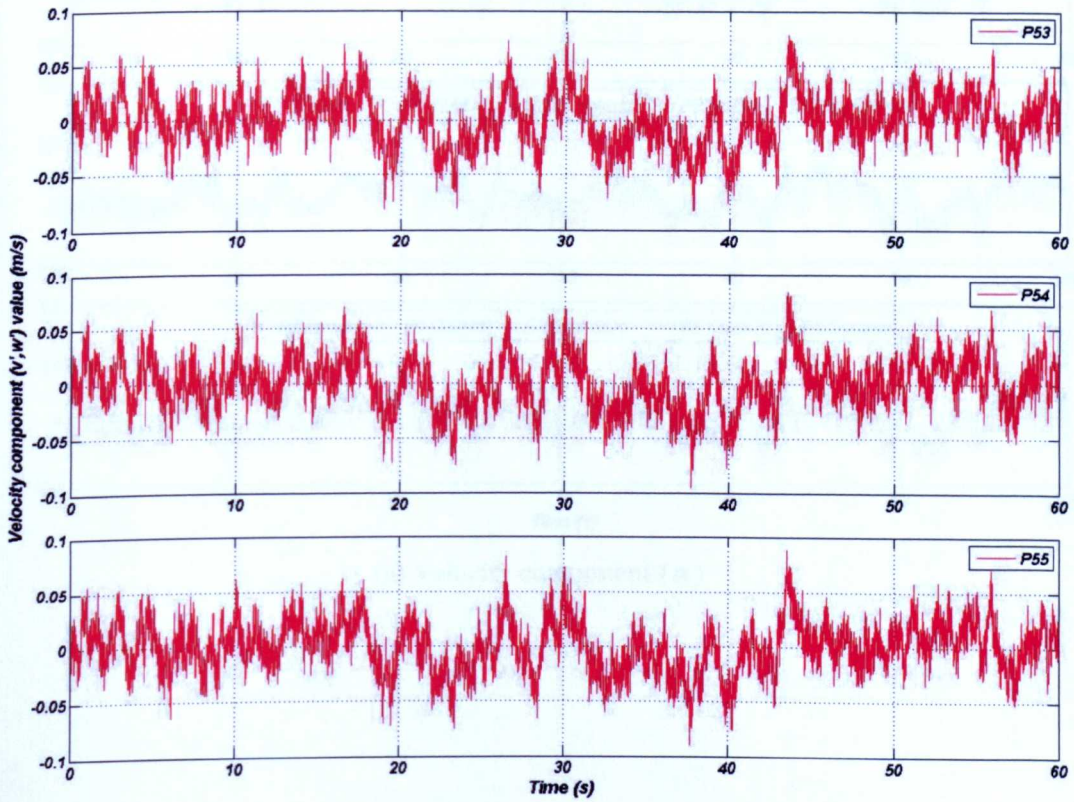


(b) Monitor points position at YZ plane

Fig 5.3.4 Schematic figure of monitor points position (B=0.2m, D=0.2m)



(a) $u = \bar{u} + u'$ velocity component



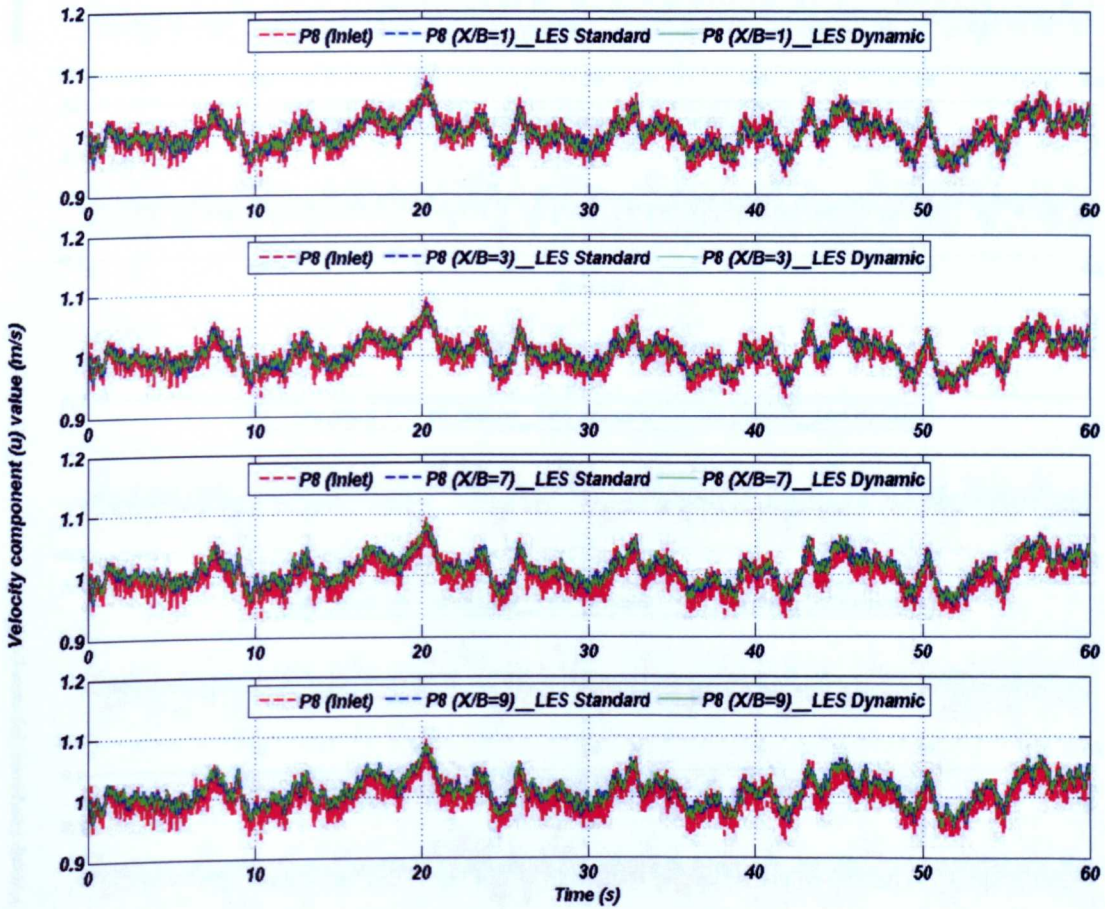
(b) v and w velocity components

Fig 5.3.5 Velocity components' time history curves at different monitor points

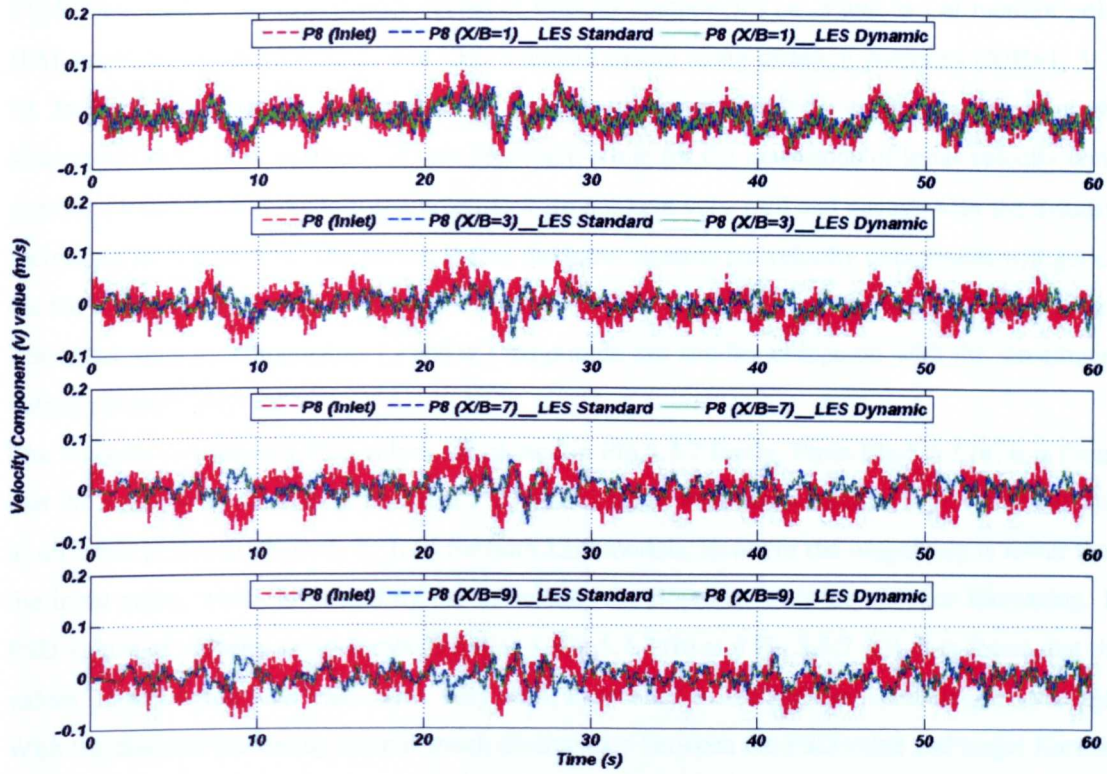
Fig.5.3.4 plots the monitor point's position. Fig.5.3.5 plots the time history data of velocity components at the position P53, P54 and P55 (which are located at the inlet boundary) generated from the proposed ARMA model.

5.3.2 Simulation Results Discussion

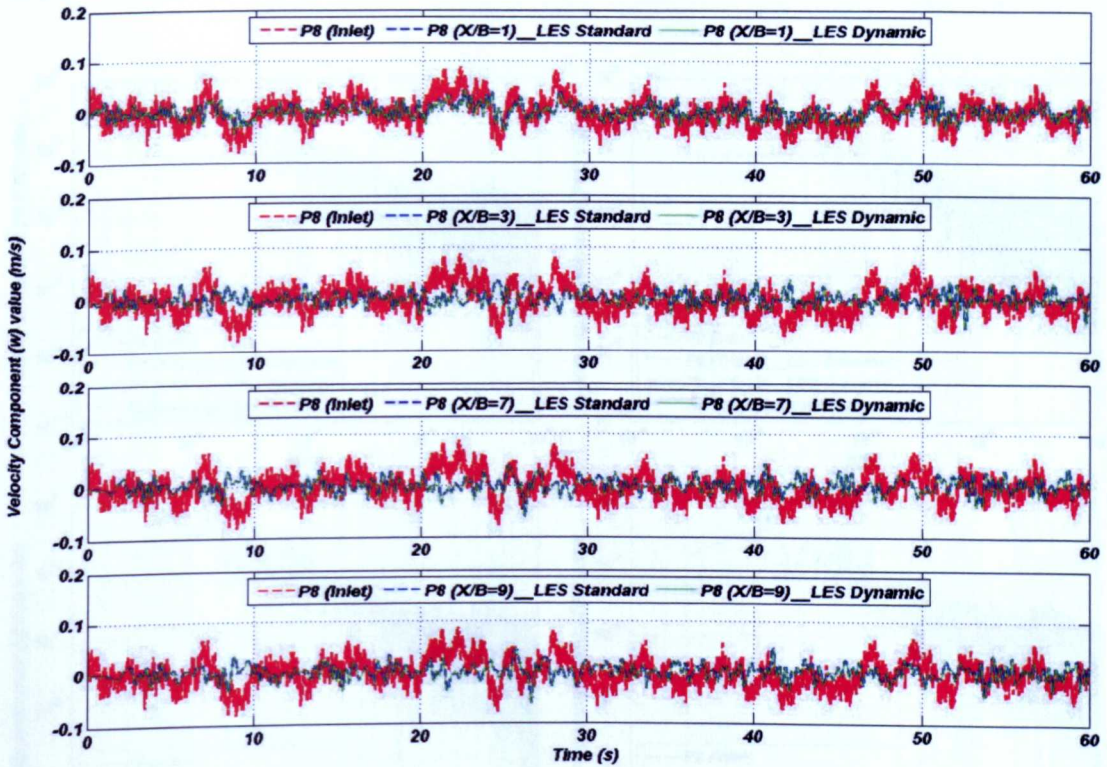
To validate current buffeting simulation method based on the CFD technique, the time history curve and power spectra of velocity components at monitor P8, the value of cross-correlation and auto-correlation at some monitor P8 and P6 along different positions ($X/B=1, 3, 7, 9$) in the empty domain are discussed.



(a) Velocity component (u)



(b) Velocity component (v)

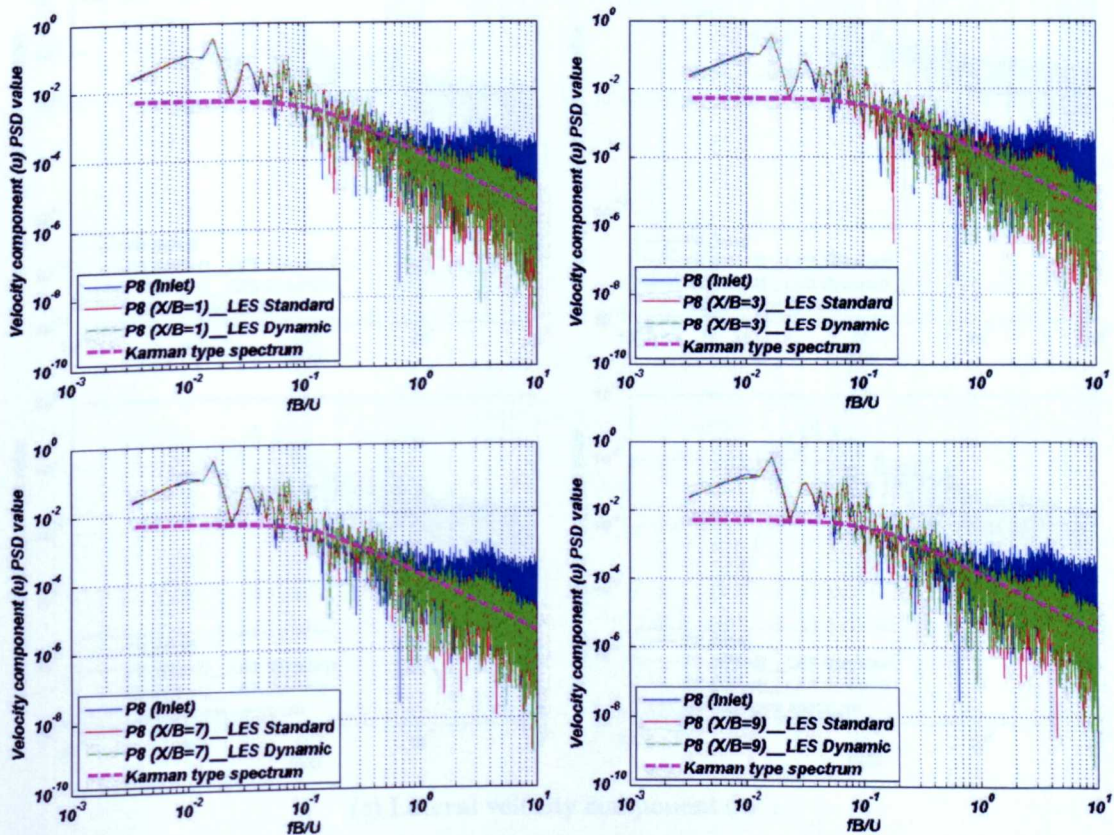


(c) Velocity component (w)

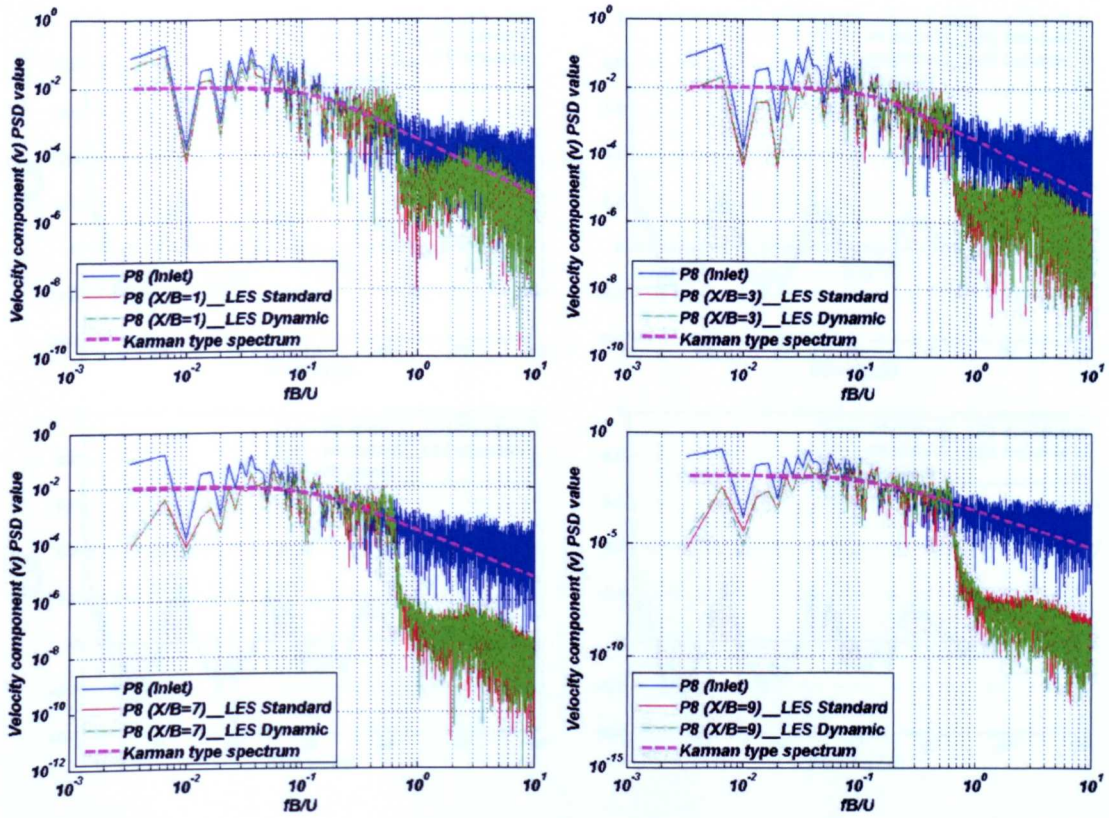
Fig 5.3.6 Velocity components' time history curves at P8 along different positions (coarse mesh)

Fig.5.3.6 compares the time history curves of velocity components (u , v and w) of monitor point (P8) generated by LES-Dynamic and LES-Standard model along different positions ($X/B=1, 3, 7, 9$). In Fig.5.3.6 it can be found that the random characteristics and variation process of the streamwise velocity component (u) are kept well, while for the magnitude of input velocity components (v and w) and random characteristics are not kept very well and decays with the distance increasing in X direction. The reason is that the input streamwise velocity component will generate the new turbulence after LES calculation, which interacts with the input velocity components. The input velocity components (v and w) magnitude are smaller compared with the streamwise velocity component (u).

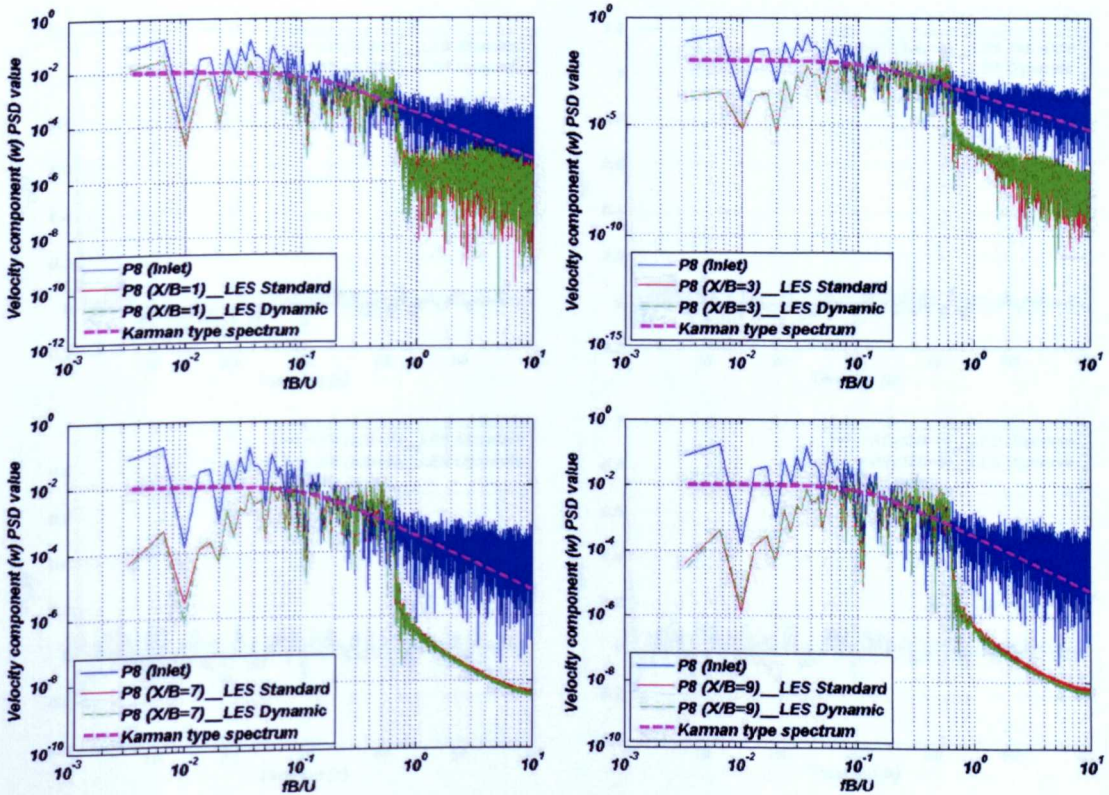
The velocity components PSD values are plotted in Fig.5.3.7 firstly. From Fig.5.3.7 (a) it is found that the streamwise velocity component PSD values agree with target Karman type spectrum well at different positions ($X/B=1, 3, 7, 9$) for both LES models, however the magnitude is lower than the input value, which is caused by the turbulence development with the distance increasing. In PSD values of velocity components (v and w) (Fig.5.3.7 (b) and Fig.5.3.7 (c)), it is found that the values do not agree with each other very well, especially in the high reduced frequency range. With the distance increasing there is much discrepancy between the PSD value and target Karman type spectrum, which further indicates the variation process of the velocity components time history data in Fig.5.3.6 (b) and (c).



(a) Streamwise velocity component (u)

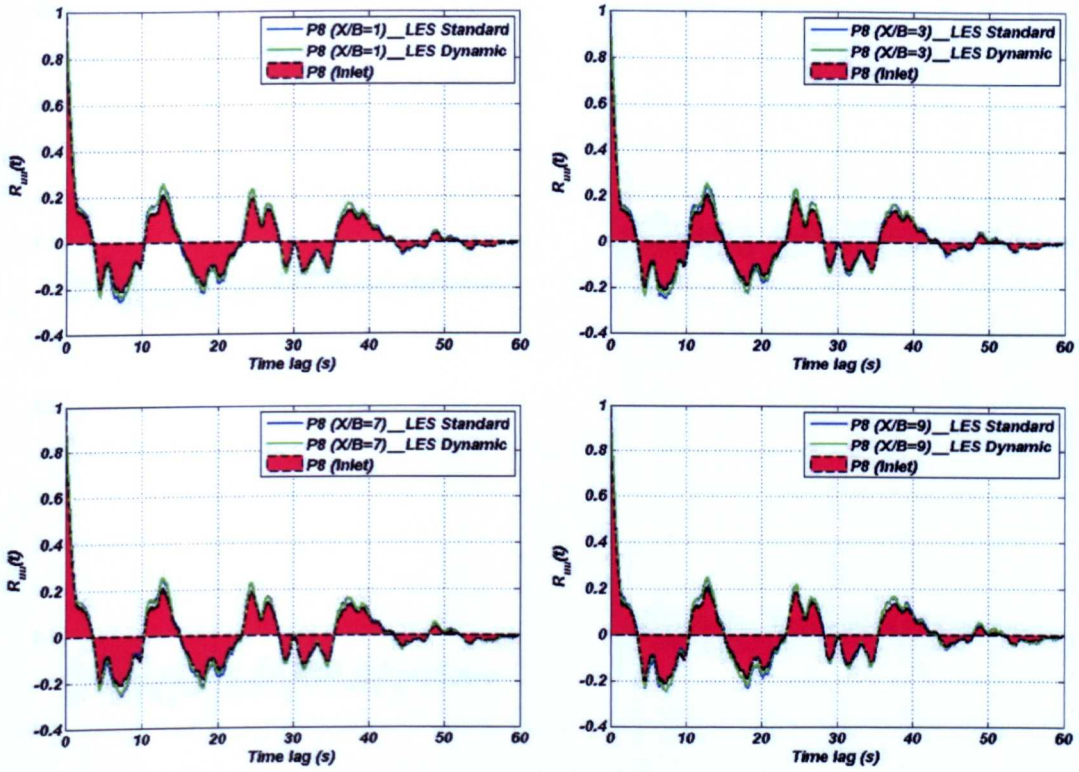


(b) Vertical velocity component (v)

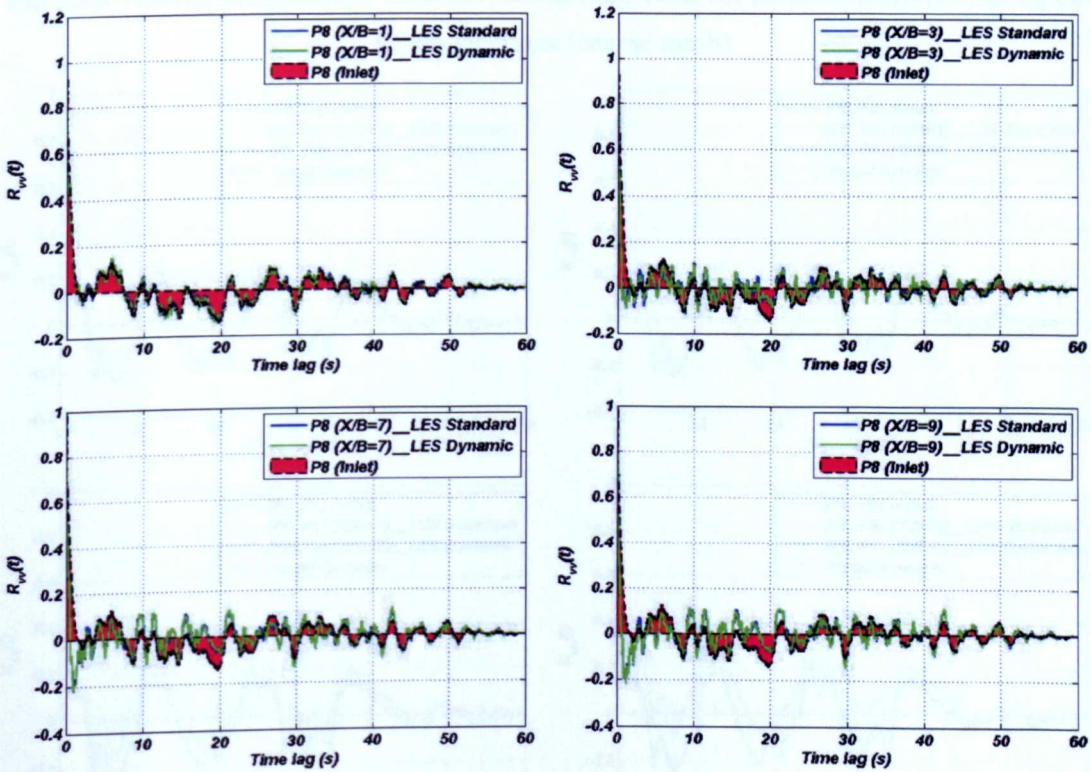


(c) Lateral velocity component (w)

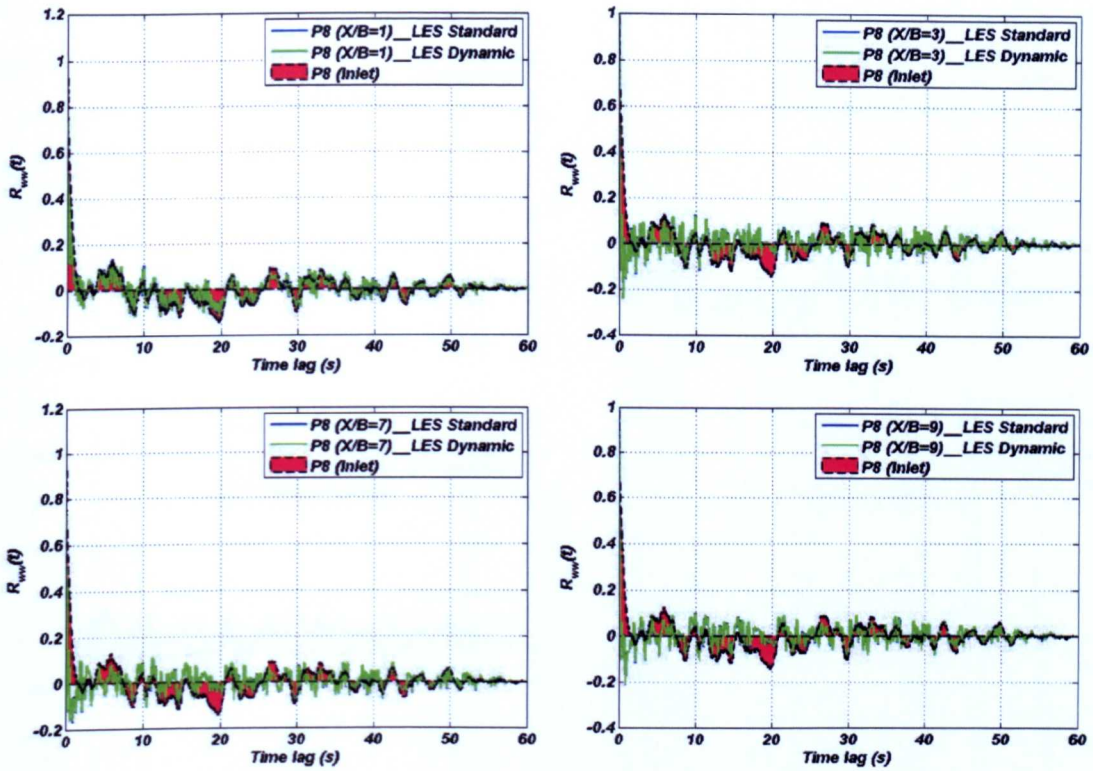
Fig 5.3.7 Velocity components' PSD value at monitor point (P8) along different positions



(a) Streamwise velocity component (u)

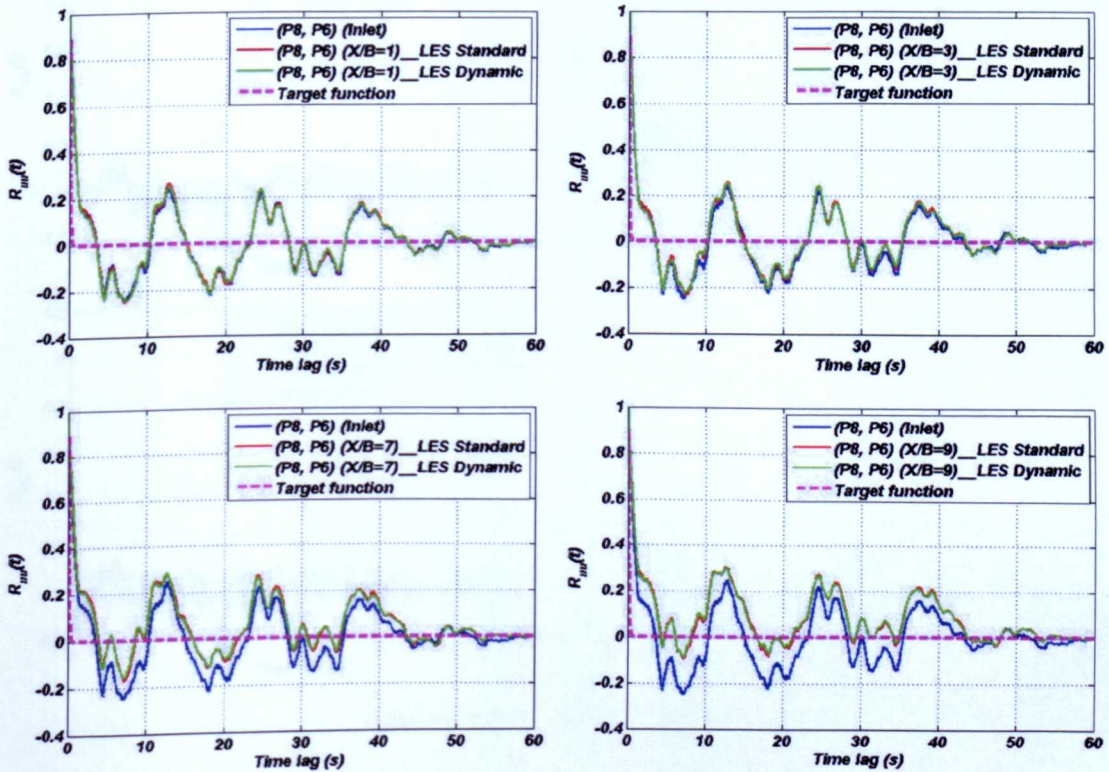


(b) Vertical velocity component (v)

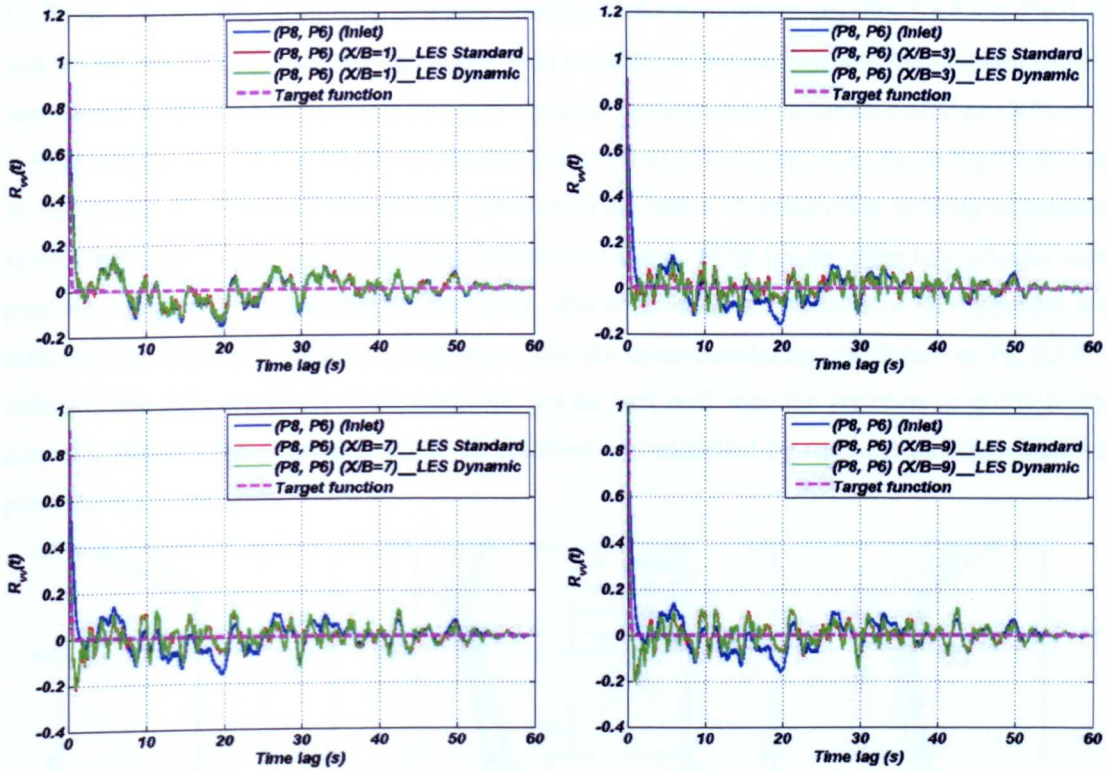


(c) Lateral velocity component (w)

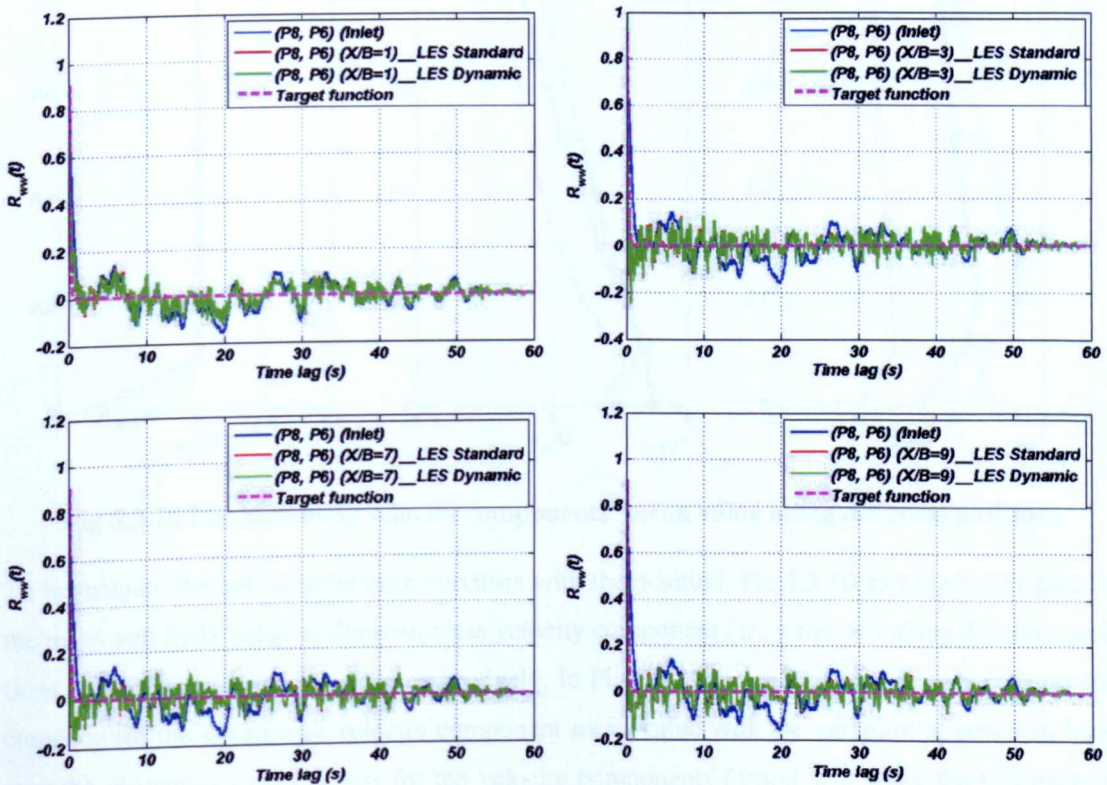
Fig 5.3.8 Velocity components' autocorrelation coefficient for monitor point (P8) along different locations (coarse mesh)



(a) Streamwise velocity component (u)



(b) Vertical velocity component (v)



Lateral velocity component (w)

Fig 5.3.9 Velocity components' spatial cross-correlation coefficient at monitor point P6 and P8 (coarse mesh)

To further investigate the current simulated results of velocity components, Fig.5.3.8 and Fig.5.3.9 plot for the velocity components (u , v and w) the values of autocorrelation and cross-correlation coefficients based on LES standard and LES dynamic models along different positions ($X/B=1, 3, 7, 9$) at monitor point P8 and between monitor points P8 and P6 respectively. From Fig.5.3.8 it can be found that for both LES models the autocorrelation value of streamwise velocity component agrees with target input value well along different positions, while for the other two velocity components (v and w) some discrepancies occur, which indicates the turbulence development will influence the input two velocity components. For the cross-correlation coefficient in Fig.5.3.9, it indicates that the correlation relationship can not be kept well with the variation of position. The reason is that the input turbulence will be resolved and modelled by the LES model, which will generate new turbulence.

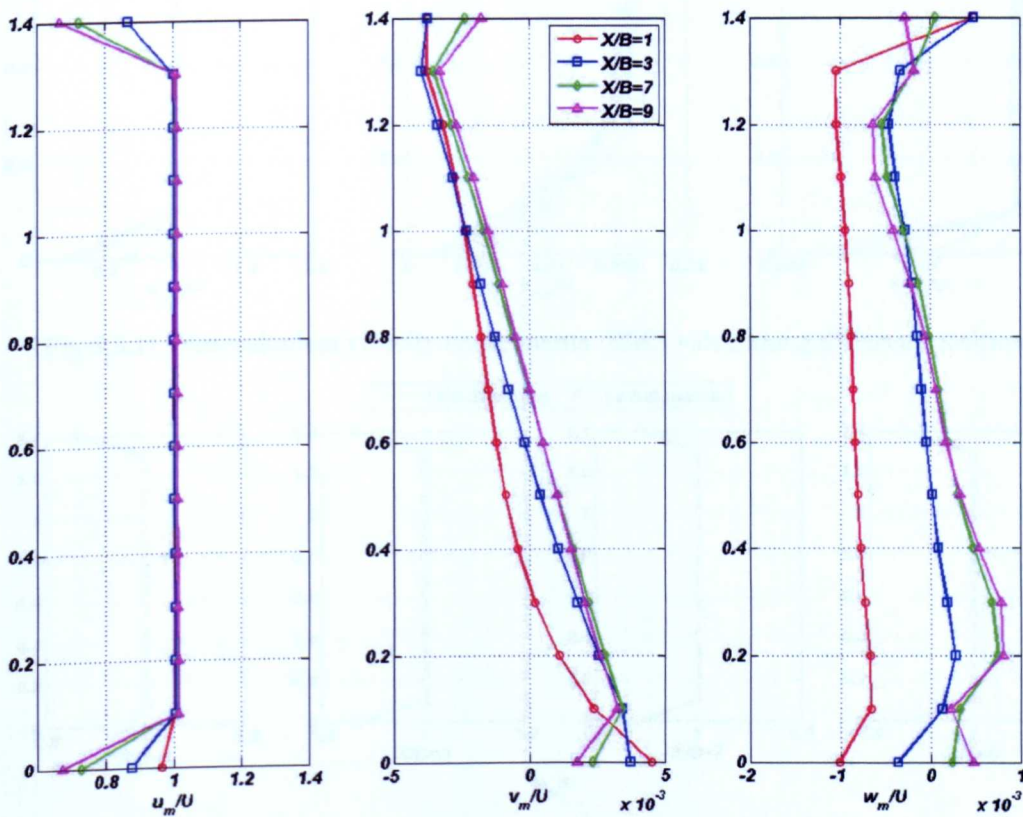


Fig 5.3.10 Dimensionless velocity components' mean value along different positions

To investigate the inflow turbulence variation with the position, Fig.5.3.10 and Fig.5.3.11 plot for the mean and RMS value of dimensionless velocity component (u , v and w) along different positions in the computational domain respectively. In Fig.5.3.10 it can be found that there is no discrepancy for the streamwise velocity component mean value with the variation of position, however the discrepancy only occurs for the velocity components (v and w), while the influence on the velocity component (w) is clear. In Fig.5.3.11 it is found that the same variation as the velocity mean value takes place on the RMS value of streamwise velocity component (u), while some

discrepancies also occur on the RMS values of other velocity components. The above discrepancy further shows the influence of different position on the velocity component (v and w).

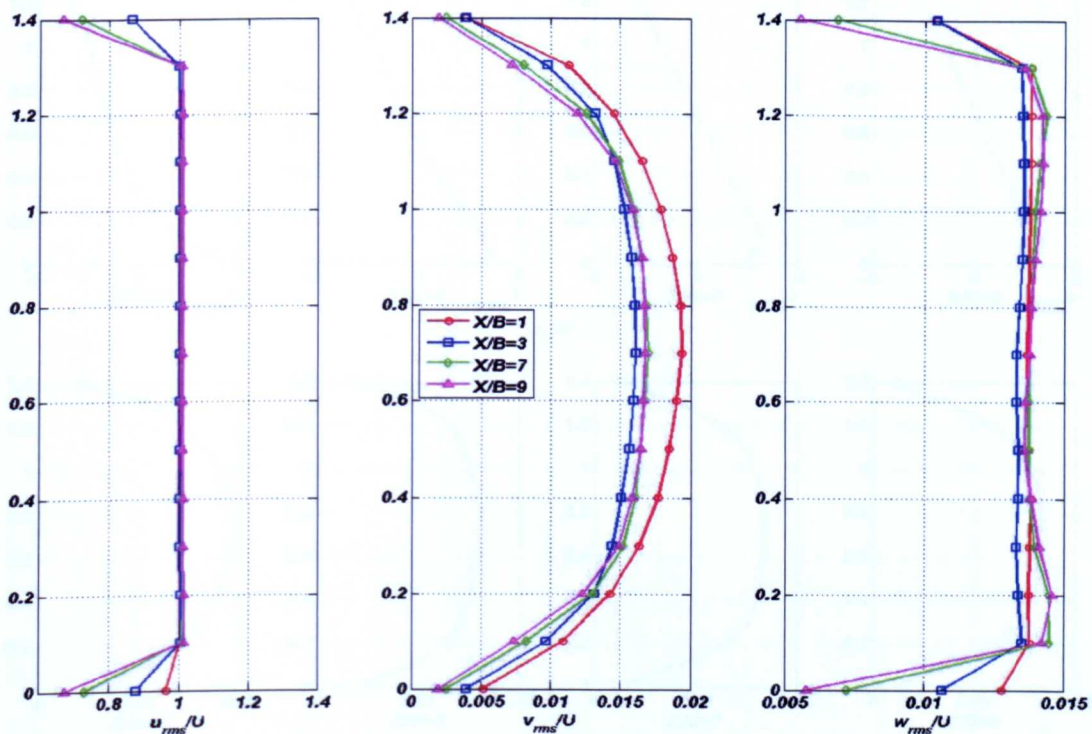


Fig 5.3.11 Dimensionless velocity components' RMS value along different positions

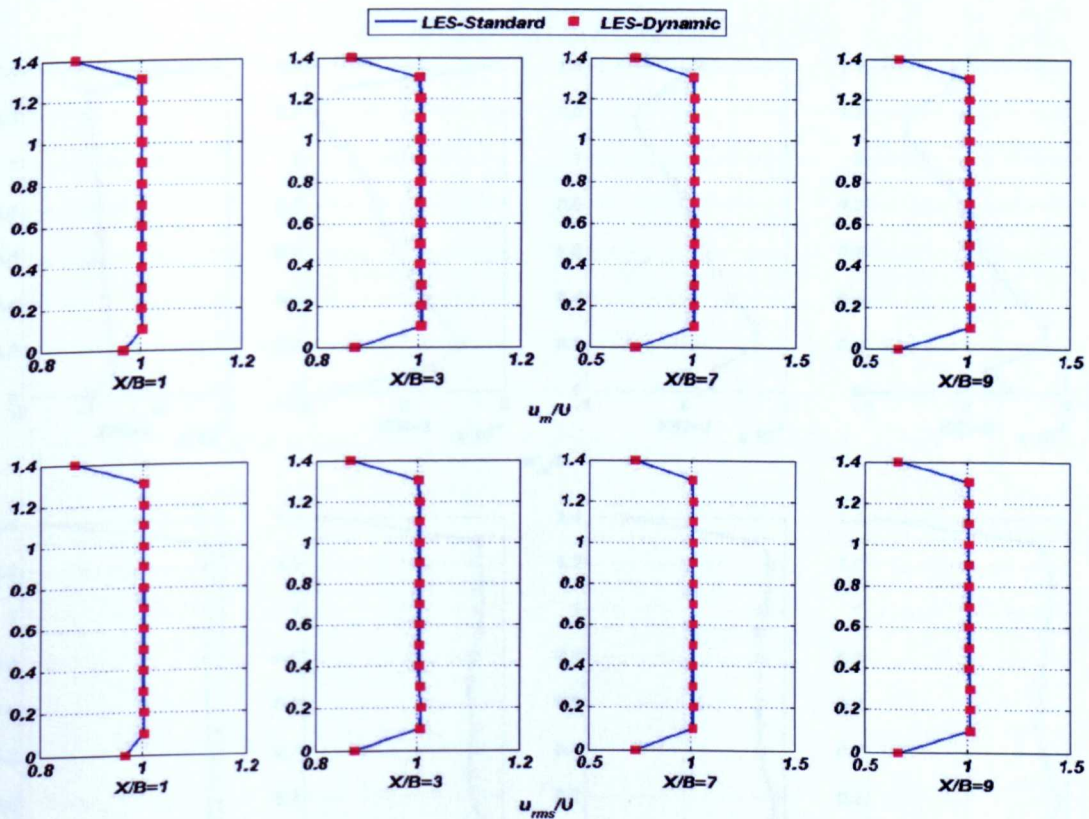


Fig 5.3.12 Velocity component (u) mean and RMS value of LES standard and dynamic model

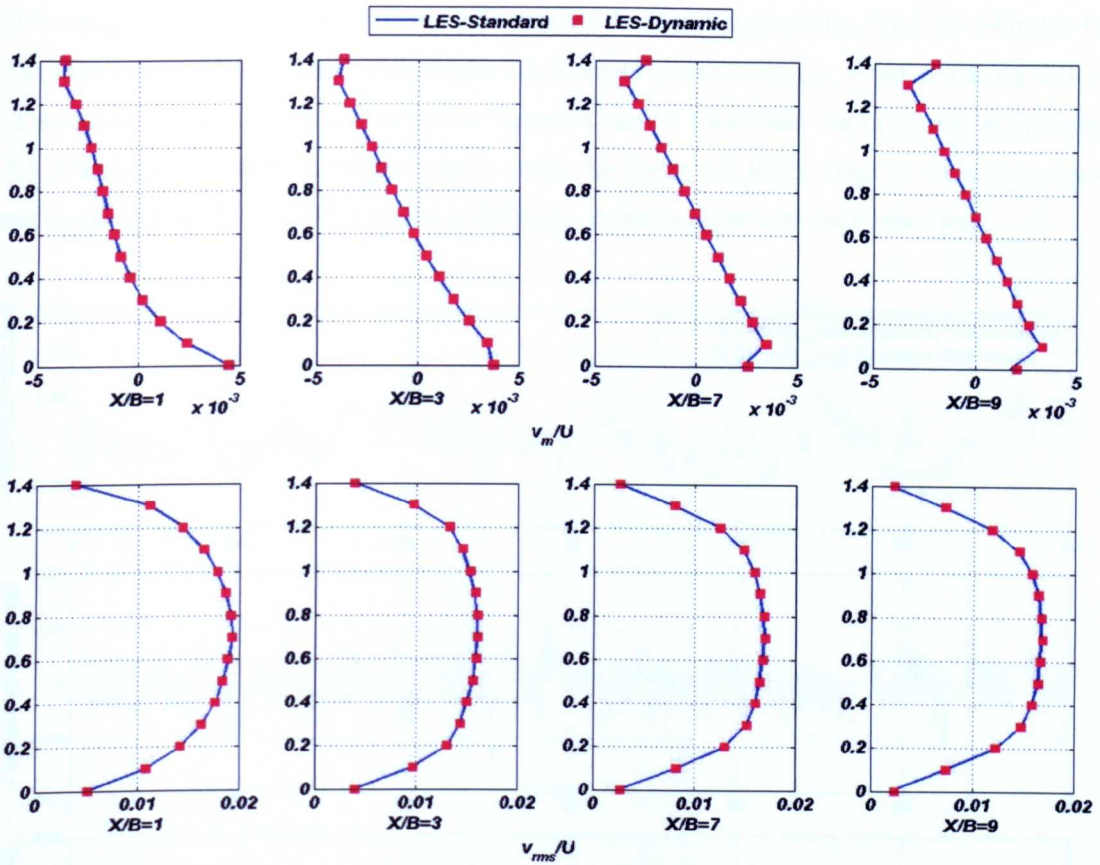


Fig 5.3.13 Velocity component (v) mean and RMS value of two different LES models

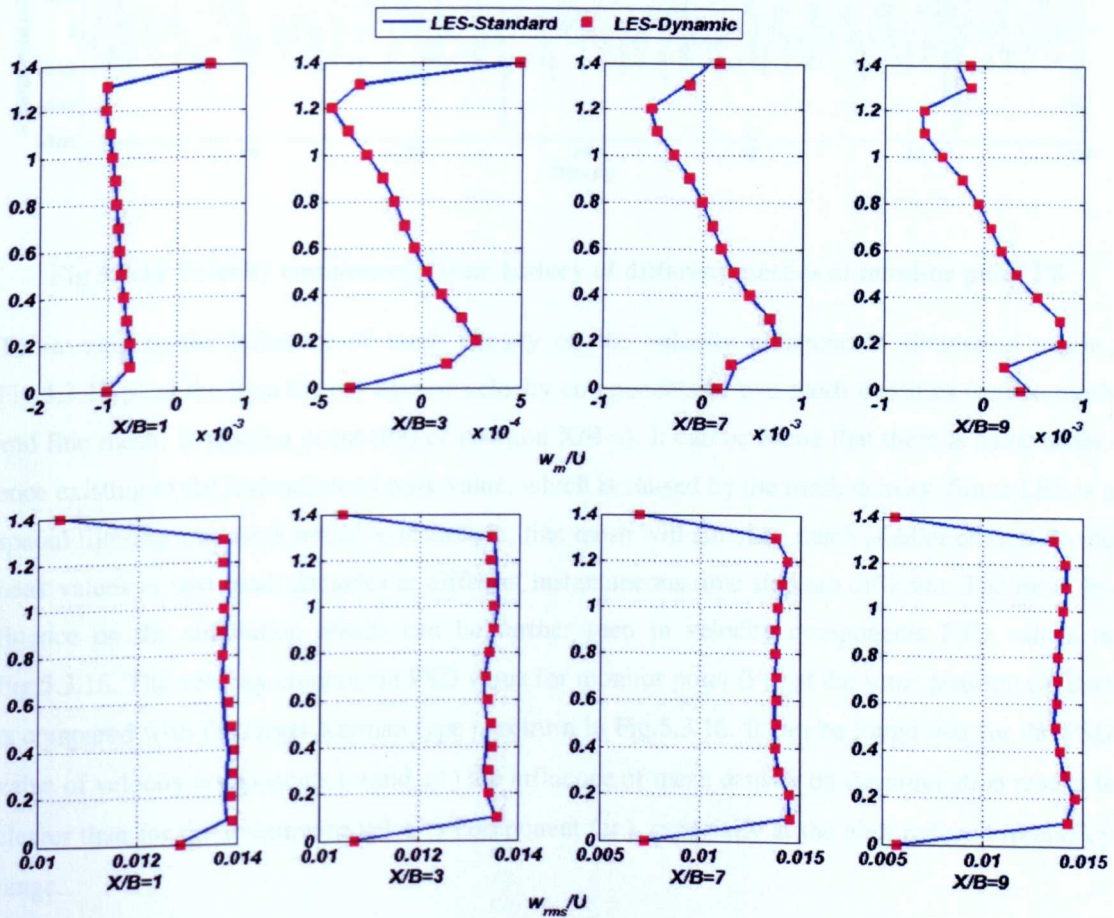


Fig 5.3.14 Velocity component (w) mean and RMS value of two different LES models

To investigate the influence of different LES models the simulation results, Fig.5.3.12-Fig.5.3.14 plots the mean and RMS value of dimensionless velocity components (u , v and w) along different positions respectively. From the above figures it can be found that the influence of different LES models on current simulation results is small, the mean and RMS value of velocity components generated by different LES model at different positions agree with each other well.

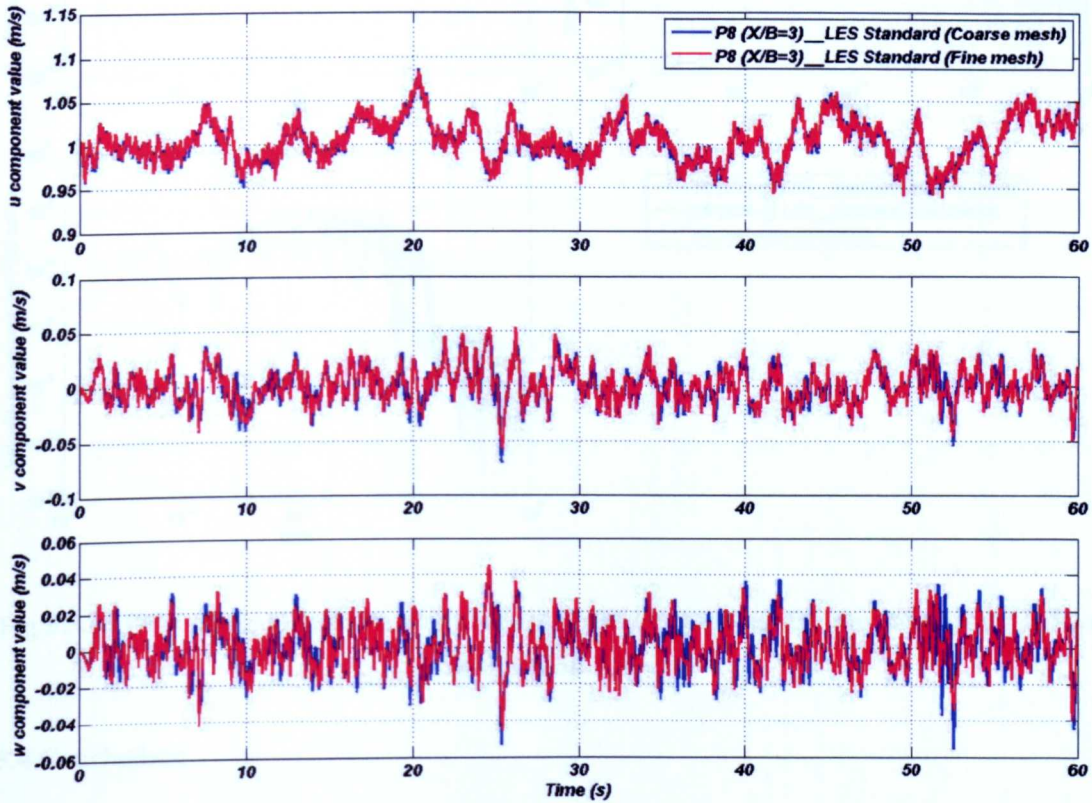


Fig 5.3.15 Velocity components' time history of different meshes at monitor point P8

To investigate the influence of mesh density on the velocity components simulation results, Fig.5.3.15 plots the time history data of velocity components of two mesh densities (coarse mesh and fine mesh) at monitor point (P8) of position $X/B=3$. It can be found that there is some difference existing in the instantaneous peak value, which is caused by the mesh density. Since LES is a spatial filtering and mesh sensitive technique, fine mesh will simulate much smaller eddies. So the peak values of two mesh densities at different instantaneous time step are different. The mesh influence on the simulation results can be further seen in velocity components PSD values in Fig.5.3.16. The velocity component PSD value for monitor point (P8) at the same position ($X/B=3$) is compared with the target Karman type spectrum in Fig.5.3.16. It can be found that for the PSD value of velocity components (v and w) the influence of mesh density on the simulation results is clearer than for the streamwise velocity component (u), especially at the high reduced frequency range.

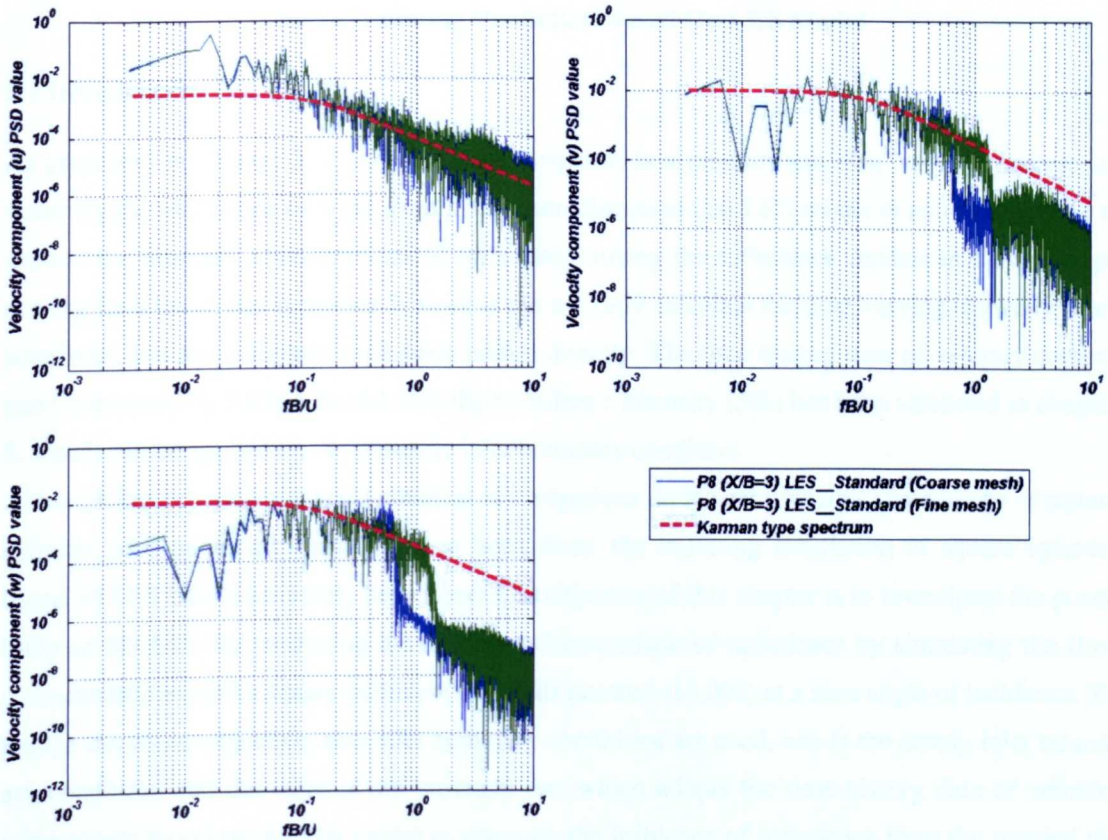


Fig 5.3.16 PSD values of Velocity components of different meshes for the monitor point P4 at the position X/B=3

5.4 Conclusions

3D large eddy simulations with the unsteady inlet boundary of 5% turbulence intensity are validated in the empty domain. Based on the results and analysis, it is found that currently proposed inflow turbulence generation technique based on the ARMA model is effective and fast inflow turbulence generation technique, which avoids the time consuming procedure like the approach of WAWS. From the results of different models, it is found that current LES models (standard LES and dynamic model) can use this unsteady boundary condition. However, in the PSD value of velocity components it can be found that the magnitude of PSD value is different in the high reduced frequency range. And in the simulation results of velocity components at different position, it can be found that with the variation of distance to the inlet boundary condition, the PSD value of velocity components (u , v and w) will be lower than the target spectrum, which is caused by the turbulence development and the turbulence eddies generated at the inlet boundary interacting with the ones from the simulation of LES models. And from the results of comparison between the case of coarse mesh and the one of fine mesh, it can be found LES is a grid sensitive simulation.

Chap 6 Buffeting Prediction Based On LES Model

6.1 Introduction

As presented in chapter 2, Bridge buffeting response is a random and time varying process induced by the turbulence of wind. And it has been discussed that LES model is an effective one to capture the unsteady characteristics of turbulence among the turbulence models in current engineering field problems in chapter 3, since it can not only calculate the time varying unsteady characteristics, but also simulate large scale eddies directly. The time history data of velocity components generated by ARMA model with the turbulence intensity (5%) has been validated in chapter 5, which can be applied on the unsteady inlet boundary condition.

Although the experimental and numerical investigations on the aerodynamic phenomena of square cylinder such as vortex shedding have been done, the buffeting simulation of square cylinder based on LES model has rarely been done. The objective of this chapter is to investigate the possibility of 3D LES for predicting the unsteady characteristic of turbulence by simulating the flow characteristic around a square cylinder (Reynolds number=13,000) at a zero angle of incidence. To realize the above objective, two inlet boundary conditions are used, one is the steady inlet boundary condition, and the other is the unsteady one which adopts the time history data of velocity components based on ARMA model to consider the influence of turbulence from the upwind direction in the buffeting analysis of civil engineering structure. The general aerodynamic parameters such as Strouhal number, the mean value of drag coefficient and RMS value of lift and drag coefficient is examined and compared with other CFD or experimental results.

6.2 Numerical Simulation of Square Cylinder

Since the geometrical dimension of square cylinder section is similar to other structural cross sections such as buildings, it has been widely investigated in the past. Especially the numerical simulation of flow around the square cylinder becomes so popular based on different turbulent models. In general the classical steady RANS model is firstly adopted. However, the RANS model simulates all scales of turbulence proposing the challenge for the accurate prediction of flow around the bluff body. Lubcke *et al.* (2001) compared the simulation results of RANS and LES model for the flow around a square section. It was found that the RANS method failed to capture the dynamics of the flow, especially in the near wake region of the cylinder. This is due to the fact that the RANS model models all scales of turbulence while the LES resolves the major scale of the turbulence and only models the small scales. Sohankar *et al.* (1999) employed 2D and 3D LES with an implicit and second order finite volume code to study the flow around a square cylinder at moderate Reynolds numbers ranging from 150 to 500. It was concluded that 3D results agreed with the experiment very well for Reynolds number beyond 300. For high Reynolds numbers, Srinivas *et al.* (2006) studied the flow around a square cylinder at a Reynolds number of 21,400 using the LES technique with higher-order spatial discretization. Through the analysis, it was found that the

predicted time averaged flow agreed with the experimental results very well. The turbulent normal stresses and shear stress are predicted very well by LES. The vortices shed in the near wake region undergo breakup and established the cascade mechanism of energy transfer as the turbulent flow develops. Except for the investigations on the influence of Reynolds number, Nakayama and Ven-gadesan (2002) discussed the 2nd and 4th order central difference scheme, 3rd and 5th order upwind-biased difference schemes influence based on SGS model.

The above discussions regarding the LES calculation of the square cylinder are all based on standard Smagorinsky model. However with further development of the LES technique, other updated models have been proposed. Sohankar *et al.* (2002) compared different subgrid scale models such as the standard Smagorinsky, and the standard Dynamic and dynamic one-equation model at Reynolds number 22,000. From the results, it could be found that the results produced by the dynamic one-equation model show a better agreement with the experiments than the other two subgrid models. This is because the dynamic one equation model does not require any free constants and there is no arbitrary averaging of the dynamic coefficient involved to maintain numerical stability as in the standard dynamic model. It was also found that the dynamic model predicted the lowest Reynolds stress tensor among three models, while in the wake region higher pressure leading to the lower drag forces was predicted.

6.3 Numerical Description of Simulation Cases

To discretize the fluid governing equations 2nd order central differencing scheme of space discretisation is adopted and 2nd order backward Euler scheme of the time discretisation is used. The block structured grid is used in the whole computational domain. The domain dimension can be seen in Fig.6.3.1. The fluid domain boundary and dimension can be seen in Fig.6.3.2. Two inlet boundary conditions are considered to compare the different influence of inlet boundary condition on the flow around the square cylinder, one is the steady one, and the other is unsteady one which adopts the time history data of velocity components used in chapter 5. The outflow boundary condition is specified as opening, the no-slip wall boundary condition is specified as the solid wall, the automatic wall model in CFX is used to consider the wall effects, the top and bottom face of the computational domain are specified as the symmetry boundary, the front and back face of the domain are also specified as the same symmetry condition. Since LES is sensitive of mesh density, here the simulation cases with coarse mesh (360,000 elements—LES1, Fig.6.3.1 (a), (c)) and medium mesh (600,000 elements—LES2, Fig.6.3.1 (b)) are firstly considered. And the spanwise length or the depth of domain also has some influence on the simulation result. Okajima (1983) presented that flow had strong three dimensional characteristics at high Reynolds numbers and there is rather small influence on the mean flow parameters at low Reynolds number with spanwise length increasing. To study whether the spanwise dimension influences the flow around square cylinder, another case with the depth of 4D (D: the height of square cylinder, 800,000 element—LES3, Fig.6.3.1 (d)) is also considered. In this part of study, to the steady inlet boundary

condition other cases based on the standard LES model (LES1-Standard), LES dynamic model (LES1-Dynamic) and LES WALE (LES1-WALE) model are also considered and compared. And for the unsteady inlet boundary condition, the case IC1 is adopted, different LES models are also used in this case.

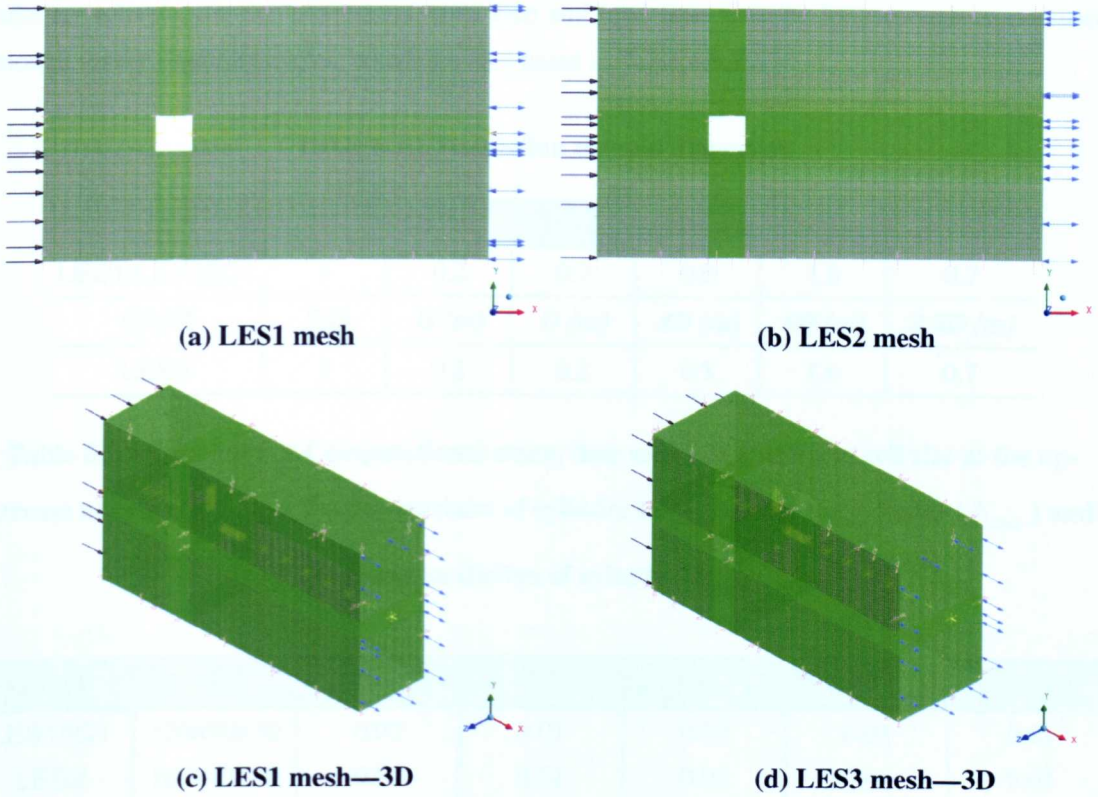


Fig 6.3.1 LES1, LES2 and LES3 mesh

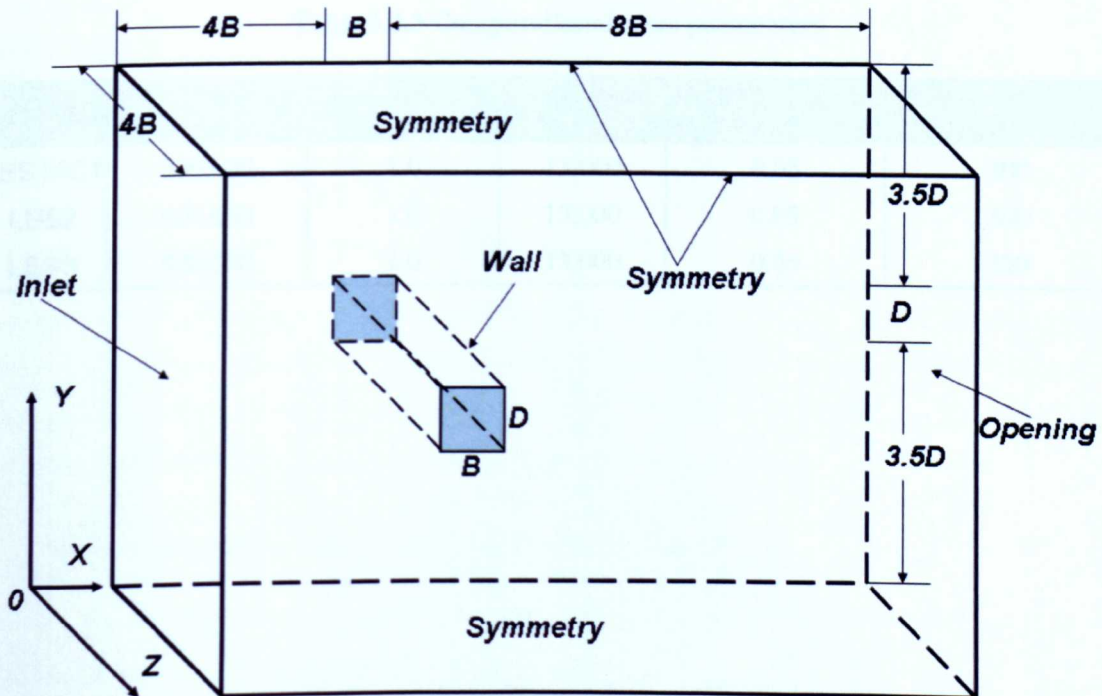


Fig 6.3.2 Domain dimension and boundary conditions

The detail of the domain dimension for the simulation cases is listed in Table.6.3.1, here B is the width of square cylinder, and D is the height of square cylinder. The detailed grid density and the closest grid line to the wall boundary are listed in Table.6.3.2. Table.6.3.2 also lists the mesh cell size of three cases for three directions and the simulation time step. To make sure simulation results are reliable, the nondimensional time step and total time must be long enough to consider enough vortex shedding cycles, which are also listed in Table.6.3.3.

Table 6.3.1 Simulation domain dimension

CASE	B/D	B (m)	D (m)	3B (m)	8B (m)	3.5D (m)
LES1/LES2/IC1	1	0.2	0.2	0.6	1.6	0.7
CASE	B/D	B (m)	D (m)	4B (m)	8B (m)	3.5D (m)
LES3	1	0.2	0.2	0.8	1.6	0.7

Table 6.3.2 Summary of Computational cases: time step (Δt), uniform cell size at the upstream of cylinder (Δ_{up}), the downstream of cylinder (Δ_{down}), near the cylinder (Δ_{near}) and the spanwise diction of cylinder $\Delta_{spanwise}$

Case	Grid	Δ_{up}	Δ_{near}	Δ_{down}	$\Delta_{stepwise}$	Δt
LES1/IC1	120x80x30	0.02	0.01	0.02	0.01	0.01
LES2	160x10x30	0.02	0.01	0.02	0.01	0.01
LES3	120x80x40	0.02	0.01	0.02	0.01	0.01

Table 6.3.3 Computational cases parameters

CASE	Grid Density (element Num)	Inlet Velocity (m/s)	Reynolds Number	Nondimensional Time Step	Nondimensional Total Time
LES1/IC1	300,000	1.0	13,000	0.05	300
LES2	600,000	1.0	13,000	0.05	300
LES3	800,000	1.0	13,000	0.05	300

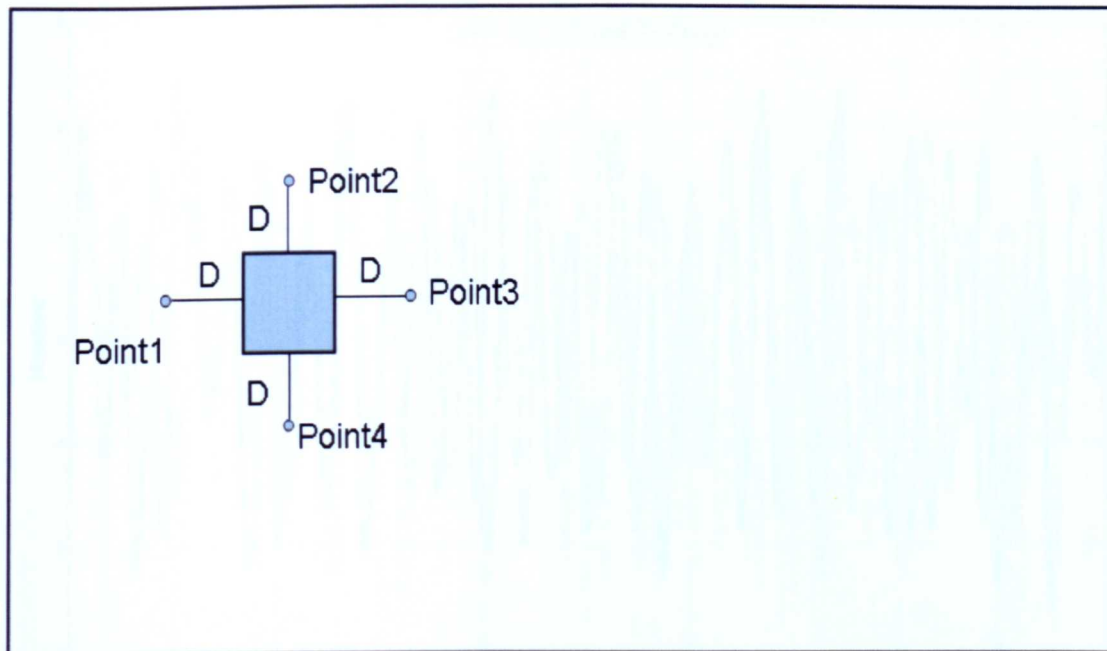


Fig 6.3.3 Monitor points position

Table 6.3.4 Positions of monitor points in the computational domain

<i>Position</i>	<i>Point 1</i>	<i>Point 2</i>	<i>Point 3</i>	<i>Point 4</i>
<i>Case</i>				
LES1/IC1	D=0.2 m	D=0.2 m	D=0.2 m	D=0.2 m

Fig.6.3.3 and Table.6.3.4 show 4 monitor points' position in the computation domain for all cases.

6.4 Results and Discussions

In this part, the results from the steady and unsteady inlet boundary conditions are discussed separately, and the simulation results of different LES models are compared.

6.4.1 Simulation Results of Steady Inlet Boundary Condition

In this section, the influence of mesh sensitivity, spanwise depth and different LES models on the flow characteristics around the square cylinder is presented by comparing the time history curves and power spectra of lift coefficient, the time averaged value of velocity components, RMS value and Reynolds stress with other numerical and experimental results.

(1) Lift Force Coefficient Time History and Power Spectrum Results

Firstly, the time history curves of lift force coefficient at nondimensional time steps for three cases LES1, LES2 and LES3 are plotted in Fig.6.4.1.

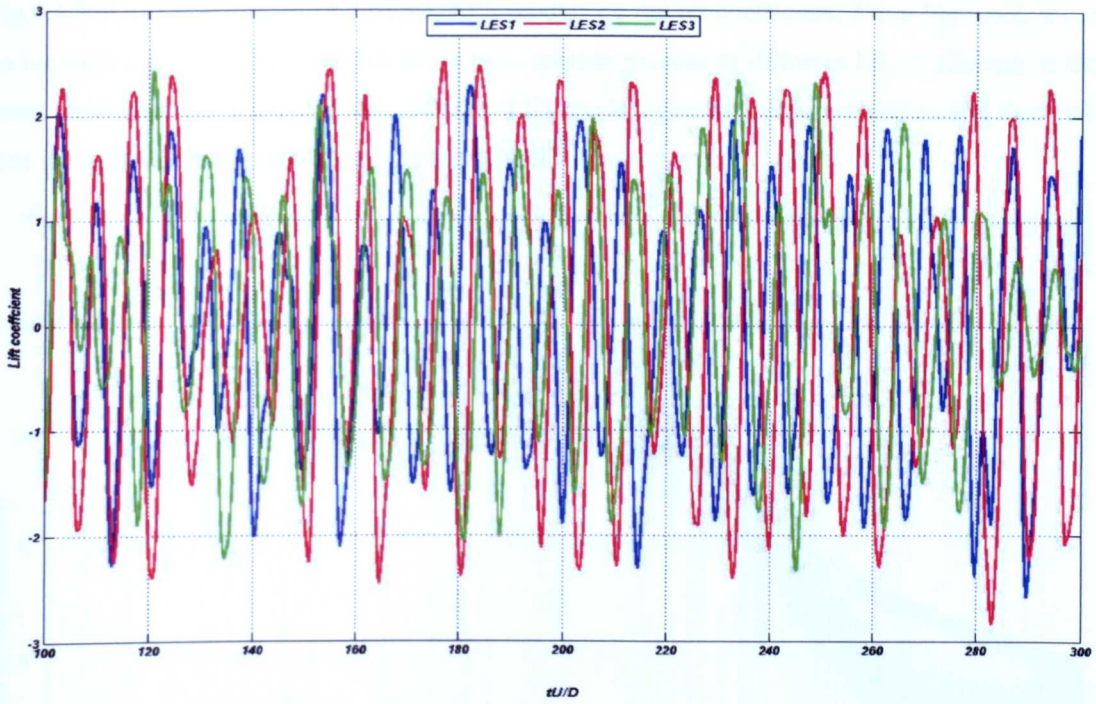


Fig 6.4.1 Lift coefficient's time history curves of LES1, LES2 and LES3

From Fig.6.4.1, it can be found that the peak value alternately takes place in three cases. The peak value of lift coefficient for LES1, LES2 and LES3 occurs at different nondimensional time steps, which further expresses LES is a grid sensitive technique. And the magnitude of lift coefficient value is different, even for the case LES1 and LES2 which both have the same dimension of simulation domain. However the mesh density of LES2 is finer than that of LES1.

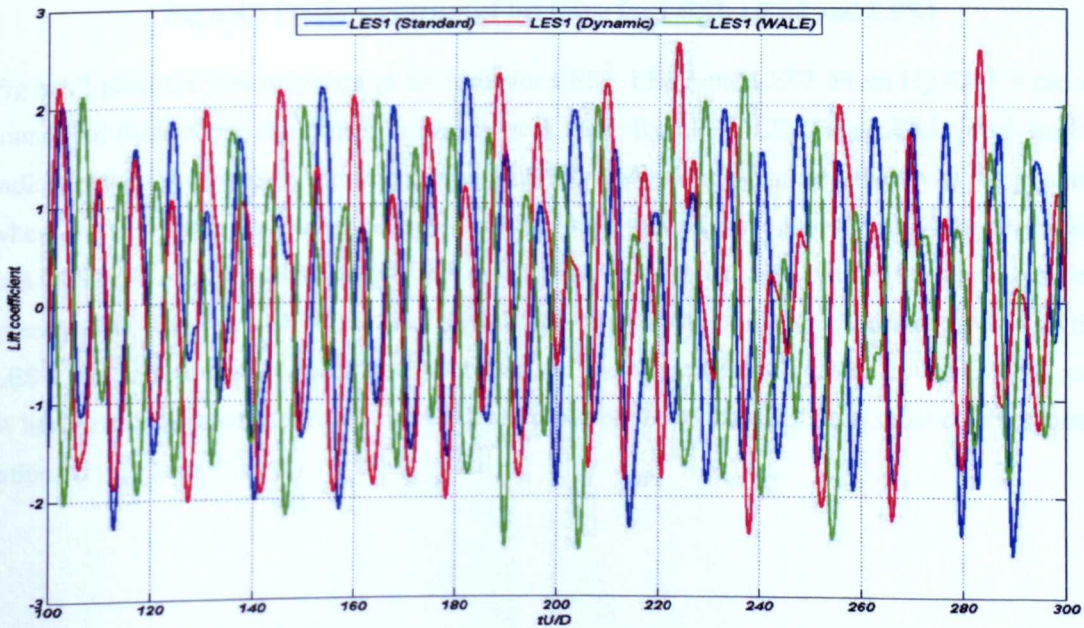


Fig 6.4.2 Lift coefficient's time history curves of LES1 (Standard), LES1 (Dynamic) and LES1 (WALE)

Fig.6.4.2 plots the influence of different LES models on the lift coefficient. From Fig.6.4.2, it can be found that different LES models show the variation process of different lift coefficients at the same mesh density, indicating that different LES models generate different eddies and these eddies will influence the pressure around the cylinder.

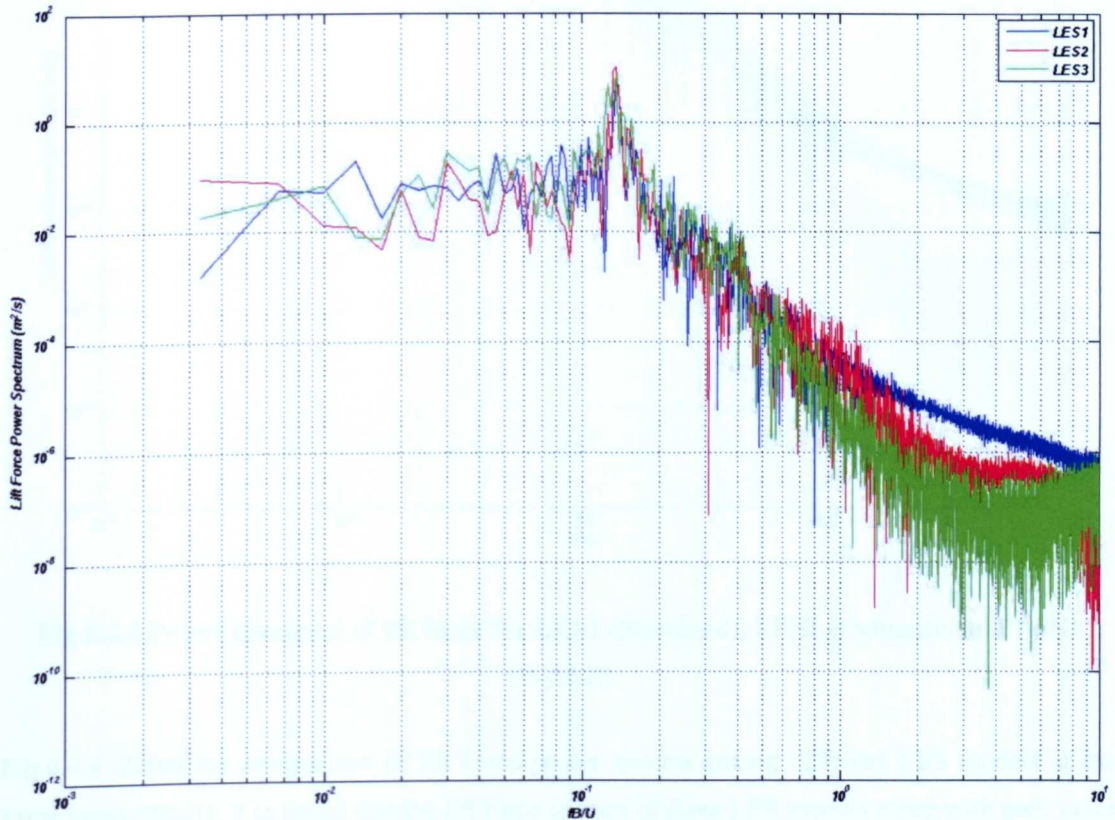


Fig 6.4.3 Power spectrum of lift force for LES1, LES2 and LES3

Fig.6.4.3 plots the power spectra of lift force for LES1, LES2 and LES3. From Fig.6.4.3 it can be found that there is one significant frequency peak value for LES1, LES2 and LES3, which further indicates the leading edge vortex shedding (LEVS) occurs. At the same time, from the position where the frequency peak value occurs, it can be found that it is the same for LES1 (coarse mesh) and LES2 (fine mesh), which shows that current coarse mesh can also predict the significant frequency peak value as well as the fine mesh at the same spanwise depth. And compared with the LES3, the peak frequency value is smaller than the one of the first two cases. By the comparisons of lift coefficient power spectra for three cases, it can be found that LES1 can satisfy current simulation.

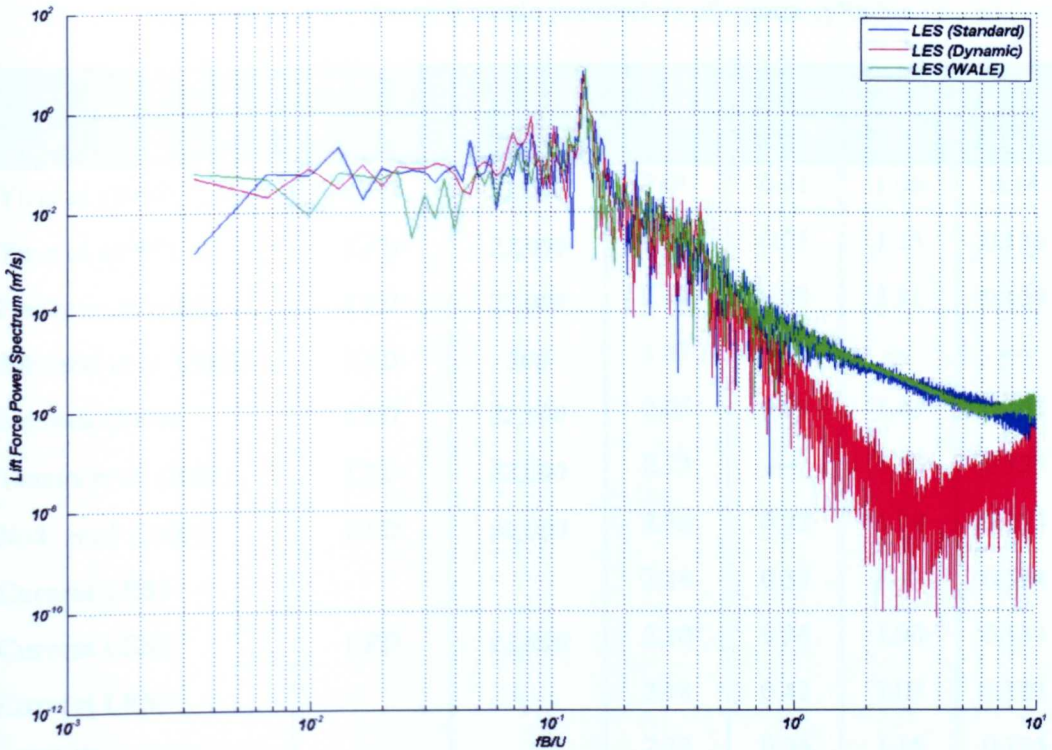


Fig 6.4.4 Power spectrum of lift force for LES1 (Standard), LES1 (Dynamic) and LES1 (WALE)

Fig.6.4.4 shows the comparison of lift force power spectra among different LES models at the same mesh density, it is found that the lift force spectra of three LES models agree with each other before the reduced frequency 1 Hz, however after this frequency, especially in the high reduced frequency range, the lift force power spectrum for LES (Dynamic) model is lower than the other two cases. The reason is that the LES constant of LES dynamic model varies, unlike the one in LES (Standard) and LES (WALE) model.

(2) General Aerodynamic Parameters

In this part of study, the drag coefficient (\bar{C}_D) mean value and RMS value of lift coefficient (C_L^{rms}) and drag coefficient (C_D^{rms}) and Strouhal number (St) are considered firstly. Table.6.4.1 summarizes the general aerodynamic parameters of square cylinder based on other numerical and experimental technique at different Reynolds numbers.

Table 6.4.1 General aerodynamic parameters of square cylinder

Author	Method	Reynolds Number	\bar{C}_D	C_D^{rms}	C_L^{rms}	St
Yu <i>et al.</i> (1995)	CFD	22,000	2.01	0.21	1.06	0.14
Yu <i>et al.</i> (1997)	CFD	22,000	2.14	0.25	1.15	0.135
Franke <i>et al.</i> (1991)	CFD	22,000	2.15	0.38	2.11	0.136
Sohankar <i>et al.</i> (2002)	CFD	500	1.87	—	—	—
Shimada (2002)	CFD	22,000	2.05	0.09	1.43	0.141
Tamura <i>et al.</i> (2003)	CFD	22,000	2.13	—	1.20	0.125
Noda <i>et al.</i> (2003)	CFD	50,000	2.36	0.22	1.24	0.133
Current LES1			2.14	0.39	1.18	0.134
Current LES2	CFD	13,000	2.10	0.36	1.90	0.134
Current LES3			2.18	0.42	1.09	0.132
LES1 (Dynamic)			2.13	0.36	1.15	0.134
LES1 (WALE)	CFD	13,000	2.16	0.39	1.20	0.136
Lee (1975)	Experiment	—	2.05	0.22	1.22	—
		3,000	—	—	—	0.132
Okajima (1982)	Experiment	300	—	—	—	0.130
Bearman <i>et al.</i> (1982)	Experiment	22,000	2.10	—	—	—
Igarashi (1987)	Experiment	3,000	2.10	—	—	—
Durao <i>et al.</i> (1988)	Experiment	14,000	—	—	—	0.133
Sakamoto <i>et al.</i> (1989)	Experiment	—	2.22	0.13	1.45	0.134
Norberg (1993)	Experiment	14,000	2.11	—	—	—
Lyn <i>et al.</i> (1995)	Experiment	22,000	—	—	—	0.130
Tamura <i>et al.</i> (2003)	Experiment	22,000	2.05	—	1.23	0.120
Noda <i>et al.</i> (2003)	Experiment	68,900	2.16	0.21	1.18	0.131

Table.6.4.1 lists the values of Strouhal number calculated from peak values of the power spectra in Fig.6.4.3 and Fig.6.4.4. From the comparison with other experimental and CFD values in the table, it is found that current computed results agree with other experimental and numerical results well, although there are some differences. Compared with the Strouhal number at a Reynolds number of 14,000 calculated by Durao *et al.* (1988), the percentage of the difference of current simulations is small in the acceptance range, which is 0.7%. The reason of this difference is that different turbulence models or numerical methods are applied in the CFD simulation. While for the experimental

technique, the difference is from the experimental condition. At the same time the process of variation of Strouhal number at different Reynolds numbers is plotted in Fig.6.4.5, from which it can be found that when the Reynolds number is above 10,000, the Strouhal number remains an almost constant value of 0.130. When the Reynolds number rises from 10 to 1,000, the basic characteristics of increasing St with Re at low Re is evident. When the Reynolds number is at 22,000 in Table.6.4.1, the Strouhal number is 0.130 in the study by Lyn *et al.* (1995), 0.135-0.140 by Yu *et al.* (1995, 1997) in the CFD study, 0.120-0.125 by Tamura *et al.* (2003) CFD and experimental study, 0.136 and 0.147 by Franke *et al.* (1991). Generally, with the Reynolds number increases the Strouhal number remains constant (Reynolds number > 1,000). For different LES models, the Strouhal number for current LES standard model is 0.134, while the number is 0.134 for current LES dynamic model and 0.136 for current LES WALE model.

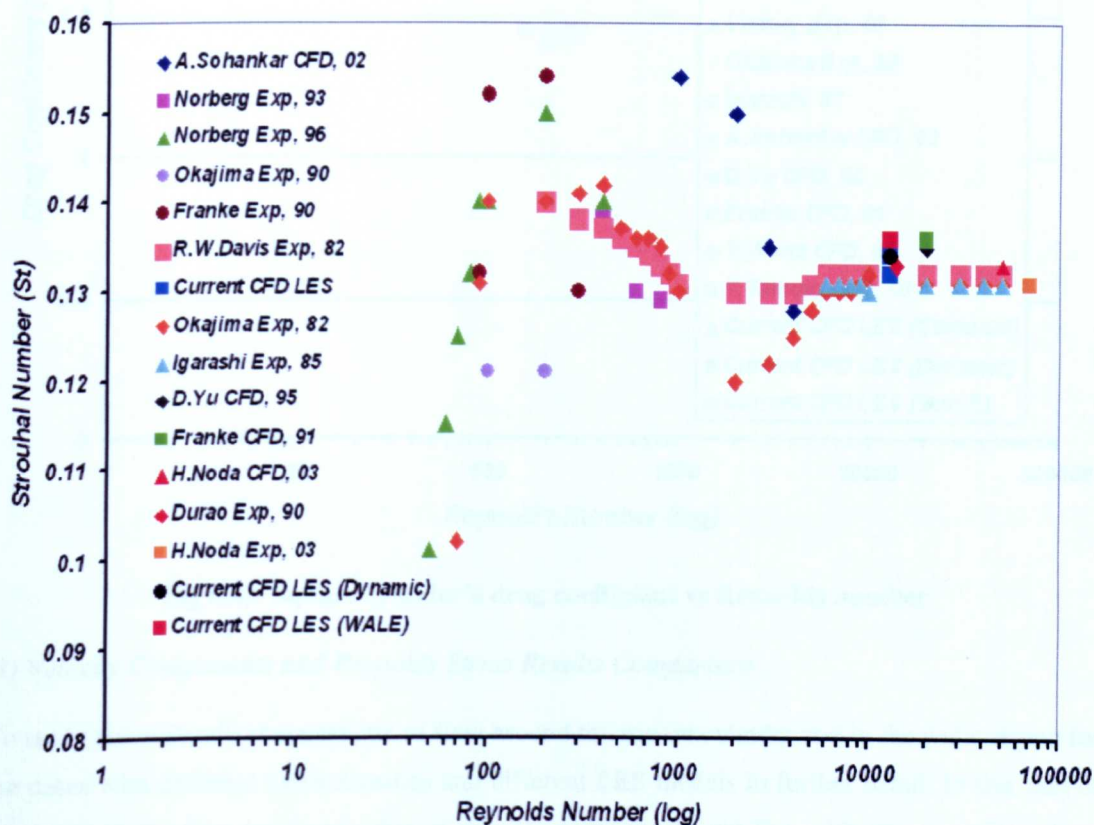


Fig 6.4.5 Square cylinder’s Strouhal number vs Reynolds number

The general aerodynamic parameters such as the RMS value of lift coefficient and drag coefficient at different Reynolds numbers are also listed in Table.6.4.1. Even for the same Reynolds number, the RMS value of drag and lift coefficient value are different, and this is also from the same reasons as stated above. For the mean value of drag coefficient, the maximum percentage difference of the calculated value from the current simulation considering mesh density is 3.3%, while for different LES models it is 1.0% which is in the acceptable range compared with the experimental results of Norberg (1993) at Reynolds number `14,000. The drag coefficient value remains more or less the constant 2.10. The variation process for the mean value of drag coefficient at different

Reynolds numbers is plotted in Fig.6.4.6; from this figure it can be found that when Reynolds numbers is below 1,000, there is a large discrepancy. Between Reynolds numbers of 100 and 1,000 there is a parabolic curve, which has been studied both experimentally (Okajima, 1995). This curve is generated by the fact that the transition from the laminar to turbulence occurs within this range.

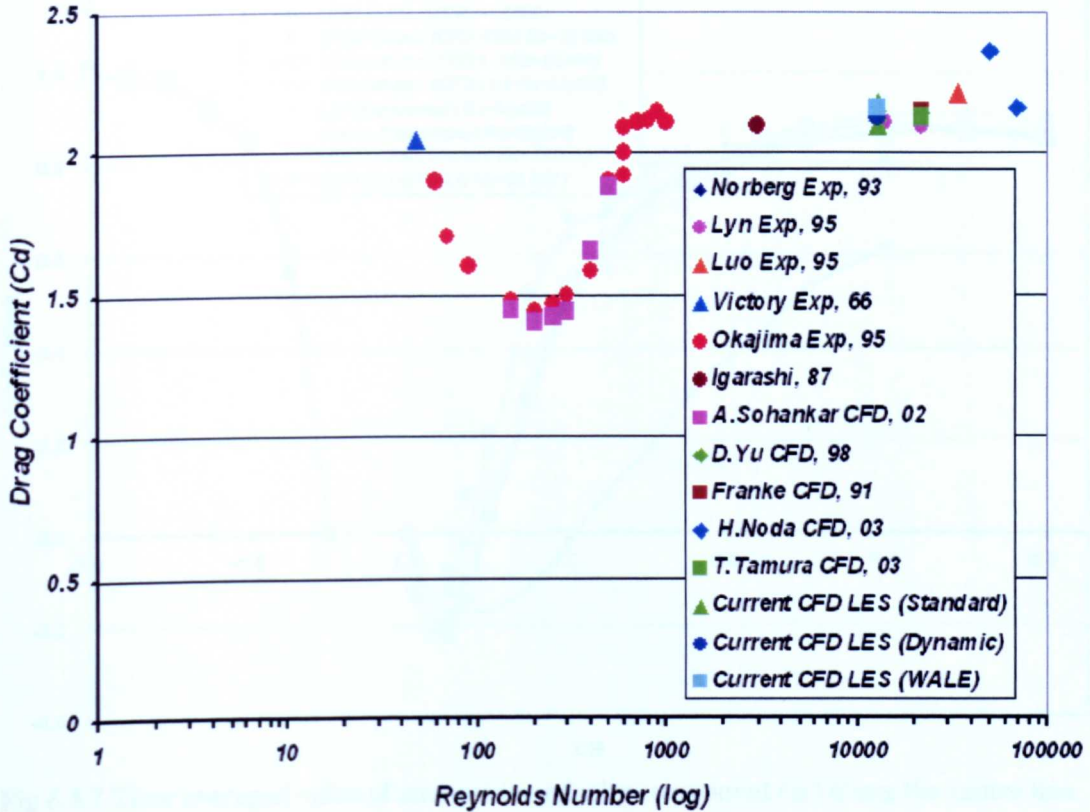


Fig 6.4.6 Square cylinder’s drag coefficient vs Reynolds number

(3) Velocity Components and Reynolds Stress Results Comparison

To study the unsteady characteristic of flow around the square cylinder and in the wake region for the cases with different mesh densities and different LES models in further detail. In this part of the analysis, the time averaged value of velocity components and Reynolds stress profiles along the centre line of the domain and vertical middle line at the top side of a square cylinder will be discussed firstly.

Fig.6.4.7 plots the time averaged mean values of streamwise velocity component from current simulation cases and other experimental and CFD results at the centreline of the computational domain respectively. It can be found that the results of LES1, LES2 and LES3 agree with the CFD simulation results from Murakami (1998) based on the Reynolds stress model (RSM) and LES model at a Reynolds number of 22,000 very well, compared with the experimental results by Lyn *et al.* (1995) at a Reynolds number of 14,000 and Durao *et al.* (1988) at a Reynolds number of 22,000, it also shows good agreement. However there is a large discrepancy in the wake region

between the numerical simulations by Murakami (1998) based on the standard $k - \epsilon$ model and current simulation, and other CFD and experimental results, the reason being that $k - \epsilon$ model simulates the turbulence in the wake region based on the statistical model, which underestimates the simulated energy transfer.

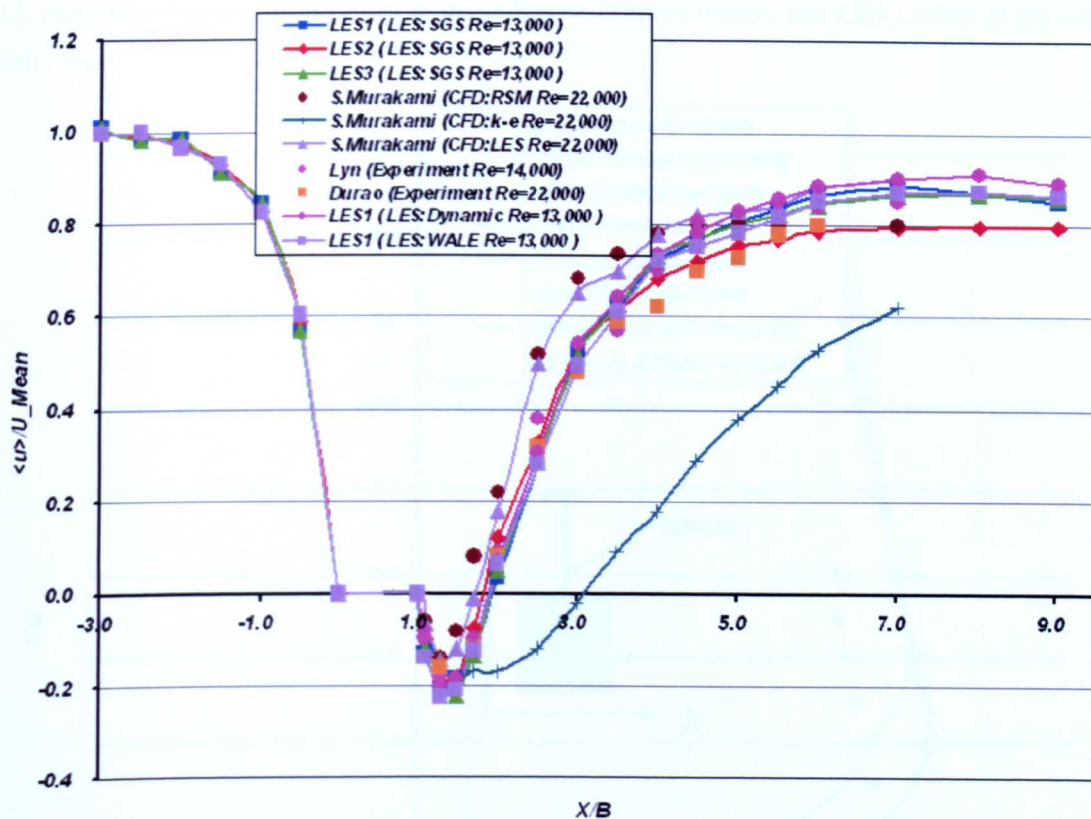
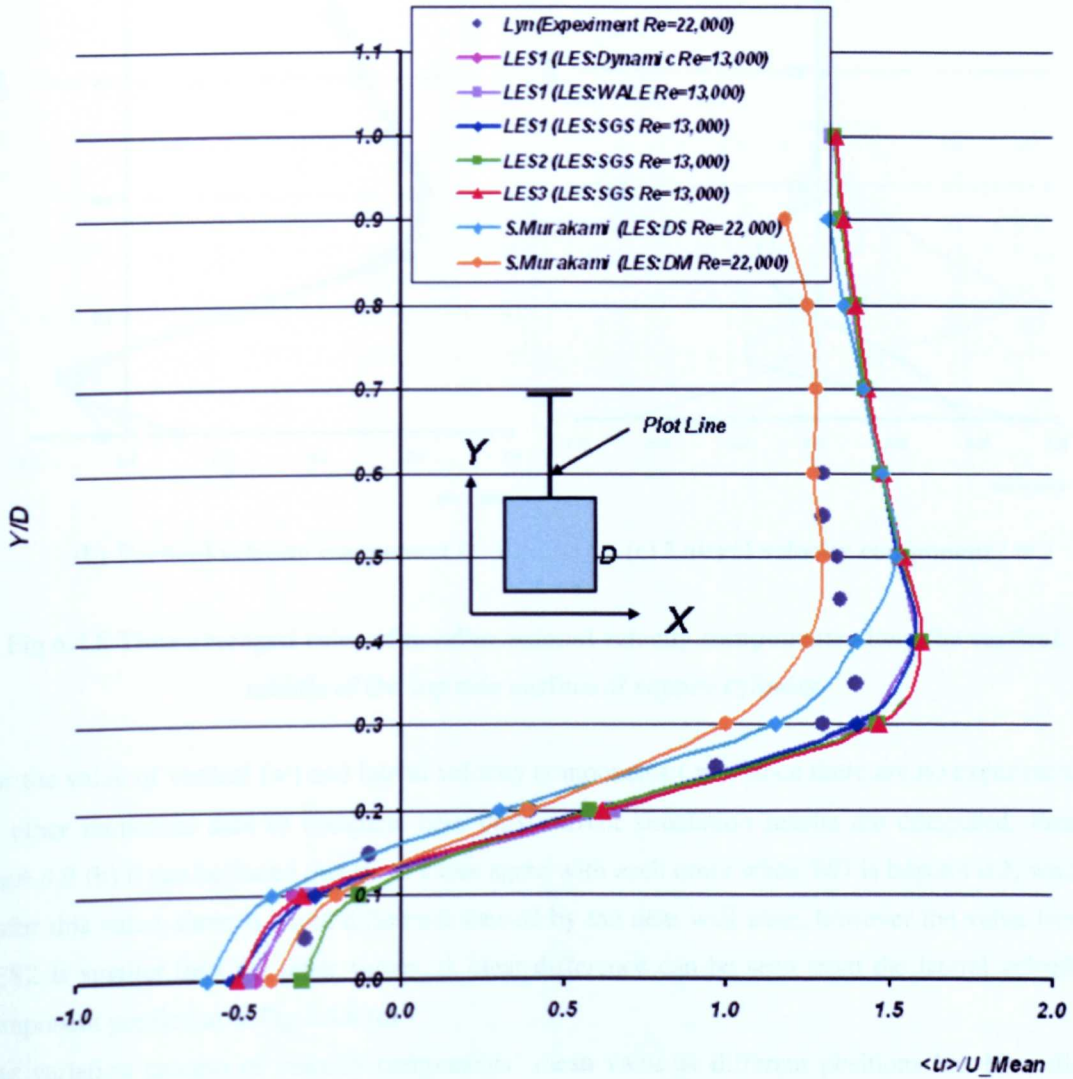


Fig 6.4.7 Time averaged value of streamwise velocity component (u) along the centre line

Comparing the results among the cases with different mesh density, it can be found that the values of streamwise velocity components of LES1 and LES3 in the wake region, especially from $X/B = 4.0$ to 9.0 , are higher than the value of LES2 with fine mesh density, further illustrating that the LES technique is a grid sensitive simulation method. Comparing different LES models' simulation results, it is found that in the wake region LES (Dynamic) model result is higher than the one from LES (WALE) model.

Fig.6.4.8 shows the vertical profiles of the streamwise, vertical and lateral velocity components mean values predicted by different mesh cases and LES models. To validate the results, the experimental results from Duraõ *et al.* (1988) and numerical results from Murakami (1998) are used to compare the distribution of the streamwise velocity component. In Fig.6.4.8 (a), a clear difference can be found between the LES numerical results from Murakami (1998) and the results from this study, which are caused by the difference of mesh and model and the different wall functions, and current simulations adopt automatic wall function in CFX. At the same time when Y/D is beyond 0.5 , current LES results agree with Murakami LES: DS result very well, which means that the influence of wall function is smaller. Comparing numerical results with the experimental result

from Lyn (1995), there are some discrepancy between numerical results and the experimental one. Comparing the streamwise velocity component near the wall, it can be found that the predicted value is different from the experimental and numerical simulation. While for current simulation results, it is found that beyond $Y/D = 0.1$ current results agree with each other well, below $Y/D = 0.1$, there are some discrepancy due to the influence of mesh density and LES models at the near wall zone.



(a) Streamwise velocity component (u)

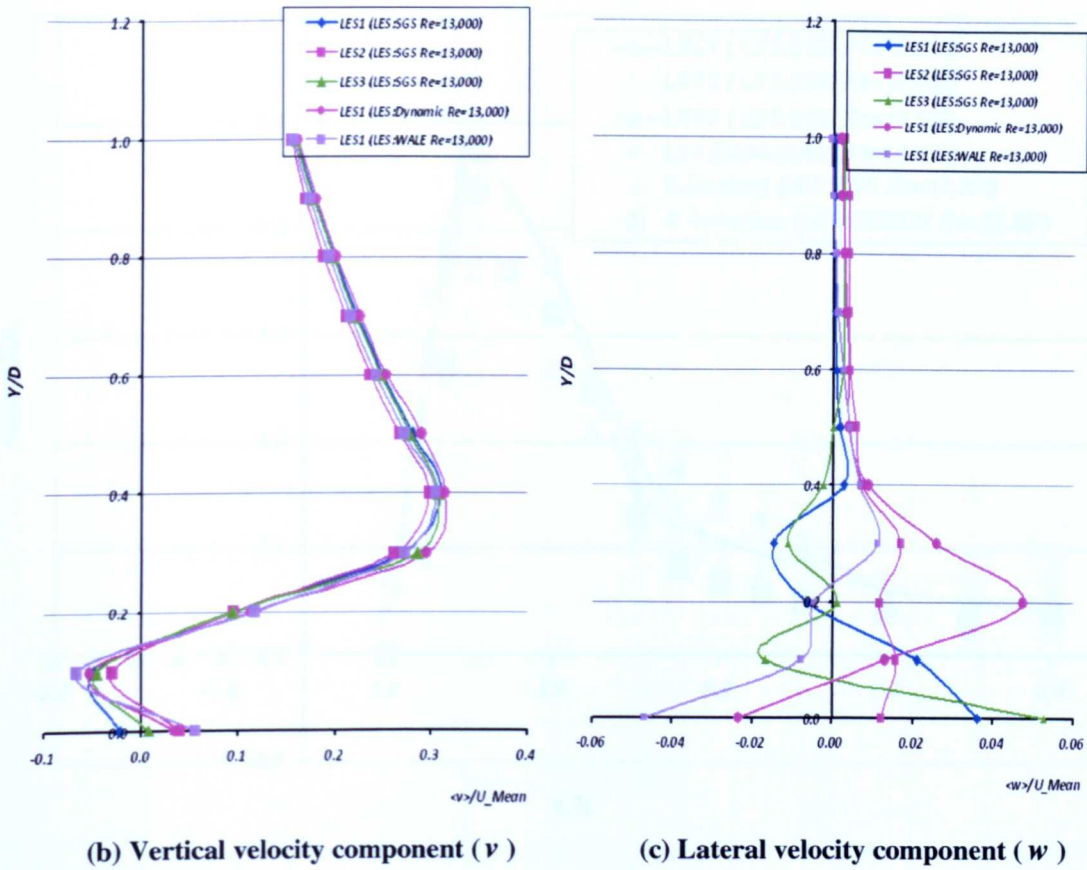
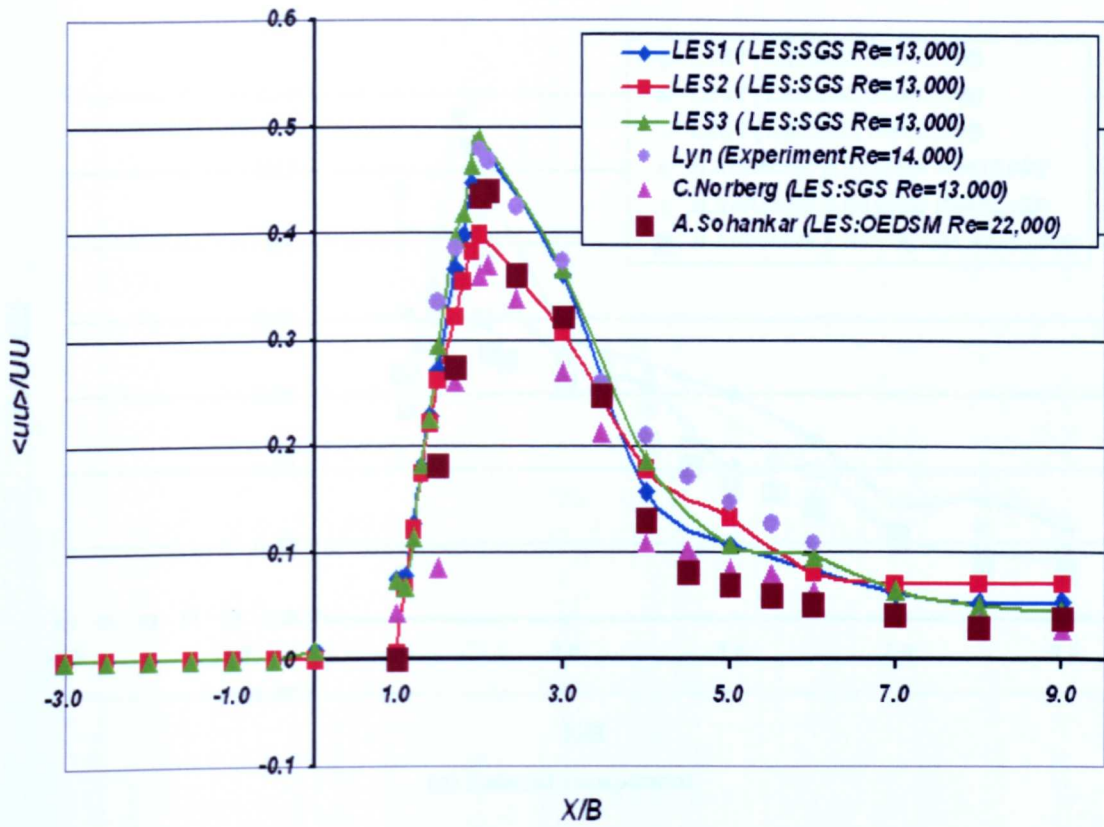


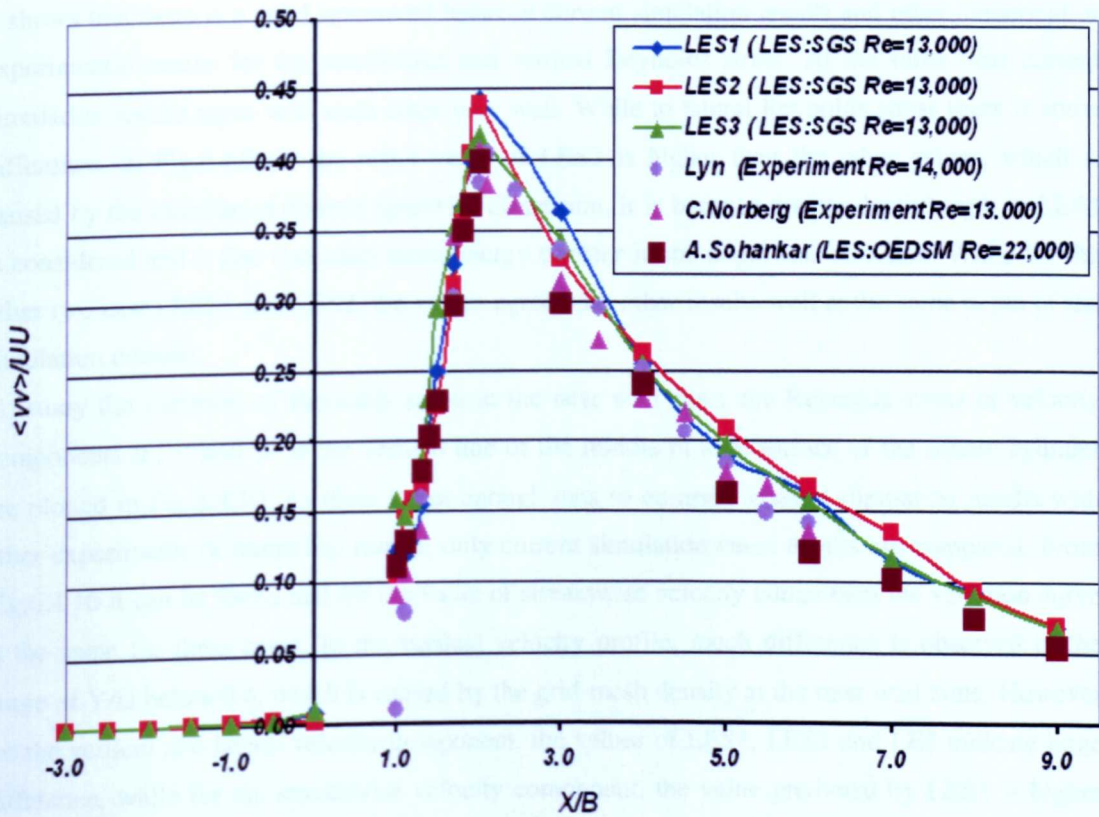
Fig 6.4.8 Time averaged value of nondimensional velocity components along the vertical middle of the top side surface of square cylinder

For the value of vertical (v) and lateral velocity components (w), since there are no experiments or other numerical data to compare, here only current simulation results are compared. From Fig.6.4.8 (b) it can be found that those cases agree with each other when Y/D is beyond 0.2, while under this value, there is slight difference caused by the near wall zone, however the value from LES2 is smaller than the other values. A clear difference can be seen from the lateral velocity component prediction in Fig.6.4.8 (c).

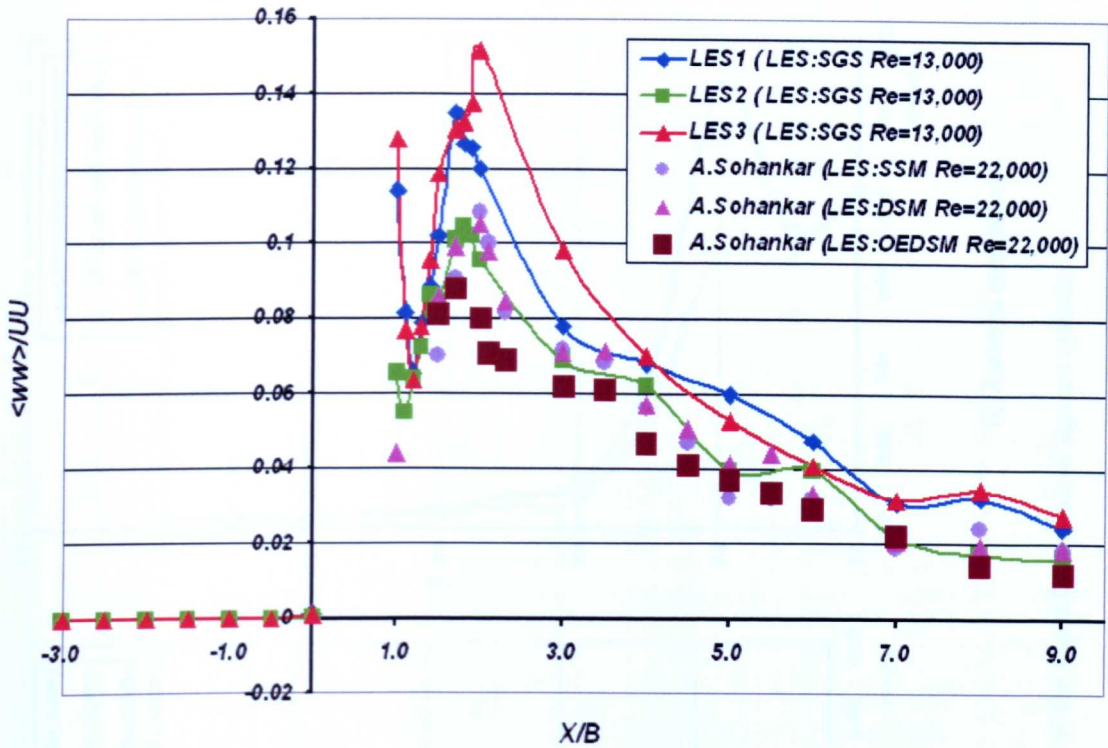
The variation process of velocity components' mean value at different positions has been discussed in the above discussions. Further data regarding Reynolds stress, which is very important in the buffeting prediction, will be discussed in the following content. From Fig.6.4.9 to Fig.6.4.10, the simulated Reynolds stress components in the streamwise direction ($\langle uu \rangle / UU$), the spanwise direction ($\langle ww \rangle / UU$) and the vertical direction ($\langle vv \rangle / UU$) are plotted along the centre line of the domain and the vertical line at the middle of side surface of a square cylinder. To validate current simulation results, numerical simulation results from Norberg (1993) at a Reynolds number of 13,000 and Sohankar (2002) at a Reynolds number of 22,000 and the experimental result from Lyn (1995) at a Reynolds number of 14,000 are adopted.



(a) Streamwise component



(b) Vertical component

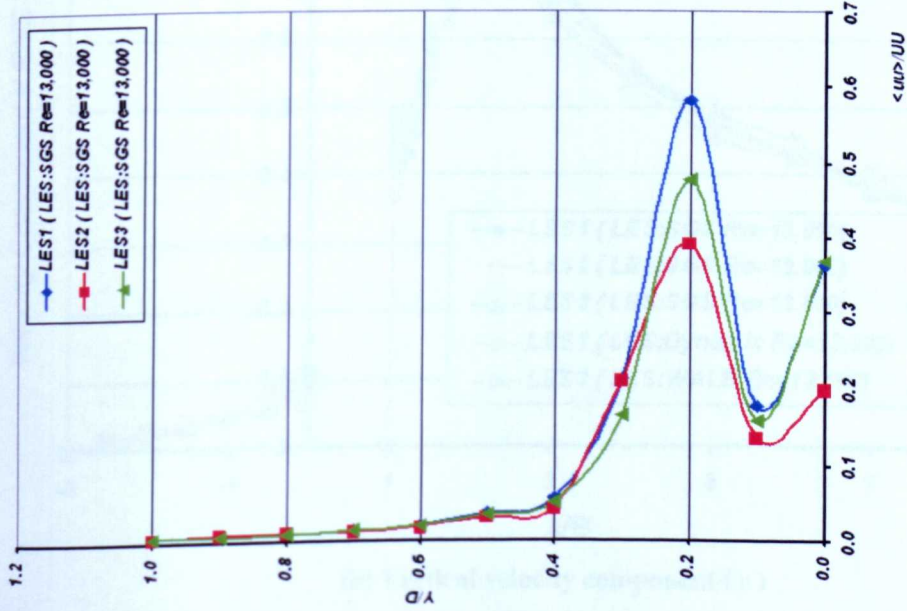


(c) Lateral component

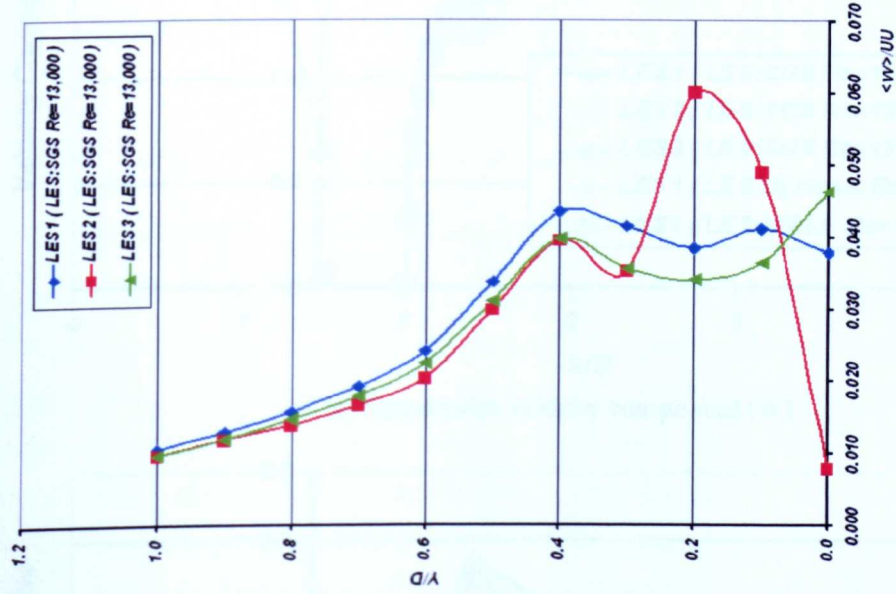
Fig 6.4.9 Nondimensional Reynolds stress along the center line

Fig.6.4.9 shows the variation of Reynolds stress along the centre line of the computational domain, it shows that there is a good agreement between current simulation results and other numerical or experimental results for the streamwise and vertical Reynolds stress. At the same time current simulation results agree with each other very well. While to lateral Reynolds stress there is some difference, in Fig.6.4.9 (c) the result value of LES3 is higher than the other values, which is caused by the calculation domain spanwise dimension, it is because greater depth length in LES3 is considered and it also considers more energy transfer in the depthwise direction. While for the other two cases LES1 and LES2, the values agree with other results well at the same depth of the simulation domain.

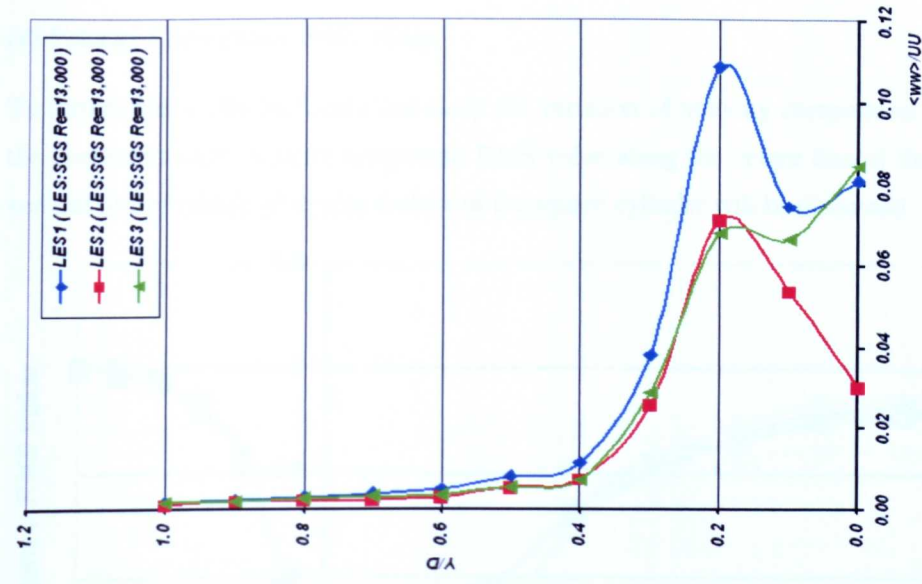
To study the variation of Reynolds stress at the near wall zone, the Reynolds stress of velocity components u , v and w at the vertical line of the middle of side surface of the square cylinder are plotted in Fig.6.4.10. As there is not enough data to compare current simulation results with other experiments or numerical results, only current simulation cases results are compared. From Fig.6.4.10 it can be found that for the value of streamwise velocity component the variation curve is the same for three cases. In the vertical velocity profile, much difference is observed in the range of Y/D below 0.4, which is caused by the grid mesh density at the near wall zone. However for the vertical and lateral velocity component, the values of LES1, LES2 and LE3 indicate large difference, while for the streamwise velocity component, the value predicted by LES1 is higher than the other two cases.



(a) Streamwise component



(b) Vertical component

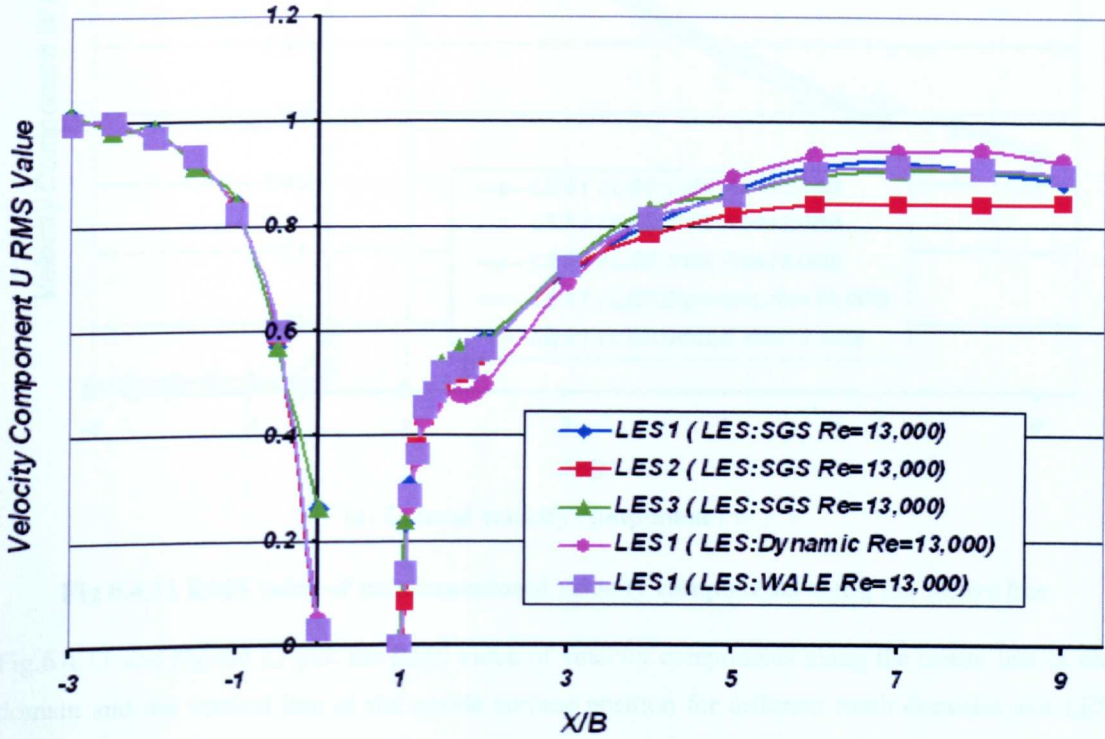


(c) Lateral component

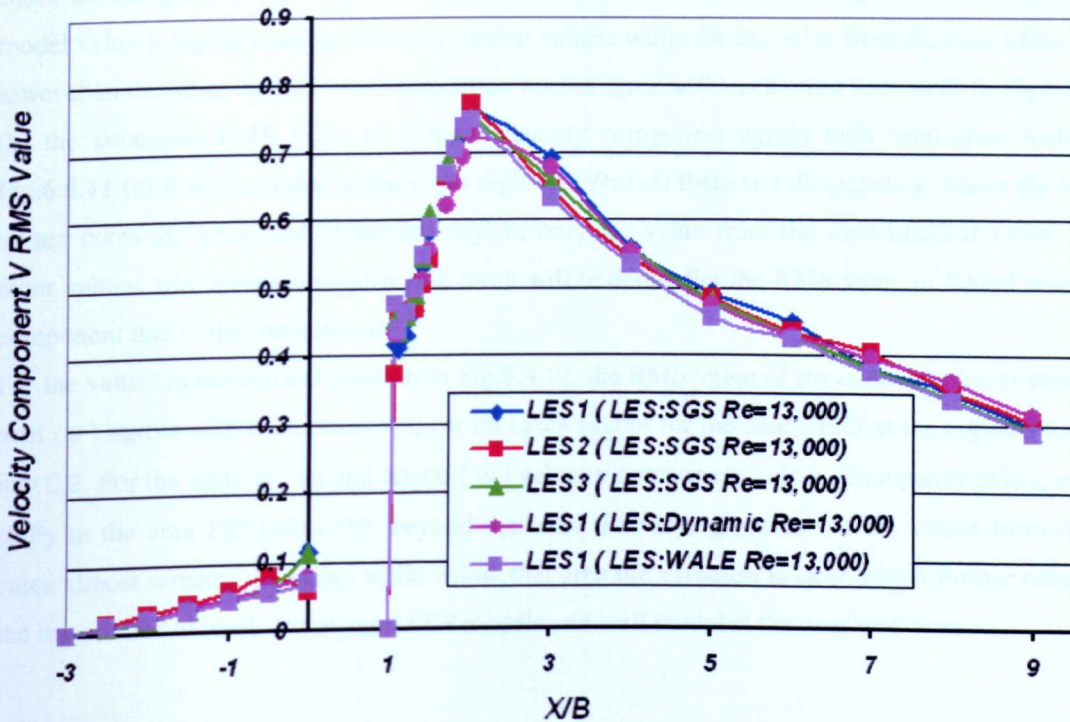
Fig 6.4.10 Nondimensional Reynolds stress along the vertical middle line of the top side surface of square cylinder

(4) Velocity Components RMS Value

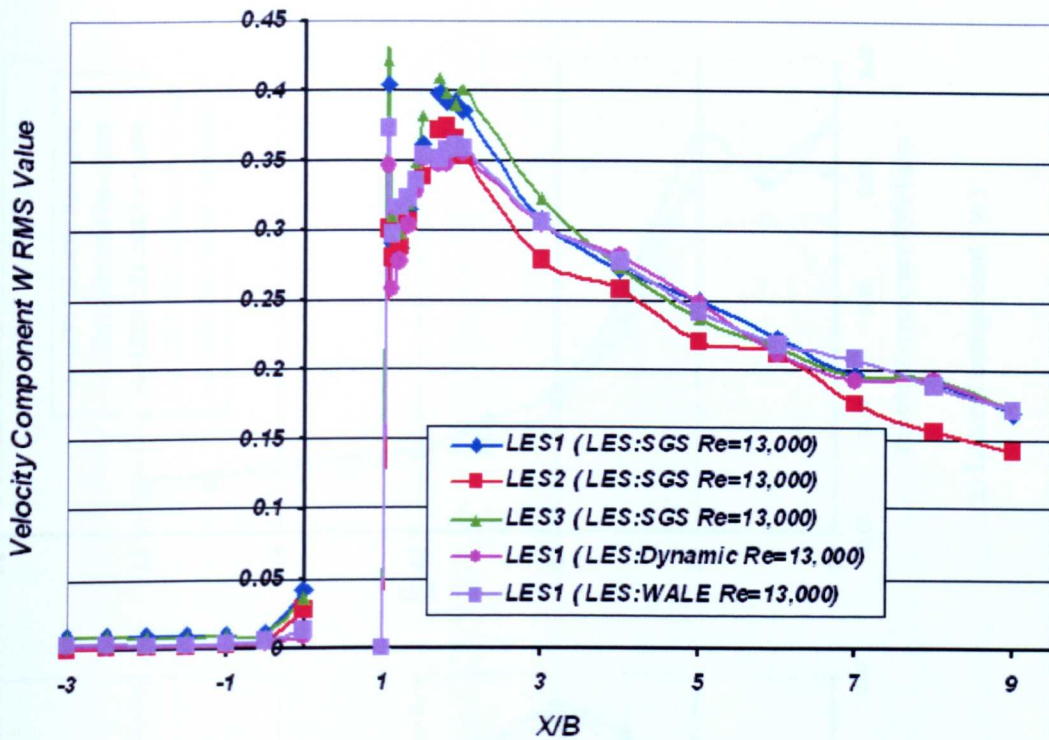
To further predict the buffeting and study the variation of velocity components statistical values, the nondimensional velocity component RMS value along the centre line of the domain and the vertical line of middle of upside surface of the square cylinder will be discussed.



(a) Streamwise velocity component (u)



(b) Vertical velocity component (v)



(c) Lateral velocity component (w)

Fig 6.4.11 RMS value of nondimensional velocity components along the centre line

Fig.6.4.11 and Fig.6.4.12 plot the RMS value of velocity components along the centre line of the domain and the vertical line of the upside surface position for different mesh densities and LES models. Due to data limitations from other experimental or numerical studies, only current LES cases are compared. From Fig.6.4.11 (a) it can be found that in wake region LES1 (Dynamic) model value is higher than the other simulation values, while for the value from the case LES2 it is lower than the other models, other simulation results agree with each other very well. In Fig.6.4.11 (b) the simulated RMS value of vertical velocity component agrees with each other well. In Fig.6.4.11 (c) it is found that in the wake region ($X/B=1-3$) there is a discrepancy, where the large vortex cores are generated. After this region, only the value from the case LES2 is lower than other values, which represents that fine mesh will underpredict the RMS value of lateral velocity component due to the mesh density.

For the values at the vertical position in Fig.6.4.12, the RMS value of streamwise velocity component (u) agrees with each other well for all cases except for the case LES2 at the region Y/D below 0.2. For the vertical (v) and lateral (w) velocity components, clear discrepancy exists, especially in the area Y/D below 0.2, beyond that area the varying process of the values from other cases almost remains the same, while below that area the variation is clear which further presents the importance of mesh density and LES models and wall model at the near wall zone.

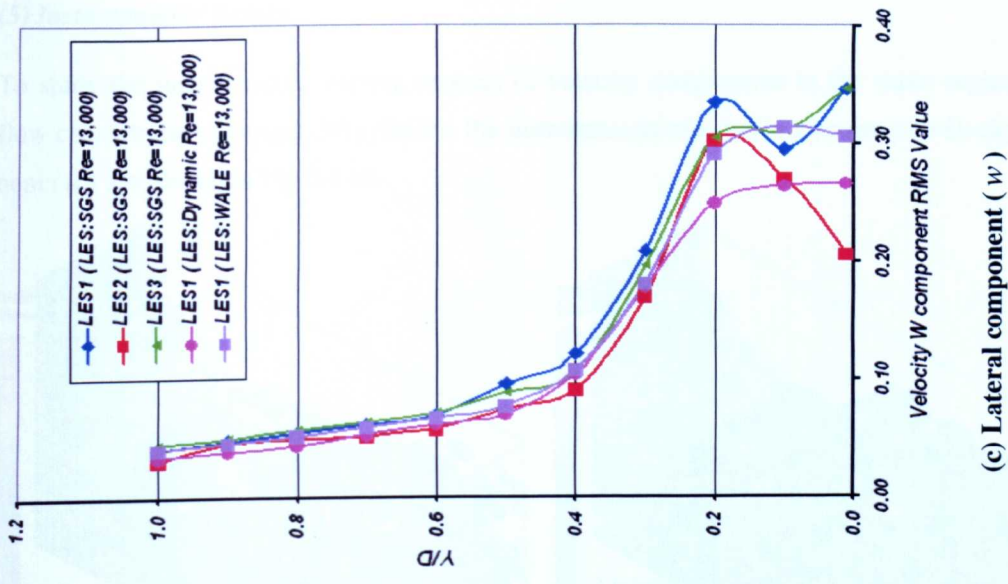
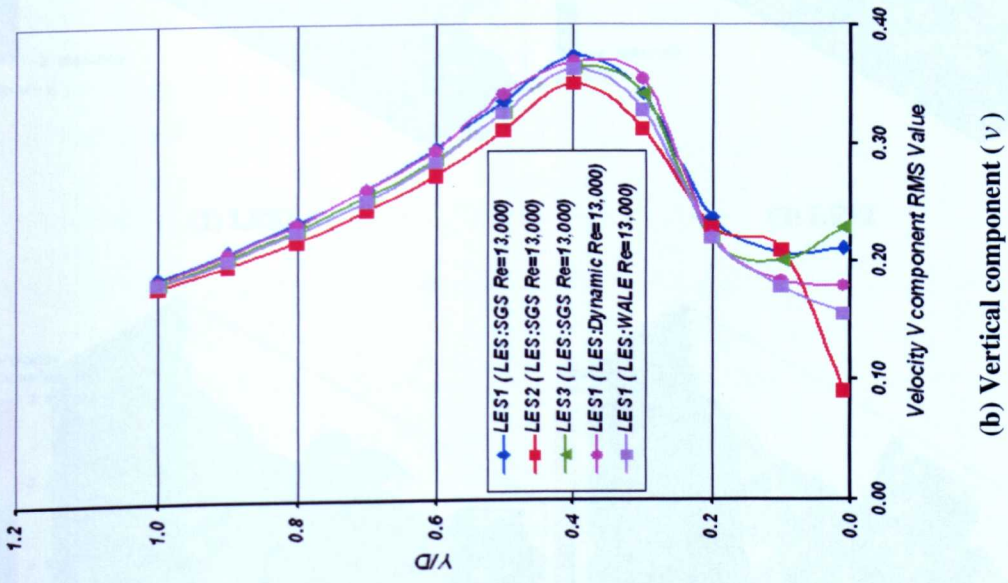
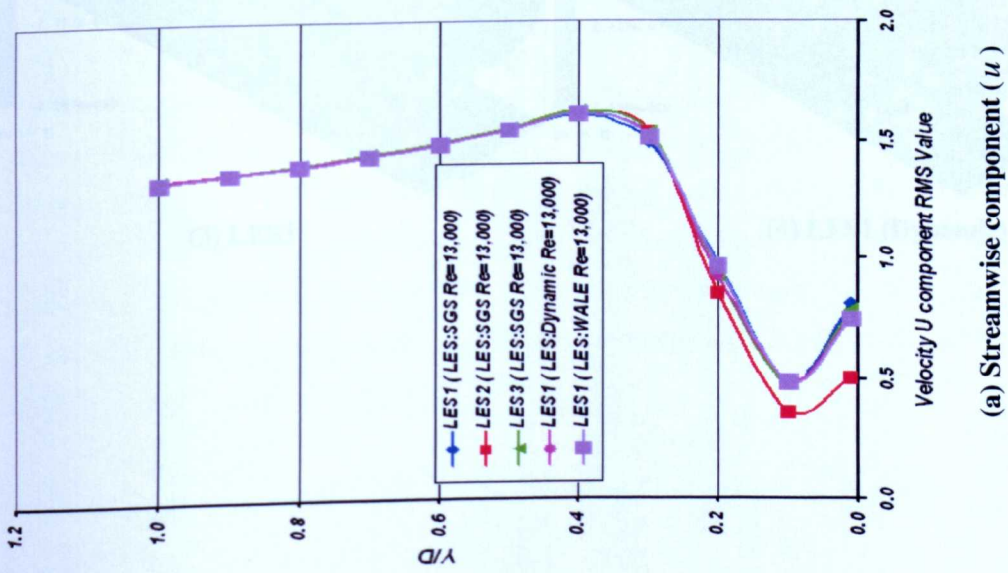
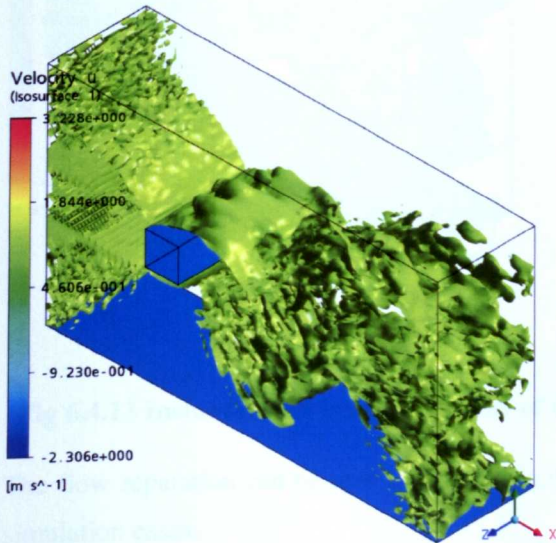


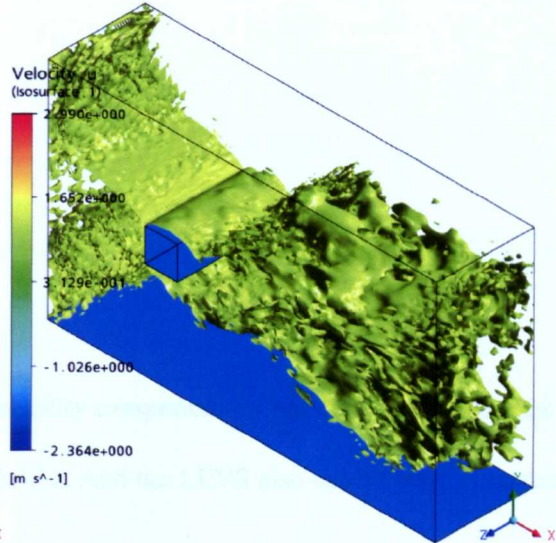
Fig 6.4.12 RMS value of nondimensional velocity components along the vertical middle line of the top side surface of square cylinder

(5) *Instantaneous Results*

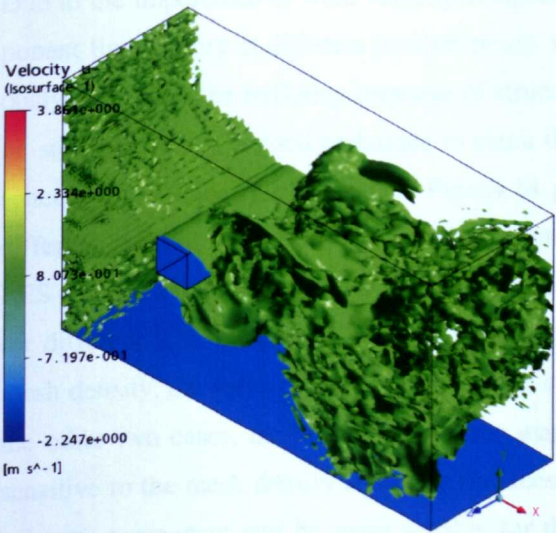
To study the instantaneous varying process of velocity components in the wake region and the flow characteristics around the cylinder, the instantaneous results for streamwise velocity component (u) are plotted in Fig.6.4.13.



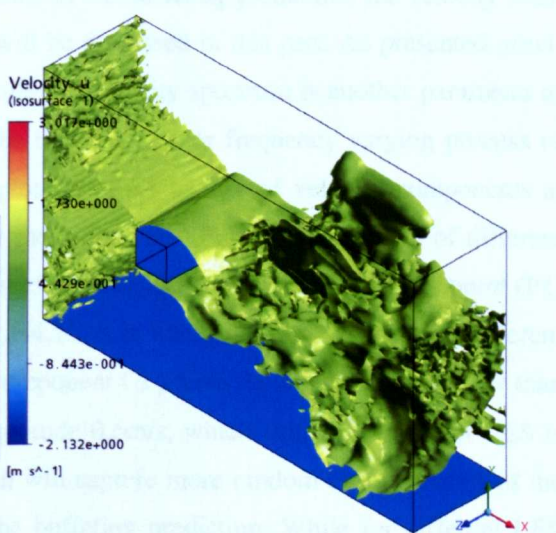
(1) LES1



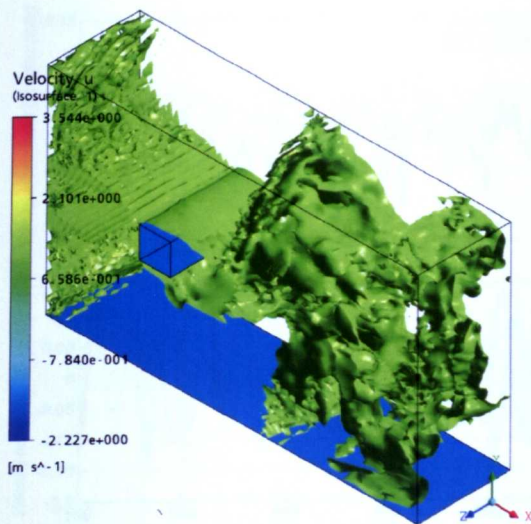
(2) LES2



(3) LES3



(4) LES1 (Dynamic)



(5) LES (WALE)

Fig 6.4.13 Instantaneous isosurface value of velocity component (u) of current simulations

The flow separation can be seen clearly in Fig.6.4.13. And the LEVS also can be seen in current simulation cases.

(6) Velocity Components Time History Curve of Monitor Points

Due to the importance of wind velocity components in the buffeting prediction, the velocity component time history at different monitor points will be discussed in this part. As presented previously, to predict the buffeting response of structure the velocity spectrum is another parameter to be studied, LES is a good technique to catch the time varying or frequency varying process of space points' velocity components. Fig.6.4.14 plots the time history of velocity components at different monitor P1 for three cases of different mesh densities. For the comparison of different LES models, Fig.6.4.15 plots the time history curves of velocity components at monitor point (P1) for different LES models. In Fig.6.4.14 and Fig.6.4.15, it is found that for the cases of different mesh density, the value of streamwise velocity component (u) from the case LES2 is higher than the other two cases, the value varies at the magnitude 0.6m/s, which further shows that LES is sensitive to the mesh density and more fine mesh will capture more random characteristics of the velocity component and be more suitable for the buffeting prediction. While for different LES models the simulated value of streamwise velocity component (u) based on the LES Standard model is lower than the other models, while for the velocity component (w) the vibrating magnitude of LES Standard model is higher than the other two. It shows that different LES models will generate different velocity time history.

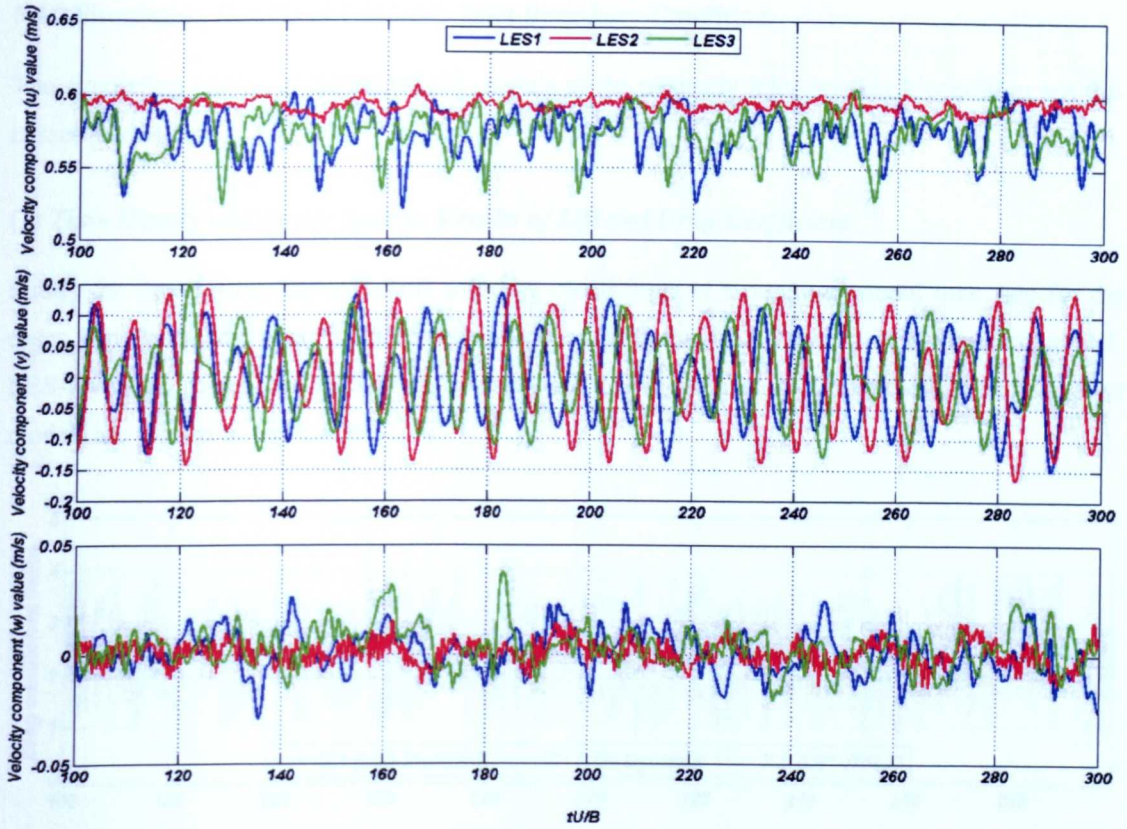


Fig 6.4.14 Velocity components' time history of LES1, LES2 and LES3 at point P1

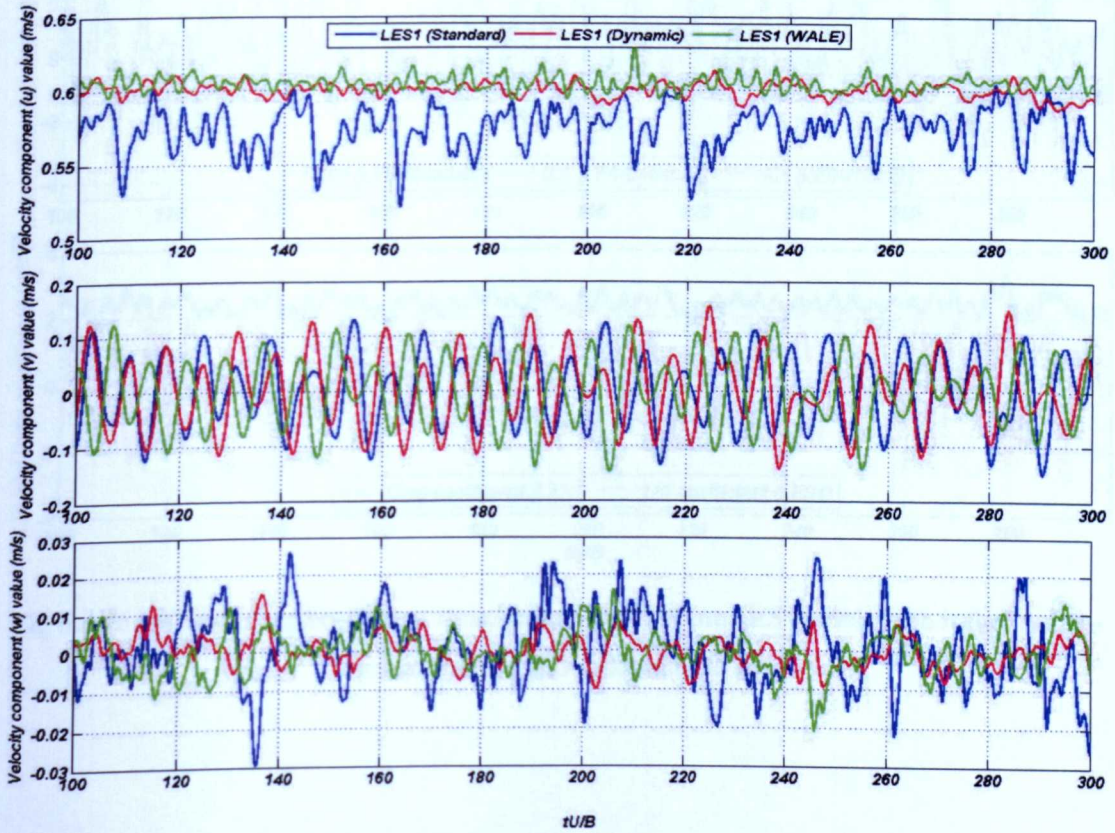


Fig 6.4.15 Velocity components' time history of LES1 (Standard), LES1 (Dynamic) and LES1 (WALE) at point P1

6.4.2 Simulation Results of Unsteady Inlet Boundary Condition

The simulation results of different LES models at the unsteady inlet boundary condition are discussed in this part.

(1) Time History and Power Spectra Results of Lift and Drag Coefficient

Firstly the time history curves of lift and drag coefficients of a nondimensional time step for the cases IC1 (unsteady inlet boundary condition) of different LES models, LES-Standard model, LES-Dynamic model and LES-WALE model and LES1 (steady inlet boundary) (LES-Standard model) are plotted in Fig.6.4.16.

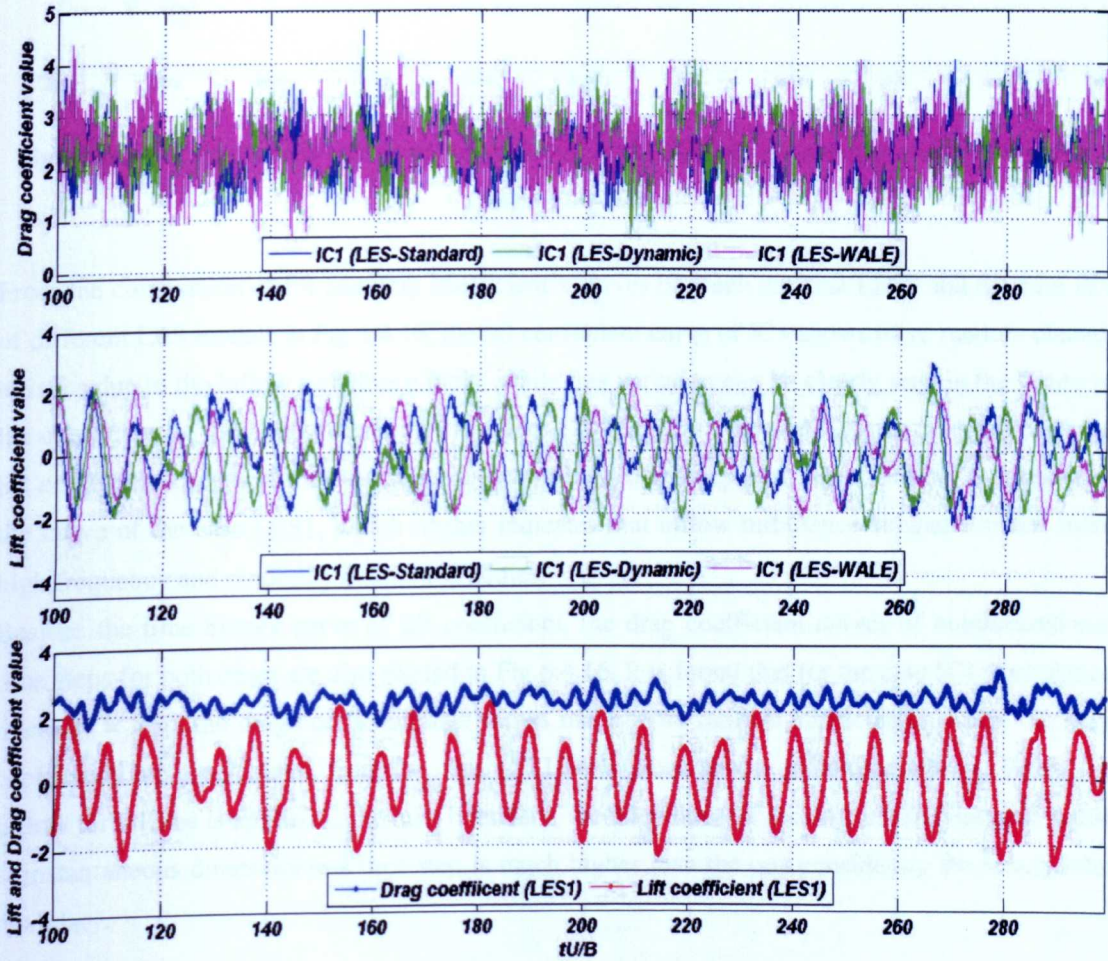


Fig 6.4.16 Lift and drag coefficient time history of different LES models with inflow turbulence at the nondimensional time step

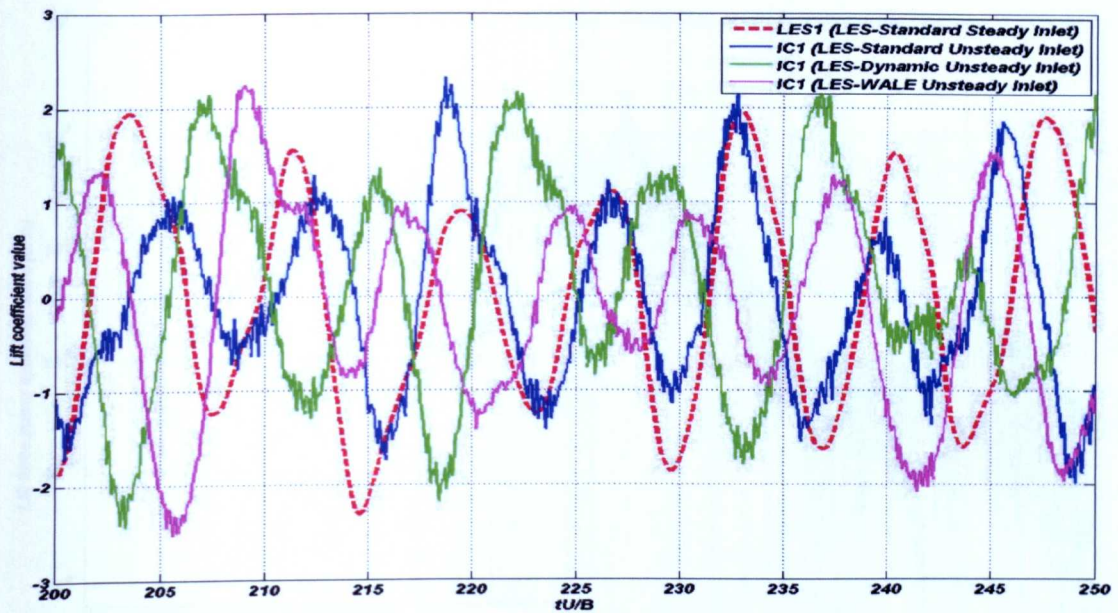


Fig 6.4.17 Lift coefficient curves of the case IC1 and LES1 at the nondimensional time step range (200-250)

From the comparison of lift and drag coefficient's curves between the case LES1 and the case IC1 of different LES models in Fig.6.4.16, the lift coefficient curve of IC1 shows more random characteristics due to the inflow turbulence input, while this variation can be clearly seen in the figure of lift coefficient at the nondimensional time steps (200-250) in Fig.6.4.17. It can be found that the lift coefficient curves of the case IC1 have more high frequency part, which are not as smooth as the curve of the case LES1, which further indicates that inflow turbulence simulates much more high frequency and randomly distributed eddies.

Besides the time history curve of lift coefficient, the drag coefficient curves of nondimensional time steps for both cases are also plotted in Fig.6.4.16. It is found that for the case IC1 (turbulence intensity = 5%), the drag coefficient also shows much more random characteristics than the drag coefficient curve calculated from the case of LES1 without inflow turbulence effects. When the inflow turbulence is applied at the inlet boundary, the magnitude of the drag coefficient peak value at instantaneous dimensionless time step is much higher than the one considering the steady inlet boundary.

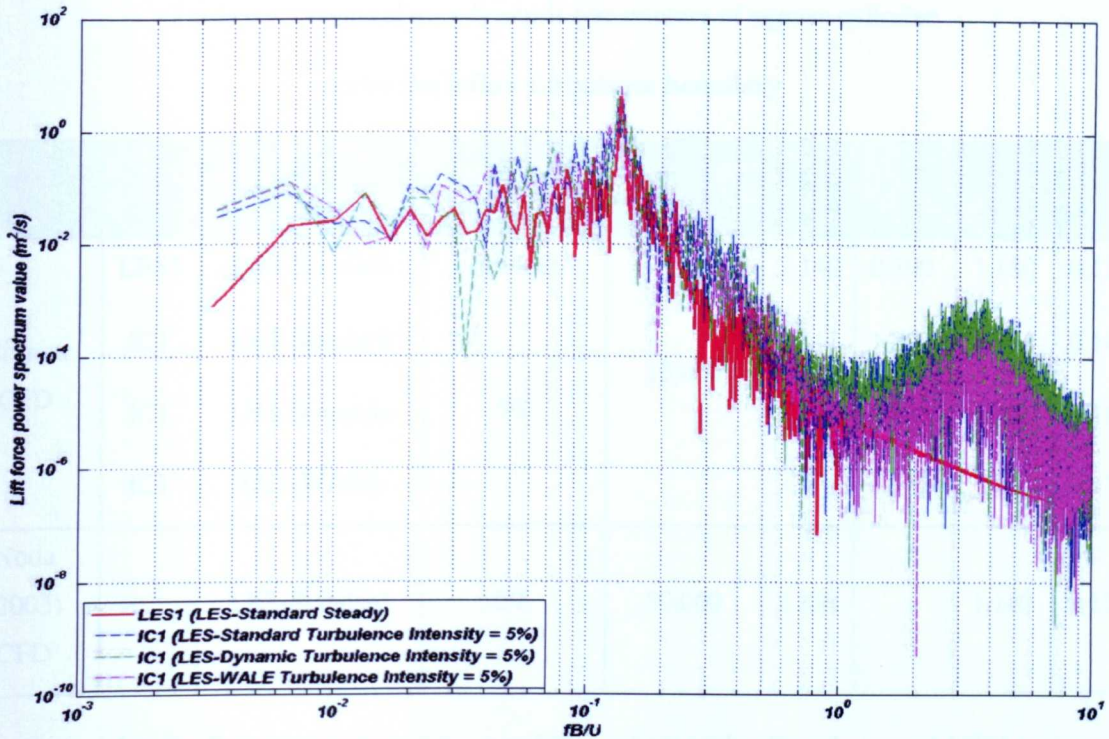


Fig 6.4.18 Power spectra of lift coefficient for the case IC1 of different LES models and the case LES1

Apart from the time history curves, power spectra provide another approach to discern variation trend in lift force coefficients in the frequency domain. Fig.6.4.18 plots the lift coefficients' spectra for the cases IC1 (LES-Standard, LES-Dynamic, LES-WALE model) and LES1 (LES-Standard). It can be found that for the power spectrum of lift coefficient a significant peak frequency exists for both cases LES1 and IC1. Except one significant frequency there are some other peak frequencies in the high reduced frequency range for the case IC1 considering inflow turbulence. The reason is that except the leading-edge large eddies around the square cylinder, the dominant vortex shedding frequency is controlled by the eddy frequency in the wake region, the inflow turbulence generates much higher frequency eddies which contribute to the generation of high frequency eddies and the high frequency variation lift force around the square cylinder.

(2) Global Aerodynamic Parameters

Table.6.4.2 summarizes the general aerodynamic parameters such as the RMS values of drag and lift coefficient the mean value of drag coefficient and the Strouhal number for the cases IC1 and LES1. To compare current simulation results with other CFD data, the simulation results of CFD for a square cylinder at a Reynolds number of 50,000 with 5% inflow turbulence from Noda *et al.* (2003) study are listed.

**Table 6.4.2 General aerodynamic parameters of square cylinder
under the inflow turbulence boundary**

Author	Case	Model	Turbulence Intensity	Re Number	\bar{C}_D	C_D^{rms}	C_L^{rms}	St
Current CFD	LES1	LES-Standard	Smooth	13,000	2.140	0.390	1.180	0.134
	IC1	LES-Standard	5%		2.311	1.890	1.121	0.140
	IC1	LES-Dynamic			2.342	1.913	1.131	0.136
	IC1	LES-WALE			2.374	1.942	1.123	0.136
Noda (2003) CFD		LES-Standard	5%	50,000	2.358		1.140	0.138

In Table.6.4.1, the Strouhal number of the case IC1 is a little higher than the one of LES1 without considering the inflow turbulence input. The percentage value of IC1 compared with the case LES1 is from 1.5% to 4.5%. For the mean value of drag coefficient it can be found that the value from the case with the input turbulence is higher than the one from the case LES1, the percentage being 8.0% to 10.9%. For the RMS value of drag coefficient, it is clearly found that when considering the inflow turbulence intensity, the RMS value of drag coefficient is clearly increased, and it is higher than that of the case LES1, the percentages being 398%. However, the lift coefficient RMS value shows no such variation and the value of the case IC1 is smaller than the value of LES1, the percentage is 4.2% to 5.0%, so the inflow turbulence will not only influence the instantaneous value of drag coefficient but also the statistical RMS value clearly.

(3) Results Comparison of Velocity Components and Reynolds Stress

To further validate current simulation results and study the flow characteristics around the cylinder or in the wake region for cases IC1 and C1 (here C1 is the case LES1) in further detail, the time averaged value of velocity component, Reynolds stress and the profile of RMS value along the centre line of the domain and vertical middle line at the top side of the square cylinder are discussed in this part of analysis. Fig.6.4.19 predicts and compares the time averaged mean value of streamwise velocity component for the cases IC1 and LES1 at the centre line of the computational domain considering LES-Standard, LES-Dynamic and LES-WALE model respectively. It is found that the simulated results from the case IC1 of different LES models and the case of LES1 agree with each other at the front position of bluff body. In the wake region, there is not much discrepancy between the case IC1 and the case LES1.

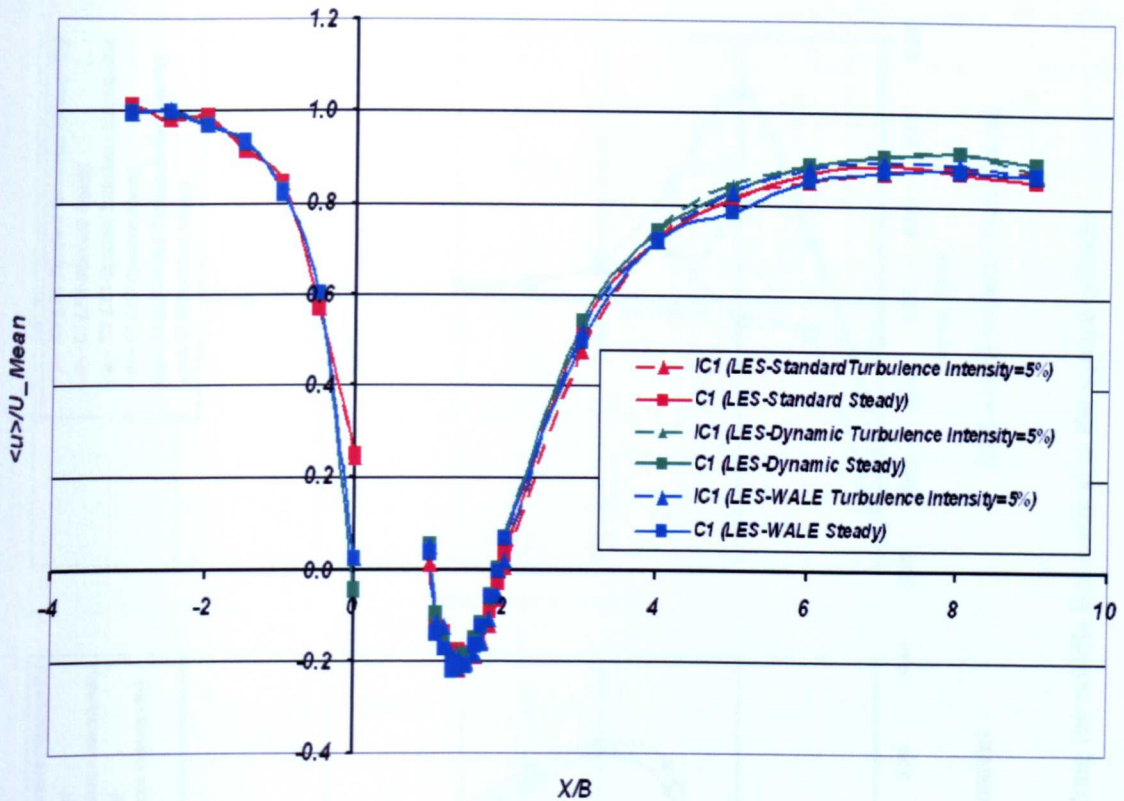
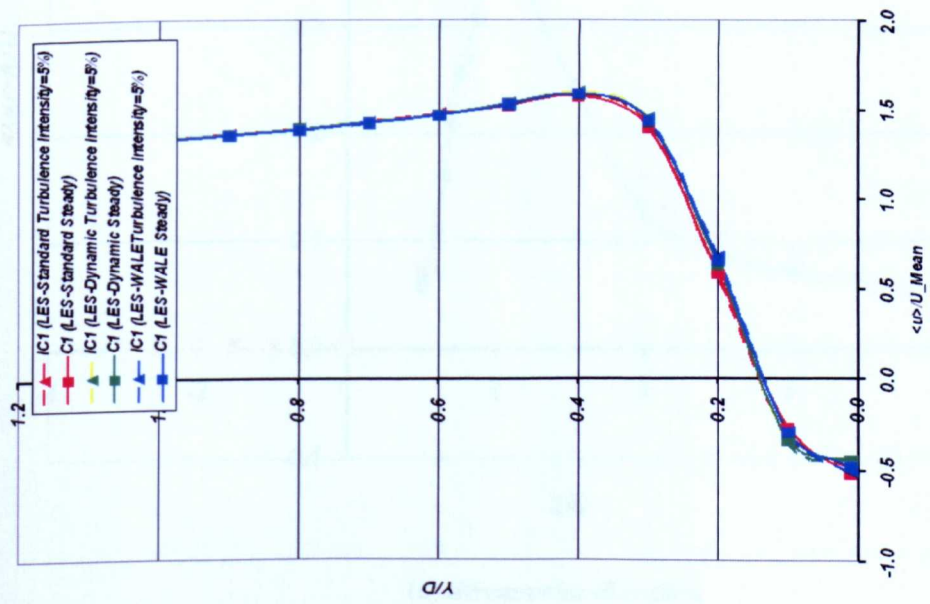
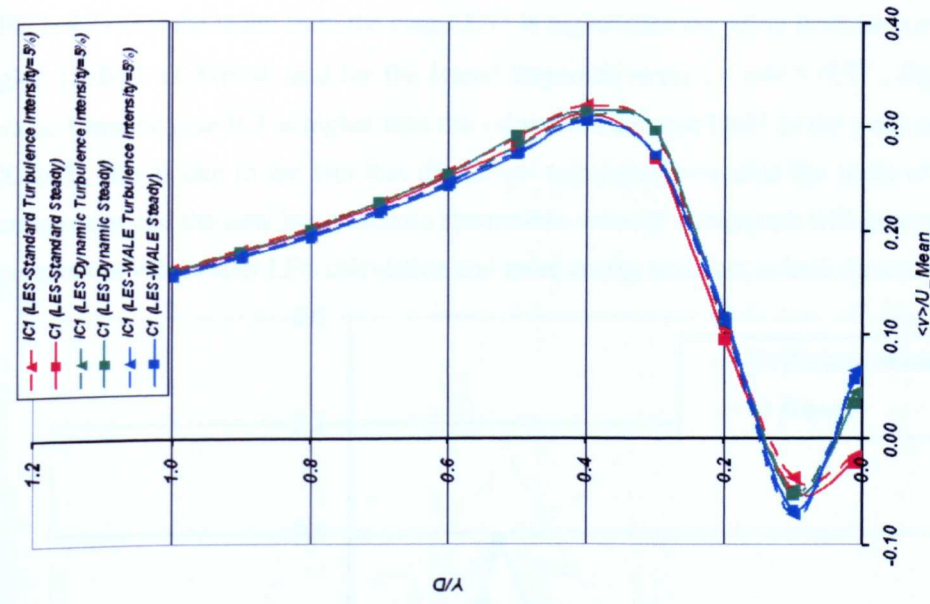


Fig 6.4.19 Time averaged value of dimensionless streamwise velocity components along the centre line of simulation domain

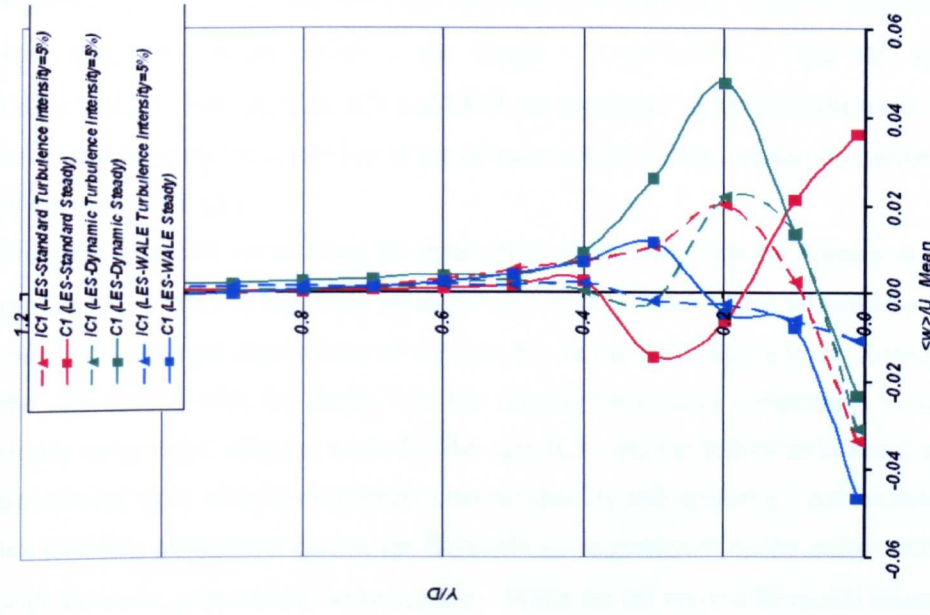
Fig.6.4.20 shows the vertical profiles of the mean streamwise (u), vertical (v) and lateral velocity (w) component predicted by the case IC1 and LES1. In Fig.6.4.20 (a) and (b), it can be found that current values of streamwise and vertical velocity component from LES1 and IC1 agree with each other very well, which means that the influence of the inflow turbulence on both velocity components' mean value is not large around the square cylinder, but for the vertical velocity component at the near wall region the case LES1 with LES standard model is different from the other LES models. For the lateral velocity component, a difference occurs. From Fig.6.4.20 (c) it can be found that the inflow turbulence boundary condition influence on the lateral velocity component simulation value is clear especially in the area below $Y/D = 0.4$, since this area is located at the flow shear layer, where the velocity component varies quickly.



(a) Streamwise velocity component



(b) Vertical velocity component

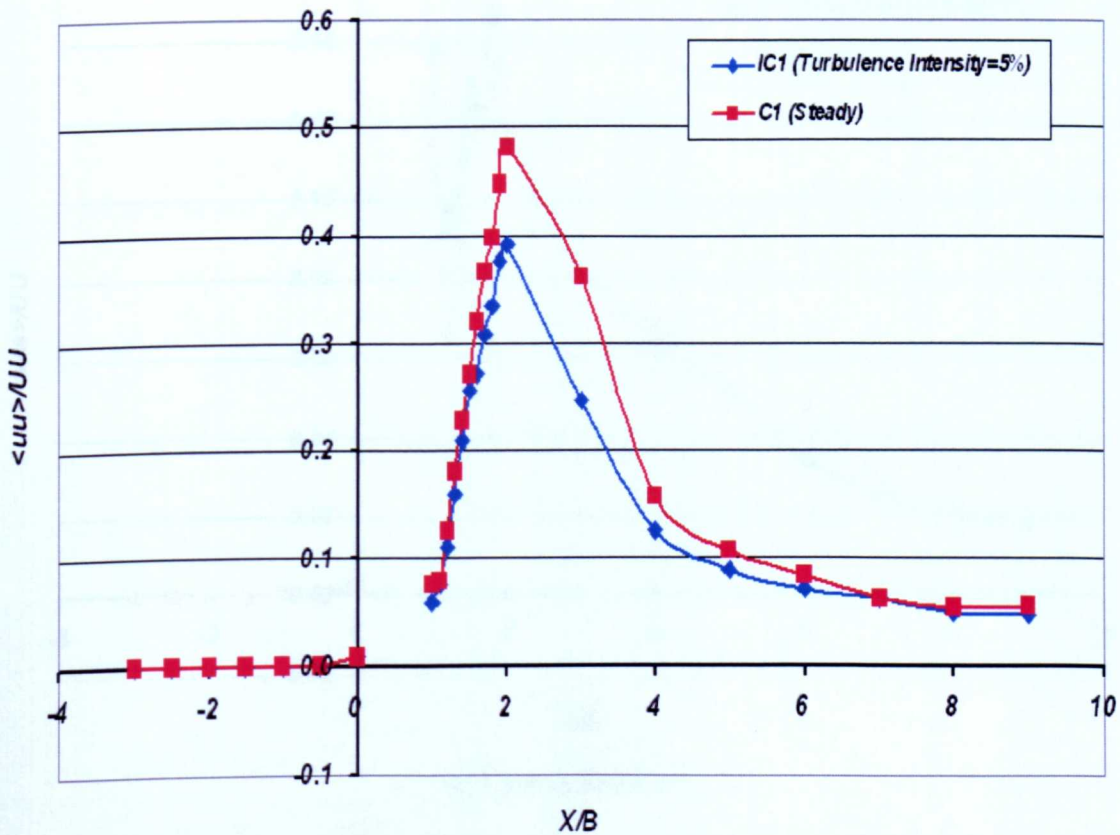


(c) Lateral velocity component

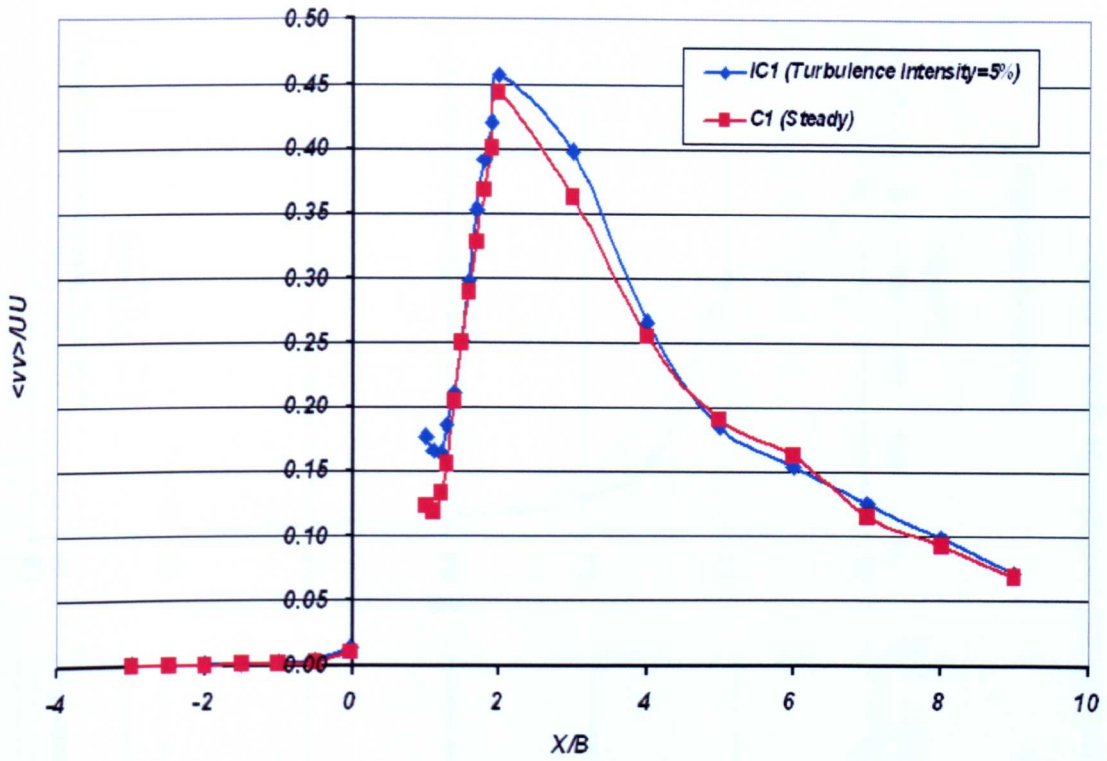
Fig 6.4.20 Time averaged value of dimensionless velocity components along the middle line vertical to the square cylinder

Fig.6.4.21 to Fig.6.4.22, the simulated dimensionless Reynolds stress components in the streamwise direction ($\langle uu \rangle / UU$), the lateral ($\langle ww \rangle / UU$) and the vertical direction ($\langle vv \rangle / UU$) from the case IC1 and LES1 are plotted to verify the correctness of current simulation results along the centre line of the domain and the vertical middle line at the top side surface of the square cylinder.

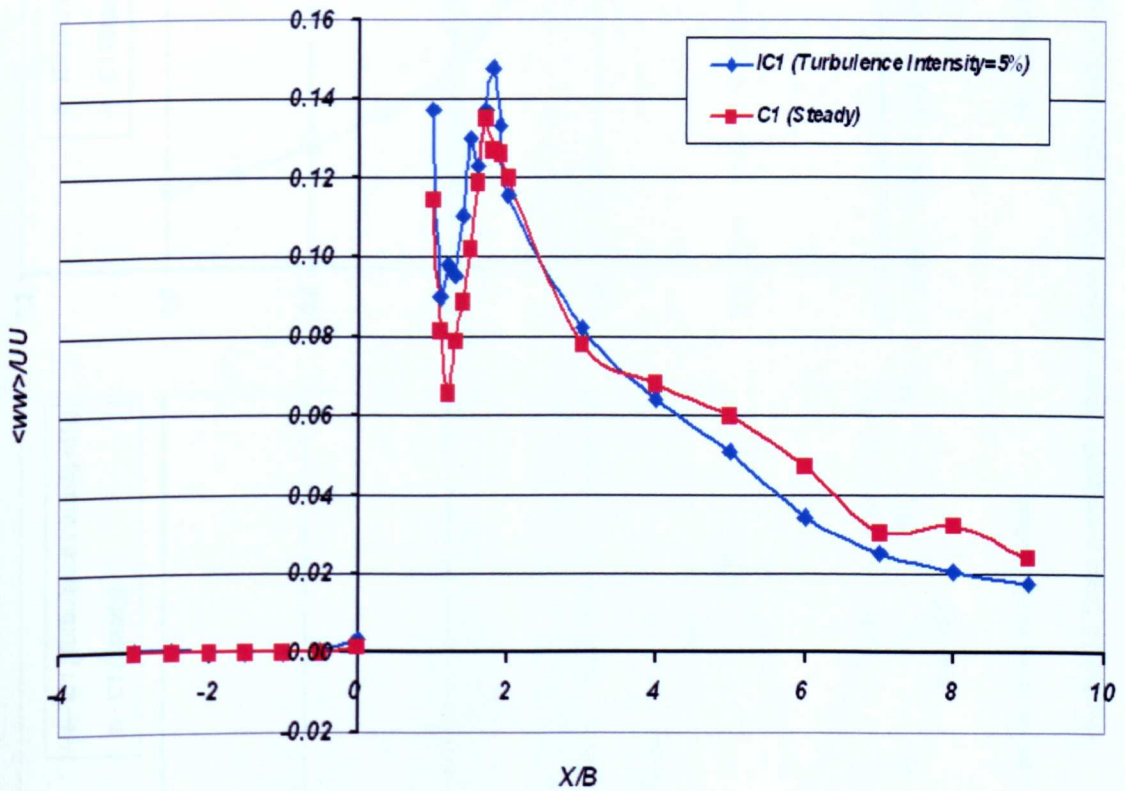
From the Reynolds stress along the center line of the computational domain in Fig.6.4.21 (a), it can be found that the Reynolds stress ($\langle uu \rangle / UU$) value of the streamwise direction for the case LES1 is larger than the one of the case IC1 in the wake region (from $X/B=1$ to $X/B=6$). For the case (LES1) with the steady inlet the velocity streamwise components is dominated by the steady mean input velocity, while for the case IC1 with the inflow turbulence, the time varying streamwise input velocity component changes quickly and randomly. And in this region the vortex shedding phenomena occurs, the Reynolds stress generated by the inflow turbulence interacts with the stress generated by wake vortices. While for the vertical Reynolds stress ($\langle vv \rangle / UU$, Fig.6.4.21 (b)) the value from the case LES1 is higher than the value from the case IC1 in the region ($X/B=2$ to $X/B=4$) and for the lateral Reynolds stress ($\langle ww \rangle / UU$, Fig.6.4.21 (c)) the value from the case IC1 is higher than the value from the case LES1 in the wake region ($X/B=1$ to $X/B=2$), this is due to the fact that the inflow turbulence considers the input of lateral velocity component and the new input random streamwise velocity component will generate new velocity component values after LES calculation and more energy transfers in both directions.



(a) Streamwise direction

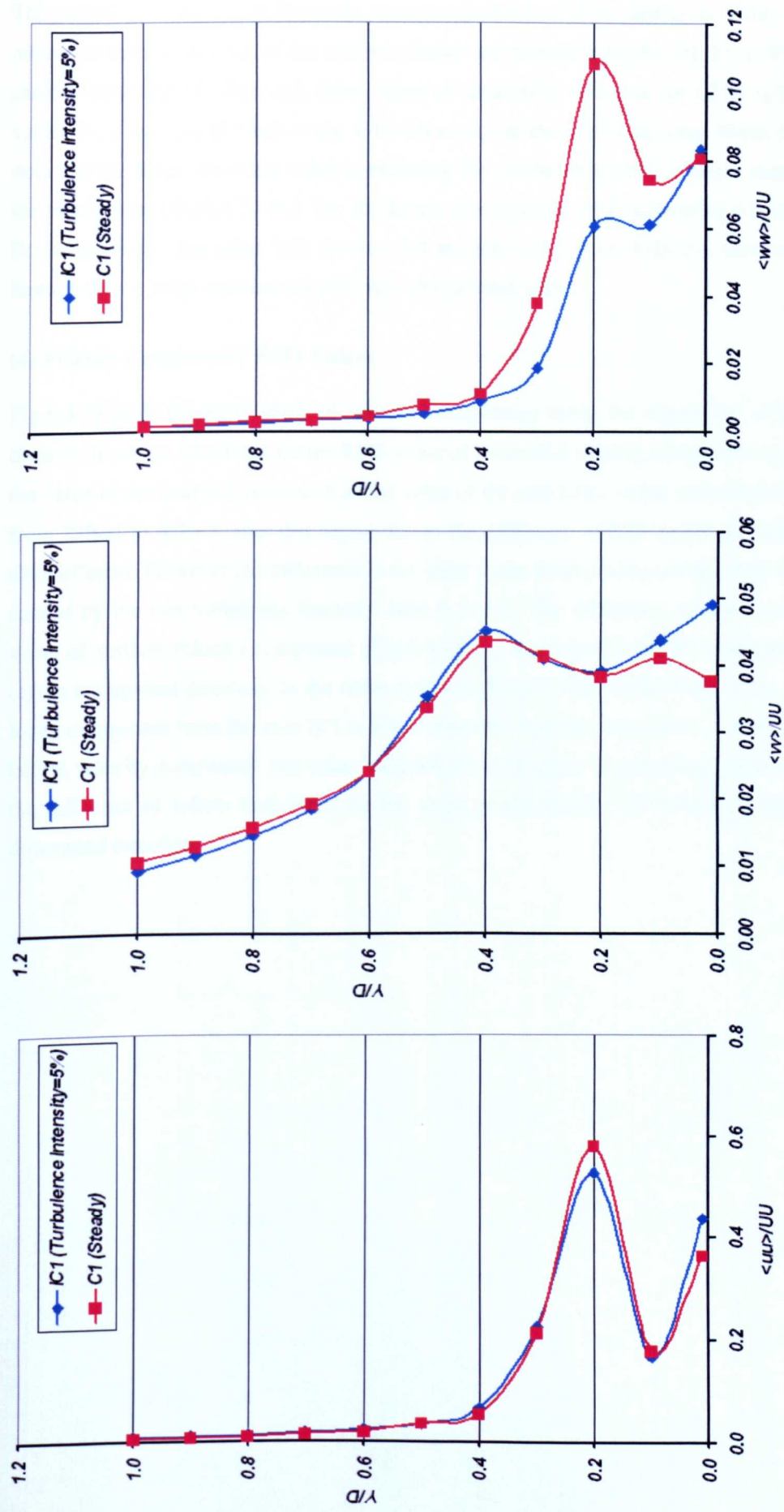


(b) Vertical direction



(c) Lateral direction

Fig 6.4.21 Dimensionless Reynolds stress along the center line of the domain



(a) Streamwise direction

(b) Vertical direction

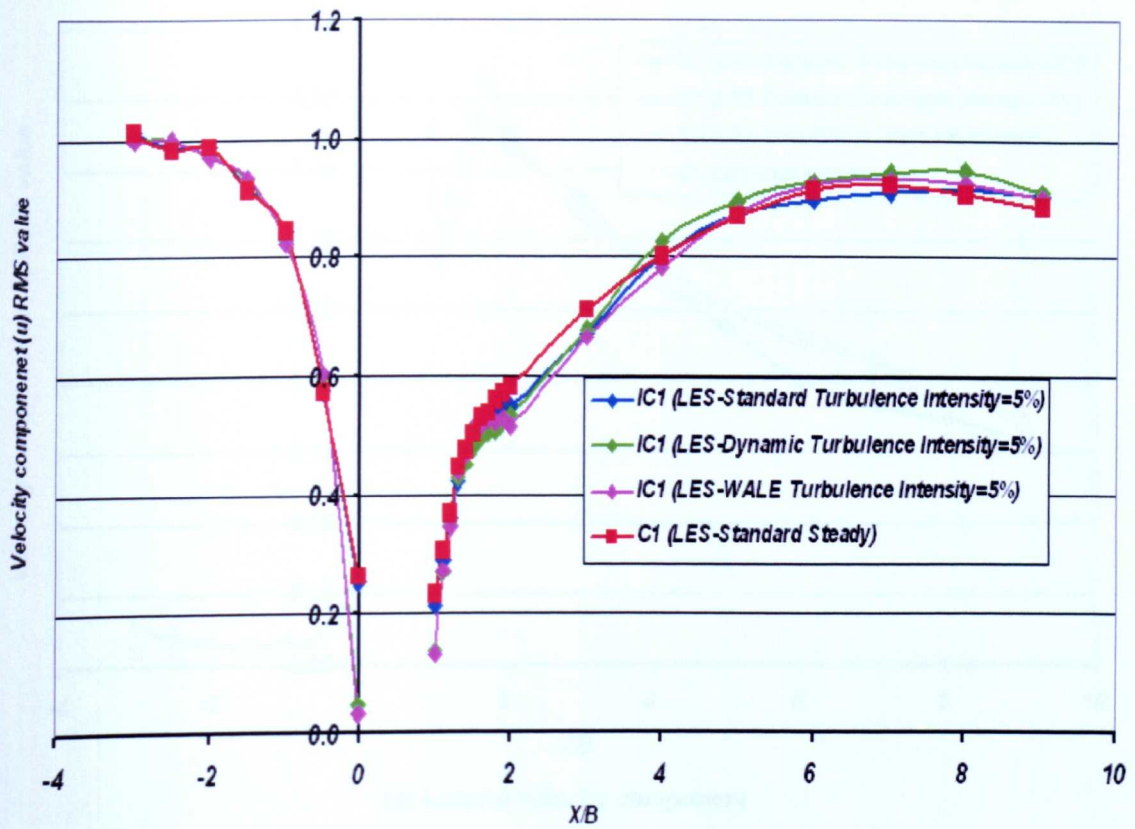
(c) Lateral direction

Fig 6.4.22 Time averaged value of dimensionless Reynolds stress along the middle line vertical to the square cylinder

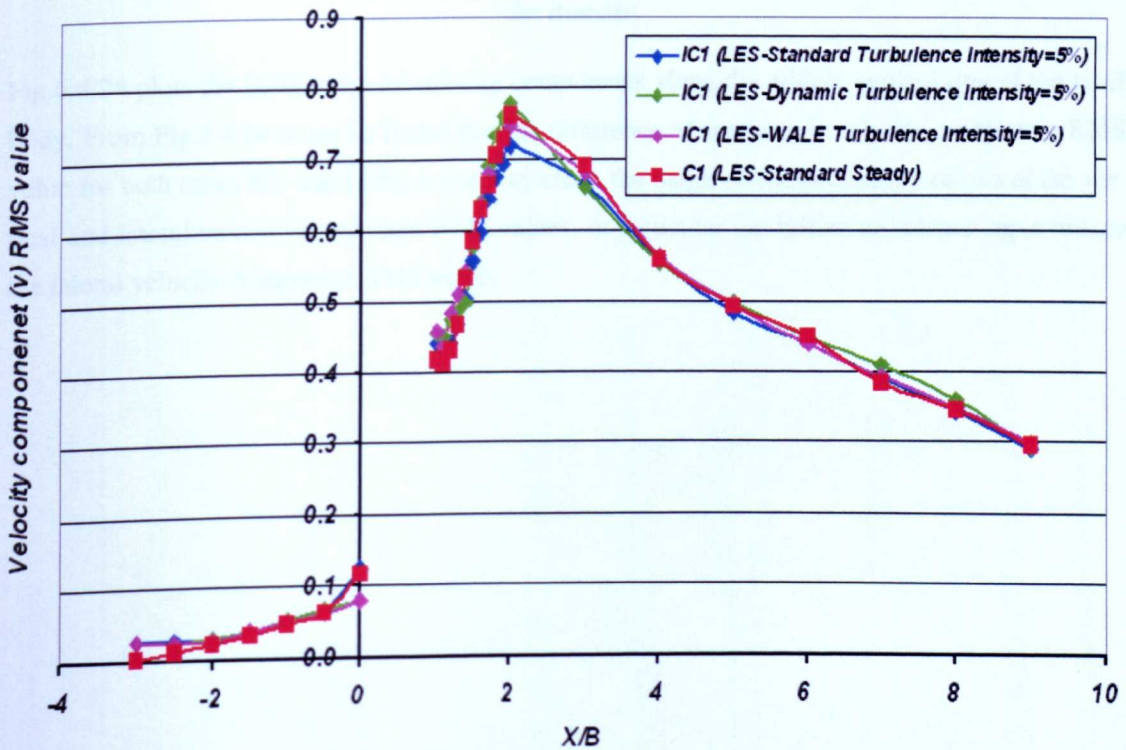
The vertical profiles for the Reynolds stress components of three directions at the vertical line of middle of the side surface of the square cylinder are plotted in Fig.6.4.22. From Fig.6.4.22 (a) it can be found that the Reynolds stress value of streamwise direction for LES1 is larger than the values from the case IC1 below the $Y/D=0.4$ except at the near wall zone. While for the vertical direction the Reynolds stress value considering the inflow turbulence is larger than the one with the steady inlet (Fig.6.4.22 (b)). For the lateral direction the input turbulence will also reduce the Reynolds stress value when Y/D is below 0.4 and above this value $Y/D=0.4$, there is no much difference for the value between the case IC1 and the case LES1.

(4) Velocity Components' RMS Values

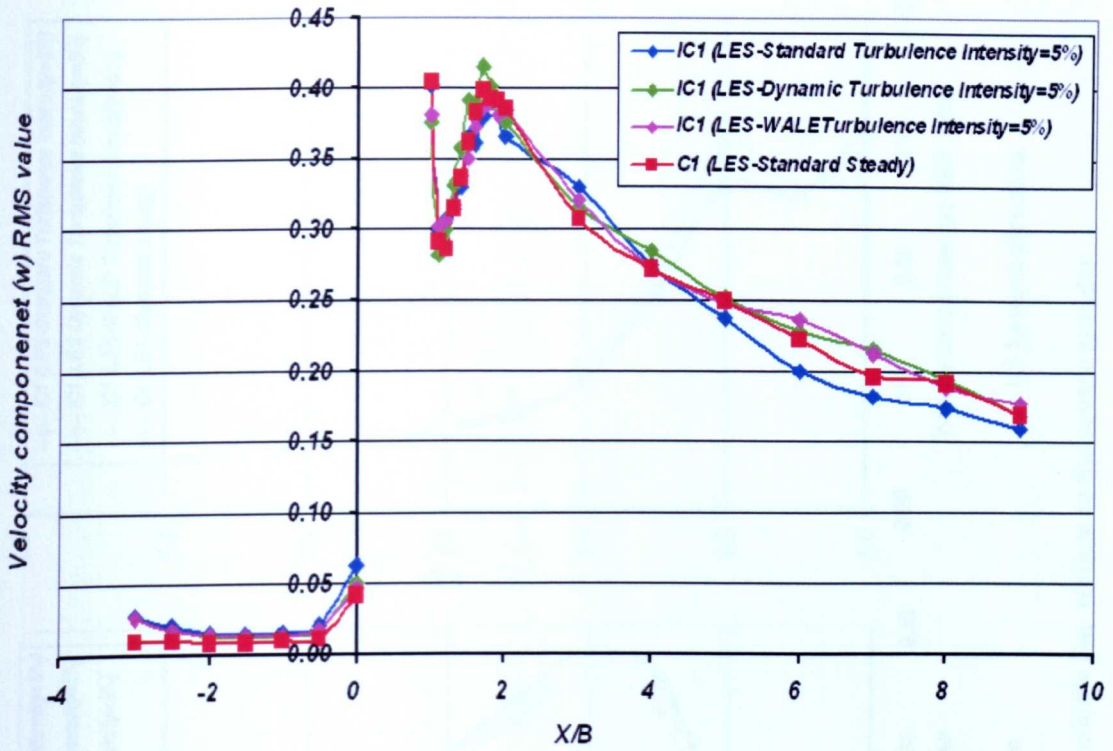
Fig.6.4.23 plots the RMS value of velocity components along the centre line of the simulation domain. It can be found that for the RMS value of horizontal velocity component in Fig.6.4.23 (a), the value of the case IC1 is lower than the value of the case LES1 in the wake region of bluff body from $X/B=1$ to $X/B=3$, after this region due to the difference of LES model the value variation is also different. However the difference is not clear in the front position of the bluff body, which is caused by the low turbulence intensity, here it is 5%. The difference can be seen for the RMS value of vertical velocity component (Fig.6.4.23 (b)) and lateral velocity component (Fig.6.4.23 (c)) in the upwind direction. In the wake region ($X/B=2$ to $X/B=4$) the RMS value of vertical velocity component from the case IC1 is lower than that from the case LES1. For the RMS value of lateral velocity component, the value variation for both cases is very clear, which further shows the influence of inflow turbulence on the value in the upwind more strongly than that in the downwind direction.



(a) Streamwise velocity component



(b) Vertical velocity component



(c) Lateral velocity component

Fig 6.4.23 RMS value of dimensionless velocity components along the centre line of the domain

Fig.6.4.24 plots the RMS value of velocity components along the middle vertical line of the bluff body. From Fig.6.4.24 it can be found that the difference of streamwise velocity component RMS value for both cases IC1 and LES1 is not very clear, the major difference mainly occurs at the vertical and lateral velocity component RMS values, in particular the inflow turbulence input reduce the lateral velocity component RMS value.

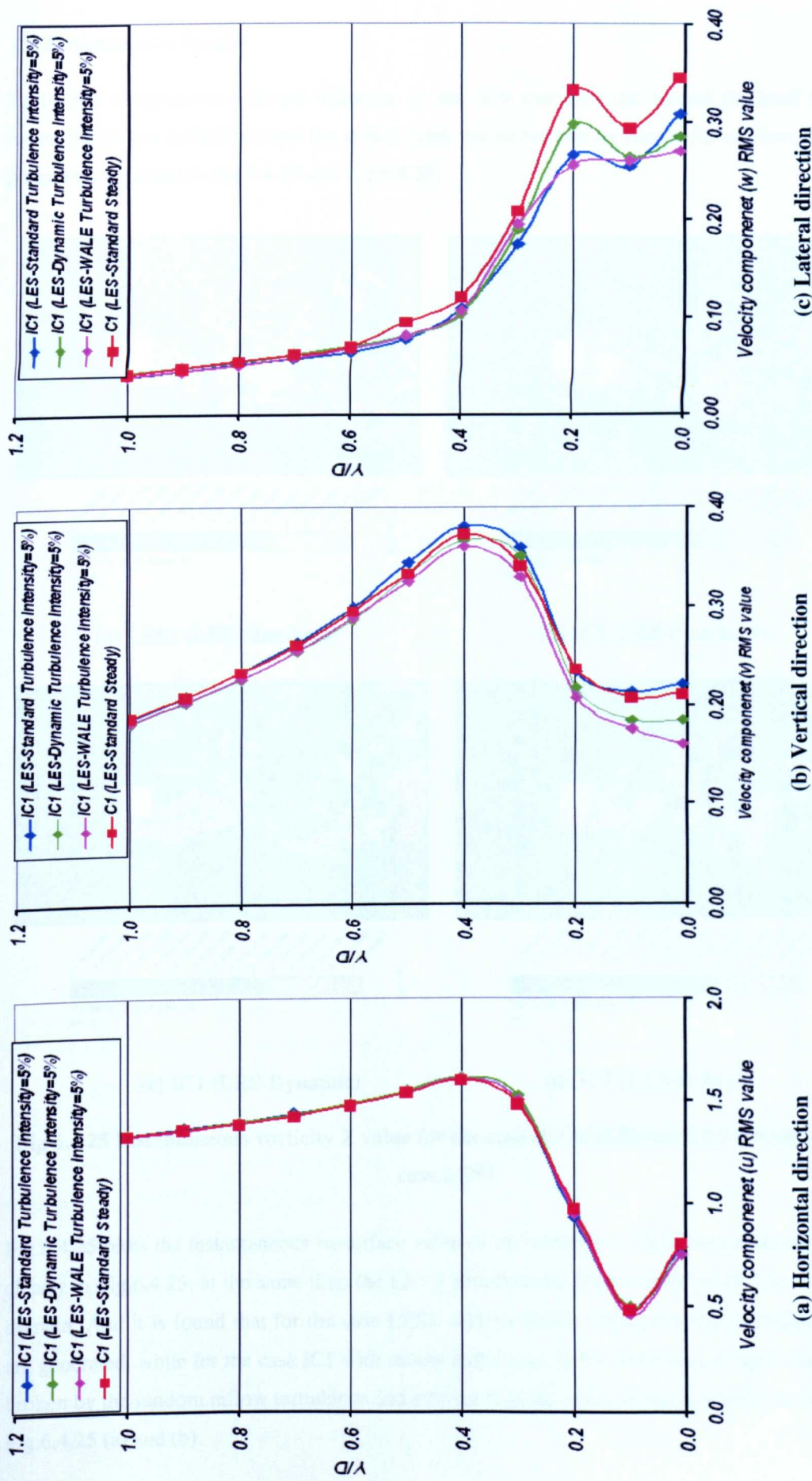


Fig 6.4.24 RMS value of dimensionless velocity components along the middle line vertical to the square cylinder

(5) *Instantaneous Results*

To further compare the different influence on the flow characteristic around the bluff body between the inflow turbulence and the steady inlet, the instantaneous results for the vorticity z and pressure are plotted in Fig.6.4.25 and Fig.6.4.26.

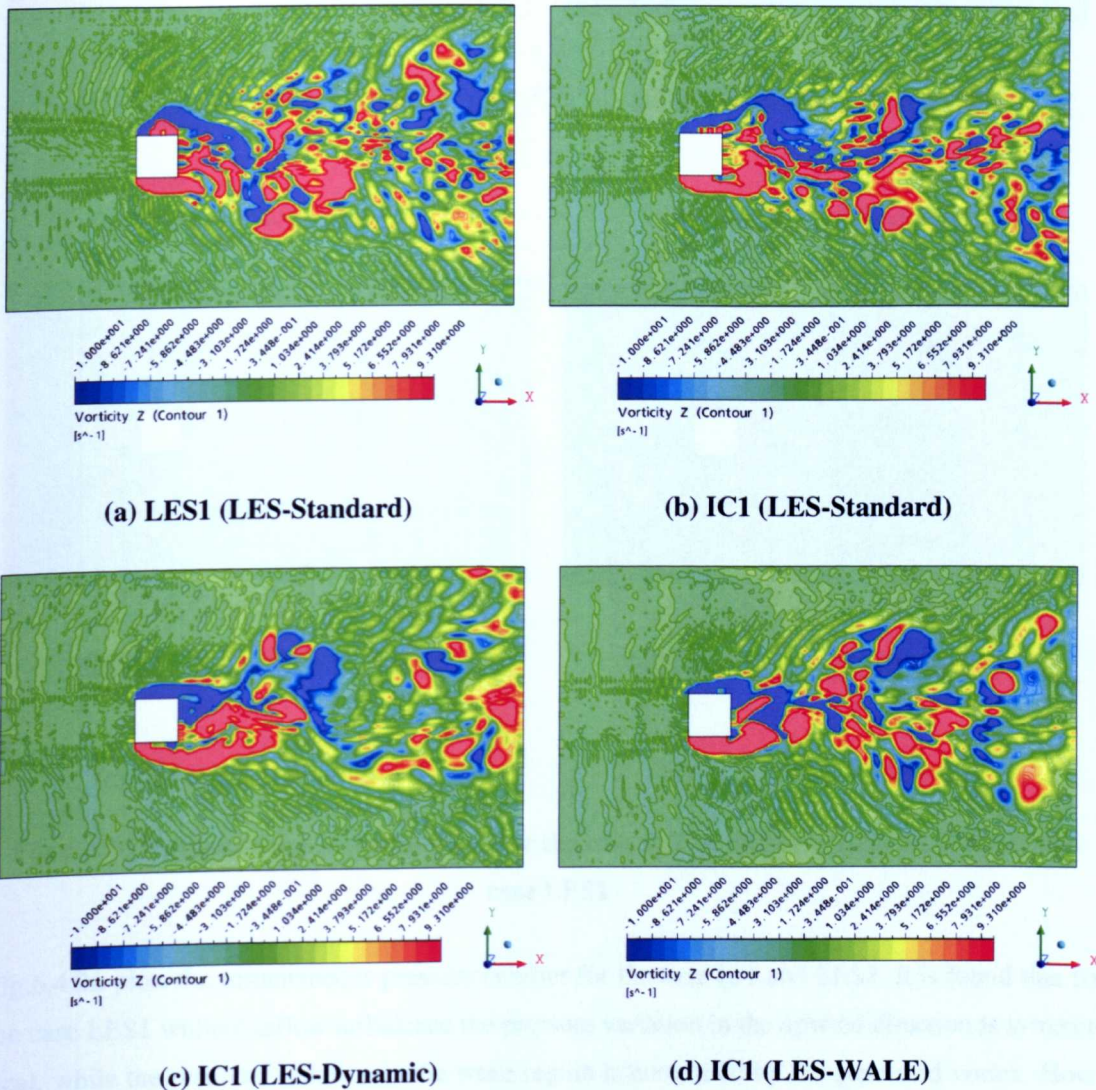


Fig 6.4.25 Instantaneous vorticity Z value for the case IC1 of different LES models and the case LES1

Fig.6.4.25 plots the instantaneous isosurface value of the vorticity z . Flow separation can be seen clearly in Fig.6.4.25, at the same time the LEVS aerodynamic phenomena can also be seen in the domain. And it is found that for the case LES1 without inflow turbulence many smaller vortices are generated, while for the case IC1 with inflow turbulence, in the wake region many vortices are broken by the random inflow turbulence and interact with the wake vortices, which can be seen in Fig.6.4.25 (a) and (b).

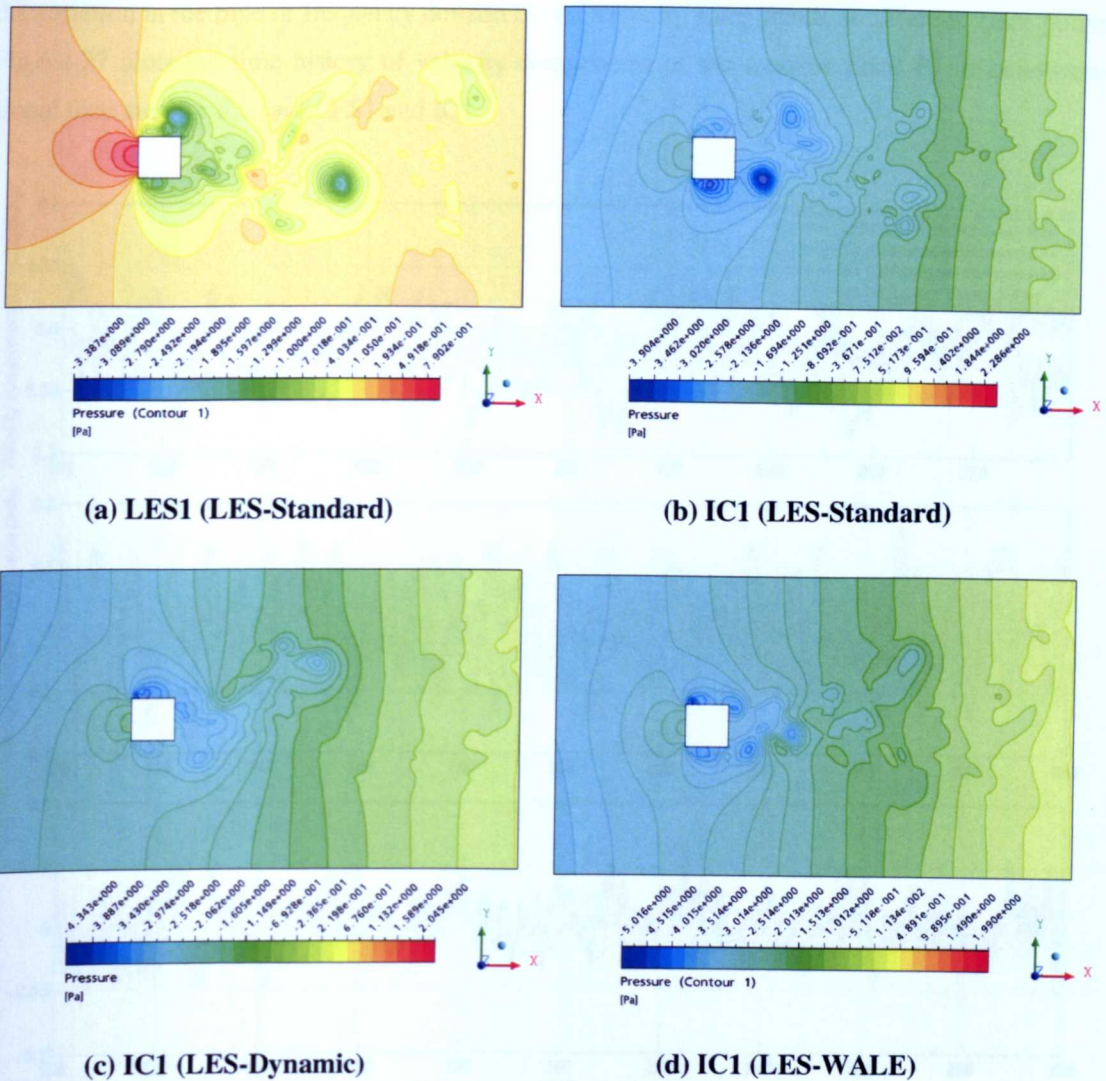


Fig 6.4.26 Instantaneous pressure value for the case IC1 of different LES models and the case LES1

Fig.6.4.26 plots the instantaneous pressure contour for the case IC1 and LES1. It is found that for the case LES1 without inflow turbulence the pressure variation in the upwind direction is symmetrical, while the pressure variation in the wake region is controlled by the generated vortex. However for the case IC1 considering inflow turbulence in the upwind direction the pressure is not symmetrical due to the input of random inflow turbulence and there is a clear pressure wave propagating from the upwind direction, which can be clearly seen in the wake region. The pressure generated by the inflow turbulence input interacts with the pressure in the wake region, which disturbs the pressure distribution from the wake vortices.

(6) Monitor Points Velocity Spectra

In this part of study, the time history variation and power spectra of monitor points' velocity components will be discussed. As presented in the preceding section, LES is a good technique to catch

the variation in the time or frequency domain for the velocity components at different space points. Fig.6.4.27 plots the time history of velocity components of the monitor point P1 at nondimensional time step for the case LES1 and IC1.

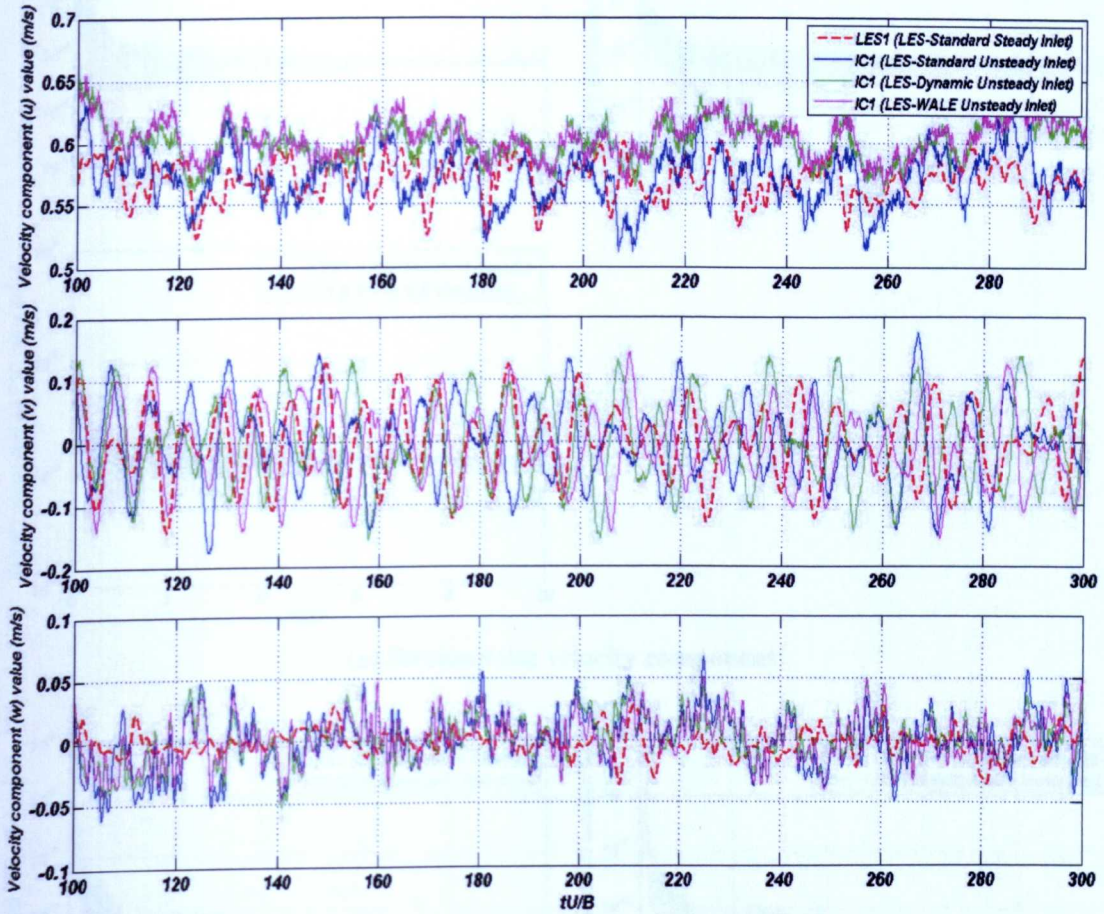
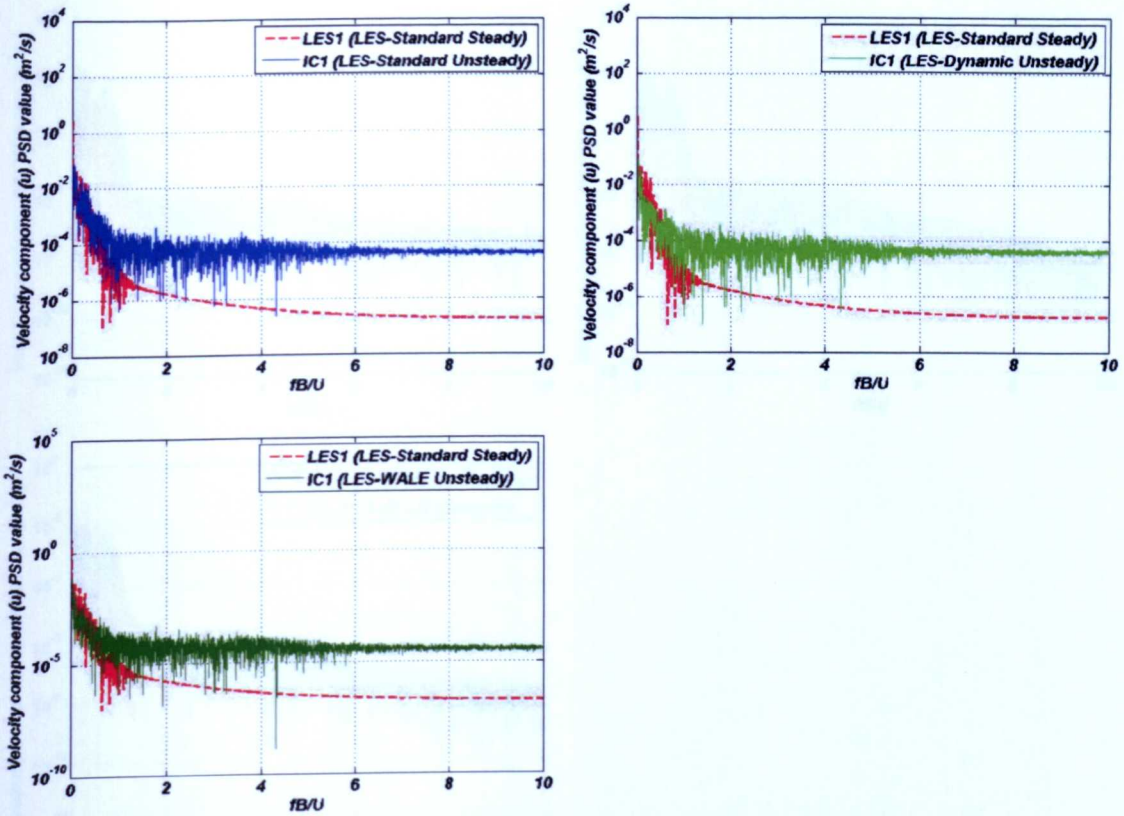
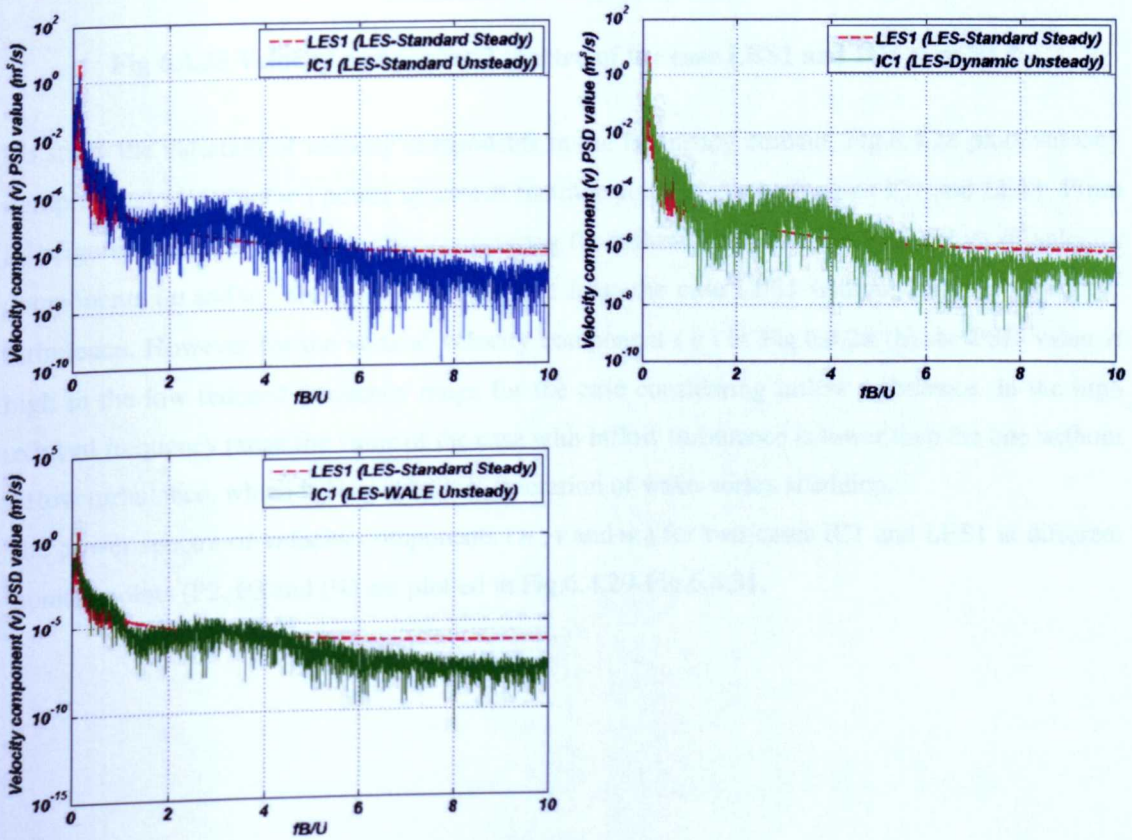


Fig 6.4.27 Velocity components' time history of different LES models at the monitor point P1

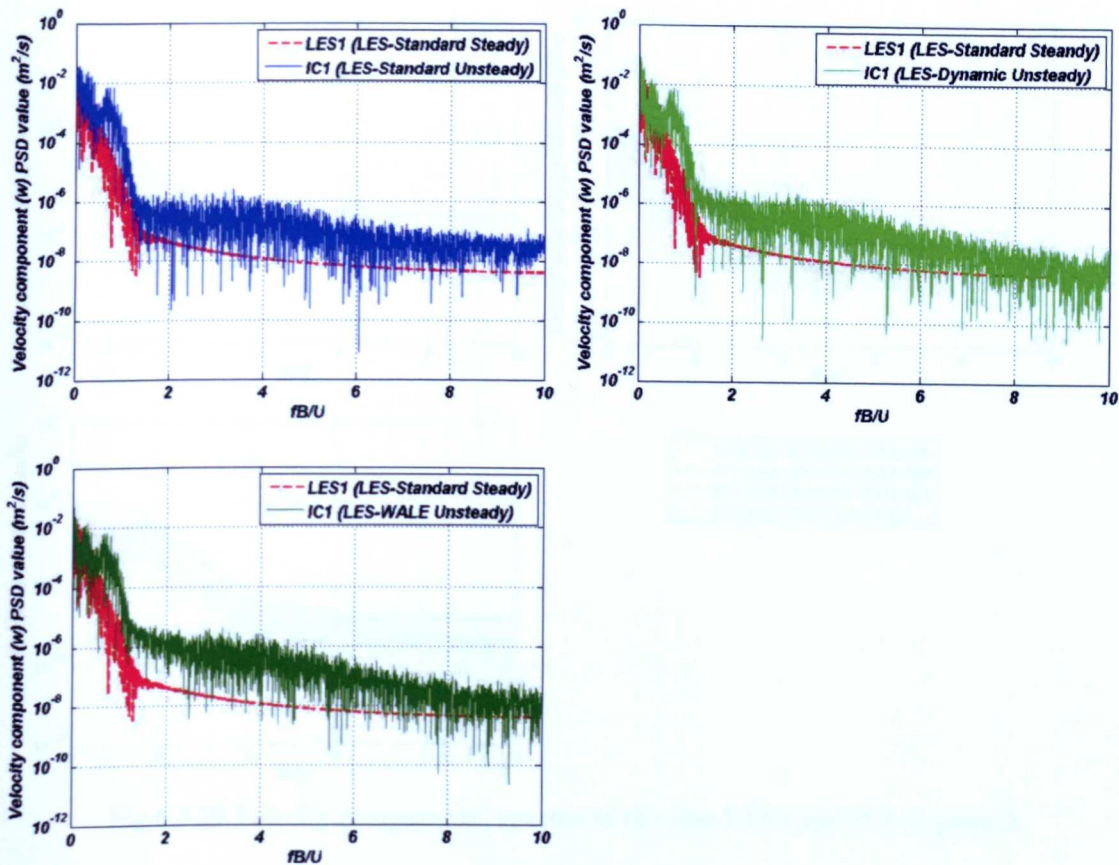
From Fig.6.4.27, it can be found that the value of velocity components at monitor point P1 for the case IC1, shows more random characteristics than that for the case LES1, since the case IC1 considers the influence of inflow turbulence. However to different LES models, it can be found that the value simulated by the model (LES-Dynamic and LES-WALE) is higher than the model (LES-Standard).



(a) Streamwise velocity component



(b) Vertical velocity component



(c) Lateral velocity component

Fig 6.4.28 Velocity components' spectra of the case LES1 and IC1 at point 1

To study the variation of velocity components in the frequency domain, Fig.6.4.28 plots velocity components' (u , v and w) power spectra at monitor point P1 for both cases IC1 and LES1. From this figure, it can be found that after considering the inflow turbulence the PSD values of velocity components (u and w) are higher than the one from the case LES1 without considering inflow turbulence. However for the vertical velocity component (v) in Fig.6.4.28 (b) the PSD value is high in the low reduced frequency range for the case considering inflow turbulence. In the high reduced frequency range the value of the case with inflow turbulence is lower than the one without inflow turbulence, which is caused by the generation of wake vortex shedding.

The power spectra of velocity components (u , v and w) for two cases IC1 and LES1 at different monitor points (P2, P3 and P4) are plotted in Fig.6.4.29-Fig.6.4.31.

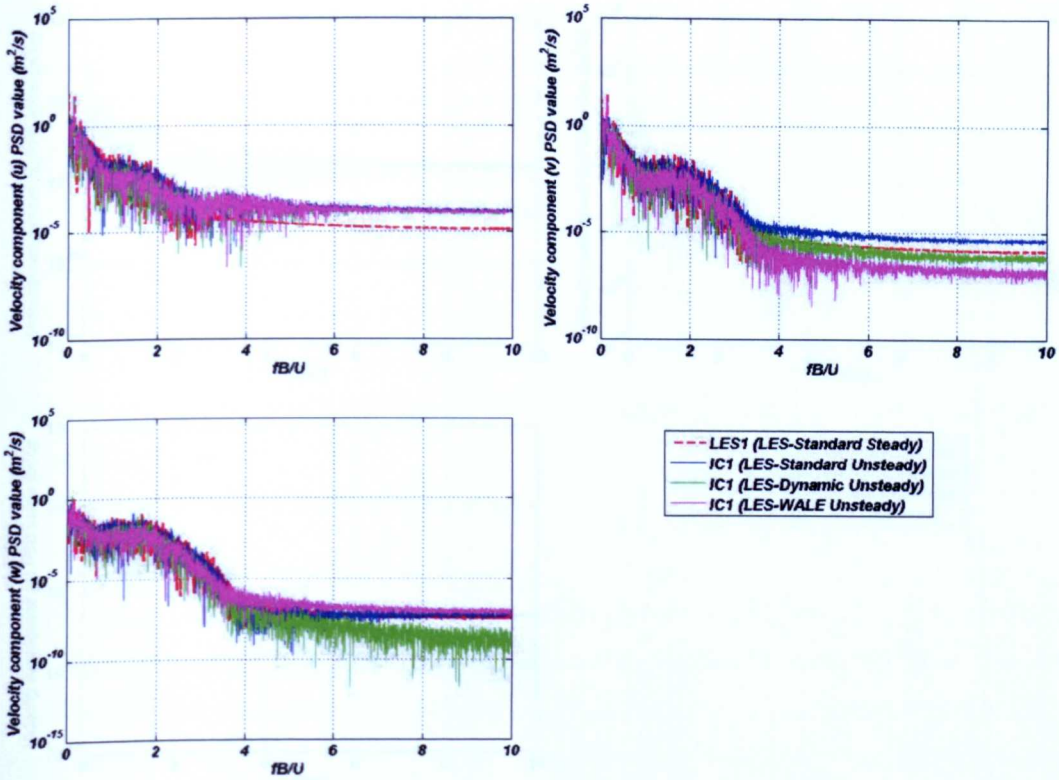


Fig 6.4.29 Velocity components' spectra of the case LES1 and IC1 at point 2

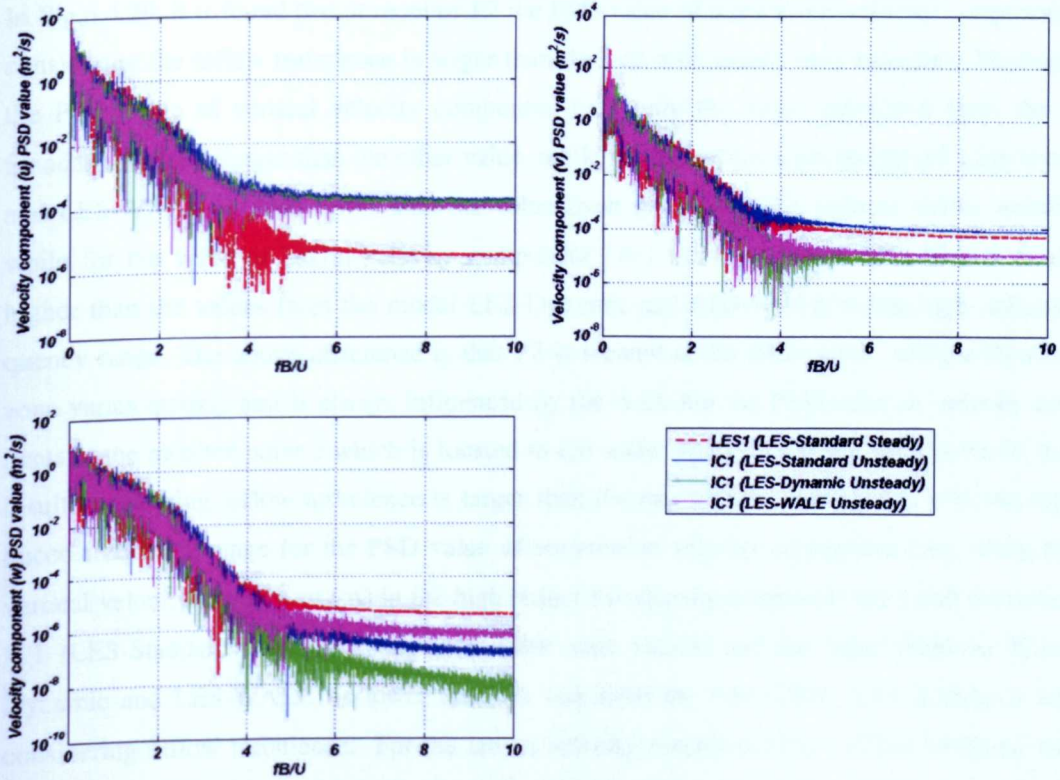


Fig 6.4.30 Velocity components' spectra of the case LES1 and IC1 at point 3

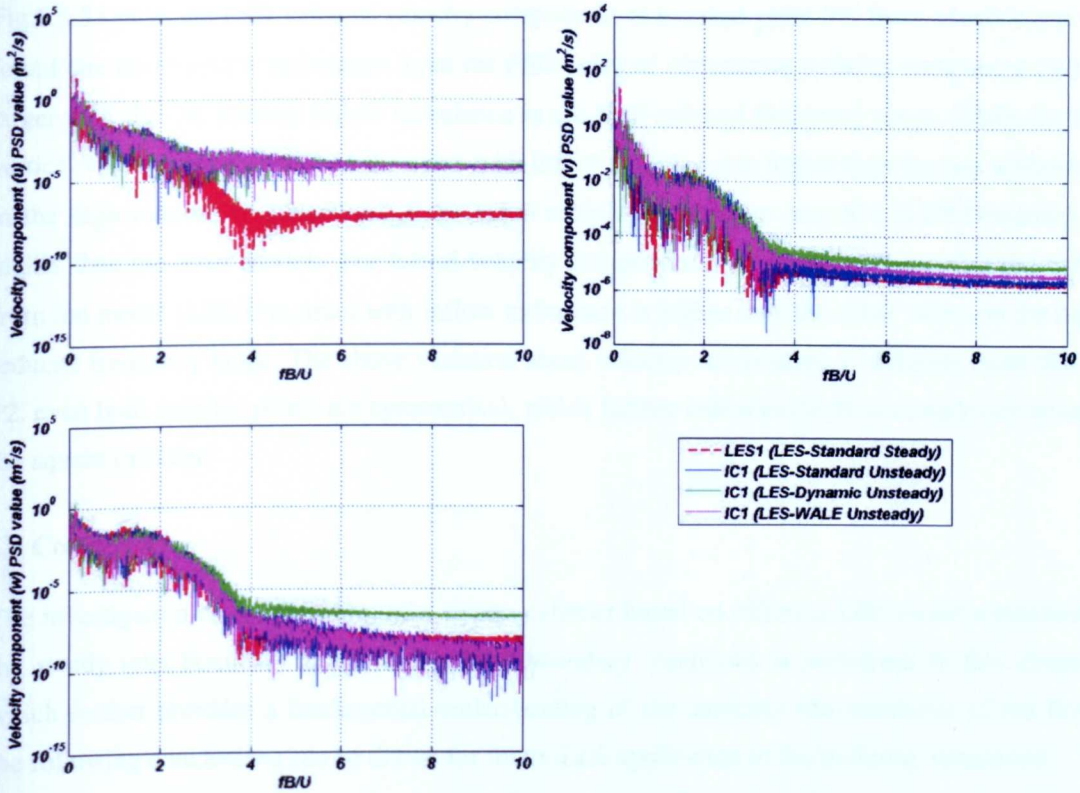


Fig 6.4.31 Velocity components' spectra of the case LES1 and IC1 at point 4

In Fig.6.4.29, it is found that at monitor P2 the PSD value of streamwise velocity component (u) considering the inflow turbulence is larger than the one with steady inlet boundary. However for the PSD value of vertical velocity component (v) only the value calculated from the LES-Standard model is larger than the other value, while for the values from the model LES-Dynamic and LES-WALE are also lower than the value from the case LES1 without inflow turbulence, while for the value of lateral velocity component (w) from the model LES-WALE is clearly higher than the values from the model LES-Dynamic and LES-WALE in the high reduced frequency range. The above difference is that P2 is located at the shear layer, and the flow of this zone varies quickly and is always influenced by the wall. For the PSD value of velocity components at the monitor point 3 which is located in the wake region in Fig.6.4.30, it is found that the result considering inflow turbulence is larger than the one without considering it in the high reduced frequency range for the PSD value of streamwise velocity component (u), while for the vertical velocity component (v) in the high reduced frequency range only the value from the case IC1 (LES-Standard model) is larger than the other values, and the value from the IC1(LES-Dynamic and LES-WALE) is lower than the one from the case LES1 (LES-Standard) without considering inflow turbulence. For the lateral velocity component (w), it can be found that the value from the case LES1 (LES-Standard) without inflow turbulence is larger than the value from the case with inflow turbulence, which indicates that the input turbulence will generate new vortices which interact with the wake vortices and influence the wake vortices generation.

Fig.6.4.31 plots the PSD value of velocity components at monitor point P4, from which it can be found due to the inflow turbulence input the PSD value of streamwise velocity component (u) is larger than the one without inflow turbulence in the high reduced frequency range. While for the vertical velocity component (v) the value with inflow turbulence is higher than the one without it, in the high reduced frequency range the value calculated from the case IC1 (LES-Dynamic) is higher than the other models. For lateral velocity component (w) it can be found that the value from the model (LES-Dynamic) with inflow turbulence is higher than the other values in the high reduced frequency range. The above variation about velocity components is different from that at P2, even both monitor points are symmetrical, which further indicates the flow complexity around the square cylinder.

6.5 Conclusions

The investigation on the flow around a square cylinder based on different LES model considering the steady inlet boundary and unsteady inlet boundary conditions is performed in this chapter, which further provides a fundamental understanding of the unsteady characteristics of the flow; the following conclusions can be drawn for future LES application in the buffeting simulation.

(1) The mesh density and spanwise depth influence on the flow around the square cylinder have been investigated. It is found that LES is a mesh sensitive simulation model and fine mesh density will generate more eddies with high frequency part. From the comparisons of mean velocity components as well as the mean Reynolds stress components with experimental data at different locations for a square cylinder, as well as the variation of Strouhal number and drag coefficient. Current LES results agree with other experimental results and numerical findings well, which validates the effectiveness of LES model to simulate the unsteady characteristics around the square cylinder.

(2) From the lift and drag force coefficient time history curves (Fig.6.4.1), it can be found that the inflow turbulence boundary condition generates more random characteristics and higher frequency part than the one from the steady inlet boundary. The forces acting upon the square cylinder body are directly related to the flow structure and the formation of vortices at the leading and trailing edge. These vortices strongly interact with each other as well as with the body surfaces. The incoming flow turbulence will influence the flow pattern around the bluff body, and the separated shear layer strongly interacts with the oncoming turbulence. At the same time, for the force spectrum, the turbulence inflow condition will increase the drag and lift force PSD magnitude in the high frequency range.

(3) From the mean value, Reynolds stress and RMS value of velocity components along the central line and the middle vertical line position, it can be found the turbulence inflow condition influences much more on the velocity component (v and w) value than the horizontal component (u), however in the downstream direction, this influence is not clear due to the vortex shedding.

(4) From the comparison of the velocity spectra it can be found that the PSD value of streamwise velocity component considering the turbulence inflow condition can capture the unsteady parts of velocity components in the high frequency range, while this part can not be simulated in the conventional LES technique under the steady inlet boundary condition. However for the PSD values of other two velocity components, although the inflow turbulence can agree with the target spectrum very well, these two components value can not be kept very well after current LES calculation.

Chap 7 Buffeting Response Simulation Based On FSI

7.1 Introduction

In chapter 5, the numerical procedure of inflow turbulence generation has been proposed and validated. The buffeting simulation with inflow turbulence has been done and the influence of inflow turbulence on the flow around a square cylinder has been studied in chapter 6. It is known that the fluctuating structural load is caused by turbulent eddies flowing past or impinging upon the structure in case of turbulence buffeting. The incident turbulence is usually made up of eddies with a broad range of scales and, hence, frequencies. The prediction of the response of a structure to turbulence buffeting may be conveniently considered in two parts. The first concerns the fluid-dynamic problem of predicting the loading on the structure from the known mean and fluctuating components of the flow. The second concerns the structural problem of predicting the response of the structure from the known fluid-dynamic loading and structure characteristics. So in this chapter the buffeting response of square cylinder with constant damping ratio (5%) based on FSI theory proposed in chapter 3 is simulated. To test the analytical procedure and closely coupled model proposed in chapter 3, a square cylinder with the same dimension and mesh density as the one used in chapter 6 is adopted. Since the across-flow oscillation is important to predict the buffeting response of bluff body, in current simulations the movement of bluff body is controlled in the across-flow direction, and two types of inlet boundary conditions are considered to compare the different influence of them on the flow around the square cylinder, one is the steady inlet boundary and the other is the unsteady one. The simulations of this chapter are realized by ANSYS_CFX code.

7.2 Descriptions of Simulation Cases

The same block structured grid as the one used in chapter 6 is also used in current simulation cases of this chapter. And the same domain dimension as the one in chapter 6 is used here, which can be seen in Fig.6.3.2. The steady and unsteady inlet boundary conditions are considered, and the unsteady one considering the inflow turbulence is realized by the inflow turbulence generation technique based on ARMA model proposed previously. The unsteady inlet boundary of current simulations is realized by CFX USER FORTRAN code. The same time history data of velocity

components used in chapter 5 and 6 is also adopted here, the turbulence intensity of three velocity components (u , v and w) is 5% and the mean inlet velocity is 1m/s. The outflow boundary condition is also specified as opening, the top and bottom face of the computational domain are specified as the symmetry boundary, and the front and back face of the domain are also specified as the same symmetry condition (see Fig.6.3.2). And the no-slip wall boundary condition is specified as the solid wall, the automatic wall model is used to consider the wall effects. To compare the different response of square cylinder from different LES models, the standard LES, LES dynamic and LES WALE models are considered in current simulations.

As described in structural dynamics, for the multi-degree-freedom system the structural movement can be expressed by Eq.7.2.1:

$$[m]\{\ddot{y}\} + [c]\{\dot{y}\} + [k]\{y\} = \{f(t)\} \quad (7.2.1)$$

Where $[m]$, $[c]$ and $[k]$ is the mass, damping and stiffness matrix separately, $f(t)$ is the external excitation force. In current simulations, only one degree freedom of heaving direction (in the vertical direction of computational domain) is considered, so Eq.7.2.1 can be simplified as:

$$\ddot{y} + 2\xi\omega\dot{y} + \omega^2 y = f(t) / m \quad (7.2.2)$$

Where $\xi = k / (2m\omega)$ is the viscous damping ratio of structure, here $\xi = 5\%$, m is the mass of square cylinder, and $\omega = 2\pi\sqrt{k/m}$ is the circular frequency of structure (unit: rad). In general, the aerodynamic responses of a square cylinder are classified into two patterns according to the Scruton number ($Sc = 2m / \rho BH \times 2\pi\xi$, ρ : air density). At small Scruton numbers, the unstable oscillation starts from the resonance velocity, and the unstable area is separated to galloping and vortex-induced vibrations at large Scruton numbers [Tamuara, 2003]. In current computation, the the case of Scruton number=20 is investigated.

In CFX code, the mesh deformation and the dynamical movement equation of square cylinder described by Eq.7.2.2 are specified by the motion of nodes on the wall boundary of structure using CFX Expression Language (CEL). And the motion of other nodes is determined by the mesh motion model limited to the displacement diffusion model (Eq.7.2.3) to keep the relative mesh distribution of the initial mesh. The displacements applied on the wall boundary are diffused to other mesh points by solving Eq.7.2.3:

$$\nabla \cdot (\Gamma_{disp} \nabla \delta) = 0 \tag{7.2.3}$$

Where δ is the displacement relative to the previous mesh locations and Γ_{disp} is the mesh stiffness, which determines the degree to which regions of nodes move together. Eq.7.2.3 is solved at the start of each outer iteration or time step. To diffuse the specified displacements throughout the mesh, the value of mesh stiffness is applied. There are three types of mesh stiffness technique (increasing near small volumes, increasing near boundaries and specified stiffness values) in CFX code. Current simulations adopt the option of increasing near small volumes, which does not require the solution of additional equations (as for boundary dependent options) and will make the mesh quality benefit from having larger control volumes and absorb more mesh motion. The following relationship is used to determine the mesh stiffness, Γ_{disp} , applied in the displacement diffusion equation:

$$\Gamma_{disp} = \left(\frac{1}{\nabla} \right)^{C_{stiff}} \tag{7.2.4}$$

Eq.7.2.4 provides an exponential increase in the mesh stiffness as the control volume size, ∇ , decreases. The stiffness model exponent, C_{stiff} , determines how quickly this increase occurs.

To provide the complete freedom to change the grid topology and physical distribution across the interface, a control surface approach and physically based intersection algorithm are used to perform the connection across a General Grid Interface (GGI) attachment, in which an automatic surface trimming function is performed to account for mismatched surface extent. Across the interface, the numerical algorithms and the control surface treatment of the numerical fluxes are designed and implemented to provide the maximum robustness and accuracy. So the treatment of the interface fluxes is fully implicit and fully conservative in mass, momentum, energy, scalars, etc.

7.3 Square Cylinder Response's Prediction Based On Different LES Models

In this part of research, the simulation cases considering the steady and unsteady inlet boundary conditions based on different LES models and FSI theory are adopted to investigate the buffeting response of square cylinder induced by the flow in the across-flow direction.

7.3.1 Result Discussion of Steady Inlet Boundary Condition

The time history curves of lift coefficients of different models are plotted in Fig.7.3.1 to predict the response of square cylinder at the steady inlet boundary condition, it can be found that the amplitude of peak value of lift coefficient is different and the reduced time step of it is also different, the reason is that the flow pattern and vortices around the square cylinder predicted by different LES models are different, which will generate different lift and drag forces, and then these forces will induce the different across-flow oscillation of square cylinder. The above detailed variation process can be seen in Fig.7.3.2 at reduced time steps ($t/U/D$) (100-200), in which it can be found that the amplitude of lift coefficient is different even at the same time step. In addition the lift coefficient values of different LES models have different phase angles, which further present the influence of different LES models on the final simulation results.

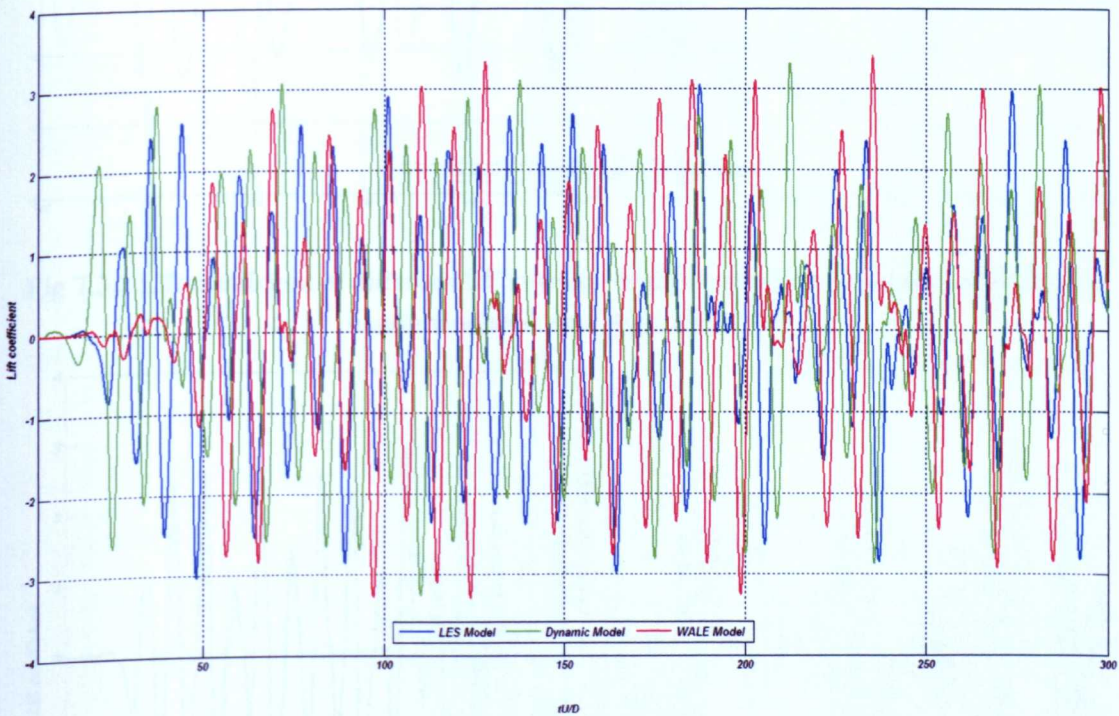


Fig 7.3.1 Lift coefficient of different LES models at the steady inlet boundary condition

To study the response of square cylinder with further step, Fig.7.3.3 shows different response stages of square cylinder by plotting the time history variation of lift coefficient based on the standard LES model, it can be found that three response stages (stage 1, stage 2 and stage 3) exist in the whole response process in Fig.7.3.3, which shows a mix-band response. Stage 1 and stage 2 can be approximated as a narrow band response, in which the vortices exist and take place

alternately, and generate some symmetrical lift forces, and to stage 3 it can be seen as a broad band response and much more irregular turbulence eddies are generated with the development of turbulence. And due to the interaction between the structure and flow, the structure itself and flow field exchange the energy between two physical field with time variation, and much more complex eddies, resulting in the irregular lift force, are generated.

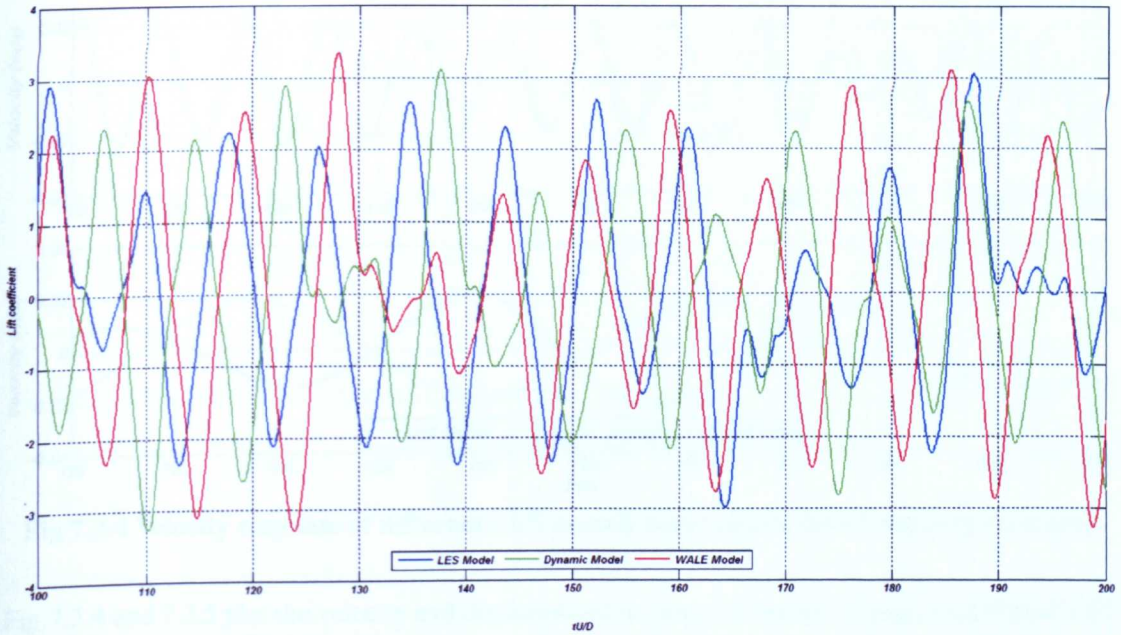


Fig 7.3.2 Lift coefficient of different LES models of the steady inlet boundary condition at nondimensional time steps (100-200)

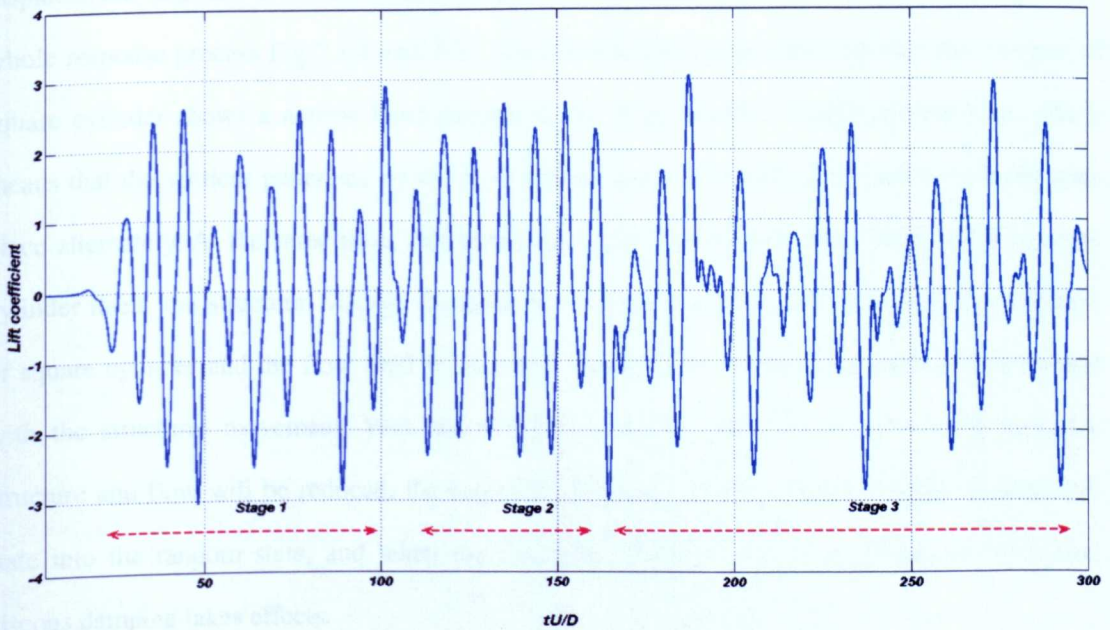


Fig 7.3.3 Response stage vs lift coefficient of standard LES model at the steady inlet boundary condition

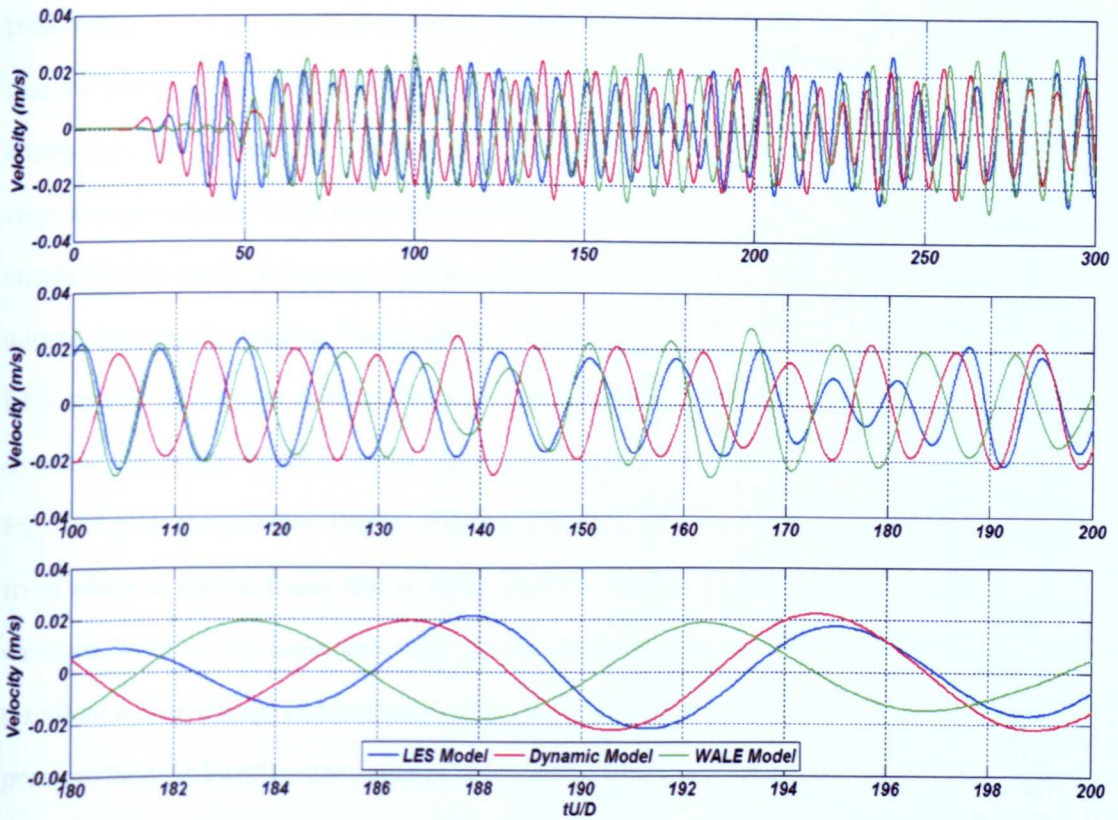


Fig 7.3.4 Velocity response of different LES models at the steady inlet boundary condition

Fig.7.3.4 and 7.3.5 plot the velocity and displacement response of square cylinder of different LES models at the steady inlet. From Fig.7.3.4, it can be found that the amplitude of velocity and displacement response of different LES models takes place at different reduced time step. To the whole response process Fig.7.3.4 and 7.3.5 show a mix-band response, however the response of square cylinder shows a narrow band process at the range 80-150 of reduced time step, which means that the vortices generated by the flow around and at the back of the square cylinder take place alternately. At the same time, due to the interaction between the flow field and the square cylinder itself, the structural viscous damping restricts the harmonic and symmetrical oscillation of square cylinder and the flow field pattern and vortex eddies around the structure will change with the structural movement. With the turbulence development the interaction between the structure and flow will be reduced, the response of square cylinder will change the symmetrical state into the random state, and when the structural movement becomes strong, the structural viscous damping takes effects.

Fig.7.3.6 plots the PSD value of lift force of different LES models, and Fig 7.3.7 plots the PSD value of displacement response of square cylinder. From both figures it can be found that there are

peak values at a fixed significant reduced frequency to different LES models, which is caused by that the vortex shedding dominates the vortices around the square cylinder, and this phenomenon shows the lock-on explicitly. And it is also found that the magnitude of lift force and displacement response predicted by LES dynamic model is higher than the other ones from LES WALE and standard LES model, it is caused by the LES model itself. It is known that LES dynamic model adopts dynamically varying Smagorinsky constant and a fixed constant is used in the standard LES model. To the high reduced frequency range the displacement PSD value predicted by LES dynamic and WALE model is higher than that of standard LES model.

Fig.7.3.8 plots the pressure contour of different LES models at three time steps (5s, 15s, and 25s), from which it can be found that to different LES models the pressure contour shows different variation even at the same time step due to the application of different LES models. Since turbulent eddies change continuously as they are convected by the mean flow, the instantaneous pressure fields induced by them change continuously as well. At the same time it is also found that with the time varying, the flow around and at the back of the square cylinder is also different, which further presents that the flow pattern will show more complex variation process due to the influence of LES model itself and the interaction between the flow and structure.

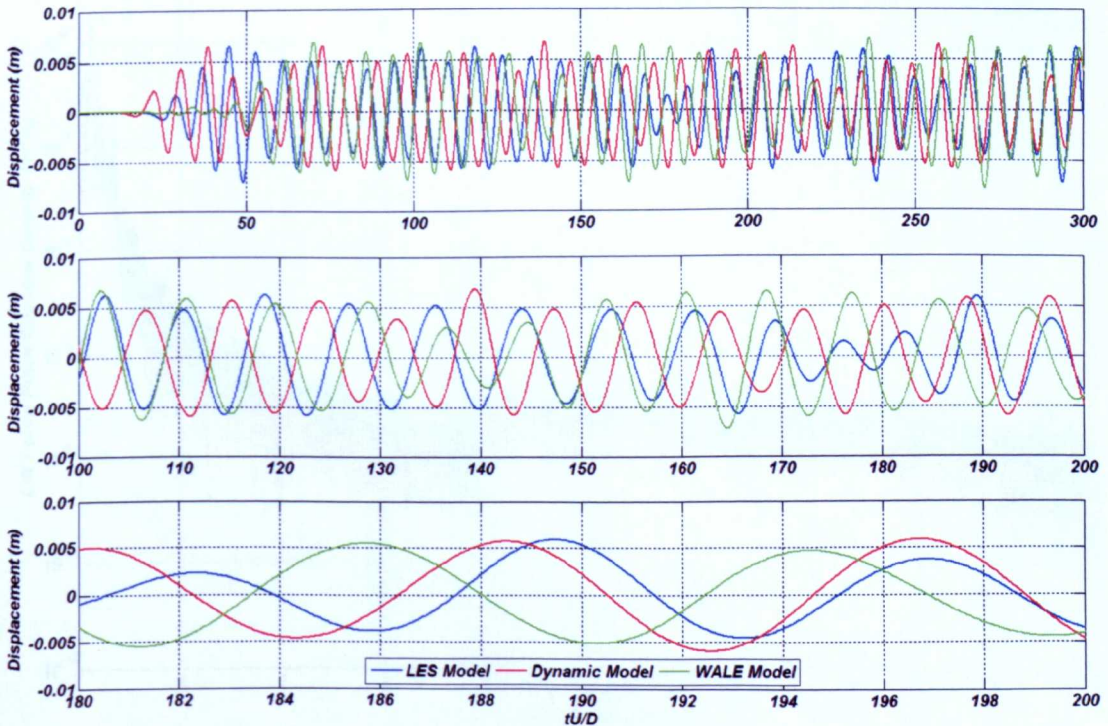
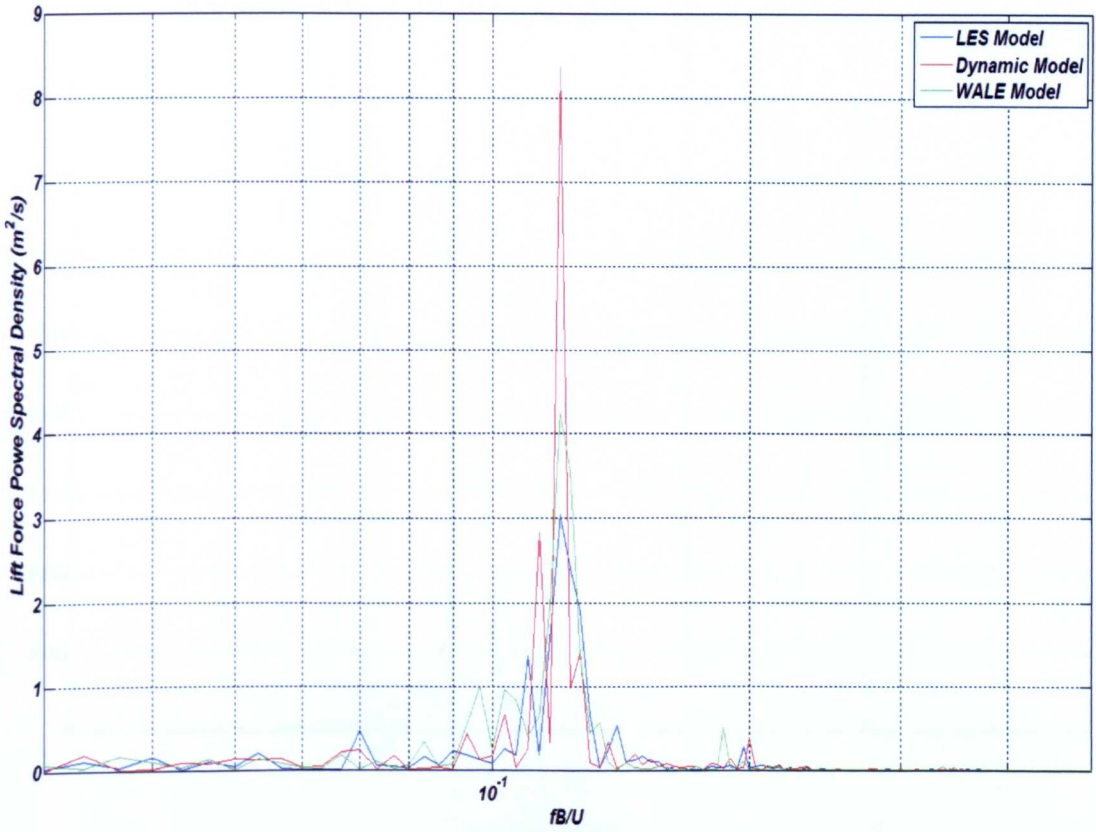
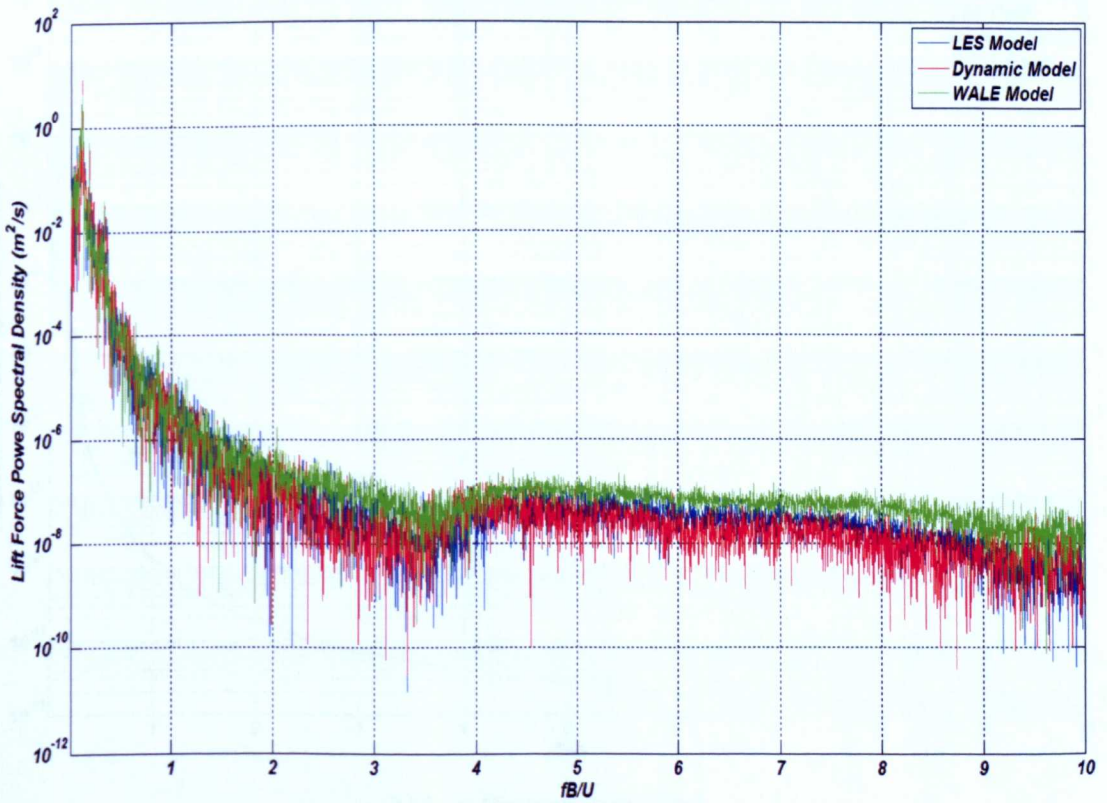


Fig 7.3.5 Displacement response of different LES models at the steady inlet boundary condition

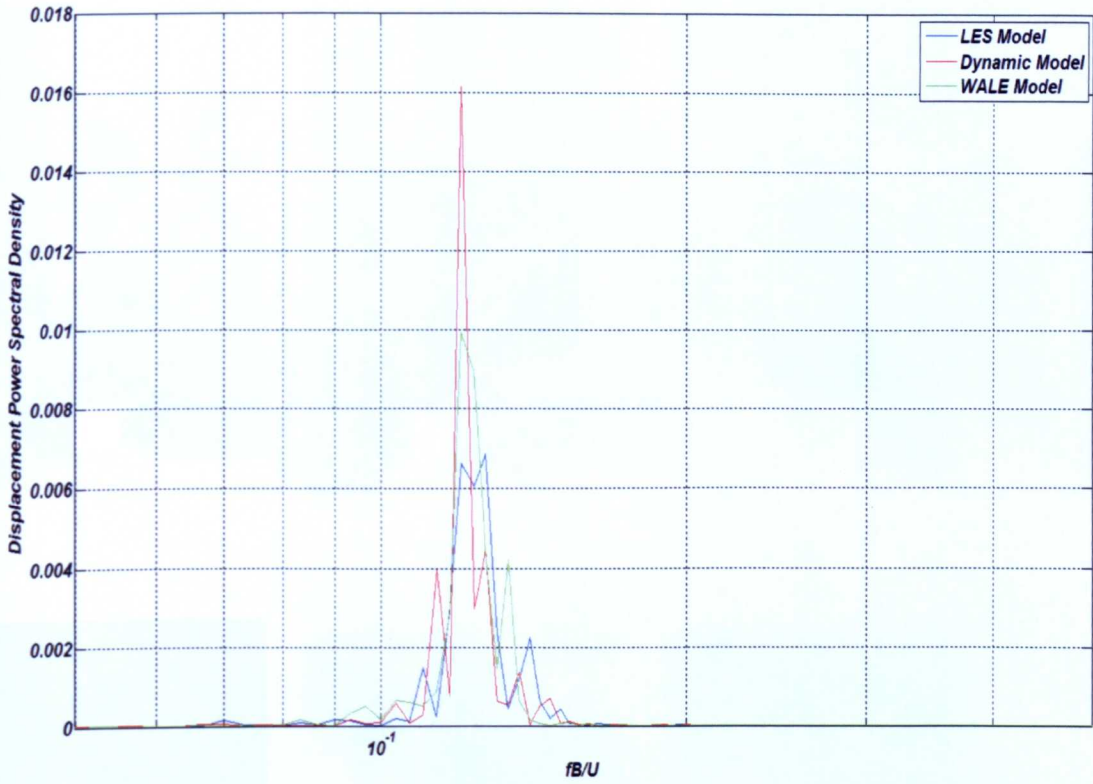


(a) Log fB/U

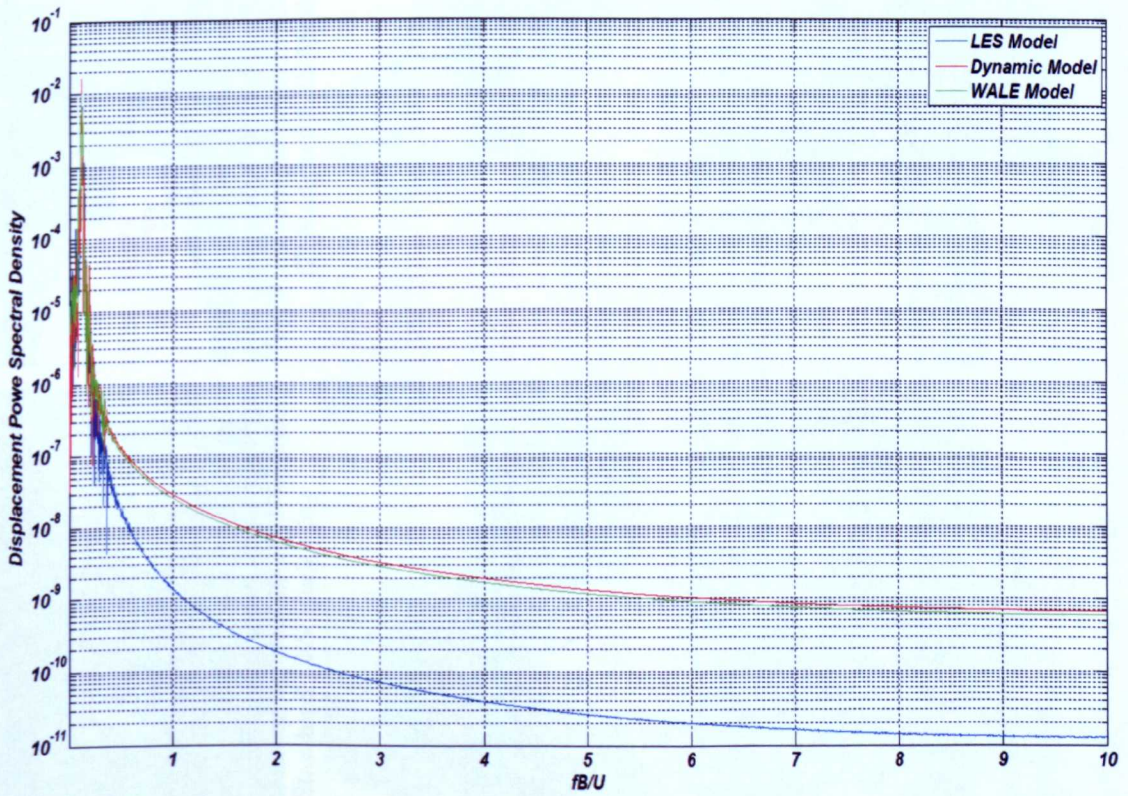


(b) Log lift force

7.3.6 PSD values of lift force of different LES models at the steady inlet boundary condition

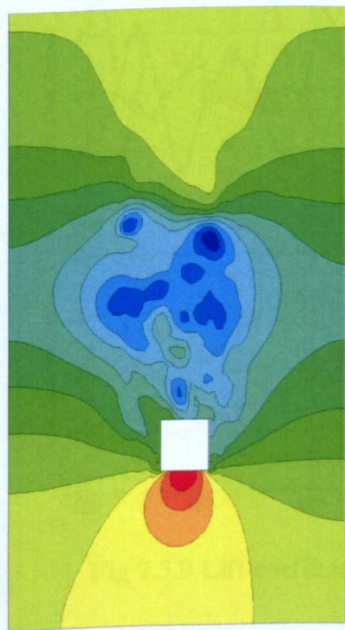


(a) Log fB/U

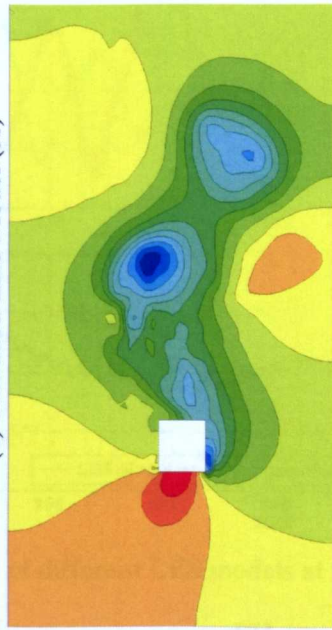


(b) Log displacement value

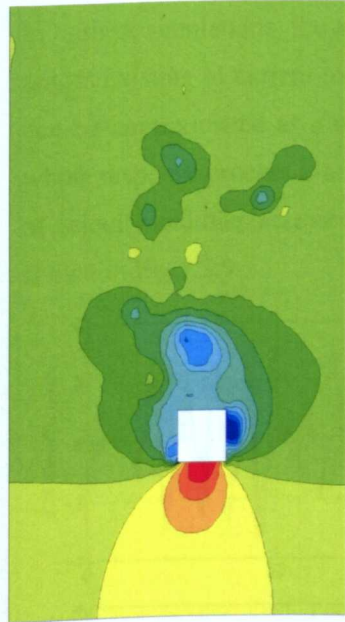
7.3.7 PSD values of displacement response for different LES models at the steady inlet boundary condition



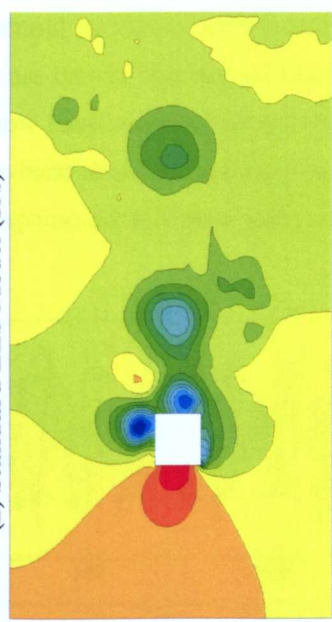
(1) Standard LES Model (5s)



(1) LES Dynamic Model (5s)



(2) Standard LES Model (15s)



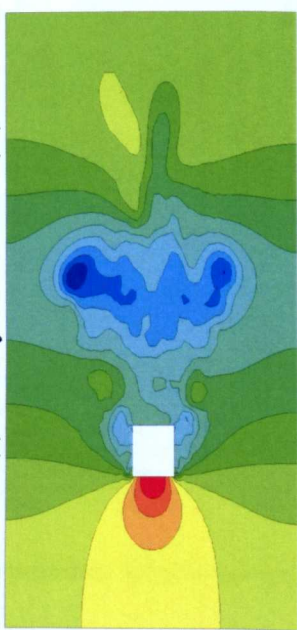
(2) LES Dynamic Model (15s)



(3) Standard LES Model (25s)



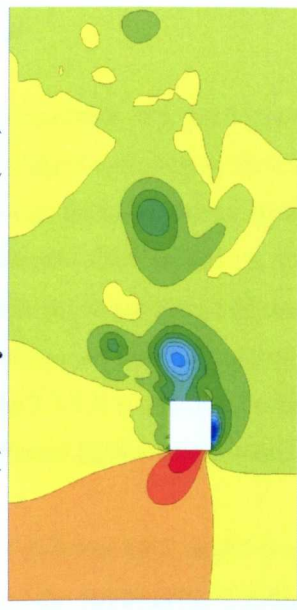
(3) LES Dynamic Model (25s)



(1) LES WALE Model (5s)



(2) LES WALE Model (15s)



(3) LES WALE Model (25s)

7.3.8 Pressure contour of square cylinder from different LES models of the steady inlet boundary condition at different time steps

7.3.2 Result Discussion of Unsteady Inlet Boundary Condition

The structural response predicted by the steady inlet boundary condition has been discussed previously, and it is not enough to predict the structural buffeting response without considering the inlet turbulence, so the structural response with the unsteady inlet boundary condition is discussed in this section.

Fig.7.3.9 and 7.3.10 plot the lift and drag coefficients of different LES models at the unsteady inlet boundary condition, it can be found that to different LES models the magnitude and the emergence time (reduced time step, tU/D) of peak values of lift and drag coefficients are different, which is caused by the different vortex eddies predicted by different LES models. In Fig.7.3.9 it is also found that there are much more small peak values along the curves of lift coefficient of different LES models, which is caused by the small eddies generated by the input of inflow turbulence.

Fig.7.3.11 and 7.3.12 plot velocity and displacement response of different LES model at the unsteady inlet boundary condition, from both figures it can be found that due to the application of different LES models in current simulations, the structural oscillation shows different characteristics, and there are some phase angles existing in current response curves. And the oscillation induced by the flow of current simulations can be approximated as a narrow band response approximately after the reduced time step 100, but the whole response process is a mix-band response including the broad and narrow band. The variation process of velocity and displacement response doesn't show many small peak values as the curve of lift coefficient shown in Fig.7.3.9.

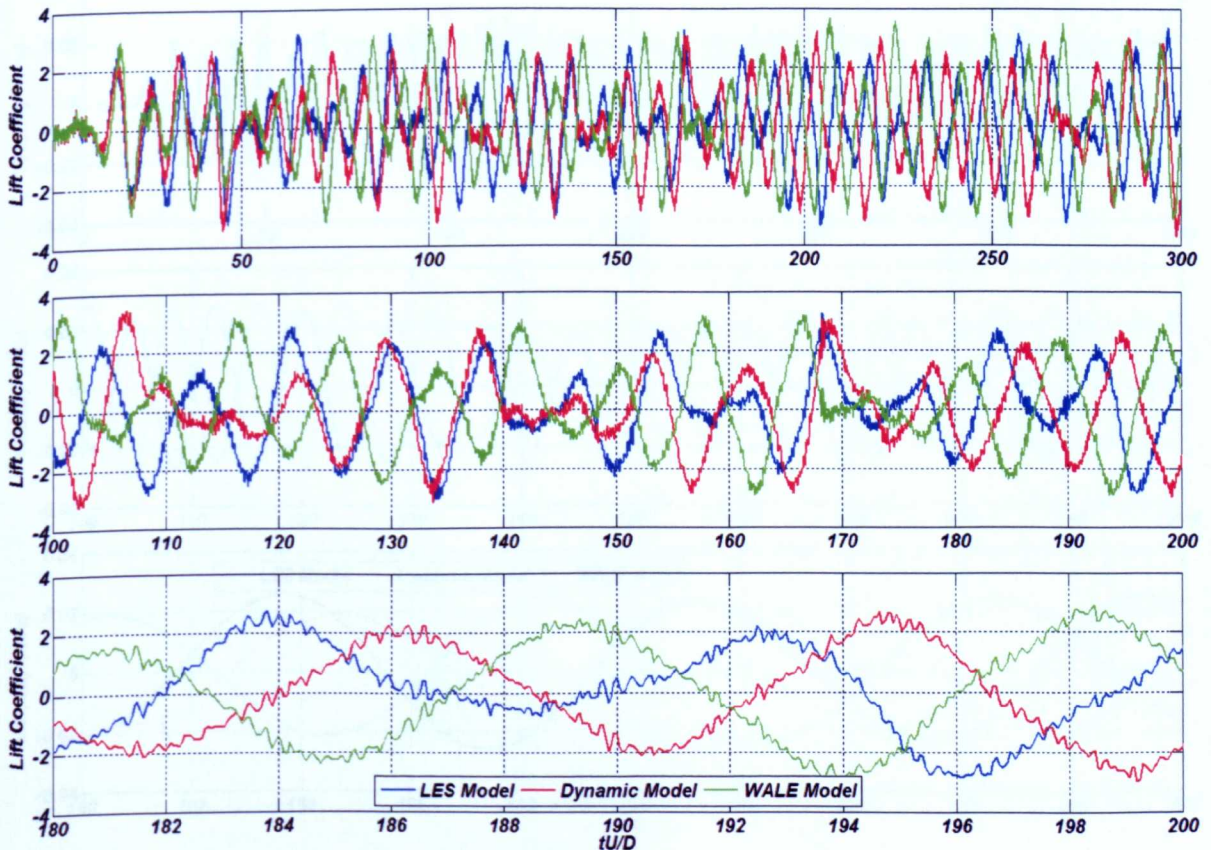


Fig 7.3.9 Lift coefficient of different LES models at the unsteady inlet boundary condition

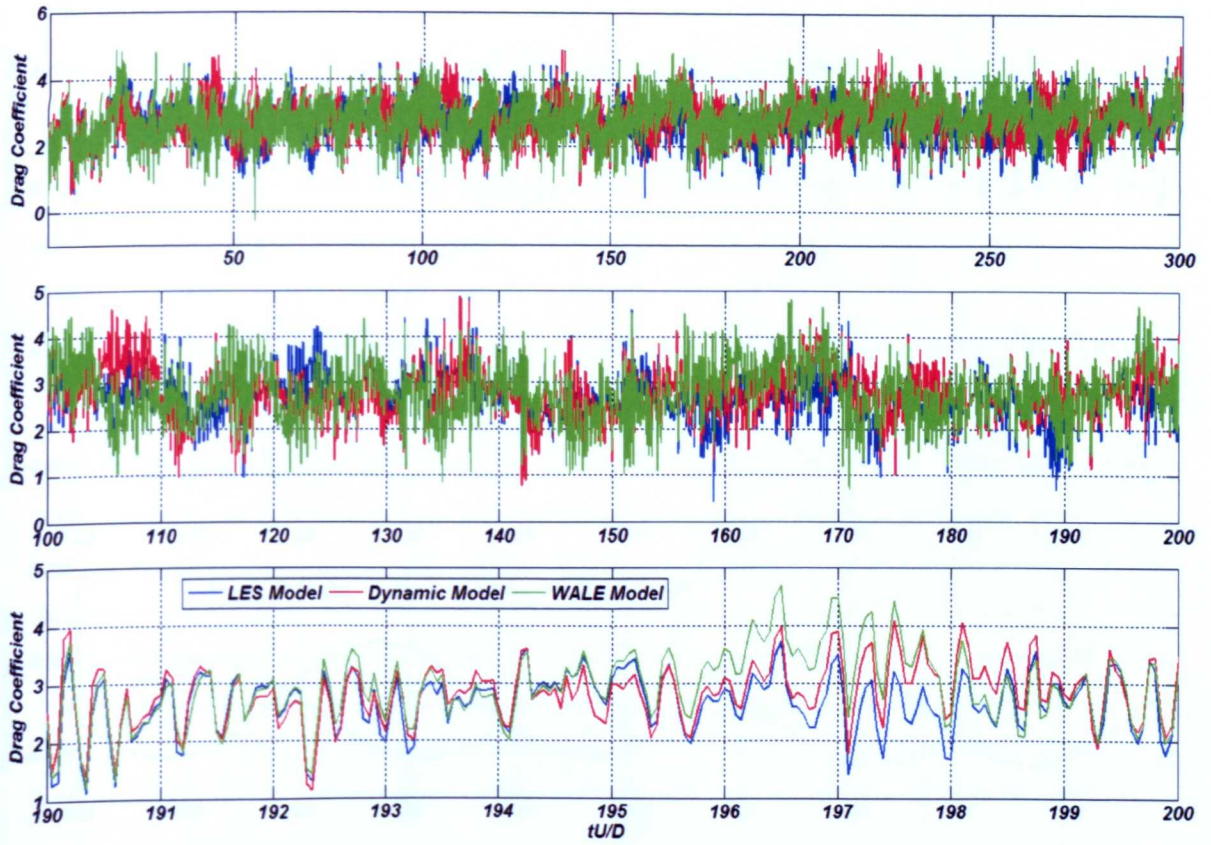


Fig 7.3.10 Drag coefficient of different LES models at the unsteady inlet boundary condition

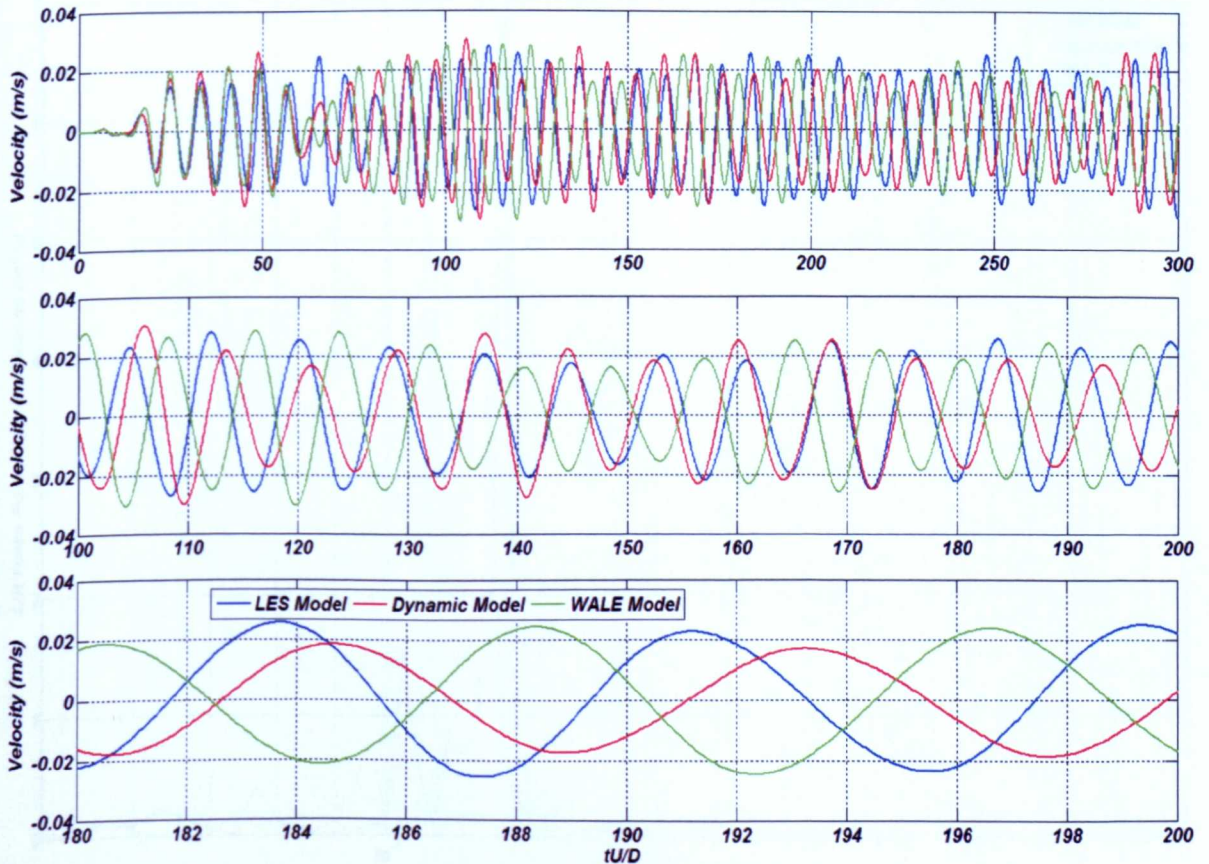


Fig 7.3.11 Velocity response of different LES models at the unsteady inlet boundary condition

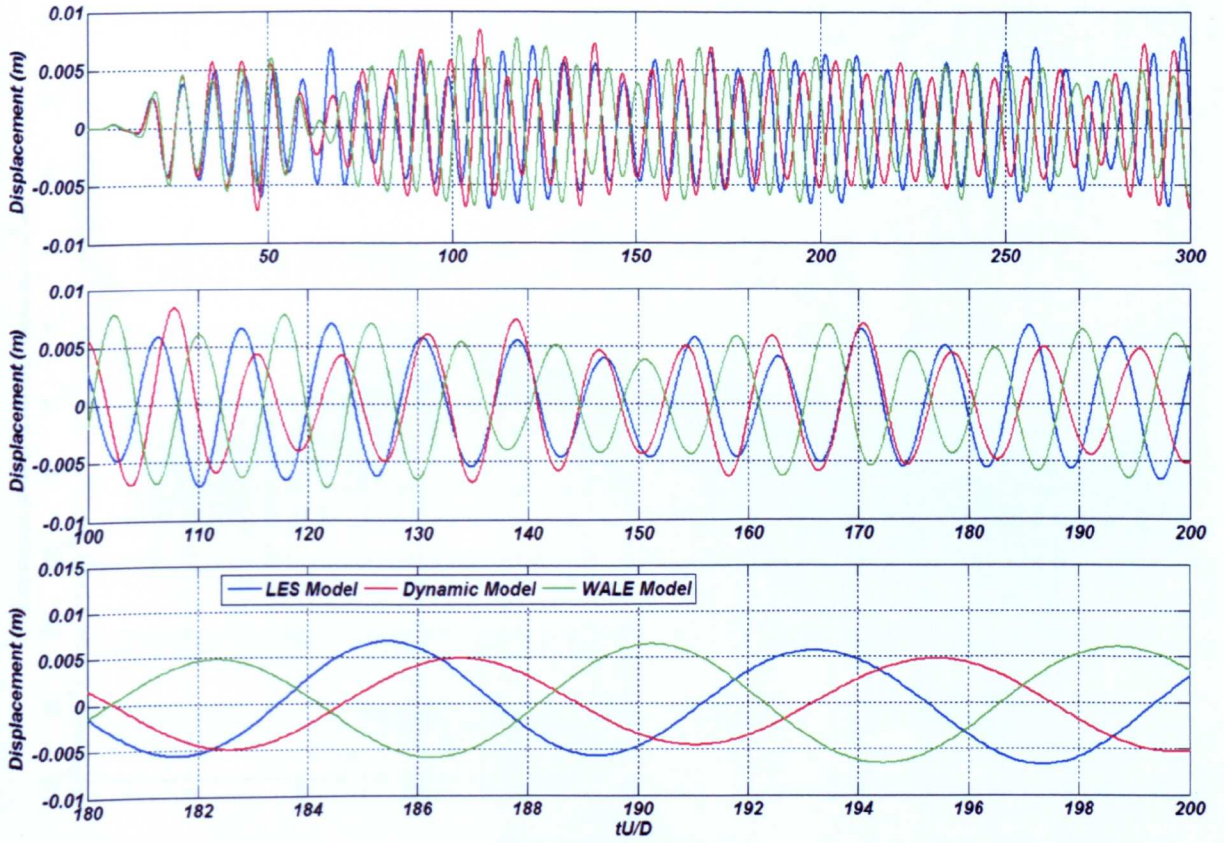
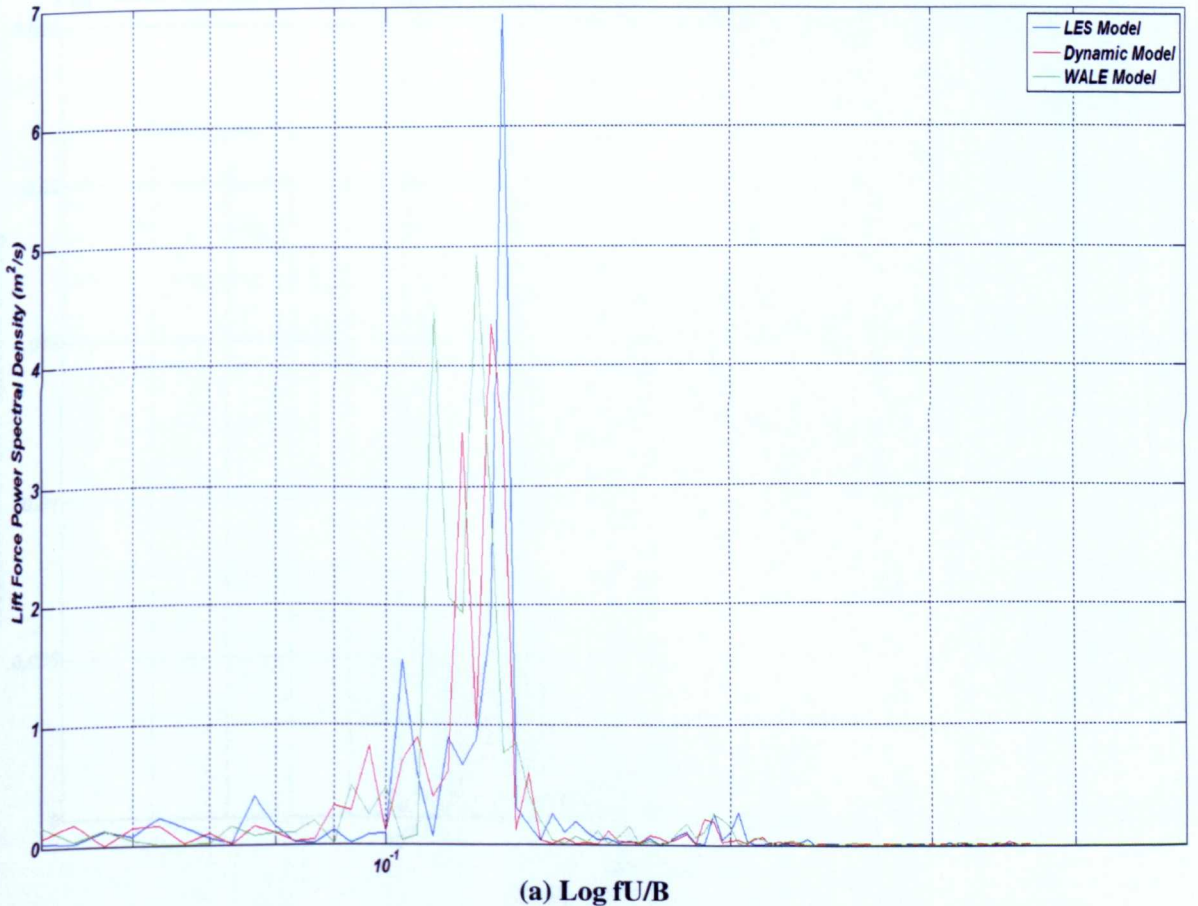
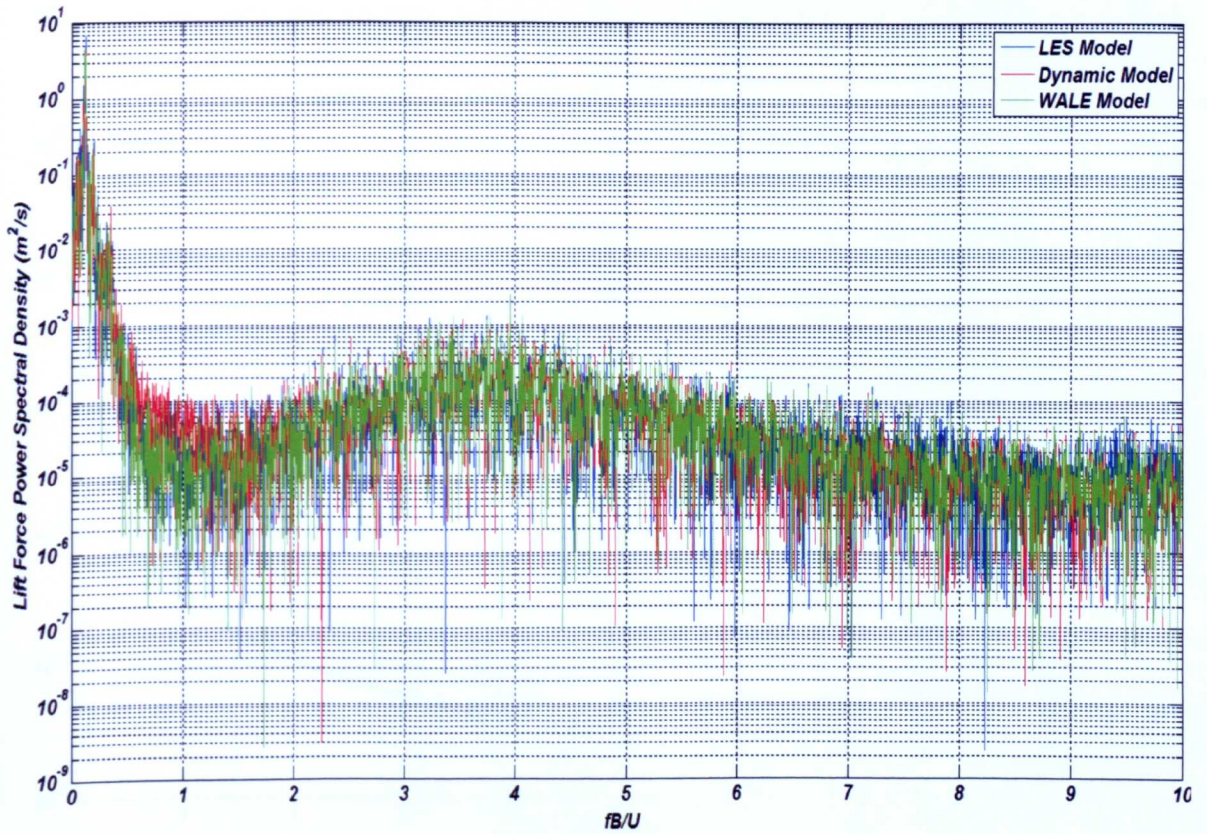


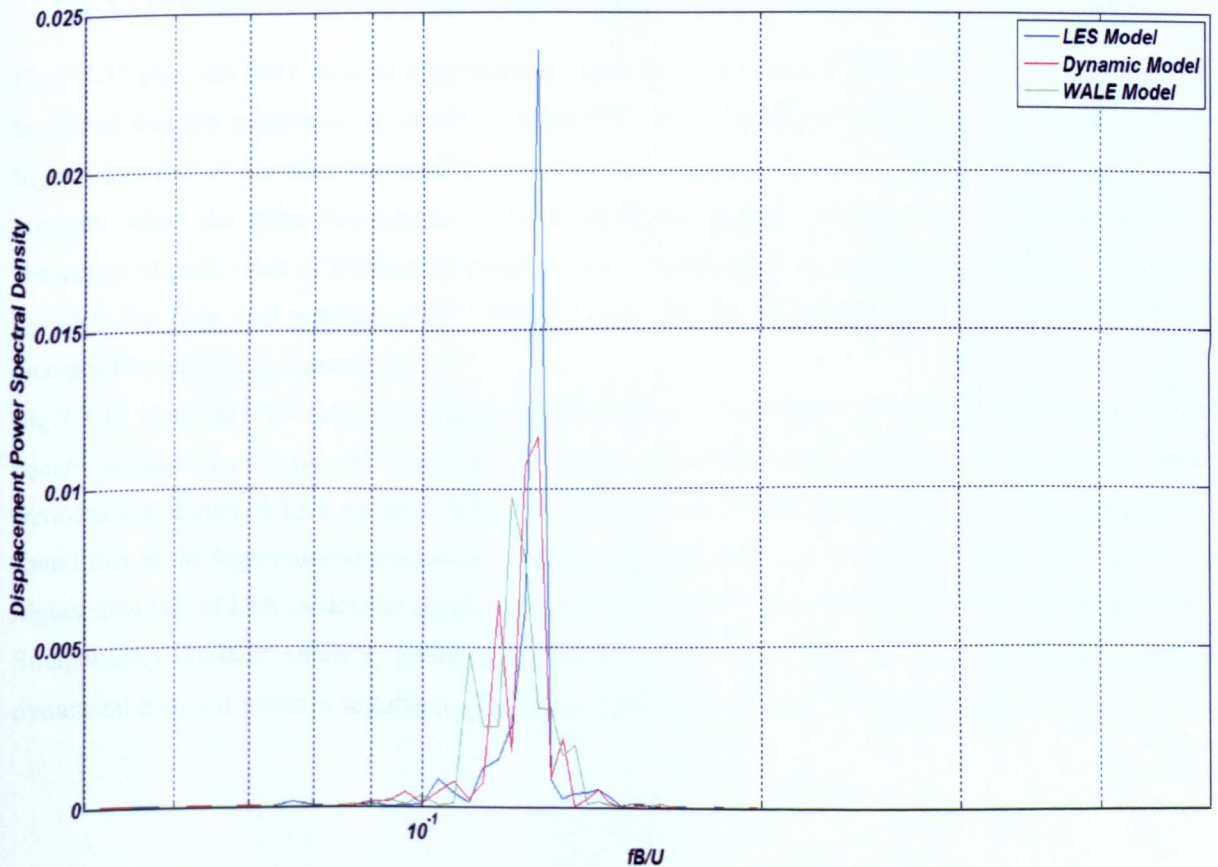
Fig 7.3.12 Displacement response of different LES models at the unsteady inlet boundary condition



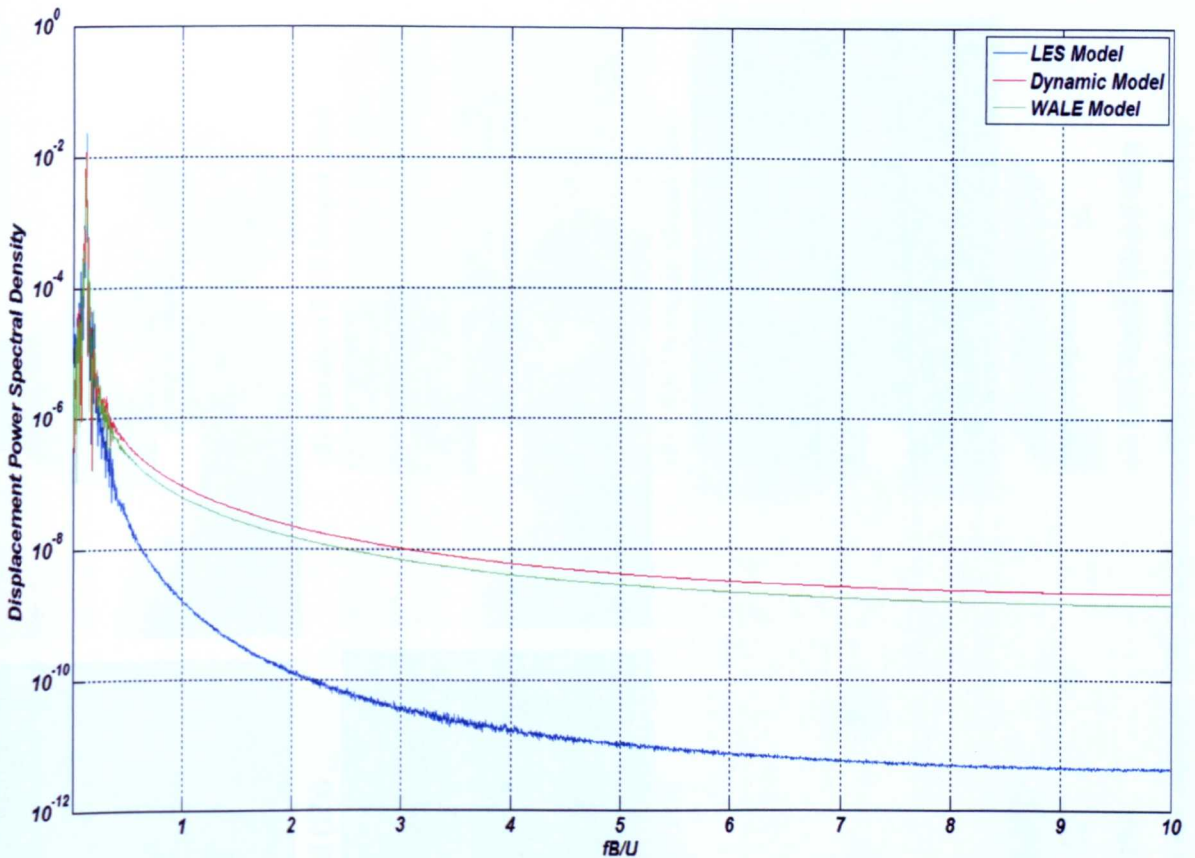


(b) Log Lift Force

Fig 7.3.13 Lift force PSD of different LES models at the unsteady inlet boundary condition



(a) Log fU/B

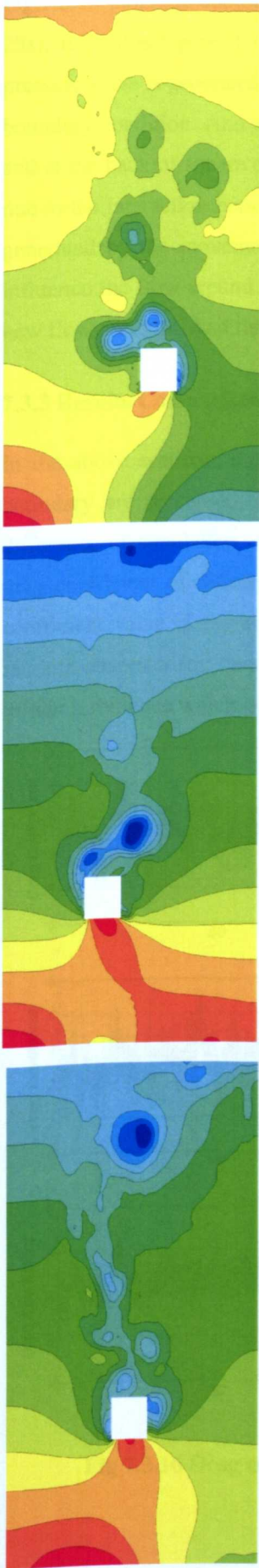


(b) Log Displacement

Fig 7.3.14 Displacement PSD of different LES models at the unsteady inlet boundary condition

Fig.7.3.13 plots the PSD value of lift force of different LES models at the unsteady inlet boundary; it can be found that the magnitude of significant frequency of lift force predicted by standard LES model is higher than that of the other two LES models, the reason is that LES model adopts a fixed Smagorinsky constant while the other two models adopt dynamically varying constant value. And the significant frequency of peak value of lift force is different, due to considering the input of turbulence and interaction between the flow and structure itself, which changes the significant frequency of lift force and then changes the oscillation of structure.

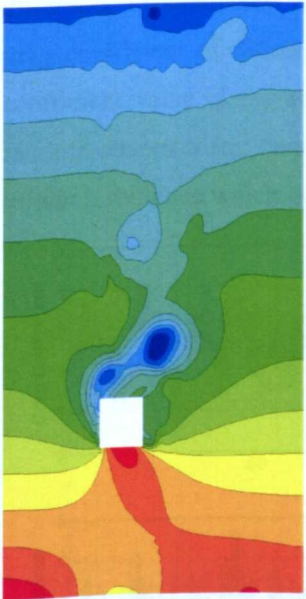
Fig.7.3.14 plots the PSD value of displacement response of the oscillation induced by the flow around the square cylinder, and it can be found that in current simulations the magnitude of significant reduced frequency predicted by LES model is higher than that of the other LES models, while in Fig.7.3.14 (b) it is found that in the high-reduced frequency range the value predicted by LES dynamic and WALE model is higher than that of LES model, the reason is that in current simulations, standard LES model adopts a fixed Smagorinsky constant value to predict and simulate the eddies, while the other two models use the dynamical constant which is suitable to predict and capture small eddies of high frequency.



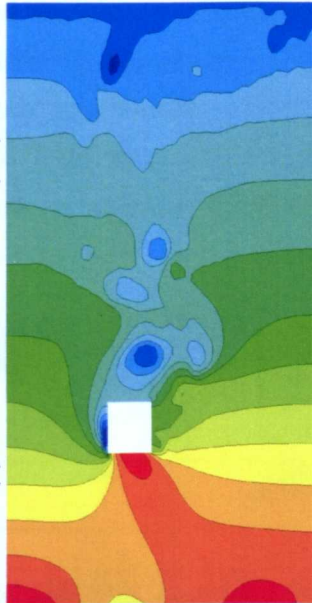
(1) Standard LES Model (5s)



(1) LES Dynamic Model (5s)



(2) Standard LES Model (15s)



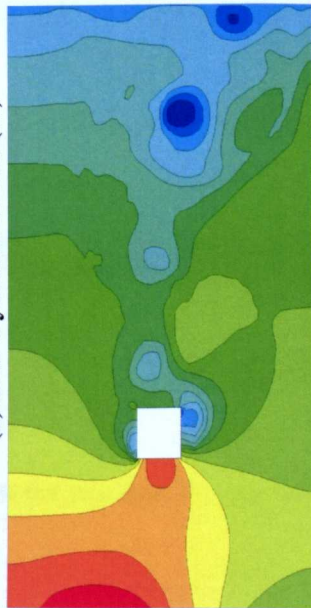
(2) LES Dynamic Model (15s)



(3) Standard LES Model (25s)



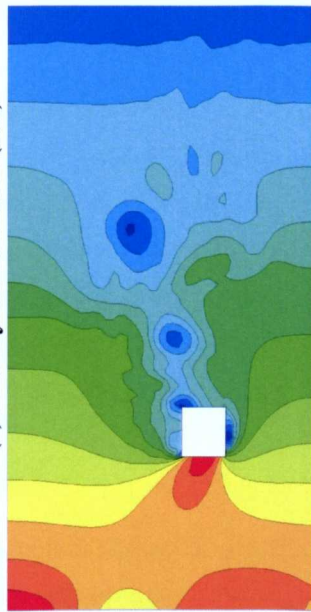
(3) LES Dynamic Model (25s)



(1) LES WALE Model (5s)



(2) LES WALE Model (15s)



(3) LES WALE Model (25s)

Fig 7.3.15 Pressure contour of square cylinder from different LES models of the unsteady inlet boundary condition at different time steps

Fig.7.3.15 plots the contour of pressure of different LES models at different reduced time steps (5s, 15s, 25s), from this figure it is found that due to the input of inflow turbulence at the inlet, the unsteady pressure wave is generated which is not the same as the simulation results shown in the case of steady inlet boundary condition. And at the same reduced time step the predicted pressure around the square cylinder and at the back of square cylinder is different due to the application of different models. At the same time due to the interaction between the flow and structure, the flow around the structure will absorb the energy generated by the movement of structure, and new flow pattern and vortices are generated, which will influence the flow around and at the back of the square cylinder in the computation domain and generate new flow pressure. And then these vortices will influence the structural response finally.

7.3.3 Results Comparison of Two Inlet Boundary Conditions

In the above sections, the simulation results of structural response under the steady and unsteady inlet boundary are discussed. In this part, the simulation results are presented and compared to find the *difference of simulation results between two inlet boundary conditions*. Fig.7.3.16 plots the variation of drag coefficient of different LES models for both inlet boundary conditions, it can be found that drag coefficient value of the unsteady inlet boundary condition has much more peak values and shows more random characteristic than that of the steady inlet boundary condition. This variation is generated by the inflow turbulence which generates more vortex eddies and random characteristic.

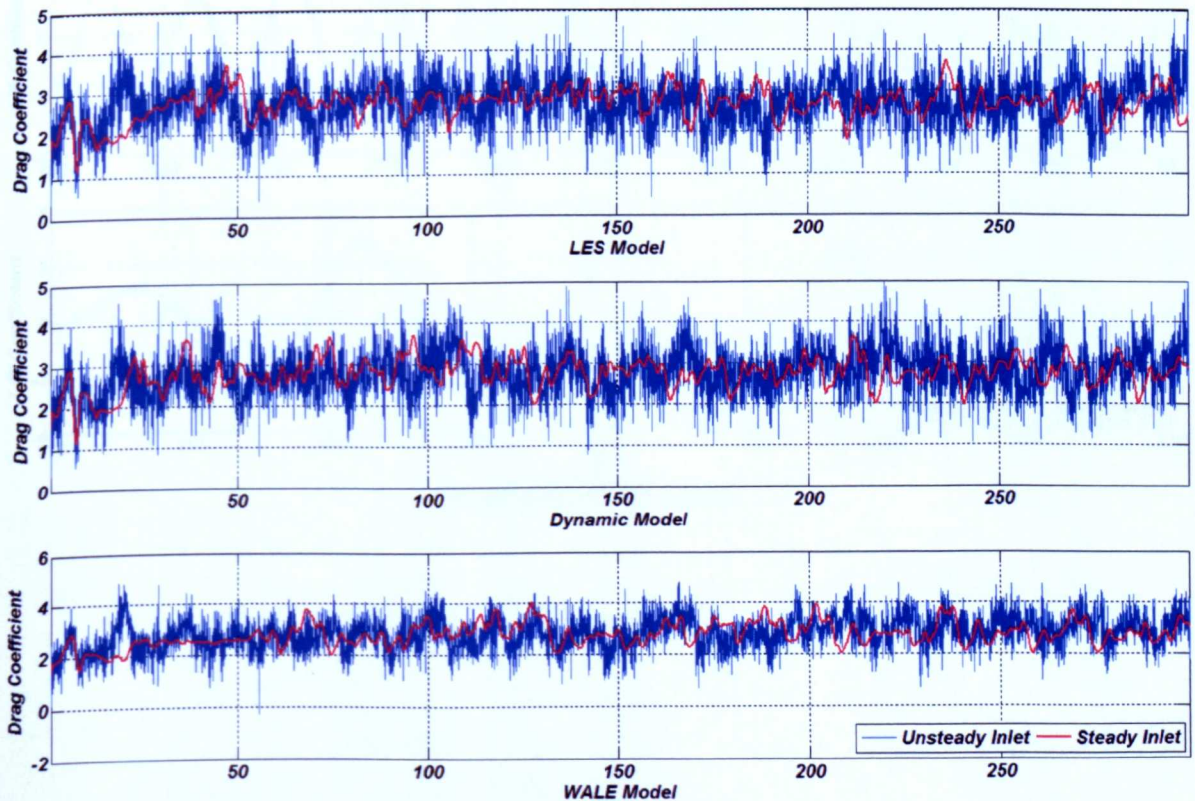
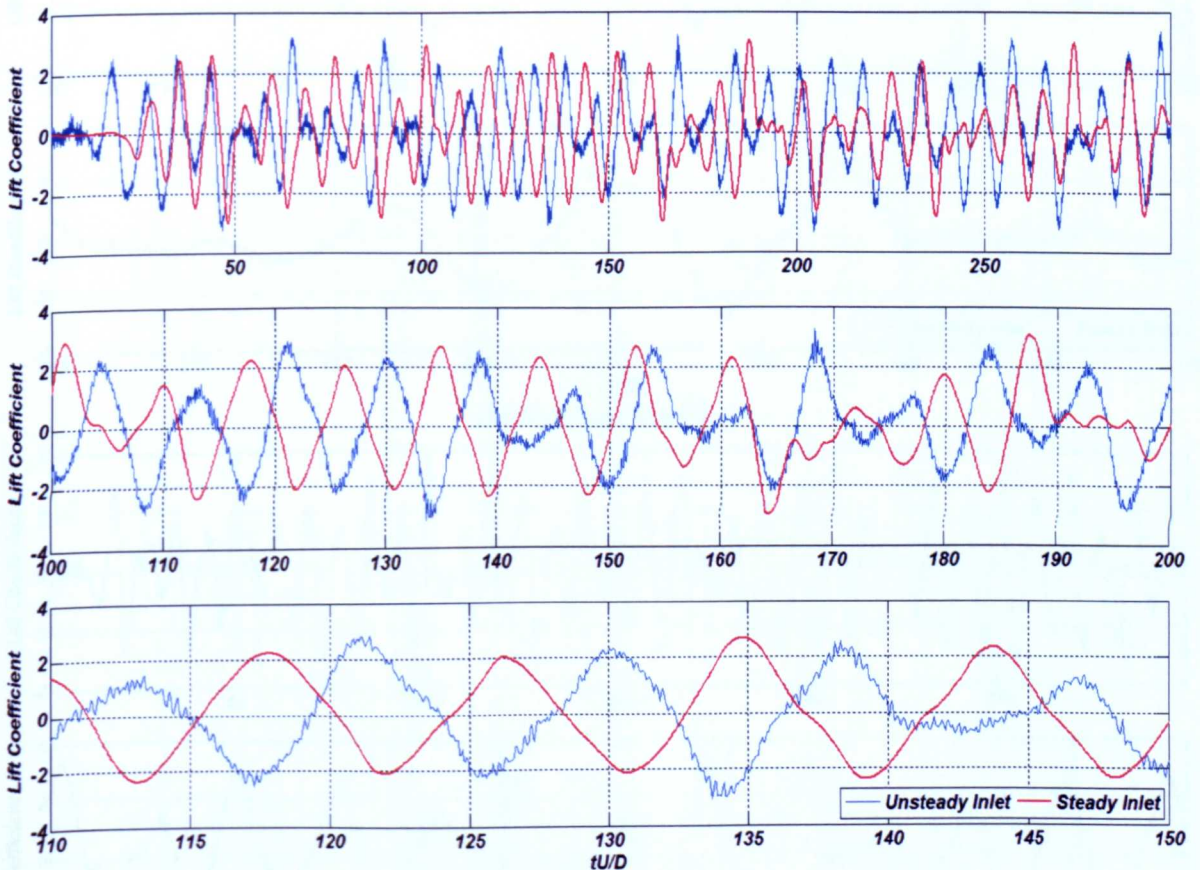
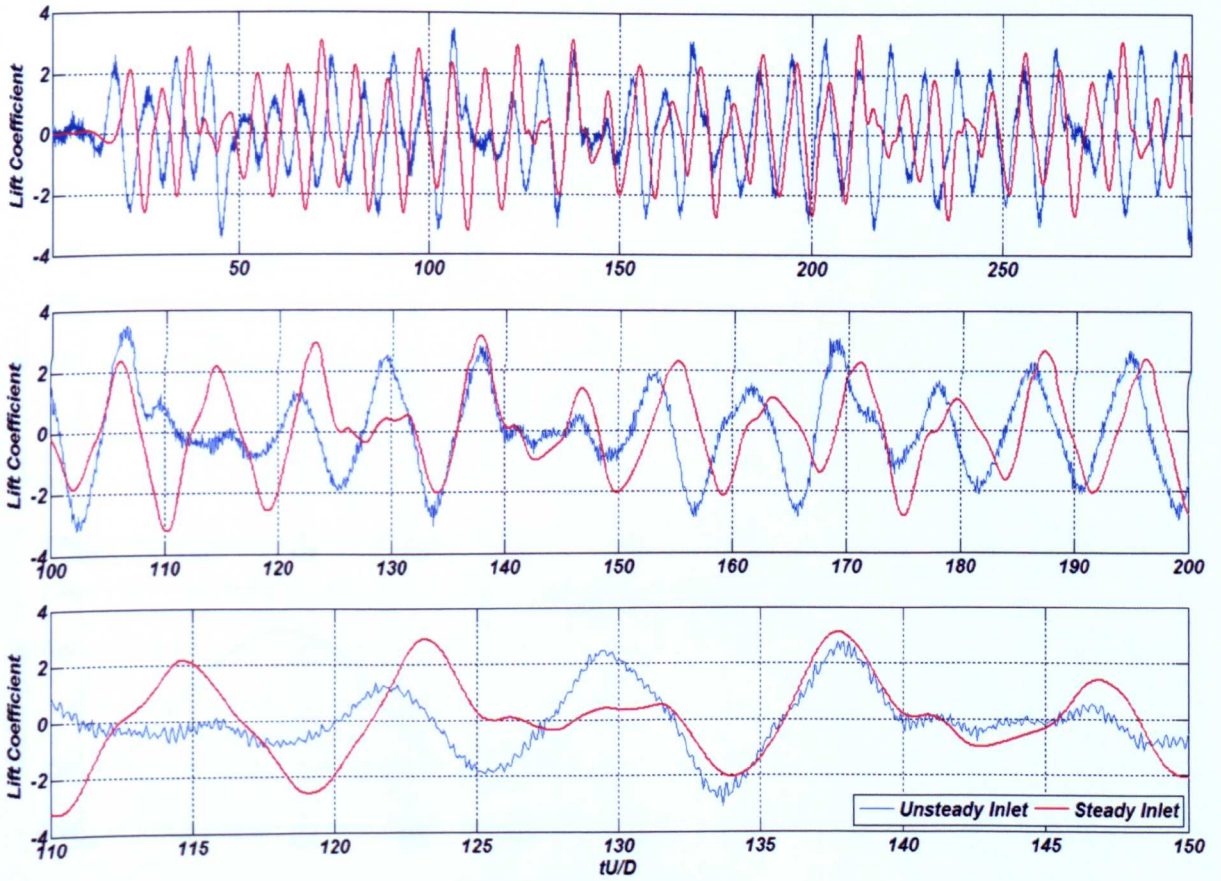


Fig 7.3.16 Drag coefficient of different LES models for two inlet boundary conditions

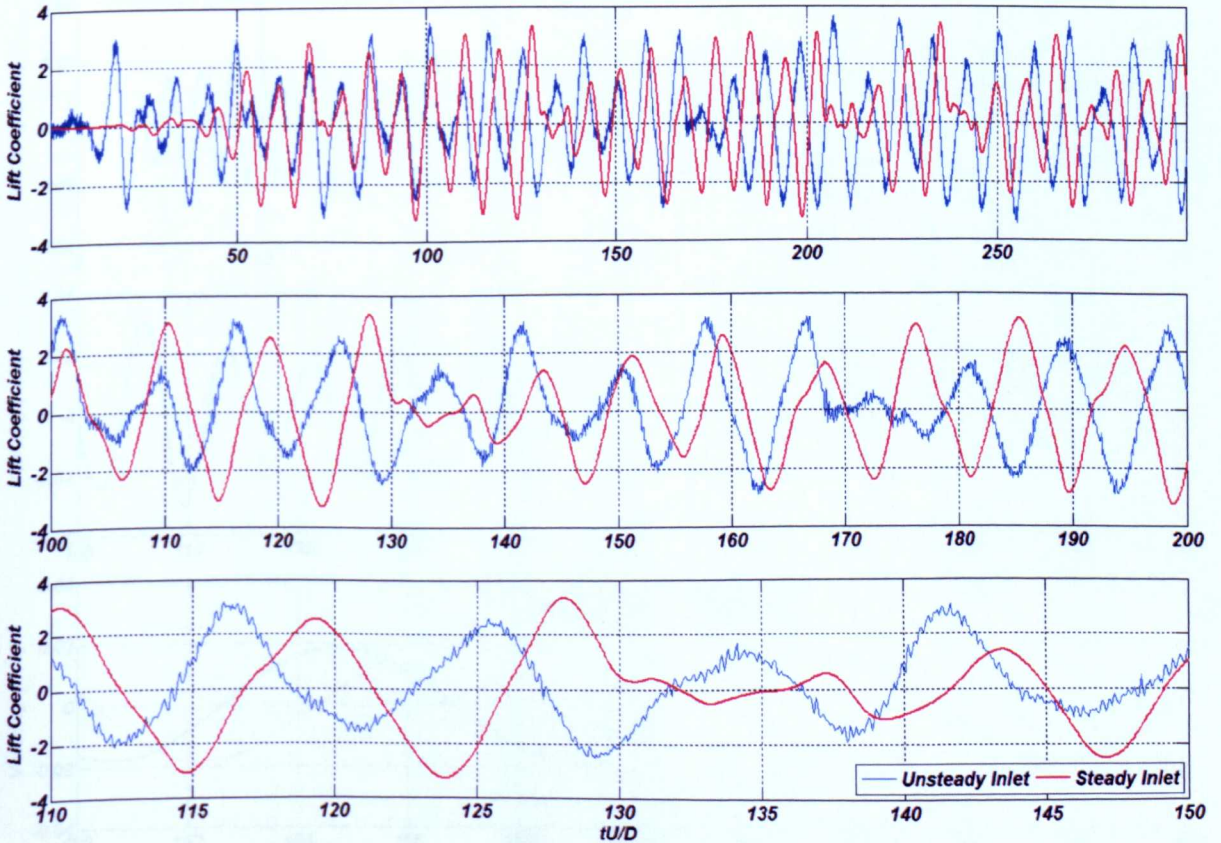
To investigate the difference of structural response between two inlet boundaries with further step, Fig.7.3.17 plots the variation of lift coefficient of different LES models between two different inlet boundaries at different time steps, it can be found that to three LES models the time history peak values of lift coefficient vary with time variation, and it is also found that the amplitude of lift coefficient of different LES models from the unsteady inlet boundary condition is not as smooth as the one from the steady inlet boundary condition and has much more peak values than the other two models, which is caused by the input of inflow turbulence generating many small eddies. And from the time history curves of lift coefficient of different models it is also found that during the reduced time step range (110-150) the time history curve of lift coefficient of standard LES model shows more harmonic characteristic than that of the other two LES models



(a) Standard LES Model

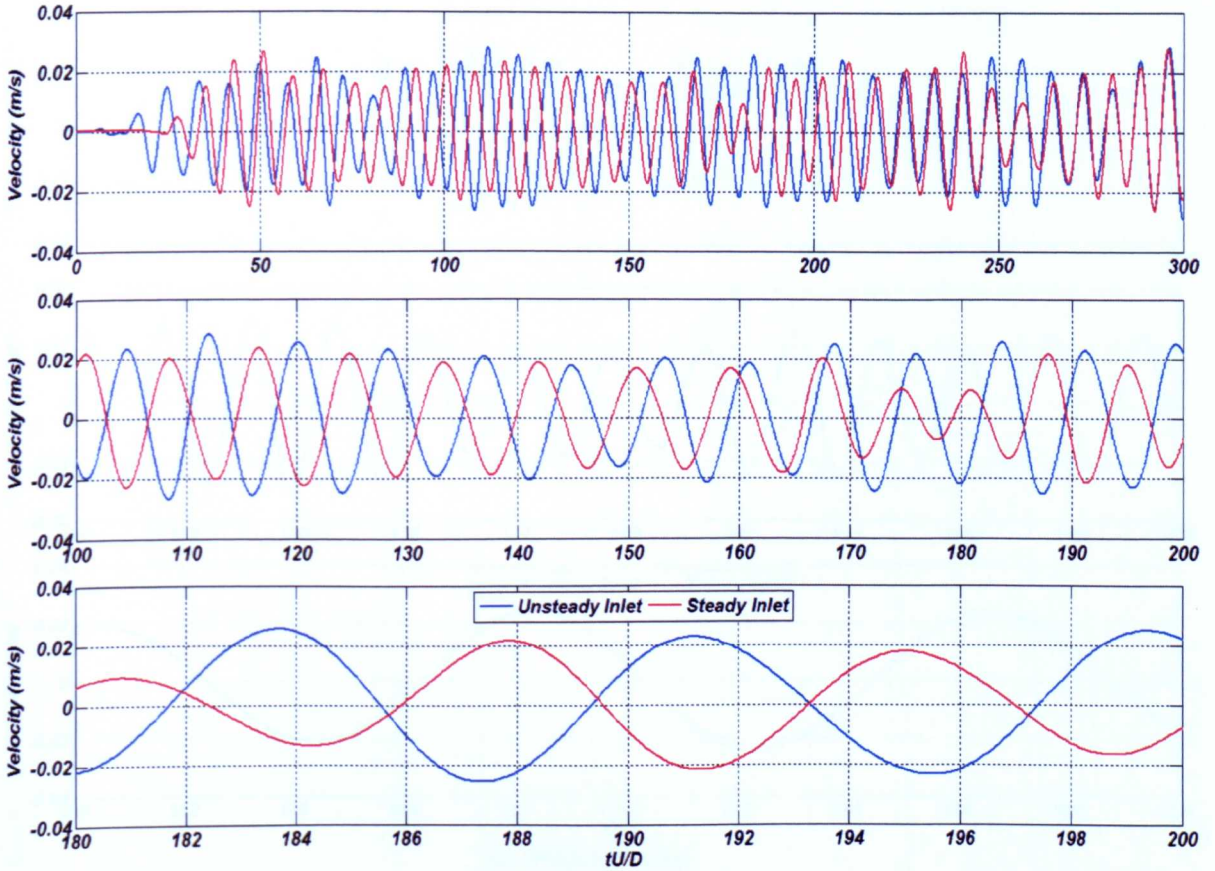


(b) Dynamic Model

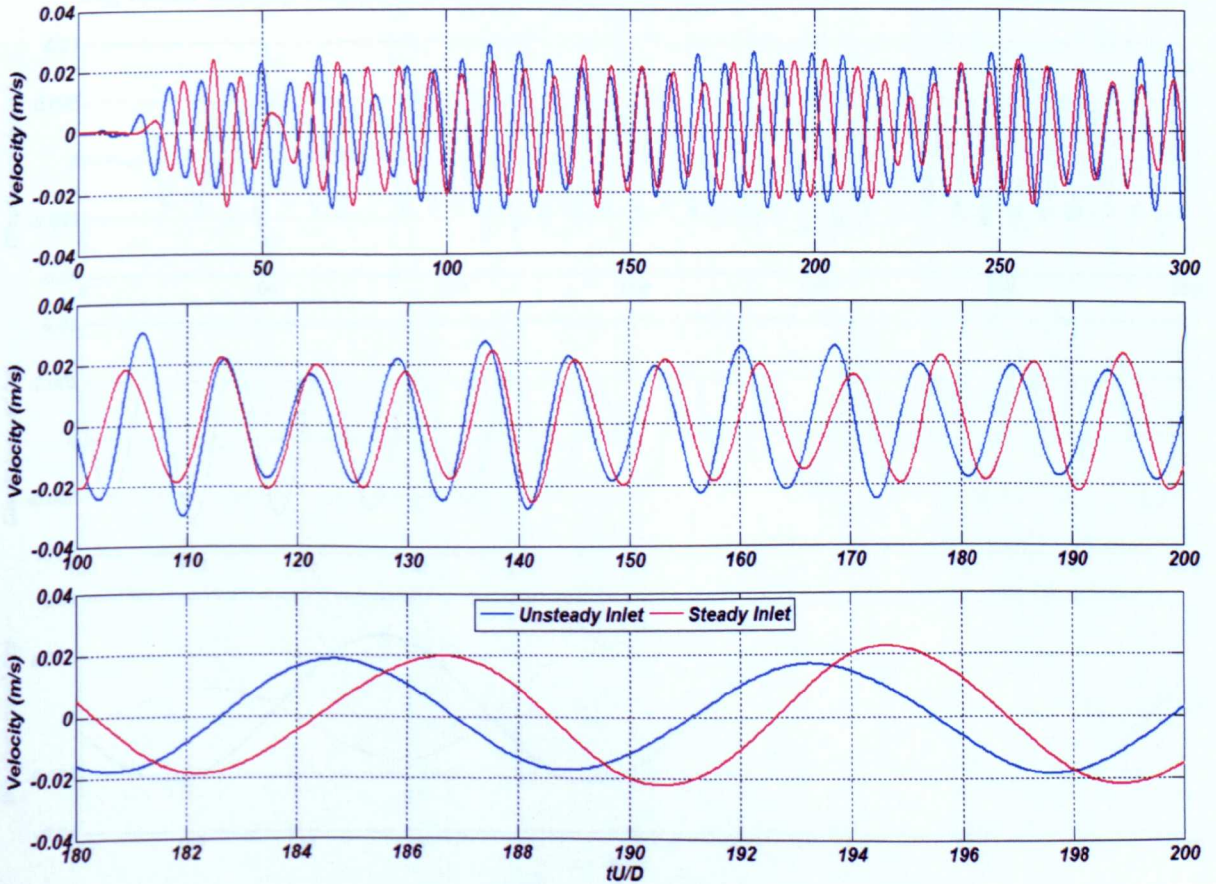


(c) WALE Model

Fig 7.3.17 Lift coefficient of different LES models for two inlet boundary conditions



(a) Standard LES Model



(b) Dynamic Model

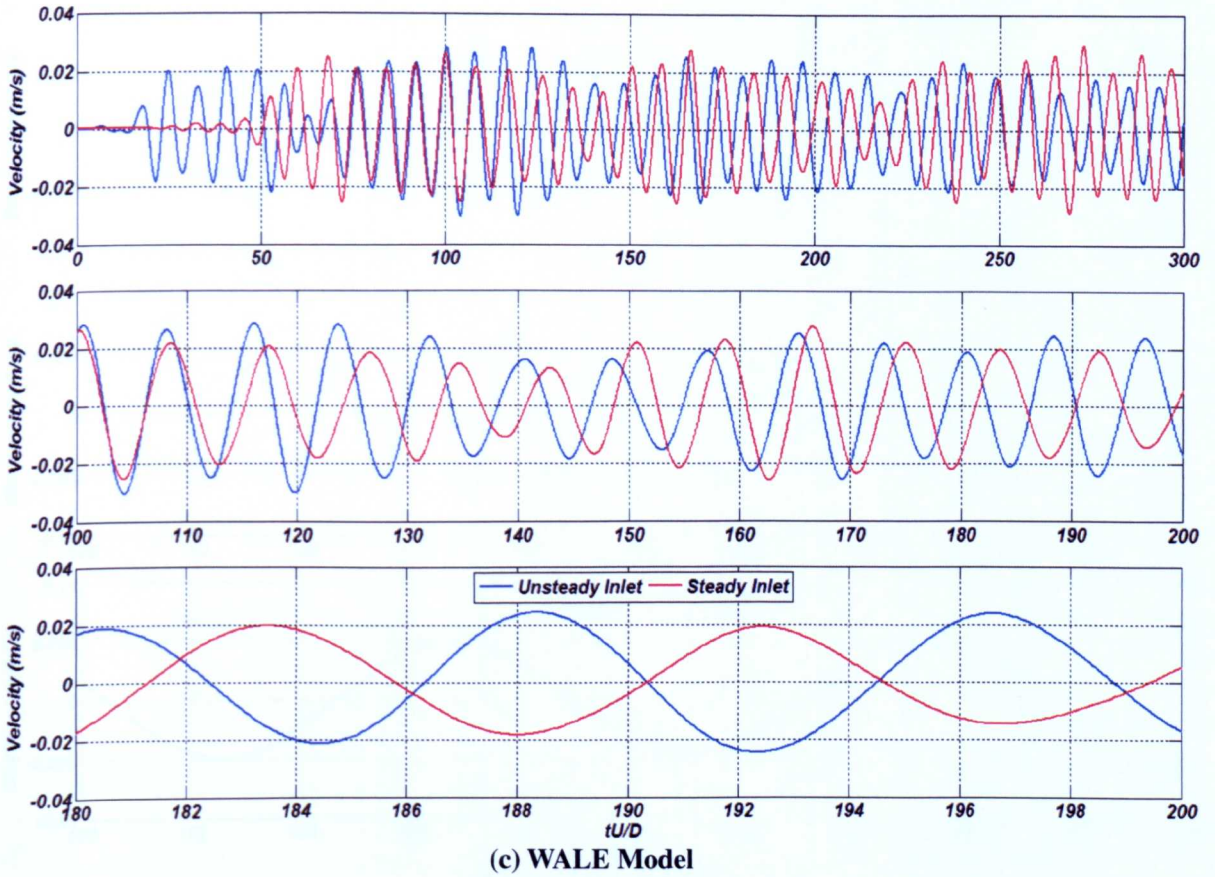
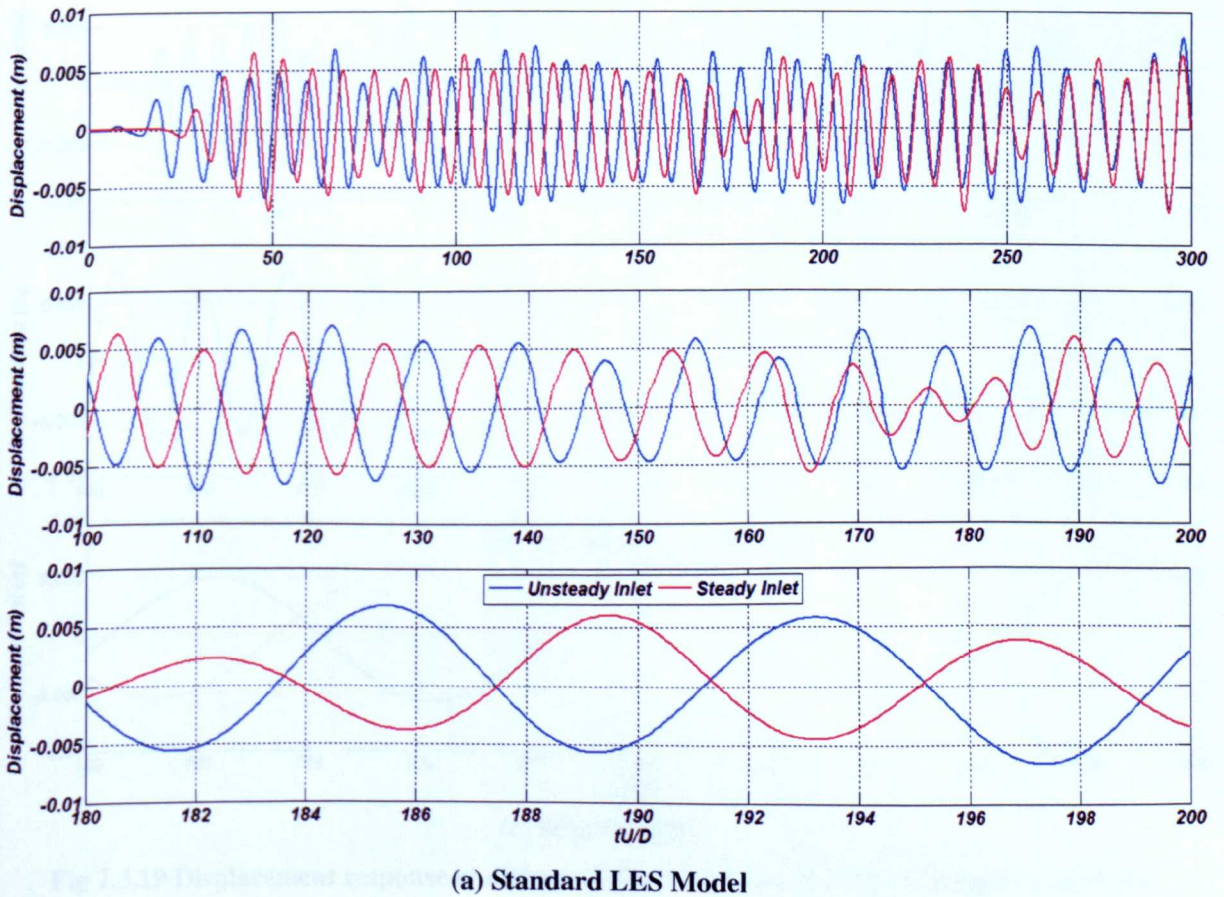
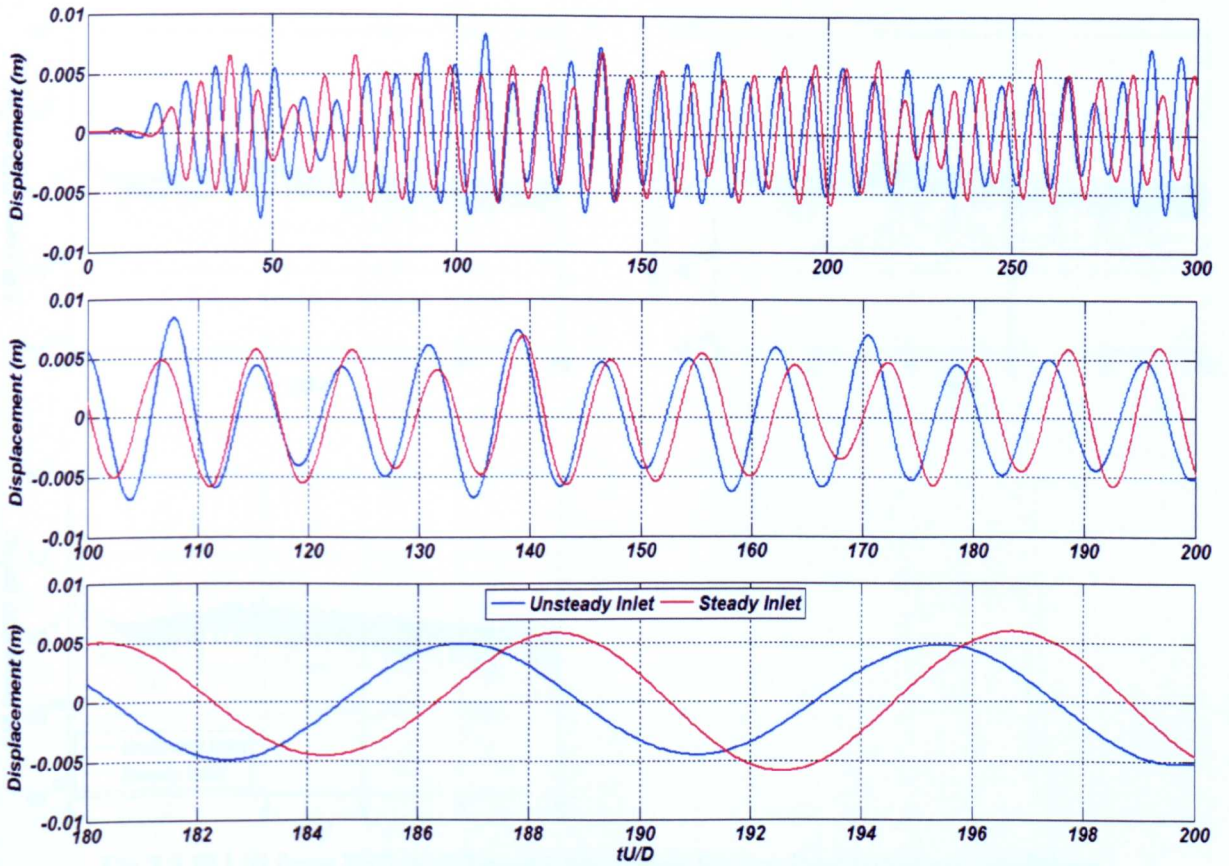
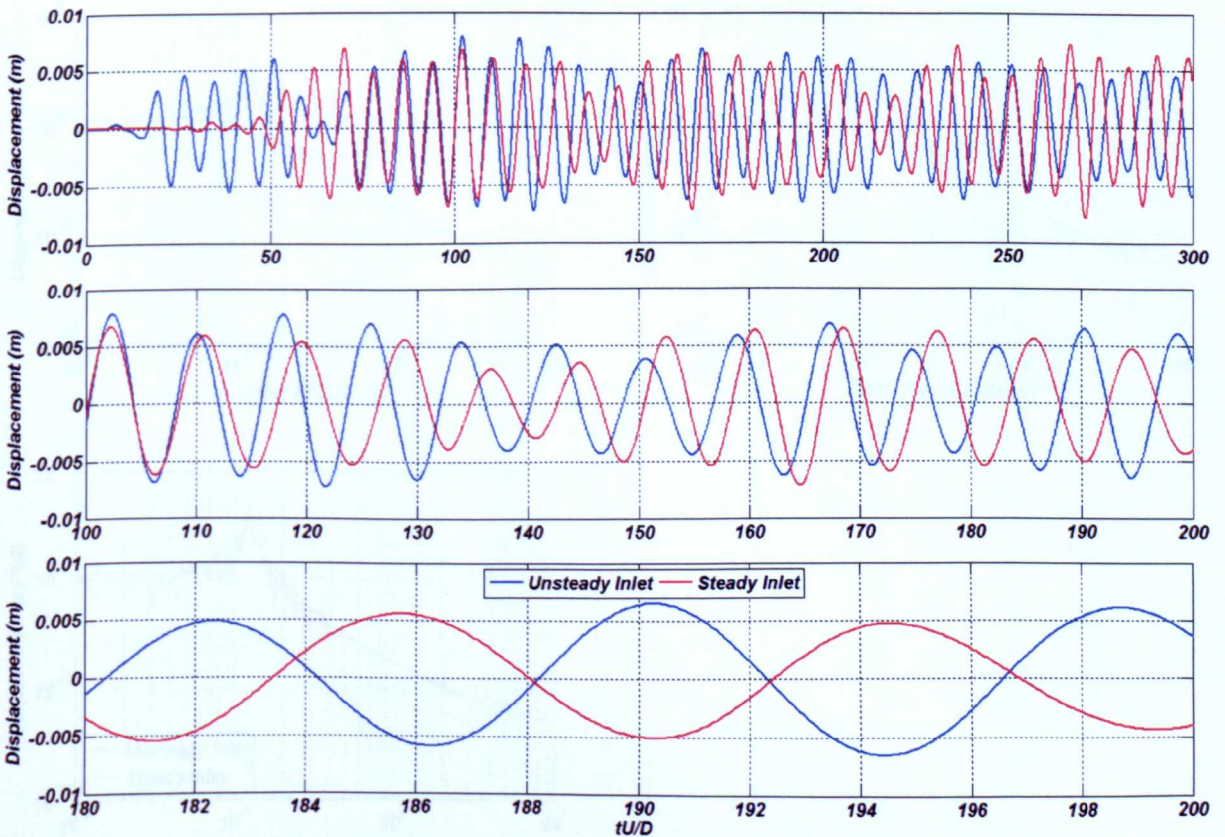


Fig 7.3.18 Velocity response of different LES models for two inlet boundary conditions





(b) Dynamic Model



(c) WALE Model

Fig 7.3.19 Displacement response of different LES models for two inlet boundary conditions

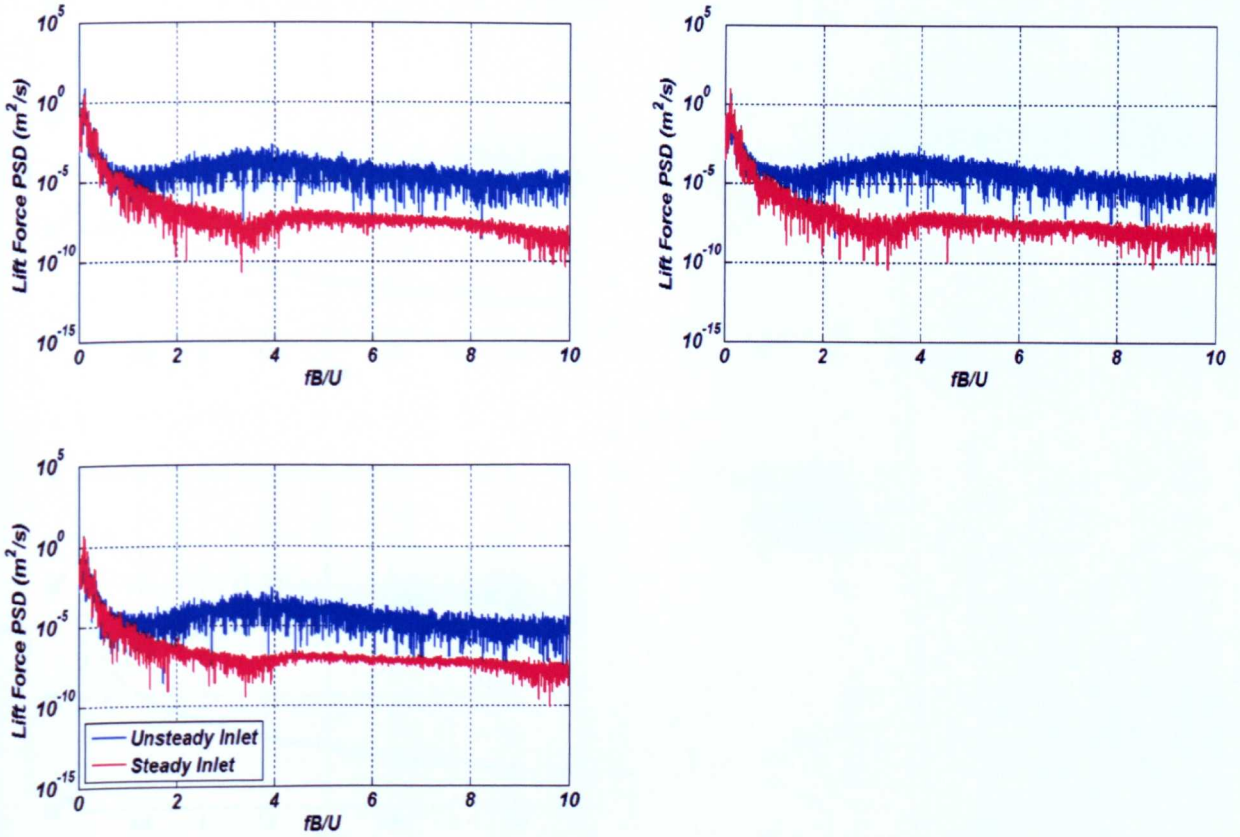


Fig 7.3.20 Lift force PSD of different LES models for two inlet boundary conditions

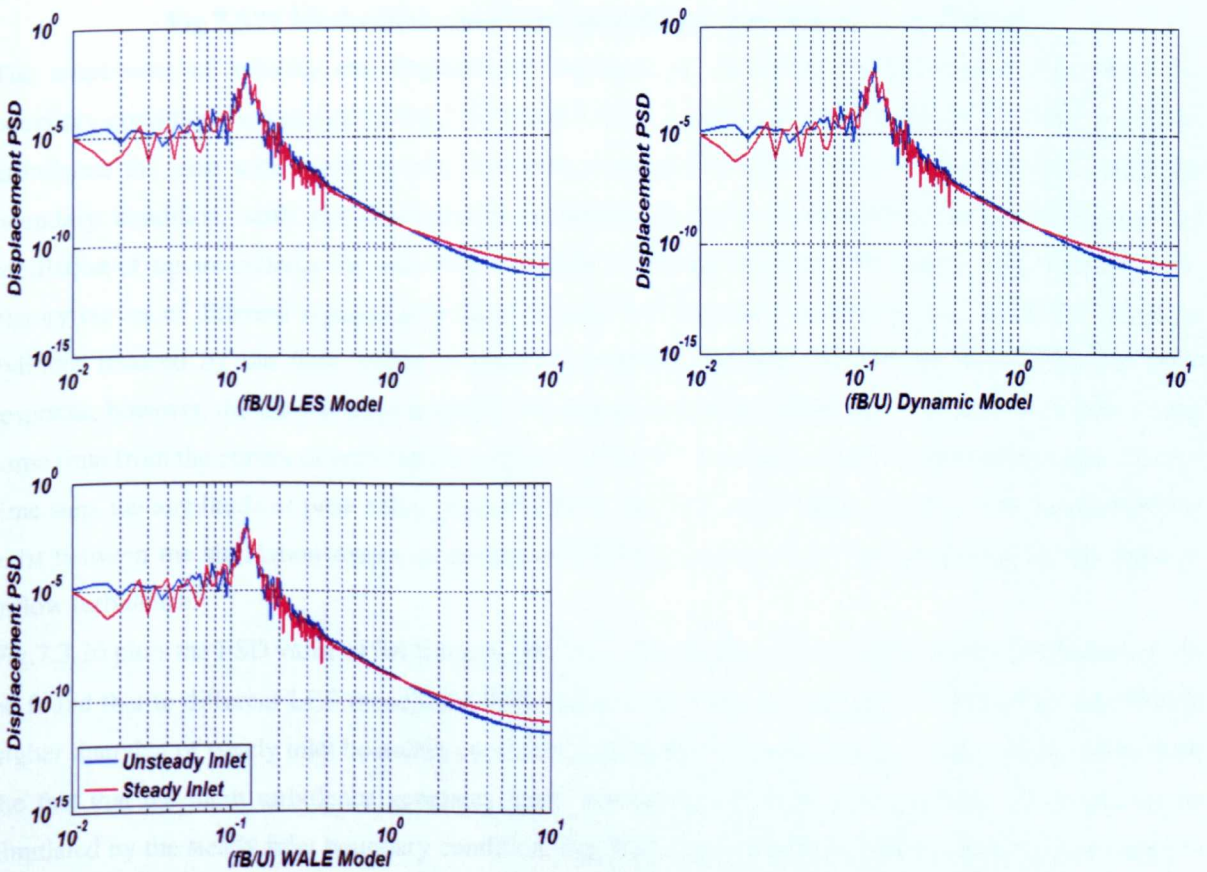


Fig 7.3.21 Displacement PSD of different LES models for two inlet boundary conditions

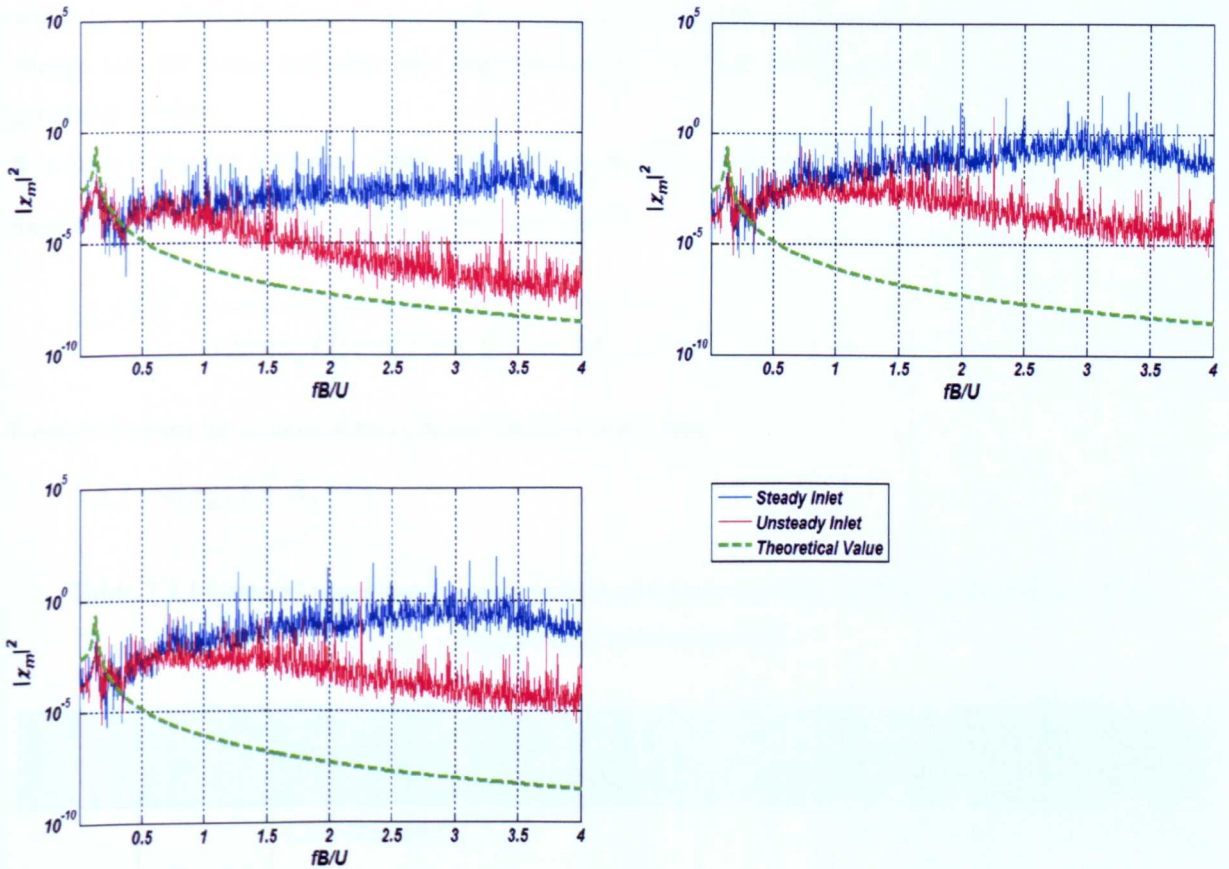


Fig 7.3.22 Mechanical admittance of different inlet boundary conditions

The amplitudes of velocity and displacement response of oscillating square cylinder for both inlet boundary conditions are plotted in Fig.7.3.18 and 7.3.19; it can be found that due to the input of inflow turbulence the case with unsteady inlet boundary condition oscillates earlier than that of steady inlet boundary condition, with the development of turbulence much more eddies are generated and the oscillation of square cylinder for both inlet boundary conditions develops with further step. From the time history curves of different reduced time steps of both inlet boundary conditions, the oscillation of square cylinder induced by the flow shows a mix-band response including the narrow band and wide band response, however, the narrow band response only happens in a very small reduced time step range. At the same time from the curves of both inlet boundary conditions, it is also found that even at the same reduced time step, the amplitude of peak value of oscillation is different, some phase angles or time step difference exist between the simulation results of both inlet boundary conditions, which are caused by the input of inflow turbulence.

Fig.7.3.20 plots the PSD value of lift force of different LES models at two inlet boundary conditions; it can be found that to different LES models the PSD value of lift force of unsteady inlet boundary condition is higher than that of steady inlet boundary condition at the high reduced frequency range, which results from the fact that the input turbulence generates much smaller and high frequency eddies, which can not be simulated by the steady inlet boundary condition. Fig.7.3.21 plots the PSD value of displacement response of different LES models, it can be found that the magnitude of peak value of significant frequency generated by the unsteady inlet boundary is higher than that from the steady inlet boundary condition,

which further shows that many more vortices are generated by the input of inflow turbulence. These eddies change the lift force, and then the amplitude of the induced oscillation is also influenced by these generated vortices.

It is known that for a system which is discrete, linear, and lightly damped, the square absolute value of mechanical admittance ($|\chi_m(f)|^2$) can be expressed as:

$$|\chi_m(f)|^2 = \frac{1}{(2\pi m f_n) \left\{ \left[1 - (f / f_n)^2 \right]^2 + (2\xi f / f_n)^2 \right\}} \quad (7.2.5)$$

Here, m denotes the structural mass including the added mass,

$$S_x(f) = |\chi_m(f)|^2 S_F(f) \quad (7.2.6)$$

Table 7.3.1 General aerodynamic parameters of square cylinder of different inlet boundary conditions concerning FSI

Simulation Cases		Model	Turbulence Intensity	Re Number	\bar{C}_D	C_D^{rms}	C_L^{rms}	St
FSI	Steady Inlet	LES-Standard	Smooth	13,000	2.704	2.766	1.236	0.120
		LES-Dynamic			2.771	2.833	1.356	0.120
		LES-WALE			2.762	2.734	1.366	0.120
	Unsteady Inlet	LES-Standard	5%		2.691	3.179	1.320	0.127
		LES-Dynamic			2.762	3.236	1.377	0.123
		LES-WALE			2.810	3.270	1.485	0.120

Table.7.3.1 summarizes the general aerodynamic parameters such as the RMS values of drag (C_D^{rms}) and lift (C_L^{rms}) coefficient the mean value of drag coefficient (\bar{C}_D) and the Strouhal number (St) of different LES models of current simulations. To the mean value of drag coefficient it can be found that the values of the cases with FSI are higher than the one from the cases without FSI in Table 6.4.2, due to the interaction between the flow field and structural field, the flow around the square cylinder varies so complexly that the magnitude of drag force is increased with the movement of square cylinder. To the RMS value of drag coefficient, it is clearly found that the RMS value of drag coefficient is clearly increased, when the inflow turbulence intensity is considered, and it is higher than that of the cases of steady inlet boundary. The reason is that the input of inflow turbulence generates much more complex fluctuating forces. In addition, to the simulation cases with FSI, it can be found that the RMS value of drag coefficient is also higher than that of the cases without FSI. However, to the RMS value of lift coefficient from the simulation cases with FSI, the values are higher than that of simulation cases without FSI in Table 6.4.2, which is caused by the

interaction between the flow field and structure itself, and the interaction increases the magnitude of fluctuating lift force. To the aerodynamic parameter (Strouhal number) controlling the dominant frequency, it is found that the values with FSI are lower than that without FSI, the reason is that the dominant frequency of lift force generated by the flow and vortices around the square cylinder is influenced by the movement of square cylinder. The structure absorbs the energy generated by the flow around the square cylinder and then changes the dominant frequency.

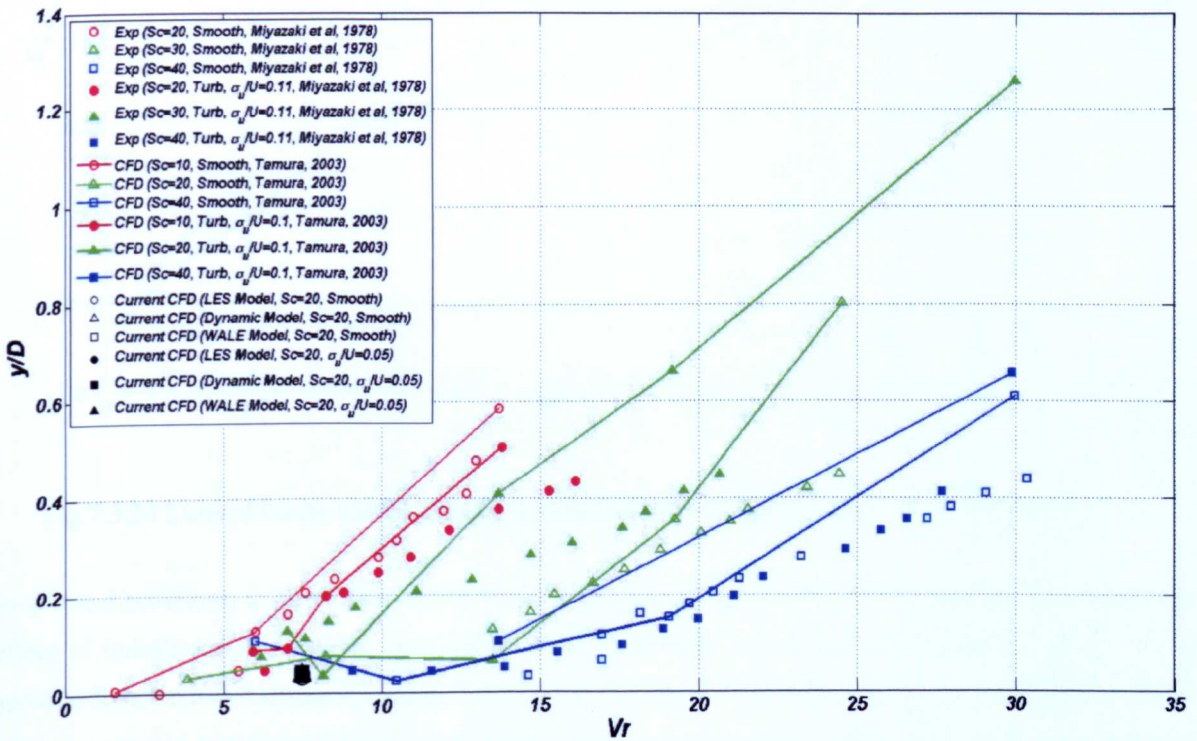


Fig.7.3.23 Response displacement for the reduced velocity (V_r)

Fig.7.3.23 shows current simulation results for response of square cylinder including the experimental data (A. Laneville *et al*, 1975 and M. Miyazaki *et al*, 1978). Comparing the results between smooth and turbulent flows, there is little effect of inflow turbulence on the onset of unstable oscillations for a square cylinder. It is confirmed that the computed results are in good agreement with the experimental data (A. Laneville *et al*, 1975 and M. Miyazaki *et al*, 1978). Concerning the dependency of responses of a square cylinder on the Scruton number, at small Sc the results show unstable oscillations from resonance speed and those at large Sc show that the unstable region is separated to vortex excitation and galloping regions. In current computations, the boundary value of Sc is 20. This value is smaller than those by Miyazaki *et al* (1978) and Tamura (2003), which is caused by the lower turbulence intensity. And the results of Tamura (2003) at Sc = 10, 40 are not influenced by the oncoming turbulence. However, in the case of Sc=20, the amplitude of the response near the onset velocity increases by the turbulence, though the value of onset velocity is not influenced by the oncoming turbulence. This phenomenon can be seen in the experimental data at Sc = 30 of Miyazaki *et al*. (1978).

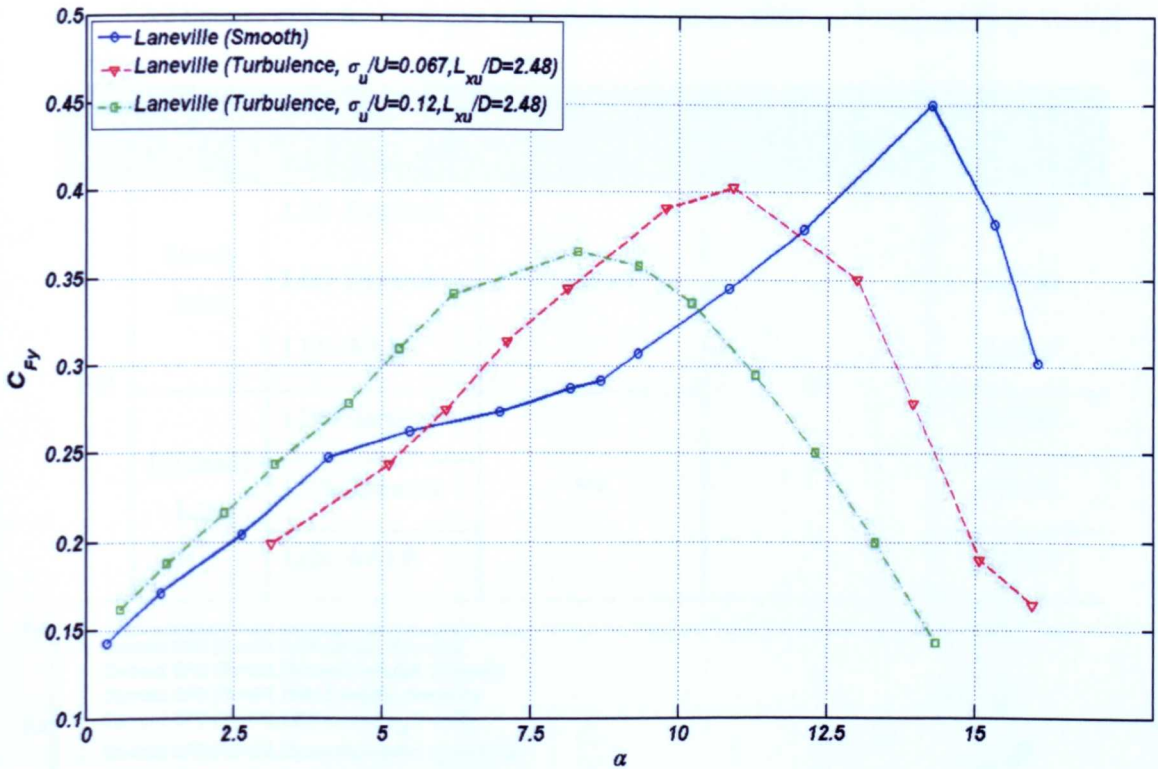


Fig.7.3.24 Lateral forces coefficients of square cylinder vs attack angle α by Laneville (1975)

In above discussions, it shows that current results for the response of $Sc = 20$ of square cylinder show the effect of turbulence on response. And the physical mechanism concerning the turbulence effects on the aeroelastic behavior of square cylinders is investigated in Fig.7.3.24, which shows the experimental results of time-averaged lateral force with angle of incidence (α) on a square cylinder in smooth and turbulent flows by Laneville *et al* (1975). Near $\alpha = 0$ the difference between the slope of lateral force ($dC_{Fy} / d\alpha$) in smooth flow and those in turbulent flows is very little. It can easily be predicted that the onset velocity of square cylinder in turbulent flow is close to that of smooth flow. On the other hand, some differences of C_{Fy} happens in the range that the attack angle is from 5 to 15. As shown in chapter 6, the flows around a square cylinder in both smooth and turbulent inflows are completely separated type at attack angle zero. Therefore, it can be expected that there is little effect of turbulence on the features of lateral force near attack angle zero. However, the inflow turbulence causes the separated shear layer to be thickened and to be close to the side surface of the cylinder. The thickened shear layer causes the occurrence of reattachment to be at smaller angle (Tamura, 2003).

Table 7.3.2 summarized the response value (y/D) of square cylinder based on different LES models at $Vr=7.5$, it can be found that the response value increases for the turbulence boundary condition, which further presnets the turbulence effects on the response of square cylinder, and it is also found by Tamura (2003).

Table 7.3.2 Square cylinder response value (y/D) based on different LES models at $Vr=7.5$

Simulation Cases		Model	Turbulence Intensity	Sc Number	y/D
FSI	Steady Inlet	LES-Standard	Smooth	20	0.0325
		LES-Dynamic			0.0340
		LES-WALE			0.0365
	Unsteady Inlet	LES-Standard			0.0390
		LES-Dynamic			0.0420
		LES-WALE			0.0393

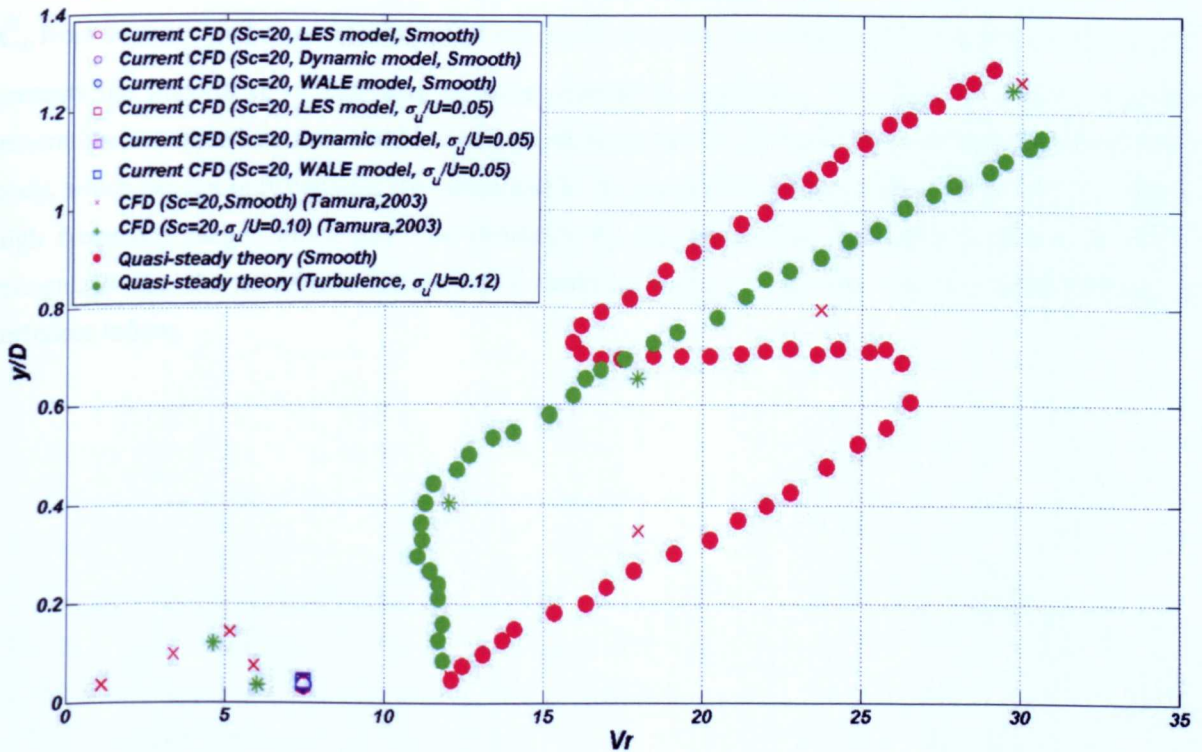


Fig.7.3.25 Response of square cylinder by different LES models and the quasi-steady theory (Sc=20)

Fig.7.3.25 shows the response obtained by different LES models and the quasi-steady theory based on Laneville's lateral force curves (A. Laneville *et al*, 1975). It can be found that two stable amplitudes of a galloping oscillation are generated from the shape of the lateral force curve for smooth flow, while the response amplitude for turbulent flow increases near the onset velocity. And It can be found that the turbulent case shows higher value of response near the onset velocity of galloping oscillation. The LES results from Tamura (2003) show that the inflow turbulence causes an increase of unstable oscillation. While for current simulations the effect of different LES models is little due to the low value of reduced velocity.

7.4 Conclusions

In this chapter, a square cylinder is used to simulate the buffeting response in the across-flow direction, and the following conclusions can be drawn from above simulations.

- (1) Current simulations basically capture the characteristics of square cylinder, and the FSI procedure of buffeting response simulation proposed in chapter 3 can be used in future buffeting response prediction. It is also found that the flow pattern around the bluff body will be complex considering FSI, the structural oscillation induced by the flow will change the flow pattern and generate new flow stress and then the flow movement with the time variation will generate new moving speed of bluff body in return.
- (2) From the PSD value of lift force, to different LES model, which model should be used to predict the buffeting response is worthwhile to considering, LES dynamic and WALE models give better results than that of standard LES model in the high frequency range.
- (3) From the values of general aerodynamic parameters, it is found the values such as C_D^{rms} , C_L^{rms} and \bar{C}_D from current simulation cases with FSI are higher than that from the cases without FSI, which further presents the importance of buffeting response simulation considering FSI. And the inflow turbulence generation technique based on ARMA model could be adopted to predict future buffeting response of bluff body, which can not only consider the turbulence in the upwind direction but also compensate the value of high frequency range, which can't be simulated by the steady inlet boundary condition. It can be recognized that the aeroelastic behavior and larger response can be seen near the onset velocity for turbulent inflow.

Chap 8 Conclusions and Future Work

In the previous chapters, the development of bridge buffeting simulation methods has been reviewed, and a cable-stayed bridge is used to investigate the effect of aeroelastic coupling, aerodynamics admittance and mode coupling on the simulation results based on the conventional simulation method of buffeting response in the frequency-domain. An alternative method known as POD is also proposed to simulate the bridge buffeting response. Besides the conventional buffeting simulation method in the frequency domain, 3D LES approach is also presented to investigate the possibility of bridge buffeting simulation considering different LES models. Due to the disadvantage of neglecting the influence of the inflow turbulence from the upwind direction, the inflow turbulence generation technique based on ARMA model is proposed and validated, by the research on the flow characteristics around a square cylinder. A FSI algorithm suitable for wind bridge interaction was proposed to predict the buffeting response, and the across-flow response of square cylinder is simulated and investigated under the steady inlet and unsteady inlet boundary conditions based on the propose FSI procedure. Some conclusions based on the above chapters will be drawn, as well as suggestions for future buffeting simulation.

8.1 Conclusions

- (1) Aeroelastic coupling analysis should be considered in future buffeting analyses, because the introduction of flutter derivatives influences the structural stiffness and damping. From the results in chapter 4, it can be found that the results of aeroelastic coupling analysis are smaller than the one from the conventional analysis method without considering this. Mode coupling effect should also be considered in future buffeting analyses. As the span of the bridge increases, the structural self vibration mode will be more complex, and the coupling effect of different modes will be obvious. The analysis shows that CQC mode combination method gives better results than those obtained by the SRSS method. The spatial distribution of gust wind load and wind flow reattachment can be considered by the unsteady aerodynamic admittance, avoiding the strip assumption and bringing the analysis closer to the condition of the real field
- (2) The POD method can decompose the wind turbulence into effective turbulence modes, which help to study the relationship between the structural self vibration modes and effective wind turbulence modes. In terms of the simulation results of POD technique, it can be found that not all wind turbulence can excite all structural self vibration mode, only some effective wind turbulence modes have such contribution.
- (3) The proposed time varying inflow turbulence generation technique based on ARMA model is an easy and effective method to consider the random inflow turbulence according to the need of target spectrum, which can be used to simulate the buffeting phenomena. From the results of velocity spectrum analysis, it can be found that the effect of inflow turbulence boundary updates the velocity spectrum, bring it closer to the target spectrum, and compensating for the disadvantages

related to the steady inflow, however some newly development numerical method is still need to compensate the decay in the PSD prediction of other two velocity components.

(4) Although the simulation results with steady inlet boundary condition can get good results for the general investigation of flow characteristics, to the high requirement of aerodynamic phenomena such as buffeting the unsteady inlet boundary condition based on ARMA model can present better results, especially to the random and unsteady characteristics of flow with high frequency.

(5) The closely coupled model proposed in chapter 3 provides an effective model for the investigation on the interaction between the wind and bridge deck system, which can not only couple the different fluid solvers and structure FE solvers via an interfacing technique, but also consider the problems related to large deformations or nonlinear deformations. From the simulation results of chapter 7, it can be found that the LES dynamic and WALE model are suitable for the prediction of flow induced oscillation of bluff body, in addition the inflow turbulence technique should be applied to the future buffeting response simulation.

8.2 Future Work

Although the method of bridge buffeting analysis has been discussed and some simulation results have been compared, there is still work to be done for future research.

(1) The coupling analyses and relationship between buffeting, vortex shedding and flutter should be further studied from the time domain or frequency domain. As suggested in chapter 1, the three aerodynamic phenomena coexist at some reduced velocity ranges. So a more complete analytical framework including flutter, buffeting and vortex shedding should be presented in the future.

(2) A buffeting response analysis method based on nonlinear random vibration should be proposed. When flutter occurs, the bridge system will show some nonlinear characteristics from the geometry to the material. So a complete nonlinear random vibration theory should be proposed to analyze the complete process from the linear state to the nonlinear state.

(3) The aerodynamic admittance and joint acceptance are still very important parameters to study the buffeting response, which can be discussed in detail based on the field test, the experimental and CFD method in future. With the span and complexity of the bridge structure shape, the structural response and vibration shape will be more complicated and show multi-mode vibration's characteristic. Therefore, the analysis procedure based on CFD and FSI considering multimode buffeting response should be proposed in the future.

References:

- [1] A. Laneville, I.S. Gartshore, G.V. Parkinson, (1975), "**An explanation of some effects turbulence on bluff bodies**", *Fourth International Conference on Wind Effects on Buildings and Structures*, London
- [2] Batina. J. T. (1990), "**Unsteady Euler airfoil solutions using unstructured dynamic meshes**", *AIAA J*, 28, No.8
- [3] Batina. J. T. (1991), "**Unsteady Euler algorithm with unstructured dynamic mesh for complex aircraft aerodynamic analysis**", *AIAA J*, 29, No.3
- [4] Bearman. P. Obasaju. E. (1982), "**An experimental study of pressure fluctuations on fixed and oscillating square cylinders**", *Journal of Fluid Mechanics*, Vol.119, 297-321
- [5] Bhardwaj M. K, Kapania. K, Reichenbach. E, Guruswamy. G. P, (1998), "**Computational fluid dynamics/computational structural dynamics interaction methodology for aircraft wings**", *AIAA J*, 36(12), 2179-86
- [6] Boonyapinyo. V, Miyata. T, Yamada. H, (1999), "**Advanced aerodynamic analysis of suspension bridges by state-space approach**", *J. Struct. Engrg, ASCE*, 125 (12), 1357-1366
- [7] Bunge. U, Gurr. A, Thiele. F, (2003), "**Numerical aspects of simulating the flow-induced oscillations of a rectangular bluff body**", *Journal of Fluids and Structures*, 18, 3-4, 405-424
- [8] Cervera. M., Codina. R, Galindo. M, (1996), "**on the computational efficiency and implementation of block-iterative algorithms for nonlinear coupled problems**", *Engineering Computations*, Vol.13. 6, 4-30
- [9] Cavagna. Luca, Guaranta. Giuseppe, Ghiringhelli. Gian. Luca, Mantegazza. Paolo, (2002), "**efficient applicaton of CFD aeroelstic methods using commerical software**"
- [10] Chen. Xin. Zhong, Matsumoto. Masaru, Kareem. Ahsan, (2000a), "**Time domain flutter and buffeting response analysis of bridges**", *J. Engrg. Mech., ASCE*, 126 (1), 7-16
- [11] Chen. Xin. Zhong, Matsumoto. Masaru, Kareem. Ahsan, (2000b), "**Aerodynamic coupling effects on flutter and buffeting of bridges**", *J. Engrg. Mech., ASCE*, 126 (1), 17-26
- [12] Chen. Xin. Zhong, Kareem. Ahsan, (2001a), "**Aeroelastic analysis of bridges under multicorrelated winds: integrated state-space approach**", *J. Engrg. Mech., ASCE*, 127 (11), 1124-1134
- [13] Chen. Xin. Zhong, Kareem. Ahsan, Matsumoto. Masaru, (2001b), "**Multimode coupled flutter and buffeting analysis of long-span bridges**", *J. Wind. Eng. Ind. Aerodyn*, 89, 649-664
- [14] Chen. Xin. Zhong, Kareem. Ahsan, (2001c), "**Nonlinear response analysis of long-span bridges under turbulent winds**", *J. Wind. Eng. Ind. Aerodyn*, 89, 1335-1350
- [15] Chen. Xin. Zhong, Kareem. Ahsan, (2002a), "**Advances in modeling of aerodynamic forces bridge decks**", *J. Engrg. Mech., ASCE*, 128 (11), 1193-1205

- [16] Chen. Xin. Zhong. Kareem. Ahsan, (2002b), "*Advanced analysis of coupled buffeting response of bridges: a complex modal decomposition approach*", *Probab. Engrg. Mech.* 17, 201-213
- [17] Chen. Xin. Zhong. Kareem. Ahsan, (2003), "*Aeroelastic analysis of bridges: effects of turbulence and aerodynamic nonlinearities*", *J. Engrg. Mech., ASCE*, 129 (8), 885-895
- [18] Chen. Y. P. Li. C. W. Zhang. C. K, (2008), "*Numerical modelling of a round jet discharged into random waves*", *Ocean Engineering*, 35, 77-89
- [19] Davenport. A. G, (1962), "*Buffeting of a suspension bridge by storm winds*", *J. Struct. Engrg. ASCE*, 88 (3), 233-268
- [20] Dettmer. W. G. Peric. D, (2007), "*A fully implicit computational strategy for strongly coupled fluid-solid interaction*", *Arch Comput. Methods Eng*, 14, 205-247
- [21] de With. G. Holdo. A. E, (2005), "*The use of turbulent inflow conditions for the modeling of a high aspect ratio jet*", *Fluid Dyn. Res*, 37, 443-461
- [22] Degand. Christoph. Farhat. Charbel, (2002), "*A three-dimensional torsional spring analogy method for unstructured dynamic meshes*", *Computers & Structures*, Vol.80, 3-4, 305-316
- [23] Deniz. S and Staubli. Th, (1997), "*Oscillating rectangular and octagonal profiles: interaction of leading- and trailing-edge vortex formation*", *Journal of Fluids and Structures*, 11, 1, 3-31
- [24] Deodatis. G, (1996), "*Simulation of ergodic multivariate stochastic processes*", *J. Eng. Mech., ASCE*, 122 (8), 778-787
- [25] Diana. G. Bruni. S. Collina. A. Zasso. A, (1998), "*Aerodynamic challenges in super long span bridges design*", *Bridge aerodynamics*, A. Larsen and S. Eisdahl, eds., Balkema, Rotterdam, the Netherlands, 131-144.
- [26] Diana. G. Cheli. F. Zasso. A. Boccione. M, (1999), "*Suspension bridge response to turbulent wind: Comparison of new numerical simulation method results with full scale data*", *Wind Engineering into the 21st Century*, G. L. Larose and F. M. Livesey eds, Balkema, Rotterdam, the Netherlands, 871-878.
- [27] Durao. D. G. Heitor. M. V. Pereira. J. F, (1988), "*Measurement of turbulent and periodic flows around a square cylinder*", *Experiments in Fluids*, Vol.6, 298-304
- [28] Elaine. Bohr. Jorge. Bailon-Cuba, Kenneth. Jansen, Luciano. Castillo, (2005), "*Inflow generation technique for large eddy simulation using equilibrium similarity analysis*", 4th *AIAA Theoretical Fluid Mechanics Meeting*
- [29] Eriksson. L. E, (1982), "*Generation of boundary-conformation grids around wing-body configurations using transfinite interpolation*", *AIAA J* 20, 10, 1313-1320
- [30] Facchini .Luca, (1996), "*The numerical simulation of Gaussian cross-correlated wind velocity fluctuations by means of a hybrid model*", *J. Wind. Eng. Ind. Aerodyn*, 64, 187-202

- [31] Farhat. C, Lesoinne. M, (2000), "**Two efficient staggered algorithms for the serial and parallel solution of three-dimensional nonlinear transient aeroelastic problems**", *Comput Methods Appl. Mech. Engrg*, 182, 499-515
- [32] Fernandez. M. A, Moubachir. Marwan, (2005), "**A Newton method using exact jacobians for solving fluid-structure coupling**", *Computers and Structures*, 83, 127-142
- [33] Franke. R, Rodi. W, (1991), "**Calculation of vortex shedding past square cylinder with various turbulence models**", *Proceedings 8th Symposium on Turbulent Shear Flows*, MUnich, Germany
- [34] Friedrich. R, Arnal. M, (1990), "**Analysing turbulent backward-facing step flow with the lowpass-filtered Navier-Stokes equations**", *J. Wind. Eng. Ind. Aerodyn*, 35, 101-128
- [35] Fu. Song, Xiao. Zhixiang, Chen. Haixin, Zhang. Yufei, Huang. Jingbo, (2007), "**Simulation of wing-body junction flows with hybrid RANS/LES methods**", *International Journal of Heat and Fluid Flow*, Vol.28, 6, 1379-1390
- [36] Germano. M, Piomelli. U, Moin. P, Cabot. W. H, (1996), "**Dynamic Subgrid-Scale Eddy Viscosity Model**", *In Summer Workshop, Centre for Turbulence Research, Stanford, CA*
- [37] Glaze. D. J, Frankel. S. H, (2003), "**Stochastic inlet conditions for large-eddy simulation of a fully turbulent jet**", *AIAA. J*, 41 (6), 1064–1073
- [38] Hangan. H, Vickery. B. J, (1999), "**Buffeting of two-dimensional bluff bodies**", *J. Wind. Eng. Ind. Aerodyn*, Vol.82, 1-3, 173-187
- [39] Hartwich P. M, Agrawal. S, (1997), "**Method for perturbing multiblock patched grids in aeroelastic and design optimization applications**", *AIAA Paper*, 2038
- [40] Havel. B, Hangan. H, Martinuzzi. R, (2001), "**Buffeting for 2D and 3D sharp-edged bluff bodies**", *J. Wind. Eng. Ind. Aerodyn*, Vol.89, 14-15, 1369-1381
- [41] Igarashi. T, (1987), "**Fluid flow and heat transfer around rectangular cylinders**", *International Journal of Heat and Mass Transfer*, Vol.30, 893-901
- [42] Iwatani. Y, (1982), "**Simulation of multidimensional wind fluctuations having any arbitrary power spectra and cross-spectra**", *J Wind Engng*, 11, 5–18.
- [43] Jochen. Fröhlich, Dominic. von Terzi, (2008), "**Hybrid LES/RANS methods for the simulation of turbulent flows**", *Progress in Aerospace Sciences*, Vol.44, 5, 349-377
- [44] Jain. A, N. P. Jone and R. H.Scanlan, (1996), "**Coupled flutter and buffeting analysis of long-span bridges**", *J. Struct. Eng., ASCE*, 122(7), 716-725
- [45] Kamakoti. Ramji, Shyy. Wei, (2004), "**Fluid-structure interaction for aeroelastic applications**", *Progress in Aerospace Sciences*, Vol.40, 8, 535-558
- [46] Kataoka. Hiroto, (2008), "**Numerical simulations of a wind-induced vibrating square cylinder within turbulent boundary layer**", *Journal of Wind Engineering and Industrial Aerodynamics*, Vol.96, 10-11, 1985-1997

- [47] Kempf. Anderas, Klein. Markus, Janicka. Johannes, (2005), "**Efficient generation of initial and inflow- condition for transient turbulent flows in arbitrary geometries**", *Flow, Turbulence and Combustion*, 74, 67-84
- [48] Kim. W. W, Menon. S. (1997), "**Application of the localized dynamic subgrid-scale model to turbulent wall-bounded flows**", *Technical Report AIAA-97-0210*, American Institute of Aeronautics and Astronautics, 35th Aerospace Sciences Meeting
- [49] Klein. M. Sadiki. A, Janicka. J, (2003), "**A digital filter based generation of inflow data for spatially developing direct numerical or large eddy simulations**", *J. Comput. Phys*, 186, 652-665
- [50] Kobayashi. H, Kawatani. M, Kim. H, (1992), "**Effects of turbulence characteristics on vortex-induced oscillation of rectangular cylinders**". *J. Wind Eng. Ind. Aerodyn*, 41, 775–784
- [51] Kondo. K, Murakami. S, Mochida. A, (1997), "**Generation of velocity fluctuations for inflow boundary condition of LES**", *J. Wind. Eng. Ind. Aerodyn*, 67&68, 51-64
- [52] Kovacs. Imre, Svensson. Holger. S, Jordet. Elljam, (1992), "**Analytical Aerodynamic Investigation of Cable-Stayed Helgeland Bridge**", *J. Struct. Engrg.*, Vol.118, 1, 147-168
- [53] Larose. L, Mann. J, (1998), "**Gust loading on streamlined bridge decks**". *Journal of Fluids and Structures*, 12, 511–536
- [54] Larose. Guy. L, (2003), "**The spatial distribution of unsteady loading due to gusts on bridge decks**", *Journal J. Wind. Eng. Ind. Aerodyn*, Vol.91, 12-15, 2003, 1431-1443
- [55] Launder. B, Spalding. D, (1974), "**The numerical computation of turbulent flows**", *Computer Methods in Applied Mechanics and Engineering*, 3, 269-289
- [56] Launder. B. E, Reece. G. J, Rodi. W, (1975), "**Progress in the development of a Reynolds stress turbulence closure**", *Journal of Fluid Mechanics*, 68, 537–566
- [57] Lee. S, Lele. S, Moin. P, (1992), "**Simulation of spatially evolving compressible turbulence and the application of tailors hypothesis**", *Phys. Fluids*, A.4, 1521-1530
- [58] Lee. B. E. (1975), "**The effects of turbulence on the surface pressure field of a square prism**", *J. Fluid Mech.*, 69, 263–282
- [59] Li. Y, Kareem. A, (1993), "**Simulation of multivariate random process: Hybrid DFT and digital filtering approach**", *J. Engrg. Mech, ASCE.*, 119 (5), 1078-1098
- [60] Li. You. Sun, Kareem. A, (1990), "**ARMA representation of wind field**", *J. Wind. Eng. Ind Aerodyn*, 36, 415-427
- [61] Liepmann. H.W, (1952), "**On the application of statistical concepts to the buffeting problem**", *Journal of Aeronautical Science*, 19, 793-810
- [62] Lilly. D. K, (1992), "**A Proposed Modification of the Germano Subgrid-Scale Closure Model**", *Physics of Fluids*, 4, 633-635
- [63] Longest. P. W, Kleinstreuer. Jr. C, Kinsey. J. S, (2000), "**Turbulent three-dimensional air flow and trace Gas distribution in an inhalation test chamber**", *Journal of Fluid Engineering*, 122, 403-411

- [64] Lubcke. H, Schimidt. St, Rung. T, Thiele. F, (2001), "**Comparison of LES and RANS in bluff-body flows**", *J. Wind. Eng. Ind. Aerodyn*, 89, 1471-1485
- [65] Lund. Thomas. S, Wu. Xiaohua, Squires. Kyle. D, (1998), "**Generation of turbulent inflow data from spatially-developing boundary layer simulations**", *Journal of Computational Physics*, 140, 233-258
- [66] Lyn. D. A, Einav. S, Rodi. W, Park. J. H, (1995), "**A laser-Doppler velocimetry study of ensemble-averaged characteristics of the turbulent near wake of a square cylinder**", *Journal of Fluid Mechanics*, Vol.304, 285-319
- [67] M. Miyazaki, T. Miyata (1978), "**Effect of turbulence scale on aerodynamic response of rectangular cylinders**", *Proceedings of the Fifth Symposium on Wind Effects on Structures*, Tokyo
- [68] Matsumoto, M, Chen, X, (1994). "**The contribution of natural vibration modes to the aerodynamic flutter**", *Journal of Structural Engineering, Japan Society of Civil Engineers*, 40A, 1025-1030 (in Japanese)
- [69] Martinuzzi. Robert. J, Havel. Brian, (2000), "**Turbulent Flow Around Two Interfering Surface-Mounted Cubic Obstacles in Tandem Arrangement**", *J. Fluids Eng.*, Vol.122, 24-31
- [70] Matthies. Hermann. G, Steindorf. Jan, (2002), "**Partitioned by strongly coupled iteration schemes for nonlinear fluid-structure interaction**", *Computers and Structures*, 80, 1991-1999
- [71] Matthies. Hermann. G, Steindorf. Jan, (2003), "**Partitioned strongly coupling algorithms for fluid-structure interaction**", *Computers and Structures*, 81, 805-812
- [72] Menter. F. R, (1994), "**Two-equation eddy-viscosity turbulence models for engineering applications**", *AIAA-Journal*, 32, 8, 1598-1605
- [73] Menter. F. R, Kuntz. M., Bender. R, (2003), "**A scale-adaptive simulation model for turbulent flow predictions**", *AIAA Paper*, 767
- [74] Mignolet. Marcp, Spanos. Pol. D, (1990), "**MA to ARMA modeling of wind**", *J. Wind. Eng Ind. Aerodyn*, 36, 429-438
- [75] Miyata. T, Yamada. H, (1988) "**Coupled flutter estimate of a suspension bridge**", *J. Wind Eng. (Japan)*, (37), 485-492.
- [76] Murakami. S, (1998), "**Overview of turbulence models applied in CWE-1997**", *J. Wind. Eng. Ind. Aerodyn*, 74-76, 1-24
- [77] Nakayama. A, Vengadesan. S. N, (2002), "**On the influence of numerical schemes and subgrid-stress models on large eddy simulation of turbulent flow past a square cylinder**", *International Journal for Numerical Methods in Fluids*, 38, 227-253
- [78] Naudascher. E, Wang. Y, (1993), "**Flow-Induced Vibrations of Prismatic Bodies and Grids of Prisms**", *Journal of Fluids and Structures*, 7, 4, 341-373
- [79] Nicoud. F, Ducros. F, (1999), "**Subgrid-Scale Stress Modelling Based on the Square of the Velocity Gradient Tensor**", *Flow, Turbulence, and Combustion*, 62 (3), 183-200

- [80] Noda. H, Nakayama. A, (2003), "**Reproducibility of flow past two-dimensional rectangular cylinders in a homogeneous turbulent flow by LES**", *J. Wind. Eng. Ind. Aerodyn*, 91, 1-2, 265-278
- [81] Norberg. C, (1993), "**Flow around rectangular cylinders: Pressure forces and wake frequencies**", *J. Wind. Eng. Ind. Aerodyn*, 49, 187-196
- [82] Novak M, (1969), "**Aeroelastic galloping of prismatic bodies**". *J Eng Mech Div Proc ASCE*, 9, 115-142
- [83] Novak. M, (1972), "**Galloping oscillations of prismatic structures**", *J Eng Mech Div Proc ASCE*, 98, 27-46
- [84] Nozawa. K, Tamura. T, (2002), "**Large eddy simulation of the flow around a low-rise building immersed in a rough-wall turbulent boundary layer**", *J. Wind. Eng. Ind. Aerodyn*, 90, 1151-1162
- [85] Okajima. A, (1982), "**Strouhal number of rectangular cylinders**", *Journal of Fluid Mechanics*, Vol.123, 379-398
- [86] Parker. R, Welsh. M. C, (1981), "**The effect of sound on flow over bluff bodies**", *University of Wales, Swansea, Mechanical Engineering Report*, MR/87/81
- [87] Piomelli. U, Balaes. E, (2002), "**Wall-layer models for Large Eddy Simulation**", *Ann Rev Fluid Mech*, 34, 349
- [88] Rodi. W, Ferziger. J. H, Breuer. M, Pourqui. M, (1995), "**in: Proc. Workshop on Large-Eddy Simulation of Flows past Bluff Bodies**", Rottach-Egern, Germany
- [89] Rodi. W, (1997a), "**Comparison of LES and RANS calculations of the flow around bluff bodies**", *J. Wind. Eng. Ind. Aerodyn*, 69-71, 55-75
- [90] Rodi. W, Ferziger. J. H, Breuer. M, Pourqui. M, (1997b), "**Status of large-eddy simulation: Results of a workshop**", *J. Fluids Eng*, 119, 248-262
- [91] Sakamoto. H, Haniu. H, (1988), "**Aerodynamic forces acting on two square prisms placed vertically in a turbulent boundary layer**", *J. Wind. Eng. Ind. Aerodyn*, Vol.31, 1, 41-66
- [92] Sakamoto. H, Haniu. H, Kobayashi. Y, (1989), "**Fluctuating force acting on rectangular cylinders in uniform flow (on rectangular cylinders with fully separated flow)**", *Trans Jpn Soc Mech Eng Ser B*, 55(516), 2310-2317
- [93] Samaras. E, Shinozuka. M, Tsurui. A, (1983), "**ARMA representation of random processes**", *J. Engrg. Mech, ASCE*, 111, 449-461
- [94] Sankaran. R, Jancauskas. E. D, (1992), "**Direct measurement of the aerodynamic admittance of two-dimensional rectangular cylinders in smooth and turbulent flows**", *J. Wind. Eng. Ind. Aerodyn*, 41-44, 601-611
- [95] Saul. W. E, Jayachandran. P, Peyrot A. H, (1976), "**Response to stochastic wind of N-degree Tall Buildings**", *Journal of the Structural Division ASCE*, 102(ST5),1059-1075
- [96] Scanlan. R. H, Tomko. J. J, (1971), "**Airfoil and bridge deck flutter derivatives**", *J. Engrg. Mech., ASCE*, 97 (EM6), 1717-1737

- [97] Scanlan. R. H. (1978a), "*The action of flexible bridges under wind. Part I: Flutter theory*", *J. Sound Vib*, 60 (2), 187-199
- [98] Scanlan. R. H. (1978b), "*The action of flexible bridges under wind. Part II: Buffeting theory*." *J. Sound Vib*, 60 (2), 201-211
- [99] Scanlan. R. H., Beliveau. J. G., Budlong. K. S., (1996), "*Indicial aerodynamic functions for bridge decks*", *J. Struct. Engrg*, ASCE, 122(7), 716-725
- [100] Schluer. J. U., Pitsch. H., Moin. P., (2004), "*Large eddy simulation inflow conditions for coupling with Reynolds-averaged flow solver*", *AIAA Journal*, 42, 3, 478-484
- [101] Selberg. A (1961), "*Oscillation and aerodynamic stability of suspension bridge*", *ACTA Polytechnica Scandinavica*, Civil Eng, and Building Constructuon No.13
- [102] Shimada. K, Ishihara. T, (2002), "*Application of a modified $k-\epsilon$ model to the prediction of aerodynamic characteristics of rectangular cross-section cylinders*", *Journal of Fluids and Structures*, 16, 4, 465-485
- [103] Shinozuka. M, (1970), "*Simulation of multivariate and multidimensional random processes*", *J. Acoustic Society of America*, 49, 357-368
- [104] Shinozuka. M, Jan. C. M, (1972), "*Digital simulation of random processes and its applications*", *J. Sound Vib*, 25 (1), 111-128
- [105] Simiu. E, Scanlan. R. H, (1996), "*Wind effects on structures. An introduction to wind engineering. Second edition*", John Wiley & Sons, New York
- [106] Smagorinsky. J, (1963), "*General Circulation Experiments with the Primitive Equations. I. The Basic Experiment*", *Month. Wea. Rev.*, 91:99-164
- [107] Smirnov. A, Shi. S, Celik. I, (2001), "*Random flow generation technique for large eddy simulations and particle dynamic modeling*", *Journal of Fluid Engineering*, 123, 359-371
- [108] Smith. Doug. (1974), "*An evaluation of computational algorithms to interface between CFD and CSD methodologies*". 99.497 Project Report, Carleton Univeristy, Canada
- [109] Sohankar. A, Norberg. C, Davidson. L, (1999), "*Numerical simulation of flow past a square cylinder*", *In 3rd ASME/JSME Joint Fluids Engineering Conference*, California
- [110] Sohankar. A, Davidson. L, Norberg. C, (2002), "*Large Eddy Simulation of Flow Past a Square Cylinder: Comparison of Different Subgrid Scale Models*", *Journal of Fluids Engineering*, 122, 39-47
- [111] Solari. G, Carassale. L, Piccardo. G, (2001), "*Double modal transformation and wind engineering applicaions*", *J. Engrg. Mech.*, ASCE, 127 (5), 432-439
- [112] Solari. G, Tubino. Federica, (2007), "*Gust buffeting of long span bridges: Double modal transformation and effective turbulence*", *J. Engrg. Struc*, 29 (8), 1698-1707
- [113] Spalart. P. R, Allmaras. S. R, (1992), "*A One-Equation Turbulence Model for Aerodynamic Flows*", *AIAA Paper*, 92, 0439

- [114] Spalart, P.R, Jou, W.-H, Strelets, M, Allmaras, S.R. "**Comments on the feasibility of LES for wings, and on a hybrid RANS/LES approach**", 1st AFOSR Int. Conf. On DNS/LES, Aug.4-8, 1997, Ruston, LA. In *Advances in DNS/LES*, C. Liu & Z. Liu Eds., Greyden Press, Colombus, OH.
- [115] Spalart. P. R, (2000), "**Strategies for turbulence modelling and simulations**", *International Journal of Heat and Fluid Flow*, 21(3), 252-263
- [116] Srinivas. Y., Biswas. G, Parihar. A. S, Ranjan. R, (2006), "**Large eddy simulation of high Reynolds number turbulent flow past a square cylinder** ", *J. Engrg. Mech., ASCE*, 132, No.3, 327-335
- [117] Stanley. S, Sarkar. S, Mellado. J, (2000), "**A study of the flow field evolution and mixing in a planar turbulent jet using direct numerical simulation**", *J. Fluid Mech*, 450, 377-407
- [118] Strelets. M, (2001), "**Detached Eddy Simulation of Massively Separated Flows**", *AIAA Paper*, 879
- [119] Tamura. T, (1999), "**Reliability on CFD estimation for wind-structure interaction problems**", *J. Wind. Eng. Ind. Aerodyn*, 81, 1-3, 117-143
- [120] Tamura. T, Dias. P. P. N. L, (2003), "**Unstable aerodynamic phenomena around the resonant velocity of a rectangular cylinder with small side ratio**", *J. Wind. Eng. Ind. Aerodyn*, 91, 1- 2, 127-138
- [121] Tamura. Tetsuro, (2008), "**Towards practical use of LES in wind engineering**", *J. Wind. Eng. Ind. Aerodyn*, Vol.96, 10-11, 1451-1471
- [122] Tang. Tao, (2007), <http://www.movingmesh.org/>
- [123] Theodorsen. T, (1935), "**General theory of aerodynamic instability and the mechanism of flutter**", *NACA Report No.496*, U.S.National Advisory Committee for Aeronautics Langley Aerodynamic forces acting on two square prisms placed vertically in a turbulent boundary layer
- [124] Travin. A, Shur. M, Strelets. M, (2000), "**Physical and numerical upgrades in detached-eddy simulation of complex turbulent flows**", *412 EUROMECH colloquium on LES of complex transitional and turbulent flows, Munich*
- [125] Von Karman, (1948), "**Progress in the Statistical Theory of Turbulence**", *Proc. Natl. Acad. Sc.*, 34, 530-539
- [126] Wyatt. T.A, May. H.I, (1973), "**The generation of stochastic load functions to simulate wind loads on structures**", *International Journal of Earthquake Engineering and Structural Dynamics*, 1(3), 217-224
- [127] Yu. D, Kareem. A, (1995), "**Two-dimensional simulation of flow around rectangular prisms**", *J. Wind Eng. Ind. Aerodyn*, 62, 131-161.
- [128] Yu. D, Kareem. A, (1997), "**Numerical simulation of flow around rectangular prism**", *J. Wind Eng. Ind. Aerodyn*. 67&68, 195-208
- [129] Zang. Yan, Street. Robert L, Koseff. Jeffrey R, (1993), "**A dynamic mixed subgrid-scale model and its application to turbulent recirculating flows**", *Phys. Fluids A*, Vol.5, 12, 3186-3198

References

- [130] Zdravkovich. M. M, (1977), "*Review-Review of Flow Interface Between Two Circular Cylinders in Various Arrangements*", *Transactions of the ASME*, 618-633
- [131] Zhang. H. Melbourne. W. H, (1992), "*Interference between two circular cylinders in tandem in turbulent flow*", *J. Wind. Eng. Ind. Aerodyn*, Vol.41, 1-3, 589-600
- [132] Zienkiewicz. O. C, Bettess. P, (1978), "*Fluid-structure dynamic interaction and wave forces. An introduction to numerical treatment*", *International Journal for Numerical Methods in Engineering*, 13, 1, 1-16
- [133] Zienkiewicz. O. C, Taylor. R. L, (1985), "*Coupled problems — a simple time-stepping procedure*", *Communications in applied numerical methods*, Vol.1, 5, 233-239

APPENDIX

Appendix 1 Buffeting Analysis Procedure Based On State Space Method

Based on the buffeting prediction theory proposed by Chen *et al.* (2002b), the equations of motion of an N degree-of-freedom bridge in terms of first M ($M < N$) structural modal coordinates q are expressed as

$$\mathbf{M}\ddot{\mathbf{q}} + \mathbf{C}\dot{\mathbf{q}} + \mathbf{K}\mathbf{q} = \mathbf{Q}_{se} + \mathbf{Q}_b \quad (\text{A1.1})$$

Where $\mathbf{M} = \text{diag}[m_j]$, $\mathbf{C} = \text{diag}[2\xi_{sj}\omega_{sj}m_j]$ and $\mathbf{K} = \text{diag}[2\xi_{sj}\omega_{sj}m_j]$ are $M \times M$ generalized mass, damping and stiffness matrices, respectively, m_j , ξ_{sj} and ω_{sj} are the generalized mass, damping coefficient and circular frequency for j th structural mode; \mathbf{Q}_{se} and \mathbf{Q}_b are $M \times 1$ generalized self-excited and buffeting force vectors, respectively. Chen *et al.* (2000a, 2001b) combined the Davenport and Scanlan's theory together and considered the aerodynamic admittance and aerodynamic coefficient influence on the buffeting force. Chen *et al.* (2000b) expressed the self excited force item (\mathbf{Q}_{se}) and buffeting force item (\mathbf{Q}_b) in Eq.A1.1 with the following expressions:

$$\mathbf{Q}_{se} = \frac{1}{2}\rho U^2 \left(\mathbf{A}_s(ik)\mathbf{q} + \frac{B}{U}\mathbf{A}_d(ik)\dot{\mathbf{q}} \right) \quad (\text{A1.2a})$$

$$\mathbf{Q}_b = \frac{1}{2}\rho U^2 \left(\mathbf{A}_{bu}(ik)\frac{\mathbf{u}}{U} + \mathbf{A}_{bw}(ik)\frac{\mathbf{w}}{U} \right) \quad (\text{A1.2b})$$

Where ρ is the air density, U is the mean wind velocity, $k = b\omega/U$ is the reduced frequency, $B = 2b$ is the bridge deck width, ω is the circular frequency of vibration; \mathbf{A}_s and \mathbf{A}_d are the aerodynamic stiffness and damping matrices, respectively, which are functions of flutter derivatives and structural mode shapes. \mathbf{A}_{bu} and \mathbf{A}_{bw} are the buffeting force matrices, which are functions of admittance and joint acceptance functions and structural mode shapes, and \mathbf{u} and \mathbf{w} are the fluctuating wind vectors at element nodes for the longitudinal and vertical components, respectively. So the equations of structural motion are expressed in the state-space format as:

$$\dot{\mathbf{Y}} = \mathbf{A}_0\mathbf{Y}_0 + \mathbf{B}_0\mathbf{Q}_b \quad (\text{A1.3})$$

Where,

$$\mathbf{Y}_0 = \begin{Bmatrix} \mathbf{q} \\ \dot{\mathbf{q}} \end{Bmatrix}, \mathbf{A}_0 = \begin{bmatrix} \mathbf{0} & \mathbf{I} \\ -\mathbf{M}^{-1}\mathbf{K}_1 & -\mathbf{M}^{-1}\mathbf{C}_1 \end{bmatrix}, \mathbf{B}_0 = \begin{Bmatrix} \mathbf{0} \\ \mathbf{M}^{-1} \end{Bmatrix}$$

$$\mathbf{C}_1 = \mathbf{C} - \frac{1}{2}\rho U b \mathbf{A}_d(k), \mathbf{K}_1 = \mathbf{K} - \frac{1}{2}\rho U^2 \mathbf{A}_s(k)$$

In Eq.A1.3 \mathbf{C}_1 and \mathbf{K}_1 are frequency dependent and no longer diagonal due to the presence of the coupled aerodynamic damping and stiffness terms.

The transfer function matrix between modal response \mathbf{q} and modal buffeting force \mathbf{Q}_b is given as

$$\mathbf{H}_q(\omega) = (-\omega^2 \mathbf{M} + i\omega \mathbf{C}_1(k) + \mathbf{K}_1(k))^{-1} \quad (\text{A1.4})$$

Conventional coupled buffeting analysis requires matrix inversion at each discrete frequency based on the evaluation of $\mathbf{H}_q(\omega)$, which places a high demand on computational effort. Such a time consuming procedure can be eliminated by using a frequency independent state-space equations of an integrated system of the bridge and aerodynamics. This can be derived by utilizing rational function approximations of the self-excited forces and introduction augmented aerodynamic states. The self-excited forces corresponding to the steady-state motion $q(t) = \bar{q}e^{i\omega t}$ can be approximated in terms of a rational function:

$$\begin{aligned} Q_{se}(t) &= \frac{1}{2} \rho U^2 (A_s + (ik)A_d) \bar{q}e^{i\omega t} \\ &= \frac{1}{2} \rho U^2 \left(A_1 + (ik)A_2 + (ik)^2 A_3 + \sum_{l=1}^m \frac{(ik)A_{l+3}}{ik + d_l} \right) \bar{q}e^{i\omega t} \end{aligned} \quad (\text{A1.5})$$

Where A_1, A_2, A_3, A_{l+3} and d_l ($d_l \geq 0; l = 1, \dots, m$) are frequency independent matrices and a parameter which can be determined by curve-fitting the experimentally obtained data of $A_s(k)$ and $A_d(k)$ defined at a set of discretized reduced velocities k_j ($j = 1, 2, \dots$) using a least-square approach. After some manipulations, the equations of motion can be expressed as the following frequency independent state-space equations:

$$\dot{\hat{\mathbf{Y}}} = \hat{\mathbf{A}}_0 \hat{\mathbf{Y}}_0 + \hat{\mathbf{B}}_0 \mathbf{Q}_b(t) \quad (\text{A1.6})$$

Where

$$\hat{\mathbf{A}} = \begin{bmatrix} \mathbf{0} & \mathbf{I} & \mathbf{0} & \dots & \mathbf{0} \\ -\bar{\mathbf{M}}^{-1} \bar{\mathbf{K}} & -\bar{\mathbf{M}}^{-1} \bar{\mathbf{C}} & \frac{1}{2} \rho U^2 \bar{\mathbf{M}}^{-1} & \dots & \frac{1}{2} \rho U^2 \bar{\mathbf{M}}^{-1} \\ \mathbf{0} & \mathbf{A}_4 & -\frac{U}{B} d_1 \mathbf{I} & \dots & \mathbf{0} \\ \vdots & \vdots & \vdots & \dots & \vdots \\ \mathbf{0} & \mathbf{A}_{3+m} & \mathbf{0} & \dots & -\frac{U}{b} d_m \mathbf{I} \end{bmatrix}, \mathbf{Y} = \begin{bmatrix} q \\ \dot{q} \\ q_{sel} \\ \vdots \\ q_{sem} \end{bmatrix}, \mathbf{B} = \begin{bmatrix} \mathbf{0} \\ \bar{\mathbf{M}}^{-1} \\ \mathbf{0} \\ \vdots \\ \mathbf{0} \end{bmatrix}$$

Here $\bar{\mathbf{M}} = \mathbf{M} - \frac{1}{2} \rho B^2 A_3$, $\bar{\mathbf{C}} = \mathbf{C} - \frac{1}{2} \rho U B A_2$, $\bar{\mathbf{K}} = \mathbf{K} - \frac{1}{2} \rho U^2 A_1$, ξ_{sel} ($l = 1 \sim m$) are the introduced new vectors representing the unsteady aerodynamic states. In present study, a further simplified framework for buffeting response analysis in both time and frequency domains can be expressed as the following equations based on the complex modal decomposition technique. So the equation A1.6 can be expressed as:

$$\dot{\mathbf{Y}} = \mathbf{A}_{ef} \mathbf{Y} + \mathbf{B} \mathbf{Q}_b \quad (\text{A1.7})$$

Where

$$\mathbf{Y} = \begin{Bmatrix} \mathbf{q} \\ \dot{\mathbf{q}} \end{Bmatrix}; \mathbf{A}_{ef} = \begin{bmatrix} 0 & I \\ -\mathbf{M}^{-1}\mathbf{K}_{ef} & -\mathbf{M}^{-1}\mathbf{C}_{ef} \end{bmatrix}, \mathbf{B} = \begin{Bmatrix} 0 \\ \mathbf{M}^{-1} \end{Bmatrix}$$

Where \mathbf{K}_{ef} , \mathbf{C}_{ef} are the effective (equivalent) stiffness and damping matrices, which are independent of frequency. The equations of the linear system in Eq.A1.7 can be used for the buffeting response analysis in the frequency domain. By introducing the following transformation

$$\mathbf{Y}(t) = \mathbf{\Gamma}\mathbf{R}(t) \quad (\text{A1.8})$$

Eq.A1.8 can be expressed in terms of $2M$ uncoupled equations:

$$\mathbf{R}(t) = \mathbf{\Lambda}\mathbf{R}(t) + \mathbf{\Gamma}^{-1}\mathbf{B}\mathbf{Q}_b(t) \quad (\text{A1.9})$$

Where

$$\mathbf{\Gamma} = [\mathbf{\Gamma}_1 \quad \mathbf{\Gamma}_2 \quad \dots \quad \mathbf{\Gamma}_{2M}] = \begin{Bmatrix} \mathbf{\Phi} \\ \mathbf{\Lambda}\mathbf{\Phi} \end{Bmatrix}, \mathbf{\Phi} = [\mathbf{\Phi}_1 \quad \mathbf{\Phi}_2 \quad \dots \quad \mathbf{\Phi}_{2M}],$$

$$\mathbf{\Gamma}^{-1}\mathbf{A}_{ef}\mathbf{\Gamma} = \mathbf{\Lambda} = \text{diag}[\lambda_j]$$

Eq.A1.8 and A1.9 can be expressed in frequency domain through a Fourier transform

$$\mathbf{q}(\omega) = \mathbf{H}_q(\omega)\mathbf{Q}_b(\omega) \quad (\text{A1.10})$$

In which the transfer matrix $\mathbf{H}_q(\omega)$ is

$$\begin{aligned} \mathbf{H}_q(\omega) &= \mathbf{\Phi}(i\omega\mathbf{I} - \mathbf{\Lambda})^{-1}\mathbf{\Gamma}^{-1}\mathbf{B} \\ &= \sum_{j=1}^M \left(\frac{\mathbf{\Phi}_j\mathbf{\Theta}_j^T / m_j + \mathbf{\Phi}_j^*\mathbf{\Theta}_j^{*T} / m_j}{i\omega - \lambda_j + i2\xi_j\omega} \right) = \sum_{j=1}^M H_{j0}(\omega)((i\omega)\mathbf{E}^j + \mathbf{F}^j) \end{aligned} \quad (\text{A1.11})$$

Where,

$$\mathbf{E}^j = \mathbf{\Phi}_j\mathbf{\Theta}_j^T + \mathbf{\Phi}_j^*\mathbf{\Theta}_j^{*T}, \quad \mathbf{F}^j = -(\mathbf{\Phi}_j\mathbf{\Theta}_j^T\lambda_j^* + \mathbf{\Phi}_j^*\mathbf{\Theta}_j^{*T}\lambda_j)$$

$$H_{j0}(\omega) = \frac{1}{m_j(\omega_j^2 - \omega^2 + i2\xi_j\omega)}$$

Using the transfer matrix in terms of the complex mode properties, the PSD matrix of the mode response can be expressed as:

$$\mathbf{S}(\omega) = \sum_{j=1}^M \sum_{l=1}^M H_{j0}^*(\omega) H_{l0}(\omega) \mathbf{S}_{Q_{bc}^{jl}}(\omega) \quad (\text{A1.12})$$

Where

$$\mathbf{S}_{Q_{bc}^{jl}}(\omega) = [(i\omega)\mathbf{E}^j + \mathbf{F}^j] \mathbf{S}_{Q_b}(\omega) [(-i\omega)(\mathbf{E}^l)^T + (\mathbf{F}^l)^T]^T$$

Response PSD can also be calculated based on Eq.A1.12, mode combination methods such as SRSS and CQC can be used when considering the mode contribution.

Published Papers

The published and under-reviewed papers during the thesis writing are listed:

1. Zhe. Liu, 2009, **Square Cylinder Large Eddy Simulation Based on Random Inlet Boundary Condition2D**, *Journal of Applied Fluid Mechanics*, Vol.3. No.1, pp.33-45 (published)
2. Zhe. Liu and Yongkun Luo, 2011, **Bridge Buffeting Analysis Based on POD and Aeroelastic Coupling Method**, *Journal of Advanced Materials Research*, Vol.163-167, (published)
3. Zhe. Liu and Huixuan Huang, 2010, **The Characteristics' Study of Flow around A Square Cylinder Based on Different LES Models**, *Journal of Zhejiang University*, (under review)
4. Zhe. Liu, 2010, **Flow Characteristics Study around Square Cylinder Considering Inflow Turbulence**, *Engineering Application of Computational Fluid Mechanics* (under review of the revised one)
5. Zhe. Liu, 2010, **Flow Induced Response of Square Cylinder at Different LES Models with Inflow Turbulence**, *Internal Conference on Civil Engineering, Architecture and Building Materials 2011* (under review)